

Nonlinear dynamics and chaos in multidimensional disordered Hamiltonian systems

Bertin Many Manda

UNIVERSITY OF CAPE TOWN

DEPARTMENT OF MATHEMATICS AND APPLIED MATHEMATICS

PHD DISSERTATION

**Nonlinear dynamics and chaos in
multidimensional disordered Hamiltonian
systems**

Author:
Bertin MANY MANDA

Supervisor:
A/Prof. Charalampos SKOKOS

May 11, 2021



Abstract

In this thesis we study the chaotic behavior of multidimensional Hamiltonian systems in the presence of nonlinearity and disorder. It is known that any localized initial excitation in a large enough linear disordered system spreads for a finite amount of time and then halts forever. This phenomenon is called Anderson localization (AL). What happens to AL when nonlinearity is introduced is an interesting question which has been considered in several studies over the past decades. Recent works focussing on two widely-applicable systems, namely the disordered Klein-Gordon (DKG) lattice of anharmonic oscillators and the disordered discrete nonlinear Schrödinger (DDNLS) equation, mainly in one spatial dimension suggest that nonlinearity eventually destroys AL. This leads to an infinite diffusive spreading of initially localized wave packets whose extent (measured for instance through the wave packet's second moment m_2) grows in time t as t^{α_m} with $0 < \alpha_m < 1$. However, the characteristics and the asymptotic fate of such evolutions still remain an issue of intense debate due to their computational difficulty, especially in systems of more than one spatial dimension. Two different spreading regimes, the so-called weak and strong chaos regimes, have been theoretically predicted and numerically identified. As the spreading of initially localized wave packets is a non-equilibrium thermalization process related to the ergodic and chaotic properties of the system, in our work we investigate the properties of chaos studying the behavior of observables related to the system's tangent dynamics. In particular, we consider the DDNLS model of one (1D) and two (2D) spatial dimensions and develop robust, efficient and fast numerical integration schemes for the long-time evolution of the phase space and tangent dynamics of these systems. Implementing these integrators, we perform extensive numerical simulations for various sets of parameter values. We present, to the best of our knowledge for the first time, detailed computations of the time evolution of the system's maximum Lyapunov exponent (MLE- Λ) i.e. the most commonly used chaos indicator, and the related deviation vector distribution (DVD). We find that although the systems' MLE decreases in time following a power law t^{α_Λ} with $\alpha_\Lambda < 0$ for both the weak and strong chaos cases, no crossover to the behavior $\Lambda \propto t^{-1}$ (which is indicative of regular motion) is observed. By investigating a large number of weak and strong chaos cases, we determine the different α_Λ values for the 1D and 2D systems. In addition, the analysis of the DVDs reveals the existence of random fluctuations of chaotic hotspots with increasing amplitudes inside the excited part of the wave packet, which assist in homogenizing chaos and contribute to the thermalization of more lattice sites. Furthermore, we show the existence of a dimension-free relation between the wave packet spreading and its degree of chaoticity between the 1D and 2D DDNLS systems. The generality of our findings is confirmed, as similar behaviors to the ones observed for the DDNLS systems are also present in the case of DKG models.



Plagiarism declaration

I, the undersigned, hereby declare that the work contained in this thesis is my original work, and that any work done by others or by myself previously has been acknowledged and referenced accordingly.

A handwritten signature in black ink, appearing to read 'Manda', with a long, sweeping underline that extends to the right.

Bertin MANY MANDA, 19 October 2020.

Acknowledgements

The completion of my doctoral project was only made possible due to the outstanding support and guidance of my supervisor A/Prof. Haris Skokos. The several months he spent proof-reading this thesis is a glance into how engaged and supportive he has been during these last 4 years.

I am grateful to my colleagues Bob Senyange, Malcolm Hillebrand and Henok Moges for proof-reading this work and for the innumerable fruitful discussions I had with them. We spent hours arguing on analytical and numerical methods, which contributed enormously to improving several aspects of my doctoral work.

During my PhD work, I had the opportunity to interact with many other people whose feedback increased my understanding of nonlinear lattice dynamics and deeply shaped the content of this work. More specifically I mention Prof. Anastasios Bountis (Nazarbayev University, Kazakhstan), Dr. George Kalosakas (University of Patras, Greece), Dr. Carlo Danieli (Max Planck Institute for the Physics of Complex Systems, Germany), Dr. Thudiyangal Mithun (University of Massachusetts, USA), Dr. Konstantinos Kaloudis (Nazarbayev University, Kazakhstan), Dr. Thomas Oikonomou (Nazarbayev University, Kazakhstan) and Mr. Malcolm Hillebrand (University of Cape Town, South Africa) with whom I had the privilege to co-author research papers. In addition, the insights I obtained from discussions with Prof. Sergej Flach (Institute for Basic Science, Korea), Prof. Panayotis Kevrekidis (University of Massachusetts, USA) and Dr. Yagmur Kati (Institute for Basic Science, Korea) are also encompassed in this work. Furthermore, I thank Prof. Giorgos Tsironis (University of Crete, Greece) who as an organizer financially assisted me to participate in the International Conference ‘Nonlinear Localization in Lattices’ which was held in Spetses, Greece in June 2018 and where I met most of the researchers I mentioned above.

Finally, I would like to thank my whole family. My brothers and sisters for their encouragement and my mother Marie Bernadette Biloa Onana who made travelling to South Africa possible through great financial and personal sacrifices.

This work was funded by the National Research Foundation of South Africa under the Grant Number: 98974. I also received additional support from the University of Cape Town. I thank the Centre for High Performance Computing of South Africa and the University of Cape Town’s ICTS High Performance Computing Centre for providing the computational resources and the personal assistance necessary for the successful completion of this work.

Publications and conference presentations

Publications related to this thesis:

- P1. B. Senyange, **B. Many Manda**, and Ch. Skokos, *Characteristics of chaos evolution in one-dimensional disordered nonlinear lattices*, Physical Review E, 2018, 98, 052229. DOI: doi.org/10.1103/PhysRevE.98.052229.
- P2. C. Danieli, **B. Many Manda**, T. Mithun, and Ch. Skokos, *Computational efficiency of numerical integration methods for the tangent dynamics of many-body Hamiltonian systems in one and two spatial dimensions*, Mathematics in Engineering, 2019, 1, 447. DOI: doi.org/10.3934/mine.2019.3.447.
- P3. **B. Many Manda**, B. Senyange, and Ch. Skokos, *Chaotic wave-packet spreading in two-dimensional disordered nonlinear lattices*, Physical Review E, 2020, 101, 032206. DOI: doi.org/10.1103/PhysRevE.101.032206.

Other publications:

- P4. M. Hillebrand, **B. Many Manda**, G. Kalosakas, E. Gerlach, and Ch. Skokos, *Chaotic dynamics of graphene and graphene nanoribbons*, Chaos: An Interdisciplinary Journal of Nonlinear Science, 2020, 30, 063150. DOI: doi.org/10.1063/5.0007761.
- P5. B. Senyange, J.-J. Plessis, **B. Many Manda**, and Ch. Skokos, *Properties of Normal Modes in a Modified Disordered Klein-Gordon Lattice: From Disorder to Order*, Nonlinear Phenomena in Complex Systems: An Interdisciplinary Journal, 2020, 23, 165. DOI: doi.org/10.33581/1561-4085-2020-23-2-165-171.
- P6. A. Bountis, K. Kaloudis, Th. Oikonomou, **B. Many Manda**, and Ch. Skokos, *Stability properties of 1-dimensional Hamiltonian lattices with non-analytic potentials*, International Journal of Bifurcation and Chaos, 2020, 30, 2030047. DOI: doi.org/10.1142/S0218127420300475.
- P7. T. Mithun, A. Maluckov, **B. Many Manda**, Ch. Skokos, A. Bishop, A. Saxena, A. Khare, and P. G. Kevrekidis, *Thermalization in the one-dimensional Salerno model lattice*, Submitted to Physical Review E, 2020. Preprint version: [physics.class-ph/2012.03652](https://arxiv.org/abs/physics.class-ph/2012.03652).

Conference presentations:

- 1. Poster presentation: *Dynamical behavior of a 2D planar model of graphene*. The International Conference on Nonlinear Localization in Lattices, Spetses, Greece, June 2018.
- 2. Poster presentation: *Chaotic wave packet spreading in nonlinear disordered media*. The UCT & SU's Science Postgraduate Symposium, Stellenbosch, South Africa, September 2019.
- 3. Oral presentation: *Chaotic wave packet spreading in the one- and two-dimensional disordered nonlinear Schrödinger equations*. The 62nd Annual Congress of the South African Mathematical Society, Cape Town, South Africa, December 2019.



Contents

Abstract	3
Plagiarism declaration	5
Acknowledgments	7
Publications and conference presentations	9
1 General introduction	13
1.1 Dynamics of disordered systems	13
1.2 Subject of the thesis	14
2 Localization and spreading of wave packets in disordered lattices	17
2.1 Anderson localization	17
2.2 Adding nonlinearity	21
2.2.1 The disordered discrete nonlinear Schrödinger equation	21
2.2.2 The disordered Klein-Gordon chain of anharmonic oscillators	22
2.3 Expected dynamical regimes	23
2.3.1 Selftrapping regime	25
2.3.2 Spreading regimes	26
2.4 A statistical physics approach in determining the various dynamical regimes	29
2.4.1 Thermal and non-thermal regions	30
2.4.2 Weak, strong chaos and selftrapping regimes	32
2.4.3 Wave packet evolution in the energy-norm parameter space	34
2.5 Characteristic measures of wave packet spreading	34
2.5.1 The 1D DDNLS model	34
2.5.2 The 2D DDNLS model	36
2.6 Dynamics of extended initial wave packet	37
2.7 Summary	37
3 Computational techniques	39
3.1 Introduction	39
3.2 Wave packet characterization	39
3.3 Wave packet initialization	40
3.3.1 Approach 1: Thermodynamical averaging	40
3.3.2 Approach 2: Setting specific energy per site	41
3.4 Variational equations	41
3.4.1 Maximum Lyapunov exponent	42
3.4.2 Deviation vector distribution	43
3.5 Numerical determination of power law exponents	43
3.6 General purpose integration schemes	44
3.6.1 The explicit Euler method	44
3.6.2 The Taylor/Lie series method	45
3.6.3 The General purpose DOP853 Runge-Kutta integrator	46
3.7 Symplectic integrators	47
3.7.1 The Baker-Campbell-Hausdorff formula	49
3.7.2 The Yoshida composition technique	50
3.7.3 Two-part split symplectic integrators	50
3.7.4 Three-part split symplectic integrators	52
3.8 Efficient integration of the 1D and 2D DDNLS systems	53

3.8.1	Two-part split symplectic integrators	53
3.8.2	Three-part split symplectic integrators	54
3.9	Summary	58
4	Chaotic dynamics of wave packet spreading in the one-dimensional disordered nonlinear Schrödinger equation	61
4.1	Introduction	61
4.2	Some aspects related to our numerical simulations	61
4.2.1	Choice of the initial deviation vector	61
4.2.2	The dynamic lattice expansion	63
4.3	The maximum Lyapunov exponent	67
4.3.1	The linear regime	67
4.3.2	The weak chaos regime	67
4.3.3	The strong chaos regime	70
4.4	The deviation vector distribution	70
4.4.1	The linear regime	71
4.4.2	The weak chaos regime	74
4.4.3	The strong chaos regime	75
4.5	Discussion and summary	77
5	Chaotic dynamics of wave packet spreading in the two-dimensional disordered nonlinear Schrödinger equation	81
5.1	Introduction	81
5.2	Some aspects related to our numerical simulations	81
5.2.1	Choice of the initial deviation vector	81
5.2.2	The dynamic lattice expansion	87
5.3	The maximum Lyapunov exponent	89
5.3.1	The weak chaos regime	89
5.3.2	The strong chaos regime	91
5.4	The deviation vector distribution	92
5.4.1	The weak chaos regime	92
5.4.2	The strong chaos regime	95
5.5	Discussion and summary	97
6	Summary and outlook	99
	Abbreviations	103
A	Frequency spectrum of the 1D DDLS model and the 1D DKG system of harmonic oscillators	105
A.1	The 1D DDLS model	105
A.2	The 1D DKG system of harmonic oscillators	107
B	Equations of motion of the 1D DDNLS system in the NM space	109
C	Statistical physics analytical computations	111
C.1	Derivation of Eq. (2.81)	111
C.2	Derivation of Eq. (2.84)	111
D	Symplectic integration of the equations of motion and variational equations of the 1D and 2D DDNLS models	115
D.1	Two-part split symplectic integration of the 1D DDNLS model	115
D.1.1	Analytic expression for the operator $e^{\tau \mathbf{L}_{A_V}}$	116
D.1.2	Analytic expression for the operator $e^{\tau \mathbf{L}_{B_V}}$	119
D.2	Three-part split symplectic integration of the 1D and 2D DDNLS models	121
D.2.1	The 1D DDNLS system	122
D.2.2	The 2D DDNLS system	123
	Bibliography	127

Chapter 1

General introduction

1.1 Dynamics of disordered systems

Disordered dynamical systems intend to model the heterogeneity of nature. They are obtained by breaking the spatial translational symmetry (isotropy) of Hamiltonian models by attributing to one or many of their parameters random values to each single degree of freedom. In principle, the random numbers are drawn from any chosen probability distribution and could directly affect the eigen-energies (see e.g. [Anderson, 1958; Gredeskul and Kivshar, 1992; Kramer and MacKinnon, 1993; Shepelyansky, 1993; Kopidakis et al., 2008; Pikovsky and Shepelyansky, 2008]), the on-site interactions (see e.g. [Kopidakis et al., 2008; Skokos et al., 2009; Skokos and Flach, 2010; Lapyteva et al., 2010; Bodyfelt et al., 2011a]), the inter-particle interactions (see e.g. [Prosen and Robnik, 1992; Dauxois et al., 1993; Barré and Dauxois, 2001; Roy and Pikovsky, 2012; Martínez et al., 2016; Hillebrand et al., 2019; Ngapasare et al., 2019; Pikovsky, 2020]) and the particle's masses (see e.g. [Achilleos et al., 2016, 2018; Ngapasare et al., 2019; Hillebrand et al., 2020]) among others. The study of disordered systems has a long standing history, starting in the mid 20th century with the explosion of modern technologies such as semiconductors. Studying a linear electron tight-binding approximation of the latter material, P. W. Anderson [Anderson, 1958; Kramer and MacKinnon, 1993] discovered that initially localized electron matter waves remain in that state for an infinitely long time. This phenomenon is now referred as *Anderson localization* (AL) and has been experimentally shown to occur in a vast number of physical systems (see e.g. [Wiersma et al., 1997; Chabanov et al., 2000; Runge and Zimmermann, 2003; Genack and Chabanov, 2005; Störzer et al., 2006; Billy et al., 2008; Hu et al., 2008; Kondov et al., 2011; Sheinfux et al., 2017]).

The question of what happens to AL when nonlinearity is introduced has attracted extensive work in theory and simulations [Shepelyansky, 1993; Shapiro, 2007; Kopidakis et al., 2008; Pikovsky and Shepelyansky, 2008; Flach et al., 2009; Skokos et al., 2009; Garcia-Mata and Shepelyansky, 2009; Veksler et al., 2009; Mulansky and Pikovsky, 2010; Lapyteva et al., 2010; Skokos and Flach, 2010; Krimer and Flach, 2010; Flach, 2010; Johansson et al., 2010; Basko, 2011; Bodyfelt et al., 2011a,b; Aubry, 2011; Ivanchenko et al., 2011; Molina et al., 2012; Vermersch and Garreau, 2012; Michaely and Fishman, 2012; Basko, 2012; Mulansky and Pikovsky, 2012; Lapyteva et al., 2012; Milovanov and Iomin, 2012; Lucioni et al., 2013; Vermersch and Garreau, 2013; Mulansky and Pikovsky, 2013; Skokos et al., 2013; Lapyteva et al., 2013; Tieleman et al., 2014; Ivanchenko et al., 2014; Antonopoulos et al., 2014; Ermann and Shepelyansky, 2014; Lapyteva et al., 2014; Basko, 2014; Flach, 2015; Achilleos et al., 2016; Flach, 2016; Martínez et al., 2016; Achilleos et al., 2018; Antonopoulos et al., 2017; Iomin, 2017; Sato and Klages, 2019; Vakulchyk et al., 2019; Rivas and Molina, 2020], as well as in experiments [Schwartz et al., 2007; Roati et al., 2008; Lahini et al., 2008; Lucioni et al., 2011]. Two typical disordered Hamiltonian models are at the center of these studies, namely the disordered Klein-Gordon (DKG) chain of nonlinear oscillators and the disordered discrete nonlinear Schrödinger equation (DDNLS). These systems were extensively studied in several of the works mentioned above. There it was shown that for large enough nonlinearity and disorder strengths, AL is destroyed. This leads to different dynamical subdiffusive spreading regimes which are characterized by a growing second moment of the wave packet, according to the power law t^{a_m} with $0 < a_m < 1$. In particular, the *weak chaos* with $a_m = 1/(1 + 2D)$ (D being the lattice's dimensionality) [Flach et al., 2009; Skokos et al., 2009; Flach, 2010] and *strong chaos* dynamical regimes where $a_m = 1/(1 + D)$ can occur [Lapyteva et al., 2010; Flach, 2010; Bodyfelt et al., 2011a].

The remarkable success of the theoretical framework explaining the diffusion process comes from the fact that nonlinearity couples normal modes, which interact with each other and allow the transfer of energy [Gredeskul and Kivshar, 1992; Shepelyansky, 1993; Flach et al., 2009; Flach, 2010]. This transfer happens in a chaotic manner whose evolution allows the randomization and thermalization of the wave packet [Flach, 2010; Basko, 2011; Skokos et al., 2013; Senyange et al., 2018; Many Manda et al., 2020].

Nevertheless, whether the system can sustain the underlying spreading for all times remains a controversial issue. Indeed a possible slowing down of the wave packet spreading is suggested by [Mulansky et al., 2011; Pikovsky and Fishman, 2011] as well as an eventual halt of it by [Johansson et al., 2010; Aubry, 2011], but the vast majority of the numerical simulations do not support such behavior [Shepelyansky, 1993; Pikovsky and Shepelyansky, 2008; Flach et al., 2009; Skokos et al., 2009; Lapyteva et al., 2010; Skokos and Flach, 2010; Bodyfelt et al., 2011a; Lapyteva et al., 2012; Skokos et al., 2013; Kati et al., 2020].

A notable distinction between all these possible outcomes is related to the tangent dynamics of the system which supports its chaotic behavior. Indeed, indicators of chaos often appears to be very sensitive to changes in the system and therefore could act as effective dynamical order parameters in several complex models [Pikovsky and Politi, 2016] and in particular in multidimensional Hamiltonian systems (see for e.g. [Barré and Dauxois, 2001; Hillebrand et al., 2019]). Therefore, understanding the characteristics of chaos in this context appears to be a fundamental, open question. Several works have been performed trying to fill this void. The connection between chaos and nonlinear wave spreading is investigated in [Mulansky et al., 2011] for small sized systems after their regularization, while an interesting chaotic behavior has been observed in the spreading of wave packets in [Tieleman et al., 2014]. In addition, [Michaely and Fishman, 2012] analyzed the temporal and spectral properties of the effective nonlinear strengths within the wave packet and identified it as noisy. Furthermore, [Vermersch and Garreau, 2013] computed the spectral entropy, which is related to chaotic and ergodic properties of systems and measured the *temporal* evolution of chaos, but only for relatively small times. Much closer to what we have studied in this thesis, the *asymptotic temporal* evolution of chaos was studied for the one-dimensional (1D) DKG system in the weak chaos regime by [Skokos et al., 2013]. There, it was depicted a constantly decaying chaos strength during the wave packet’s evolution, and was visualized the fluctuations of localized chaotic hotspots mentioned in previous studies (see e.g. [Basko, 2011, 2012; Michaely and Fishman, 2012]) as necessary for the wave packet thermalization.

1.2 Subject of the thesis

One aim of this thesis is to show that the chaotic processes which were observed in [Skokos et al., 2013] for the weak chaos regime in the 1D DKG system, which possesses a single integral of motion, also appear in the 1D DDNLS model which admits an extra integral of motion compared to the 1D DKG system, thus generalizing in some sense the results obtained in that paper. In addition, we will take that study a step further, investigating also the dynamics in the strong chaos case; as well as providing a ‘complete’ quantification of the system’s chaoticity through the calculation of observables in the system’s tangent space, such as the maximum Lyapunov exponent (MLE) [Skokos, 2010; Pikovsky and Politi, 2016] or the deviation vector distribution (DVD) statistics [Dauxois et al., 1997; Barré and Dauxois, 2001; Skokos et al., 2013]. These two quantities are complementary: While the MLE estimates the mean chaos strength of the entire system, the DVD looks at local properties of chaos giving us information about which lattice sites contribute the most to the overall chaotic dynamics. A basic novelty of our work is that we do not only focus on the 1D version of the system, but we also expand our study to the two-dimensional (2D) version of the system whose subdiffusive spreading has barely been investigated [Garcia-Mata and Shepelyansky, 2009].

In order to reach our goals, we perform large scale numerical experiments in both the 1D and 2D DDNLS lattices, as well as semi-analytical calculations in some cases to interpret our findings. We note that the equations of motion of these DDNLS models are particularly difficult to integrate from a computational point of view. This is demonstrated by the fact that results for the DKG systems, whose numerical integration is a much easier task, are typically presented for final times which are one or two orders of magnitude larger than the DDNLS systems in both one (see e.g. [Senyange et al., 2018]) and two spatial dimensions (see e.g. [Many Manda et al., 2020]). Another important point we want to emphasize is the lack of efficient numerical integration techniques for the evolution of the tangent dynamics of the DDNLS systems in one and two spatial dimensions on top of the difficulty of numerically evolving the equations of motion of these systems. Therefore, we dedicate an important part of this work to creating novel numerical methods for the fast and accurate long time integration of the equations of motion and the variational equations for both the 1D and 2D models of the DDNLS system using the so-called *tangent map method* [Skokos and Gerlach, 2010; Gerlach and Skokos, 2011; Gerlach et al., 2012]. The utilization of the tangent map method takes advantage of symplectic integrators (SIs) which are specifically designed for the numerical evolution of trajectories of Hamiltonian systems. The implementation of the techniques we develop in this work allow us to reach computational performances comparable to the ones seen in previous studies, where only the integration of the equations of motion was done despite adding the significant computational load of the variational equations. Consequently this approach helps us to extract robust asymptotic behaviors of the wave packet chaotic dynamics (quantified through the evolution of the MLE for instance).

As we will see later in this thesis, systems exhibiting AL offer a perfect testbed for the analysis of chaotic processes in nonlinear dynamical systems as the destruction of AL is a purely nonlinear phenomenon [Shepelyansky, 1993; Garcia-Mata and Shepelyansky, 2009; Flach et al., 2009]. It is remarkable that the interplay between disorder and nonlinearity results in the localization of chaos, a behavior which will be discussed in some detail in our work. We will also explain how the combined action of the non vanishing chaotic strength along with the random fluctuations of localized chaos spots are characteristics of the chaotic dynamics of wave packet spreading in disordered media. Consequently, as long as they persist the propagation of wave packets never stops, even if the system is getting closer to the integrable limit. This result is general as it was also observed for the DKG model in one [Skokos et al., 2013; Senyange et al., 2018; Senyange, 2021] and two [Many Manda et al., 2020; Senyange, 2021] spatial dimensions.

The thesis is organized as follows. In Chap. 2, we discuss the notion of AL, emphasizing its manifestation in the 1D disordered discrete linear Schrödinger (DDLs) model, and review the theory of spreading of nonlinear wave packets. In Chap. 3, we introduce the numerical quantities we calculate in our study and describe in detail the numerical techniques we developed for the integration of the equations of motion and the variational equations of the DDNLS models. In Chap. 4, we present our numerical results for the chaotic behavior of the 1D DDNLS model, while Chap. 5 is dedicated to a similar analysis but for the 2D DDNLS model. Finally, in Chap. 6 we conclude our work, summarize our findings and present a few ideas for future investigations.

Chapter 2

Localization and spreading of wave packets in disordered lattices

Introduction

In this chapter, we discuss the different regimes of wave packets' dynamics we encounter in random disordered lattices. The word 'disorder' mentioned here could refer to impurities, vacancies, dislocations, distortions or defects which occur in idealistic *perfect periodic lattices*. A periodic lattice is invariant under space translation, which means that interactions are the same at every location within the lattice, and thus constitutes an idealistic representation of physical systems in nature.

The first part of this chapter is dedicated to a rather concise review of the extended work done on the analysis of models obtained through linear approximations of disordered systems. In this context we show how initially localized wave packets remain in that state forever. This exceptionally important result was initially obtained by Anderson in his seminal paper [[Anderson, 1958](#)] where he tried to understand the *metal insulator transition*. Nowadays it is well known that this so-called Anderson localization (AL) phenomenon appears in several other fields, making it an important problem to study in modern physics (see e.g. [[Izrailev, 1990](#); [Lahini et al., 2008, 2009](#); [Krimer et al., 2009](#); [Krimer and Flach, 2010](#); [Savin et al., 2010](#)]). We can depart from linear approximations to obtain more realistic models by adding nonlinear couplings between system's components, through the inclusion of higher order terms from Taylor series expansions of the interaction potential functions. For example, high intensity photon beams propagating through optical waveguides create a nonlinear response of the medium, which in turn affects the wave propagation [[Schwartz et al., 2007](#); [Lahini et al., 2008](#)]. Thus, the second part of this chapter focuses on the effects of nonlinearity on wave localization in nonlinear disordered systems. In that part, we review what we believe are the most important aspects of this behavior.

The chapter is organized as follows. In [Sec. 2.1](#) we present a fundamental linear disorder model in order to define AL. In [Sec. 2.2](#) we present the nonlinear models we are going to investigate, while in [Sec. 2.3](#) we elaborate using (semi-) analytical arguments the different dynamical behaviors of the nonlinear wave packet in disordered lattices. [Section 2.4](#) is similar to [Sec. 2.3](#), but we base our analysis on statistical physics arguments. In [Sec. 2.5](#) we explain the mechanism of effective wave packet propagation in the different dynamical regimes, while in [Sec. 2.6](#), we discuss the implications of the existence of initial extended wave packets which turn out to be of practical importance for numerical simulations of two-dimensional systems. Finally, in [Sec. 2.7](#) we summarize the content of the chapter.

2.1 Anderson localization

The classical theory of electron transport in conductive metals predicts that electron delocalization is due to nonelastic multiple scatterings of the electron, which collides with atomic nuclei which are several times heavier, leading to the well know result of Ohm's law with the Drude conductivity $\sigma_E \propto \tau$. Here τ is the average time elapsed between two collisions and σ_E is the conductivity within the metal. Therefore, $v\tau$ is the electron mean-free-path (with v being the average electron's velocity), which characterizes the mean distance between two successive scatterings of the electron. An interesting question which arises is what happens if disorder (in the form of a random potential around each nuclei generated from an arbitrary source) is introduced and tuned up higher and higher within the system? Will the conductivity be reduced due to the increasingly smaller electron mean-free-path? Or, will this process result to something more peculiar?

Anderson decided to tackle this problem in the mean-field approximation of the electron tight binding model whose Hamiltonian reads [Anderson, 1958; Kramer and MacKinnon, 1993]

$$\mathcal{H}_L = \sum_{l=1}^N \epsilon_l |\psi_l|^2 - \mathcal{J}_{l,l+1} (\psi_{l+1} \psi_l^* + \psi_l \psi_{l+1}^*). \quad (2.1)$$

Here $\psi_l \in \mathbb{C}$ is the wave function, which describes the state of the electron at site l and ψ_l^* is its complex conjugate. The off-diagonal matrix elements $\mathcal{J}_{l,m}$, $1 \leq l, m \leq N$, with N denoting the size of the lattice, describes the strength of the hopping between sites l and m . In addition, ϵ_l is a random parameter with units of the energy/frequency (here the system is rescaled such that $\hbar = 1$). Its value at each site is drawn from a uniform probability distribution on the interval $[-W/2, W/2]$ with density $\mathcal{P}_W = 1/W$. Consequently, W is the disorder strength as it defines the size of the interval from which the random values ϵ_l are drawn. In Eq. (2.1) we consider that the electron can only diffuse to its nearest neighbors as also shown in Fig. 2.1. In addition, we also assume that the probabilities for the electron to tunnel to

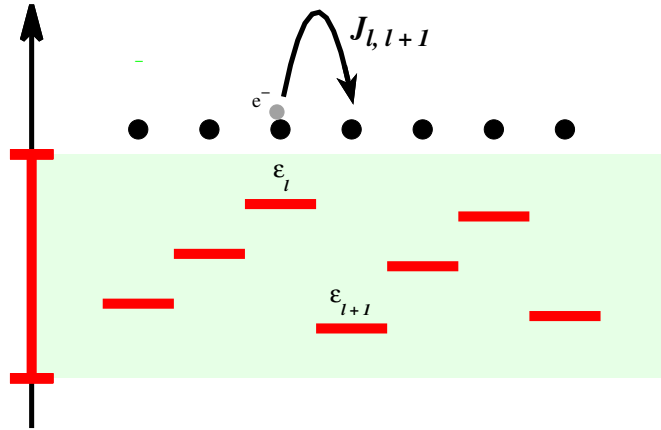


Figure 2.1: Schematic representation of the electron tight-binding model. The electron [grey dot] is attached to atom's nucleus [black dots] which are considered to be fixed. Each atomic site possesses random on-site electron binding energies [red bars] selected from a uniform distribution on the interval $[-W/2, W/2]$ of measure W [red vertical segment in the left]. The electron at site l , can tunnel either to site $l - 1$ or site $l + 1$ with equal transmission probabilities \mathcal{J} often referred as hopping [black arrow on the top of the electron]. Thus, the elements of \mathcal{J} of the form $\mathcal{J}_{l,l-1}$ and $\mathcal{J}_{l,l+1}$ are equal and taken to unity (and zero otherwise).

the left or right site are equal and we set all the non-zero elements of the matrix \mathcal{J} to $\mathcal{J}_{l,m} = 1$.

In Eq. (2.1) the N pairs $(\psi_l, i\psi_l^*)$ represent a set of canonical generalized coordinates of the system's phase space. The equations of motion of the Hamilton function (2.1) are then obtained through

$$\frac{d\psi_l}{dt} = \frac{\partial \mathcal{H}_L}{\partial (i\psi_l^*)}, \quad (2.2)$$

leading to the DDLS equation

$$i\dot{\psi}_l = \epsilon_l \psi_l - (\psi_{l-1} + \psi_{l+1}), \quad (2.3)$$

where the dot refers to the derivative with respect to time t .

We note that spatial localization means that the probability $|\psi_l|^2$ of the presence of the electron at site l exponentially decays, so that the electron does not tunnel out of the lattice [Kramer and MacKinnon, 1993; Krimer and Flach, 2010]. Over the years several methods have been developed in order to analytically and numerically observe such localization [Kramer and MacKinnon, 1993]. For instance, a crude approach consists of putting a lump of matter (preferably located at a single site) into the system and let it evolve for a very long time. If localization occurs, then at the end of the evolution we should expect a spreading of the matter to few subsequent lattice sites and a halting of this process. In this case, the number of sites on which the amount of matter is not exponentially small is a characteristic length of the system that we refer as *localization length* or *localization volume*. We shall emphasize the difference between these two appellations in the later paragraphs.

The normal modes (NMs) of a linear system represent an orthonormal basis of the system's phase space. Therefore, any system's wave packet can be written as a weighted sum over these modes and the

wave packet localization implies that the modes are also localized. Following this observation, one can therefore focus in analyzing the characteristic of the NMs of the DDLS system (2.3).

Let us outline the steps of such procedure. The solution of linear wave equations consists of plane waves of the form

$$\psi_l = A_l e^{-iEt}, \quad (2.4)$$

where A_l is the amplitude of the wave at site l and E its frequency. Substituting Eq. (2.4) into Eq. (2.3) we obtain the equivalent eigenvalue problem

$$EA_l = \epsilon_l A_l - A_{l-1} - A_{l+1}, \quad (2.5)$$

which reduces in a matrix form to

$$E\mathbf{I}\Psi = \tilde{\mathbf{A}}\Psi, \quad (2.6)$$

where $\Psi = (A_1, A_2, \dots, A_N)$,

$$\tilde{\mathbf{A}} = \begin{pmatrix} \epsilon_1 & -1 & 0 & \dots & 0 & 0 \\ -1 & \epsilon_2 & -1 & \dots & 0 & 0 \\ \vdots & \vdots & \vdots & \ddots & \vdots & \vdots \\ 0 & 0 & 0 & \dots & \epsilon_{N-1} & -1 \\ 0 & 0 & 0 & \dots & -1 & \epsilon_N \end{pmatrix} \text{ and } \mathbf{I} = \begin{pmatrix} 1 & 0 & 0 & \dots & 0 & 0 \\ 0 & 1 & 0 & \dots & 0 & 0 \\ \vdots & \vdots & \vdots & \ddots & \vdots & \vdots \\ 0 & 0 & 0 & \dots & 1 & 0 \\ 0 & 0 & 0 & \dots & 0 & 1 \end{pmatrix}. \quad (2.7)$$

Solving the eigenvalue problem (2.6) is equivalent to diagonalizing the matrix $\tilde{\mathbf{A}}$. We then obtain the normalized eigenstates $\Psi_\nu = (A_{\nu,1}, A_{\nu,2}, \dots, A_{\nu,N})$ with $\|\Psi_\nu\|^2 = \sum_l A_{\nu,l}^2 = 1$ associated with the eigenfrequencies E_ν ¹. An example of a computed NM Ψ_ν through this process of numerical diagonalization of $\tilde{\mathbf{A}}$ (see Eqs. (2.6) and (2.7)) is shown in Fig. 2.2. The parameters of system (2.1) are set to $W = 4$ and $N = 1021$. The computed NMs are sorted by increasing order of their centers' spatial position which is computed as $\bar{l}_\nu = \sum_l l |A_{\nu,l}|^2$. In Fig. 2.2, we plot the profile of the mode whose center is closest to the lattice's middle (the mode's number in the ordering in $\nu = 357$), associated with the eigenfrequency $E_\nu \approx -0.916$. The spatial exponential localization of the mode is evident from the results of Fig. 2.2(b).

The NMs of a system exhibiting AL are characterized by an asymptotic exponential spatial decay from their center (here referred as \bar{l}_ν) [Kramer and MacKinnon, 1993] of the form

$$\Psi_\nu \propto \zeta_\nu^{-1/2} e^{-(l-\bar{l}_\nu)/\zeta_\nu}, \quad (2.8)$$

where ζ_ν is the so-called localization length of mode ν . The ζ_ν values have to be finite and bounded from above for all the frequencies ν ².

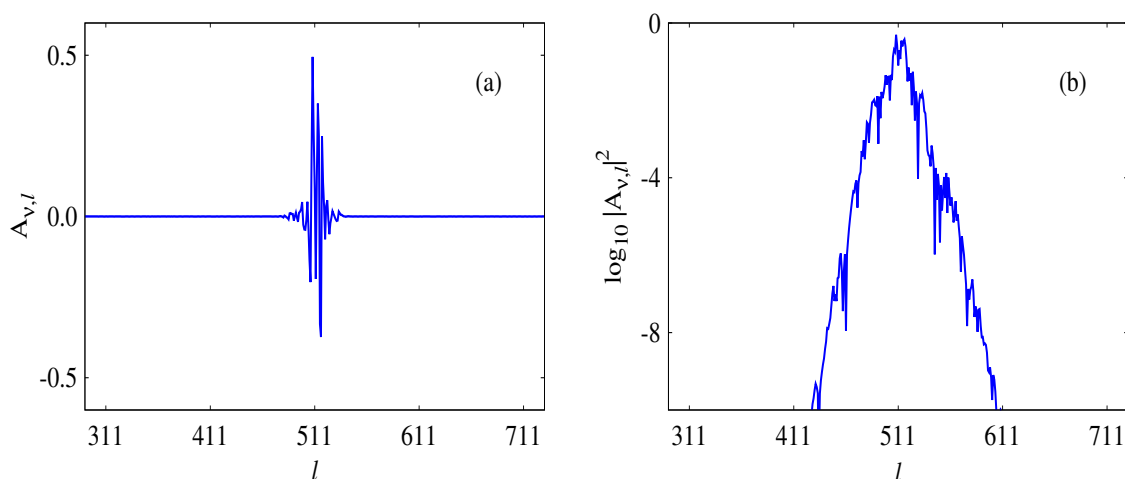


Figure 2.2: A representative NM of Hamiltonian (2.1) with $N = 1021$ sites located around the center of the lattice (mode number $\nu = 357$). Amplitudes (a) $A_{\nu,l}$ and (b) $|A_{\nu,l}|^2$. Panel (b) is in semi-logarithmic scale. The system disordered strength is $W = 4$.

¹We note that we set $\hbar = 1$ so that the energy E_ν is numerically identical to the frequency ν , as they are related through the equation $E_\nu = \hbar\nu$.

²In contrary, an extended mode exhibits an unbounded localization length i.e. $\zeta_\nu \rightarrow \infty$. In this situation, AL cannot survive as the energy will be carried by the extended mode through the whole system (2.1).

In Eq. (2.8) the key quantity is the localization length ζ_ν as it is directly related to the mode's profile. In [Kramer and MacKinnon, 1993], several numerical and analytical methods were presented for the estimation of ζ_ν (e.g. random matrix theory, Green's functions, transfer matrix methods *etc.*). Using these methods, the authors showed that in the limit of weak disorder the localization length can be expressed as

$$\zeta(E_\nu) = \zeta_\nu = \frac{24(4 - E_\nu^2)}{W^2}. \quad (2.9)$$

From Eq. (2.9), we see that the localization length ζ_ν takes its largest value at the center of the spectrum, i.e. when $E_\nu = 0$, becoming

$$\zeta(0) = \zeta_0 = 96/W^2. \quad (2.10)$$

On the other hand, in the case of strong disorder, the largest value of the localization length becomes [Laptyeva, 2013]

$$\zeta_0 = \frac{1}{\ln\left(\frac{W}{2}\right)}. \quad (2.11)$$

In order to numerically probe the validity of Eqs. (2.9) and (2.11), we compute the statistical properties of NMs. The spatial extent of the NMs of the 1D DDLS model (2.1) has been studied through extensive numerical computations in [Krimer and Flach, 2010]. In that paper, the spatial volume occupied by a mode ν is considered as the number of lattice sites where the amplitude $A_{\nu,l}$ is not exponentially small and quantified by a quantity which was named localization volume V_ν [Krimer and Flach, 2010; Laptyeva et al., 2012]. This quantity was computed as [Krimer and Flach, 2010]

$$V_\nu = \sqrt{12m_2^{(\nu)}} + 1, \quad (2.12)$$

where $m_2^{(\nu)} = \sum_l (l - \bar{l}_\nu)^2 |A_{\nu,l}|^2$ is the mode's second moment with $\bar{l}_\nu = \sum_l l |A_{\nu,l}|^2$ being the mode's center. In addition, one could also consider as an estimation of the mode's localization volume the number of sites which contribute the most to the NM spatial distribution, something which can be quantified by the mode's participation number [Krimer and Flach, 2010]

$$P_\nu = \frac{1}{\sum_l |A_{\nu,l}|^4}. \quad (2.13)$$

Thus, averaging these quantities for the NMs belonging to the spectra of several disorder realizations, we compute the average localization volume \bar{V} of the NMs in the 1D DDLS system (2.1). It is worth mentioning that the numerical analysis often focusses on the central part of the frequency spectrum where $\zeta \propto \zeta_0$. Consequently, for that frequency region, there exists a direct proportionality between the localization volume \bar{V} and localization length ζ_0 [Krimer and Flach, 2010; Senyange et al., 2020] such that

$$\bar{V} \approx \frac{a_\zeta}{W^2}, \quad (2.14)$$

where a_ζ is a real constant. The value of a_ζ of Eq. (2.14) oscillates within the interval [330, 360] (see e.g. [Krimer and Flach, 2010; Flach, 2010, 2016; Kati et al., 2020]).

In Fig. 2.3, we present results obtained in [Krimer and Flach, 2010] of the comparison between calculations of the average localization length $\bar{\zeta}$ using the transfer matrix approach (see (b)lue curve in Fig. 2.3), the averaged localization volume \bar{V} based on Eq. (2.12) (see (r)ed curve in Fig. 2.3) and of the average participation number \bar{P} based on Eq. (2.13) (see (g)reen curve in Fig. 2.3). All these results are presented as function of the disorder strength W . For small W values, the proportionality between these quantities is evident as all of them exhibit the same trend, being $\propto W^{-2}$ in agreement with Eq. (2.9). Although Eq. (2.9) was derived for small W , the numerical calculations suggest that this relation is valid for $W \lesssim 4$ [Krimer and Flach, 2010]. In the limit of strong disorder $W \rightarrow \infty$, Eq. (2.11) suggests that the localization length $\zeta_\nu \rightarrow 0$, while the definition (2.12) implies the localization volume $V_\nu \rightarrow 1$ due to the discreteness of the model. These tendencies are well captured by the results of Fig. 2.3.

According to [Kramer and MacKinnon, 1993; Krimer and Flach, 2010; Laptyeva et al., 2012; Laptyeva, 2013], the width of the eigenvalue frequency spectrum E_ν of (2.5) is

$$\Delta = W + 4, \quad \text{with} \quad E_\nu \in \left[-2 - \frac{W}{2}, 2 + \frac{W}{2}\right]. \quad (2.15)$$

Interestingly enough, this can be analytically deduced using simple algebraic manipulations (see Appendix A) based on [Kopidakis et al., 2008]. Because we will use this quantity quite often through

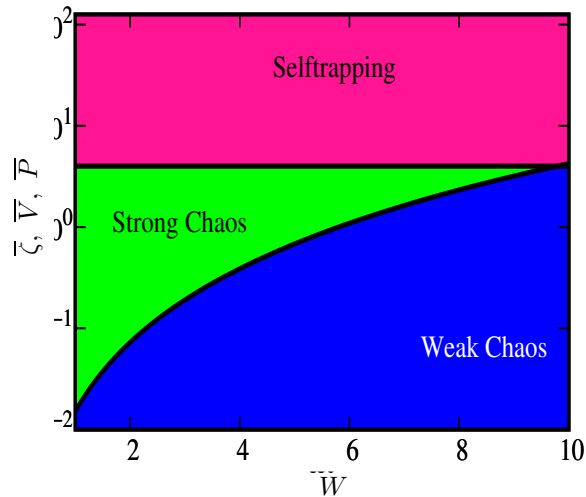


Figure 2.3: Numerical estimation of the mean localization length $\bar{\zeta}$ through the transfer matrix approach [(b)lue], the mean localization volume \bar{V} (see Eq. (2.12)) [(r)red] and the mean participation number \bar{P} (see Eq. (2.13)) [(g)reen] of the NMs with eigenfrequencies E_ν near the center of the frequency band of system (2.2) as a function of the disorder strength W . For moderate W , the values of $\bar{\zeta}$ and \bar{V} are fitted by an expression of the form a_ζ/W^2 , depicted by dashed lines. In particular, the lower dashed line close to the blue curve corresponds to the function $100/W^2$, while the upper dashed line close to the red curve to $330/W^2$ (from [Krimer and Flach, 2010]).

the rest of this thesis, it is worth defining what is called the *averaged spacing between neighboring NMs* d [Shepelyansky, 1993; Flach et al., 2009; Flach, 2010] as

$$d \propto \frac{\Delta}{\Delta l}, \quad (2.16)$$

where Δl is the wave packet's width i.e. the number of sites which have a non-negligible amount of norm/energy.

At this stage, we have characterized the dynamical features of the DDLS model (2.1) based on three quantities: (i) the mean localization volume \bar{V} (2.12), (ii) the eigenfrequency bandwidth Δ (2.15) and (iii) the average spacing between NMs d (2.16). It is worth mentioning that similar studies of the linear NMs have been performed for the disordered Klein-Gordon (DKG) chain of harmonic oscillators [Senyange et al., 2020] whose nonlinear version is also mentioned throughout this thesis.

2.2 Adding nonlinearity

We now introduce nonlinear interactions into the DDLS model (2.1) and study the fate of the localized wave packet in this context. As we are going to witness, the nonlinear interactions couple the system's NMs which in principle could exchange norm/energy. This immediately blurs the fate of the wave packet. Will the wave packet spread? If yes, is the spreading limited in time or will it last for ever? These are example of questions that arise from this problem and that we intend to tackle in this section. We describe an appropriate parameter space on which points represent wave packets with specific geometry and density characteristics and use these spaces to develop the theoretical framework governing the evolution of any initial wave packet. In this way, we are able to establish boundaries which delimit sets of parameters leading to similar wave packet dynamics, as well as provide the expected wave packet statistical characteristics within each domain.

2.2.1 The disordered discrete nonlinear Schrödinger equation

We start by presenting our principal model of investigation, the 1D DDNLS model, which can be viewed as the DDLS lattice model (2.1) into which we introduce an onsite nonlinear term, leading to the Hamiltonian function [Molina, 1998; Pikovsky and Shepelyansky, 2008; Kopidakis et al., 2008; Flach et al., 2009; Veksler et al., 2009; Iomin, 2010; Mulansky and Pikovsky, 2010; Iomin, 2017]

$$\mathcal{H}_{1D} = \sum_{l=1}^N \epsilon_l |\psi_l|^2 + \frac{\beta}{2} |\psi_l|^4 - (\psi_{l+1} \psi_l^* + \psi_{l+1}^* \psi_l), \quad (2.17)$$

where again ψ_l is a complex valued function representing the state of the wave packet at site l and β defines the nonlinearity strength. As in Eq. (2.1), the onsite parameters ϵ_l , $1 \leq l \leq N$ are drawn from a uniform distribution $\mathcal{P}_W = 1/W$ in the interval $[-W/2, W/2]$. Here W is the disorder strength and N is the total size of the lattice. The equations of motion generated from Eq. (2.2) are

$$i\dot{\psi}_l = \epsilon_l \psi_l + \beta |\psi_l|^2 \psi_l - (\psi_{l-1} + \psi_{l+1}), \quad (2.18)$$

and conserve both the total energy \mathcal{H}_{1D} (2.17), as well as the total norm of the system

$$\mathcal{S}_{1D} = \sum_{l=1}^N |\psi_l|^2. \quad (2.19)$$

It is straightforward to extend Eq. (2.17) to a 2D lattice. In that case the Hamiltonian [Garcia-Mata and Shepelyansky, 2009; Laptyeva et al., 2012]

$$\mathcal{H}_{2D} = \sum_{l=1, m=1}^{N, M} \epsilon_{l,m} |\psi_{l,m}|^2 + \frac{\beta}{2} |\psi_{l,m}|^4 - (\psi_{l+1,m} \psi_{l,m}^* + \psi_{l,m+1} \psi_{l,m}^* + \psi_{l+1,m}^* \psi_{l,m} + \psi_{l,m+1}^* \psi_{l,m}), \quad (2.20)$$

represents the total energy of the system, where $\psi_{l,m} \in \mathbb{C}$ is the wave function at site (l, m) , β is the nonlinear coefficient and $N \times M$ being the lattice size. Again, the $\epsilon_{l,m}$, $1 \leq l \leq N$, $1 \leq m \leq M$, are onsite parameters randomly drawn from a uniform distribution $\mathcal{P}_W = 1/W$ in the interval $[-W/2, W/2]$, with W being the disorder strength. The equations of motion obtained via

$$\dot{\psi}_{l,m} = \frac{\partial \mathcal{H}_{2D}}{\partial (i\psi_{l,m}^*)}, \quad (2.21)$$

are

$$i\dot{\psi}_{l,m} = \epsilon_{l,m} \psi_{l,m} + \beta |\psi_{l,m}|^2 \psi_{l,m} - (\psi_{l-1,m} + \psi_{l+1,m} + \psi_{l,m-1} + \psi_{l,m+1}), \quad (2.22)$$

and conserve in addition to the total energy of the system (2.20) its total norm

$$\mathcal{S}_{2D} = \sum_{l=1, m=1}^{N, M} |\psi_{l,m}|^2. \quad (2.23)$$

These models (Eqs. (2.17) and (2.20)) are for instance used to describe the conductivity of materials (see e.g. [Sales et al., 2018]), the behavior of DNA molecules (see e.g. [Peyrard, 2004; Dang Koko et al., 2012]), two-body interactions in ultracold atomic gases and the propagation of light through networks of coupled optical waveguides (see e.g. [Rasmussen et al., 2000; Christodoulides et al., 2003; Kivshar and Agrawal, 2003; Johansson and Rasmussen, 2004; Morsch and Oberthaler, 2006; Mithun et al., 2018]) to name a few.

2.2.2 The disordered Klein-Gordon chain of anharmonic oscillators

We will also sporadically discuss the 1D and 2D DKG models. The Hamiltonian function of the 1D version of this model [Flach et al., 2009; Laptyeva et al., 2010; Skokos and Flach, 2010] reads

$$\mathcal{H}_{1K} = \sum_{l=1}^N \frac{p_l^2}{2} + \frac{\tilde{\epsilon}_l}{2} q_l^2 + \frac{1}{4} q_l^4 + \frac{1}{2W} (q_{l+1} - q_l)^2, \quad (2.24)$$

where $\tilde{\epsilon}_l$ are random uncorrelated parameters drawn from a uniform distribution $\mathcal{P} = 1$ in the interval $[1/2, 3/2]$. In addition, q_l and p_l , $1 \leq l \leq N$ are respectively the generalized displacements and momenta and N is the total number of lattice sites. The choice of the hopping coefficient $1/2W$ into Hamiltonian (2.24) is made such that the NMs of the 1D DDLS system (2.1) and the 1D DKG model of harmonic oscillators ($q_l^4 \rightarrow 0$ in \mathcal{H}_{1K} (2.24)) are the same (see Sec. A.2 in Appendix A for further details). Thus W is considered as the strength of the disorder as it tunes the NMs localization volume. The equations of motion are derived from

$$\ddot{q}_l = -\frac{\partial \mathcal{H}_{1K}}{\partial q_l}, \quad (2.25)$$

leading to

$$\ddot{q}_l = -\tilde{\epsilon}_l q_l + q_l^3 + \frac{1}{W} (q_{l-1} - 2q_l + q_{l+1}). \quad (2.26)$$

The set of equations (2.26) conserve the value of the Hamiltonian function (2.24). Note that changing the energy value \mathcal{H}_{1K} is equivalent to tuning the nonlinear term $q_l^4/4$, therefore the value of \mathcal{H}_{1K} is used as a control parameter of the system.

The Hamiltonian function of the 1D DKG system can be extended to 2D lattices in the same fashion as done for the DDNLS model [Laptyeva et al., 2012; Senyange and Skokos, 2018; Many Manda et al., 2020], leading to the Hamiltonian

$$\mathcal{H}_{2K} = \sum_{l=1, m=1}^{N, M} \frac{p_{l,m}^2}{2} + \frac{\tilde{\epsilon}_{l,m}}{2} q_{l,m}^2 + \frac{1}{4} q_{l,m}^4 + \frac{1}{2W} \left[(q_{l+1,m} - q_{l,m})^2 + (q_{l,m+1} - q_{l,m})^2 \right]. \quad (2.27)$$

In Eq. (2.27), $\tilde{\epsilon}_{l,m}$ are random uncorrelated parameters drawn from a uniform distribution $\mathcal{P} = 1$ in the interval $[1/2, 3/2]$. Again, $q_{l,m}$ and $p_{l,m}$ are the generalized displacement and momentum at site (l, m) . As previously, W denotes the disorder strength and $N \times M$ is the total lattice size. The equations of motion are obtained from

$$\ddot{q}_{l,m} = -\frac{\partial \mathcal{H}_{2K}}{\partial q_{l,m}}, \quad (2.28)$$

and have the form

$$\ddot{q}_{l,m} = -\tilde{\epsilon}_{l,m} q_{l,m} + q_{l,m}^3 + \frac{1}{W} (q_{l-1,m} + q_{l,m-1} - 4q_{l,m} + q_{l,m+1} + q_{l+1,m}). \quad (2.29)$$

As before, these equations conserve the value of the Hamiltonian \mathcal{H}_{2K} (2.27), which can be used as tuning parameter of the nonlinearity in the system.

These models (see Eqs. (2.24) and (2.27)) are relevant for several physical processes like anharmonic vibrations in crystal lattices [Ovchinnikov et al., 2012].

2.3 Expected dynamical regimes

To understand the impact of the nonlinearity on the time evolution of the wave packet in the 1D DDNLS lattice model, we express the nonlinear wave function ψ_l in the basis of the NMs $\Psi_\nu = (A_{\nu,1}, A_{\nu,2}, \dots, A_{\nu,N})$ with $A_{\nu,l} \propto \zeta^{-1/2} \exp[-(l - \bar{l}_\nu)/\zeta]$ of the 1D DDLS model (2.1), i.e.

$$\psi_l = \sum_{\nu} \phi_{\nu} A_{\nu,l}, \quad (2.30)$$

where ϕ_{ν} are time dependent complex amplitudes which define the contribution of mode ν to the state of site l . The equations of motion (2.18) can be written in the NMs space [Pikovskiy and Shepelyansky, 2008; Kopidakis et al., 2008; Milovanov and Iomin, 2012] (see also Appendix B) as

$$i \frac{\partial \phi_{\nu}}{\partial t} = \lambda_{\nu} \phi_{\nu} + \beta \sum_{\nu_1, \nu_2, \nu_3} I_{\nu, \nu_1, \nu_2, \nu_3} \phi_{\nu_1}^* \phi_{\nu_2} \phi_{\nu_3}, \quad (2.31)$$

with

$$I_{\nu, \nu_1, \nu_2, \nu_3} = \sum_l A_{\nu,l}^* A_{\nu_1,l}^* A_{\nu_2,l} A_{\nu_3,l}, \quad (2.32)$$

being the so-called the *overlap-integral*. From Eq. (2.31), we see that the presence of the nonlinearity when $\beta > 0$ introduces complex interactions between NMs in the equations of motion through the term $\beta \sum_{\nu_1, \nu_2, \nu_3} I_{\nu, \nu_1, \nu_2, \nu_3} \phi_{\nu_1}^* \phi_{\nu_2} \phi_{\nu_3}$. The strength of the latter term depends on three parameters: (i) the norm of mode ν , $s_{\nu} = |\phi_{\nu}|^2$, (ii) the nonlinear coefficient β and (iii) the value of the overlap integral $I_{\nu, \nu_1, \nu_2, \nu_3}$. While the value of s_{ν} (and β) can be easily evaluated, the determination of the magnitude of $I_{\nu, \nu_1, \nu_2, \nu_3}$ is more complicated as we do not really have exact analytical forms for the NM expressions (2.8). Indeed, even if Eq. (2.8) predicts in a statistical manner the tail shape of most of the NMs, multi-peaked NMs having significant contributions in larger parts of the lattice do exist [Krimer and Flach, 2010]. Nevertheless, we can develop some intuition about the behavior of $I_{\nu, \nu_1, \nu_2, \nu_3}$ following the approach of [Shepelyansky, 1993; Garcia-Mata and Shepelyansky, 2009]. For instance, the fact that a NM Ψ_{ν} (2.8) spans a finite amount of lattice sites, suggests that the integral $I_{\nu, \nu_1, \nu_2, \nu_3}$ is bounded by a finite value and so we expect each mode to overlap/interact with a finite number of neighboring modes (such that a lattice site contributes to the energy of a finite number of NMs). Consequently, the introduction of the nonlinearity induces a nonlinear frequency shift

$$\delta_{\nu} \propto \beta |\phi_{\nu}|^2 = \beta s_{\nu}, \quad (2.33)$$

on the frequency of each mode ν .

Depending on the strength of the frequency shift δ_ν , three different behaviors are expected: (I) if the nonlinear frequency shift δ_ν is small enough that most of the modes of the system do not change much and still do not behave chaotically, then AL is preserved at least for a very long time interval. This case corresponds to the so-called Kolmogorov-Arnol'd-Moser (KAM) regime [Johansson et al., 2010; Aubry, 2011; Lichtenberg and Lieberman, 2013] where the system's orbits in the phase space remain on KAM tori and exhibit quasi-periodic behavior. (II) On the other hand, if δ_ν is large enough, the modes behave chaotically allowing energy/norm exchanges between themselves. In this case, a clear expansion of the wave packet is noticed, which in turn will lead to a decreasing nonlinear frequency shift in time since the amplitude at each active mode is diminishing [Shepelyansky, 1993; Pikovsky and Shepelyansky, 2008; Garcia-Mata and Shepelyansky, 2009; Flach, 2010]. In this case, two potential scenarios are possible: (IIA) the wave packet spreads and after some time the modes' interactions become weak enough to be neglected and consequently, the system's trajectories converge to KAM-like tori and AL is restored or (IIB) the system remains chaotic for all times with a decreasing chaos strength (which is proportional to δ_ν), which nevertheless is enough to maintain the spreading of the wave packet for all times. This means that unlike case (I) and scenario (IIA), in scenario (IIB) the system's trajectories do not converge to quasi-periodic orbits [Skokos et al., 2013].

We note that this is the first time that the notion of chaos is mentioned in our work. Our approach is not to give a strict definition of it (the interested reader could for example see [Goldstein et al., 2002; Skokos, 2010; Pikovsky and Politi, 2016] for more information on the subject) but to loosely relate chaos with the disappearance of quasi-periodic motion (which is often referred to as regular motion). A very useful criterion has been developed to determine the condition under which a system becomes chaotic: the so-called *Chirikov criterion* [Chirikov, 1971, 1979] which has been already successfully implemented in many physical phenomena. For example, determining the condition of appearance of the Fermi-Pasta-Ulam-Tsingou (FPUT)-recurrence (see [Berman and Izrailev, 2005; Campbell et al., 2005] and references therein), the dynamics of breathers [Flach and Ponomarev, 2008; Flach et al., 2008] and the onset of chaotic behavior in quantum systems [Shepelyansky, 1993, 1995]. It is worth mentioning that a review of the various contributions of Chirikov in the theory of chaos can be found in [Bellissard and Shepelyansky, 1998]. The theoretical attempts to describe the dynamical behavior of nonlinear disordered systems [Shepelyansky, 1993; Pikovsky and Shepelyansky, 2008; Garcia-Mata and Shepelyansky, 2009] were based on the application of the Chirikov criterion. We outline them here: a disordered nonlinear system shows a *deterministic* chaotic behavior when its perturbation parameter K satisfies

$$K = \mathcal{K}^2 \propto \left(\frac{\delta_\nu}{d_\nu} \right)^2 > 1. \quad (2.34)$$

Note that \mathcal{K} is often called the *resonance-overlap parameter*. In Eq. (2.34), δ_ν is the nonlinear frequency shift (2.33) and

$$d_\nu = \Delta/\Delta\nu, \quad (2.35)$$

is the average frequency spacing between NMs, with Δ being the size of the linear frequency spectrum and $\Delta\nu$ denoting the wave packet extent in terms of the total number of activated NMs. This approach allows the determination of the regions of the system's parameter space where similar dynamical behaviors are seen. Based on the value of \mathcal{K} (2.34) we can see the following cases: (a) $\mathcal{K} < 1$. In this case, $\delta_\nu < d_\nu$ and the nonlinear frequency shift is smaller than the average spacing between the frequencies of the NMs d_ν , i.e. no initial resonance overlap between the excited modes happens. Consequently, we expect the system to behave linearly, at least for a very long time after which eventually wave packet spreading will appear as energy exchanges between modes slowly start in Eq. (2.31) (b) $\mathcal{K} > 1$ giving $\delta_\nu > d_\nu$. In this case initial resonance overlaps between modes and wave packet spreading is expected to occur immediately. (c) $\mathcal{K} \gg 1$ such that $\delta_\nu \gg d_\nu$. In this case the nonlinear frequency shift δ_ν is very large compared to d_ν . This results to some of the nonlinear NMs to be tuned out of resonances with their frequencies shifted outside the linear frequency band. This case will be discussed in more detail in Sec. 2.3.1.

A difficulty in the determination of the above mentioned dynamical regimes [(a), (b) and (c)] is the estimation of quantities δ_ν and d_ν . Thus, it is important to be able to define these regimes in terms of more accessible parameters, which will make easier the setting up of experiments or numerical simulations. We will undertake this task in the following section. It is also worth mentioning that in the work of [Shepelyansky, 1993] only two regimes [cases (a) and (b)] are considered with respect to Eq. (2.34). For small resonance-overlaps (case (a) with $\delta_\nu < d_\nu$) no spreading and therefore localization for the initial wave packet was predicted, while for large resonance-overlaps (case (b) where $\delta_\nu > d_\nu$) extensive spreading is observed for the system with

$$\mathcal{K} \propto \frac{\beta|\phi_\nu|^2}{d_\nu} \sim \frac{\beta/\Delta\nu}{1/\Delta\nu} = \beta. \quad (2.36)$$

This prediction of constant resonance-overlap parameter of the mode interactions (as β remains fixed) suggests that the spreading of the wave packets persist for all times. We note that in the approximation above, we used the fact that $|\phi_\nu|^2 \sim 1/\Delta\nu$ and $d_\nu \sim 1/\Delta\nu$ (since Δ always remains finite) in the limit of extended wave packets i.e. $\Delta\nu \rightarrow \infty$.

2.3.1 Selftrapping regime

The analysis presented in the previous section does not provide enough information on the fate of the wave packet in the case $\delta_\nu \gg d_\nu$. We will study this case in more detail here for the 1D DDNLS system (2.17), following the work of [Skokos et al., 2009] which was based on the results presented in [Rasmussen et al., 2000; Johansson and Rasmussen, 2004; Kopidakis et al., 2008] and recently discussed in [Flach, 2016; Kati et al., 2020]. In particular, we will show that it is possible that the wave packet's evolution can lead to an asymptotically inhomogeneous behavior, where part of the wave packet remains trapped so that its amplitudes do not attain arbitrarily small values. Initial excitation leading to such behaviors are said to belong to the selftrapping regime. We note that this behavior contradicts the asymptotic homogeneous nonlinear wave packet whose existence was proposed in [Shepelyansky, 1993; Pikovsky and Shepelyansky, 2008].

The participation number

$$P = \frac{\mathcal{S}_{1D}^2}{\sum_l |\psi_l|^4}, \quad (2.37)$$

is a widely used quantity to measure the number of highly excited sites and consequently to measure the wave packet's inhomogeneity. This quantity is bounded from below by $P = 1$ corresponding to the case where the whole norm/energy is concentrated at a single lattice site and has an upper bound $P = N$ when equipartition is reached.

The Hamiltonian function (2.17) can be split into two terms

$$\mathcal{H}_{1D} = \mathcal{H}_L + \mathcal{H}_{NL}, \quad (2.38)$$

where

$$\mathcal{H}_L = \sum_{l=1}^N \epsilon_l |\psi_l|^2 - (\psi_l \psi_{l+1}^* + \psi_l^* \psi_{l+1}), \quad (2.39)$$

represents the linear part of \mathcal{H}_{1D} (2.17) (see also Eq. (2.1)) and

$$\mathcal{H}_{NL} = \sum_{l=1}^N \frac{\beta}{2} |\psi_l|^4, \quad (2.40)$$

includes the nonlinear terms of \mathcal{H}_{1D} (2.17). The \mathcal{H}_L (2.39) is bounded such that [Kopidakis et al., 2008; Skokos et al., 2009] (see also Eq. (A.6) in Appendix A)

$$\left(-2 - \frac{W}{2}\right) \mathcal{S}_{1D} \leq \mathcal{H}_L \leq \left(2 + \frac{W}{2}\right) \mathcal{S}_{1D}, \quad (2.41)$$

where $\mathcal{S}_{1D} = \sum_l |\psi_l|^2$ is the system's total norm (2.19). Trying to identify under which condition the selftrapping can be avoided, let us assume that the wave packet asymptotically spreads toward zero amplitudes. In that case, we have

$$0 \leq \lim_{t \rightarrow \infty} \left(\sum_l |\psi_l|^4 \right) < \lim_{t \rightarrow \infty} (\sup_l |\psi_l|^2) \left(\sum_l |\psi_l|^2 \right) = 0. \quad (2.42)$$

Since $\mathcal{S}_{1D} = \sum_l |\psi_l|^2 > 0$ is a constant of motion, the only possibility to achieve Eq. (2.42) is to set

$$\lim_{t \rightarrow \infty} \sup_l |\psi_l|^2 = 0. \quad (2.43)$$

Whence $\mathcal{H}_{NL} = 0$ in the limit of $t \rightarrow \infty$. This result and the inequality (2.41) imply

$$\mathcal{H}_{1D} \leq \left(2 + \frac{W}{2}\right) \mathcal{S}_{1D}. \quad (2.44)$$

As \mathcal{H}_{1D} and \mathcal{S}_{1D} are both constants of motion, the inequality (2.44) has to be true for all times. As we will see below, this is not always the case, indicating that selftrapping can happen. Indeed, we will show that selftrapping appears when the norm \mathcal{S}_{1D} exceeds a specific critical value. To demonstrate this

behavior, we consider the simple case of an initial wave packet of size $L = 1$ (single site excitation) of the form $\psi_0(0) = \sqrt{s}e^{i\theta_0}$. Thus, the constants of motion \mathcal{H}_{1D} (2.17) and \mathcal{S}_{1D} (2.19) are

$$\mathcal{H}_{1D} = \epsilon_0 s + \frac{\beta}{2}s^2, \quad \text{and} \quad \mathcal{S}_{1D} = s, \quad (2.45)$$

with ϵ_0 being the value of the onsite parameter at the initially excited site. In addition, this initial excitation at $t = 0$ yields

$$\mathcal{H}_L(t=0) = \epsilon_0 s \quad \text{and} \quad \mathcal{H}_{NL}(t=0) = \frac{\beta}{2}s^2 = \frac{\beta}{2}s^2 P^{-1}(t=0). \quad (2.46)$$

Let us now evaluate bounds for the participation number $P(t)$, $t > 0$. Inserting Eq. (2.45) into the right part of Eq. (2.41), using Eq. (2.38) to evaluate \mathcal{H}_L , as well as the fact that Eqs. (2.40) and (2.37) give $\mathcal{H}_{NL}(t) = \frac{\beta}{2}s^2 P^{-1}(t) \geq 0$, we obtain

$$\left(-2 - \frac{W}{2}\right)s + \frac{\beta}{2}s^2 + \epsilon_0 s \leq \frac{\beta}{2}s^2 P^{-1}(t), \quad (2.47)$$

which allows us to find bounds for the participation number in the form of

$$1 \leq P(t) \leq \frac{\beta s^2}{\beta s^2 - (\Delta - 2\epsilon_0)s}, \quad (2.48)$$

where $\Delta = W + 4$ (2.15). We note that the upper bound of the inequality is valid only if

$$\beta s > \Delta - 2\epsilon_0. \quad (2.49)$$

For the 1D DDNLS system, the initial nonlinear frequency shift δ of the excited single site (see for example [Laptyeva, 2013, Page 42]) is given by

$$\delta = \beta s. \quad (2.50)$$

Then from Eq. (2.49), we conclude that the δ value above which selftrapping occurs is

$$\delta = \Delta - 2\epsilon_0. \quad (2.51)$$

Equation (2.48) tells us that in the regime of selftrapping, the value of the participation number is bounded from above, which taking into account that $s^2 P^{-1}(t) = \sum_l |\psi_l|^4 < \sup_l |\psi_l|^2 s$ [Kopidakis et al., 2008; Skokos et al., 2009] leads to

$$\sup_l |\psi_l|^2 > \frac{\beta s^2 - (\Delta - 2\epsilon_0)s}{\beta s}. \quad (2.52)$$

The fulfillment of these conditions mean that the wave packet will never reach equipartition and that part of it remains trapped. Nevertheless, a limitation of the above analysis is the lack of information about the spatiotemporal behavior of the trapped part of the wave packet, although we secure that a part of it will not spread, we do not know if the resulting inhomogeneity will remain constant in time and space. We note that Eqs. (2.48) and (2.52) respectively correspond to Eqs. (14) and (15) of [Skokos et al., 2009] for the case $s = 1$ and $\epsilon_0 = 0$ considered in that paper.

2.3.2 Spreading regimes

The Chirikov criterion and the analysis of the selftrapping regime of Sec. 2.3.1 give a very good basis for the classification of the dynamical regimes occurring in disordered systems. Although the Chirikov criterion uses the NMs' nonlinear frequency shift and in particular when the resonance-overlap parameter $\mathcal{K} \gg 1$, leading to the inequality $\delta_\nu \gg d_\nu$ of case (c) in Sec. 2.3 to roughly predict the appearance of the selftrapping regime, we see that its prediction is in good agreement with the results obtained using the inequality $\delta_l > \Delta$ (2.51) [with $\Delta \gg d_\nu$] which is based on the nonlinear frequency shift of the sites' oscillations. Thus we foresee a relation of proportionality between δ_ν and δ_l . Indeed, if we excite a single mode, say mode ν , all the lattice sites within its localization volume P_ν become thermalized. Therefore the sum of norms/energies of each lattice sites within P_ν gives the total norm/energy of mode ν since the energy is an extensive parameter. As the energy is equal to the frequency here, it means that the nonlinear frequency shift of the mode ν is the cumulative nonlinear frequency shifts of all lattice sites within P_ν . Thus

$$\delta_\nu \propto P_\nu \delta_l, \quad (2.53)$$

where $\delta_l \approx \beta \sup_l |\psi_l|^2$ approximates the nonlinear frequency shift at every lattice site within P_ν . In addition, the relation between the width of the wave packet in both the NMs $\Delta\nu$ and real Δl spaces is of the form

$$\Delta\nu \propto \frac{\Delta l}{P_\nu}. \quad (2.54)$$

Consequently the resonance-overlap parameter (2.34) becomes

$$\mathcal{K} \propto \delta_\nu \cdot \frac{1}{d_\nu} \propto P_\nu \delta_l \cdot \frac{\Delta l}{P_\nu \Delta} = \frac{\delta_l}{d}, \quad (2.55)$$

where $d = \Delta/\Delta l$ was mentioned in Eq. (2.16), Δl being the number of sites with non-negligible amount of norm.

The 1D DDNLS system

We now apply the machinery developed above to determine the boundaries of the different dynamical regimes in the 1D DDNLS model. In doing so, we consider a compact, initial wave packet over L consecutive sites, with each site having the same norm s so that the total norm (2.19) is $\mathcal{S}_{1D} = L \cdot s$. Thus, $\delta_l = \delta = \beta s$ for each initially excited site. If $\beta s > \Delta$ a part of the wave packet remains trapped. The nonlinear frequency shift of every initial excited site is tuned out of resonance with the non excited surrounding and the selftrapping appears. If on the other hand, selftrapping is avoided (i.e. $\beta s < \Delta$), the wave packet starts spreading. We can distinguish between various cases. First if the initial wave packet size is smaller than the localization volume i.e. $L < \bar{V}$, it starts spreading over the sites within \bar{V} during a time τ_{in} . After that time the situation can be considered as having a new initial wave packet of size \bar{V} and *almost* uniform norm at each lattice excited sites $s(\tau_{in}) = sL/\bar{V}$. For $L \approx \bar{V}$ the norm at each site within the wave packet will not change much and $s(\tau_{in}) \approx s$. The obtained nonlinear frequency shift $\delta = \beta s(\tau_{in})$ at time τ_{in} can then be compared to the average spacing between frequencies d . Thus, if $\beta s(\tau_{in}) > d$, all the NMs in the wave packet are *strongly* resonantly interacting (this behavior corresponds to case (b) in Sec. 2.3). This regime is referred to as the *strong chaos regime* [Flach, 2010; Lapyteva et al., 2010]. On the other hand, if $\beta s(\tau_{in}) < d$ (this behavior is equivalent to case (a) above), the modes are weakly interacting and this regime is called the *weak chaos regime* [Flach, 2010; Lapyteva et al., 2010]. In summary based on the various initial wave packet excitations, the different possible dynamical regimes are

$$\begin{aligned} \text{weak chaos} & : & \beta s \frac{L}{\bar{V}} < d, \\ \text{strong chaos} & : & \beta s \frac{L}{\bar{V}} > d, \\ \text{selftrapping} & : & \beta s > \Delta. \end{aligned} \quad (2.56)$$

It is easy to see that in the case of single site initial excitation where $L = 1$, we cannot observe the strong chaos regime as $d = \Delta$ and the relations of Eq. (2.56) become

$$\begin{aligned} \text{weak chaos} & : & \beta s < \Delta, \\ \text{selftrapping} & : & \beta s > \Delta. \end{aligned} \quad (2.57)$$

Figure 2.4 depicts the location of each dynamical regime in the (W, δ) parameter space, when multi-site initial wave packets with width $L = \bar{V}$ are considered. The curve

$$\delta = \frac{\Delta}{\bar{V}} \approx \frac{W^2(W+4)}{330}, \quad (2.58)$$

denotes the boundary between the weak and strong chaos spreading regions and is obtained by estimating the localization volume as $\bar{V} \approx 330/W^2$ according to the fit presented in Fig. 2.3.

It is worth noting that in the case of a multi-site excited initial wave packet, the selftrapping in Eq. (2.56) can occur even faster as all we need is one activated site to be trapped. Indeed, at each site within the wave packet, the general condition $\delta = \Delta - 2\epsilon_l$ (2.51) is tested. In particular, for lattice's sites with $\epsilon_l \approx W/2$, the condition for selftrapping becomes

$$\delta \approx W + 4 - 2\frac{W}{2} = 4, \quad (2.59)$$

similar to the one found in [Lapyteva et al., 2010].

Let us discuss the behavior of the system's orbits in the parameter space of Fig. 2.4. During the evolution of an initial wave packet, the value of W remains always fixed. As the total norm (which also

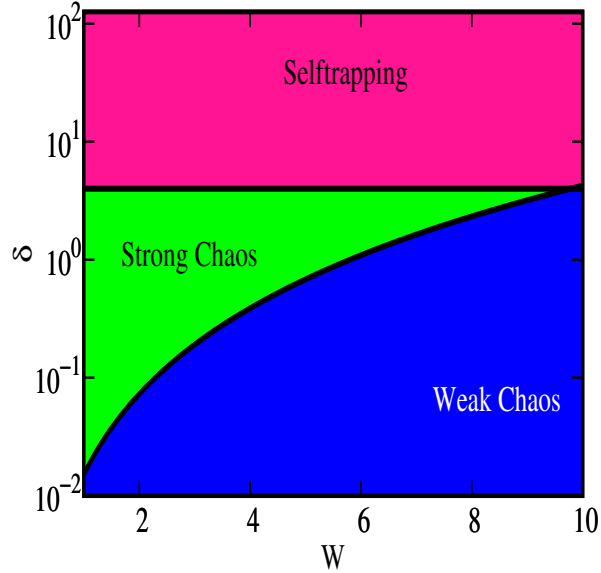


Figure 2.4: Location of the different dynamical regimes in the parameter space (W, δ) of the 1D DDNLS Hamiltonian (2.17) for the case of an initial wave packet of size $L = \bar{V}$. The upper curve corresponds to $\delta = 4$ (2.59) and the lower to $\delta = (W + 4)W^2/330$ (2.58).

remains constant as it is an integral of motion) is shared among more and more sites as the wave packet's Δl increases, the norm's amplitude at each site $s_l = |\psi_l|^2$ decreases in time and subsequently the related nonlinear frequency shift $\delta_l = \beta s_l$ decreases. Therefore this dynamical evolution is represented by points which move downward in the parameter space (W, δ) along lines perpendicular to the W axis. Thus a wave packet launched in the regime of weak chaos will remain there for all time. On the other hand, a wave packet initiated in the strong chaos regime (i.e. $\delta > d$) will remain in that region for some finite time τ_s , and eventually will cross over to the weak chaos regime (i.e. $\delta < d$) as δ is decreasing [Flach, 2010]. Finally, an initial wave packet launched in the selftrapping regime (i.e. $\delta > 4$) will always have part of its norm remaining trapped at some sites, a behavior corresponding to regions of quasi-periodic motion in the system's phase space.

The 1D DKG system

For the sake of completeness we will briefly discuss the manifestation of the various dynamical regimes in the 1D DKG system (2.24). More details on the subject can be found in [Senyange, 2021]. A correspondence between the 1D DDNLS system and the 1D DKG model described by $\sum_l \beta s_l \approx \sum_l 3W \tilde{h}_l$ is valid for small amplitude excitation of the 1D DDNLS model [Kivshar and Peyrard, 1992; MacKay and Aubry, 1994; Johansson and Rasmussen, 2004; Johansson, 2006; Lapyteva et al., 2010, 2012] where $s_l = |\psi_l|^2$ and $\tilde{h}_l = p_l^2/2 + \tilde{\epsilon}_l q^4/4 + [(q_l - q_{l-1})^2 + (q_{l+1} - q_l)^2]/4W$ are respectively the norm for the 1D DDNLS system and the energy for the 1D DKG model at site l . Considering uniform norm (energy) excitations of adjacent sites for the 1D DDNLS (1D DKG) model so that each excited site has initially norm (energy) s (\tilde{h}), the various dynamical regimes of (2.56) correspond to the following cases for the DKG system (2.24)

$$\begin{aligned}
 \text{weak chaos} & : \quad \tilde{h} \frac{L}{\bar{V}} < d/3W, \\
 \text{strong chaos} & : \quad \tilde{h} \frac{L}{\bar{V}} > d/3W, \\
 \text{selftrapping} & : \quad \tilde{h} > \Delta_K/3,
 \end{aligned} \tag{2.60}$$

where Δ_K is the width of the squared frequency spectrum of the linear DKG model. Note that in Eq. (2.60), we use the fact that the frequency bandwidth of the 1D DDLS model (2.1) corresponds to $\Delta_K W$ (see Appendix A for the derivation of this relation) and that the NMs average spacing d is the same for both 1D models. Again, we see that in the case of a single site excitation ($L = 1$), the strong chaos regime does not appear as $d/3W = \Delta_K/3$.

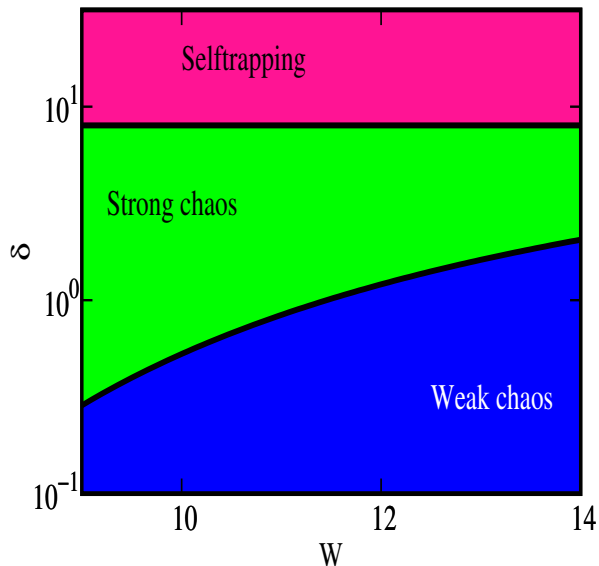


Figure 2.5: Location of the different dynamical regimes in the parameter space (W, δ) of the 2D DDNLS Hamiltonian (2.20) for the case of an initial wave packet of size $L^2 = \bar{V}$. The upper curve corresponds to $\delta = 8$ using a similar method like in Eq. (2.59) and the lower to $\delta \approx (W + 8) / (3.2e^{237/W^2})$.

The 2D DDNLS system

The dynamical regimes underlined in Eq. (2.56) are valid for the 2D DDNLS where L has to be replaced by L^2 (square excitation). Defining the different dynamical regimes in Eqs. (2.56) and (2.57), we had to find d and \bar{V} and the relation between them, something which can be done also for the 2D DDNLS system. Unfortunately in this case, the relation between the localization volume \bar{V} and the disorder strength W is not well established. This is mainly because investigating the statistical properties of the system's NMs through the diagonalization (or the transfer matrix approach) of very large matrices is a hard computational task. Nevertheless, a rough estimation of \bar{V} can be obtained by evolving single site excitations in the linear version of the 2D lattice for very long times until the halting of the wave packet spreading is observed as a result of reaching the extent of the localization volume \bar{V} . Then according to [Laptyeva et al., 2012; Many Manda et al., 2020], the wave packet participation number averaged over several disorder realizations can be considered as a good estimator of \bar{V} . Assuming the relation,

$$\bar{V} \approx a_\zeta \bar{\zeta}^2, \quad \bar{\zeta} \approx \exp\left(\frac{b_\zeta}{W^2}\right) \quad (2.61)$$

between the averaged localization volume \bar{V} and localization length $\bar{\zeta}$, we obtain fitting the data of the average participation number over 10 disorder realizations in [Many Manda et al., 2020] (see also Table 5.1 of Chap. 5) $a_\zeta \approx 3.2$ and $b_\zeta \approx 118.3$ for W values around $W = 10$ which is in the range of our interest. In Eq. (2.61) the relation $\ln \bar{\zeta} \sim 1/W^2$ was used to express the localization length in the 2D DDNLS model [Kramer and MacKinnon, 1993; Garcia-Mata and Shepelyansky, 2009]. Since the width of the linear frequency spectrum is $\Delta = W + 8$ [Laptyeva et al., 2012], we can easily determine the boundaries of the various spreading regimes in the (W, δ) parameter space (see Fig. 2.5). In particular, the line $\delta = 8$ separates the selftrapping regime from the spreading ones and $\delta = (W + 8) / (3.2e^{237/W^2})$ defines the boundary between the weak and strong chaos spreading regimes as shown in Fig. 2.5.

2.4 A statistical physics approach in determining the various dynamical regimes

So far, following [Shepelyansky, 1993; Pikovsky and Shepelyansky, 2008; Flach et al., 2009; Skokos et al., 2009; Flach, 2010; Laptyeva et al., 2010, 2012; Bodyfelt et al., 2011a; Laptyeva, 2013; Laptyeva et al., 2014] we characterized the different dynamical regimes of the DDNLS system in one and two spatial dimensions in the parameter spaces (W, δ) based on only one integral of motion of the system, namely the total norm. In what follows, we will use the existence of the system's two integrals of motion, i.e.

the total energy and the total norm, to investigate the existence of the various spreading regimes. We will do that by implementing the theory of the *grand canonical ensemble* of statistical physics [Landau and Lifshitz, 1980; Tong, 2012] which describes the thermal states of a system conserving both the total energy and the total number of particles. The latter, in the case of the DDNLS models, corresponds to the total norm. Our analysis is based on the results presented in [Rasmussen et al., 2000; Johansson and Rasmussen, 2004; Flach, 2016; Mithun et al., 2018; Kati et al., 2020].

2.4.1 Thermal and non-thermal regions

We will first describe the energy-norm parameter space for the DDNLS models and identify there the regions corresponding to the different dynamical spreading regimes we discussed so far. We relate to the thermal or Gibbs phase the region of the energy-norm parameter space whose system's states have finite temperatures, denoting as non-thermal or non-Gibbs phase the remaining regions within the system's allowed energy values. In this section, we consider the 1D DDNLS model whose energy and norm are given by Eq. (2.17) and Eq. (2.19) respectively.

Further, for the rest of this section, we consider the thermodynamic limit i.e. $N \rightarrow \infty$. Since the disorder parameter are randomly distributed with a uniform probability $\mathcal{P}_W = 1/W$ in the interval $[-W/2, W/2]$, we have [Flach, 2016]³

$$\epsilon = \lim_{N \rightarrow \infty} \frac{1}{\sum_{l=1}^N \mathcal{P}_W} \sum_{l=1}^N \mathcal{P}_W \epsilon_l = \lim_{N \rightarrow \infty} \frac{1}{N} \sum_{l=1}^N \epsilon_l = 0, \quad (2.62)$$

with the finite standard deviation

$$\sigma_\epsilon = \lim_{N \rightarrow \infty} \frac{1}{\sum_{l=1}^N \mathcal{P}_W} \sum_{l=1}^N \mathcal{P}_W \epsilon_l^2 = \lim_{N \rightarrow \infty} \frac{1}{N} \sum_{l=1}^N \epsilon_l^2. \quad (2.63)$$

We write the wave function as

$$\psi_l = \sqrt{s_l} e^{i\theta_l}, \quad (2.64)$$

where $s_l = |\psi_l|^2$ is the norm and θ_l being the local phase which contains information about the local energy h_l at site l . Substituting Eq. (2.64) into the norm reduces to

$$\mathcal{S}_{1D} = \sum_{l=1}^N s_l, \quad (2.65)$$

and the energy (2.17) reads

$$\mathcal{H}_{1D} = \sum_{l=1}^N \epsilon_l s_l + \frac{\beta}{2} s_l^2 - 2\sqrt{s_l s_{l+1}} \cos(\theta_l - \theta_{l+1}). \quad (2.66)$$

In addition, we respectively denote the ensemble average energy and norm densities

$$h = \frac{\mathcal{H}_{1D}}{N}, \quad s = \frac{\mathcal{S}_{1D}}{N}. \quad (2.67)$$

Furthermore, following [Flach, 2016; Mithun et al., 2019] we define for convenience the rescaled averaged norm and energy densities

$$x = \beta s, \quad y = \beta h, \quad (2.68)$$

respectively and use them to span the energy-norm parameter space. We first start searching the location in the (x, y) parameter space of thermal states which are bounded from below by zero ($T = 0$) and above by infinite ($T = \infty$) temperature states. If we set $\tilde{\nu} = 1/T$, then we denote the boundary of zero temperature states by the curve $y_{\tilde{\nu} \rightarrow \infty}(x)$ and the one of infinite temperature states with $y_{\tilde{\nu}=0}(x)$, where the subscript indicates the temperature of the system along each curve. Within the thermal region, the probability ρ_G to find a system with temperature T , energy \mathcal{H}_{1D} and norm \mathcal{S}_{1D} is given by [Rasmussen et al., 2000; Johansson and Rasmussen, 2004; Flach, 2016; Mithun et al., 2018]

$$\rho_G = \frac{1}{\mathcal{Z}} \exp\{-\tilde{\nu}(\mathcal{H}_{1D} + \mu \mathcal{S}_{1D})\}, \quad (2.69)$$

³The distribution of the disorder parameter is similar to the ones of the thermodynamics states in the microcanonical ensemble [Landau and Lifshitz, 1980; Tong, 2012].

where \mathcal{Z} is the so-called *the partition function*, $\tilde{\nu}$ being the inverse temperature. The variable μ is equivalent to a chemical potential in the normal grand canonical ensemble [Landau and Lifshitz, 1980; Tong, 2012].

The thermal states with zero temperature possess the minimum of energy. In expression (2.66), such a value of the energy is reached for wave functions with $\theta_{l+1} - \theta_l = 0$ and $s_l = s$

$$E^{(min)} = \sum_{l=1}^N (\epsilon_l - 2) s + \frac{\beta}{2} s^2, \quad (2.70)$$

and depends on the disorder realizations through the values of ϵ_l [Flach, 2016; Kati et al., 2020]. However in the thermodynamic limit (averaging over lattice sites)

$$h = \frac{E^{(min)}}{N} = -2s + \frac{\beta}{2} s^2, \quad (2.71)$$

which is a quantity independent of the considered disorder realization. Consequently the zero temperature states belong to the curve

$$y_{\tilde{\nu} \rightarrow \infty} = -2x + \frac{x^2}{2}. \quad (2.72)$$

In the case of a finite number of sites N and non-negligible value of W , the curve of zero temperature (2.72) is bounded as [Flach, 2016]

$$-(2 + \frac{W}{2})x + \frac{x^2}{2} \leq y_{\tilde{\nu} \rightarrow \infty}(x, \epsilon_l) \leq (-2 + \frac{W}{2})x + \frac{x^2}{2}, \quad (2.73)$$

and can be located within this interval using numerical computations [Kati et al., 2020].

We now look at the boundary curve which contains infinite temperature states $y_{\tilde{\nu}=0}$. In the same fashion as above, such states correspond to the case with maximal energy. Unfortunately, the Hamiltonian (2.66) is not bounded from above as it diverges for $s_l \rightarrow \infty$. Instead, we use the fact that if one knows the analytical form of \mathcal{Z} then

$$\mathcal{S}_{1D} = -\frac{1}{\tilde{\nu}} \frac{\partial}{\partial \mu} \ln \mathcal{Z}, \quad \mathcal{H}_{1D} + \mu \mathcal{S}_{1D} = -\frac{\partial}{\partial \tilde{\nu}} \ln \mathcal{Z}. \quad (2.74)$$

The partition function [Landau and Lifshitz, 1980; Tong, 2012; Rasmussen et al., 2000; Johansson and Rasmussen, 2004; Mithun et al., 2018]

$$\mathcal{Z} = \int_0^\infty \int_0^{2\pi} \prod_{l=1}^N d\theta_l ds_l \exp \{ -\tilde{\nu} (\mathcal{H}_{1D} + \mu \mathcal{S}_{1D}) \}, \quad (2.75)$$

contains all the thermodynamical information of the states of the system. Substituting \mathcal{H}_{1D} (2.66) in (2.75) and integrating with respect to the phases θ_l , we get

$$\mathcal{Z} = (2\pi)^N \int_0^\infty \prod_{l=1}^N ds_l I_0(2\tilde{\nu} \sqrt{s_l s_{l+1}}) \exp \left\{ -\tilde{\nu} \sum_{l=1}^N \left(\mu_l s_l + \frac{\beta}{2} s_l^2 \right) \right\}, \quad (2.76)$$

where $\mu_l = \epsilon_l + \mu$ is a disorder realization dependent constant and

$$I_0(x) = \frac{1}{\pi} \int_0^\pi e^{x \cos \theta} d\theta, \quad (2.77)$$

is the modified Bessel function of order zero. As we are solely interested in the limit for large temperatures $T \rightarrow \infty$, we can find an analytical approximation of the partition function (2.76) for $\tilde{\nu} \rightarrow 0$. The first step to achieve this goal is to approximate the modified Bessel function [Rasmussen et al., 2000; Johansson and Rasmussen, 2004; Flach, 2016; Mithun et al., 2018]

$$I_0(2\tilde{\nu} \sqrt{s_l s_{l+1}}) \approx I_0(0) \approx 1, \quad (2.78)$$

as its value is slowly changing around the origin. Thus

$$\mathcal{Z} \propto (2\pi)^N \prod_{l=1}^N \tilde{y}_\beta(\tilde{\nu}, \mu_l), \quad (2.79)$$

and the problem is reduced to finding an approximate closed expression for an integral of the form

$$\tilde{y}_\beta(\tilde{\nu}, \mu_l) = \int_0^\infty dx e^{-\tilde{\nu}\mu_l x} e^{-\tilde{\nu}\frac{\beta}{2}x^2}. \quad (2.80)$$

The details of these calculations can be found in Appendix C.1. Here, we give only the final result

$$\tilde{y}_\beta(\tilde{\nu}, \mu_l) \approx \frac{1}{\tilde{\nu}\mu_l} \left(1 - \frac{\tilde{\nu}\beta}{(\tilde{\nu}\mu_l)^2} \right). \quad (2.81)$$

Inserting Eq. (2.81) into Eq. (2.79), we get

$$\ln \mathcal{Z} \approx N \ln 2\pi - \sum_{l=1}^N \left[\ln(\tilde{\nu}\mu_l) + \frac{\tilde{\nu}\beta}{(\tilde{\nu}\mu_l)^2} \right], \quad (2.82)$$

by assuming that $\beta\tilde{\nu}/(\tilde{\nu}\mu_l)^2 \ll 1$ and applying the approximation $\ln(1-x) \approx -x$. From the value of the partition function (2.82), we estimate the ensemble average energy and norm [Rasmussen et al., 2000; Johansson and Rasmussen, 2004; Tong, 2012; Flach, 2016]

$$\mathcal{S}_{1D} = -\frac{1}{\tilde{\nu}} \frac{\partial}{\partial \mu} \ln \mathcal{Z}, \quad \mathcal{H}_{1D} = \left(\frac{\mu}{\tilde{\nu}} \frac{\partial}{\partial \mu} - \frac{\partial}{\partial \tilde{\nu}} \right) \ln \mathcal{Z}, \quad (2.83)$$

for system with infinite temperature. We obtain

$$s = \frac{\mathcal{S}_{1D}}{N} = \frac{1}{\tilde{\nu}\mu}, \quad h = \frac{\mathcal{H}_{1D}}{N} = \frac{\beta}{\tilde{\nu}^2\mu^2}. \quad (2.84)$$

Again, we refer the reader to Appendix C.2 for the detailed calculations. It follows from Eq. (2.84) that the infinite temperature states lie on the curve

$$y_{\tilde{\nu}=0} = x^2, \quad (2.85)$$

and correspond to chains of uncoupled harmonic oscillators [Rasmussen et al., 2000; Johansson and Rasmussen, 2004; Flach, 2016; Mithun et al., 2018]. As the energy (2.66) is not bounded from above, it means that every state in the (x, y) plane with $y > y_{\tilde{\nu}=0}$ cannot be described by the Gibbs probability distribution function ρ_G (2.69) and consequently it corresponds to the non-thermal region of the parameter space. In Fig. 2.6(a) we recapitulate the location of each statistical domain in the thermodynamic limit. Below the thermal phase is an inaccessible region for the system's energy and norm parameters.

2.4.2 Weak, strong chaos and selftrapping regimes

In the context developed in the previous section let us now investigate the spreading of an initial block excitation of L central sites, so that $\psi_l = \sqrt{s}e^{i\theta_l}$ inside the excited part of the initial wave packet and 0 otherwise, where s is the amplitude and $0 \leq \theta_l \leq 2\pi$ the phase of the wave function at site l . As discussed in the previous section, in-phase wave packets i.e. $\theta_{l+1} = \theta_l$ attain the minimum possible energy $E^{(min)}$ [see Eq. (2.70)]. Therefore, such initial wave packets will always belong to the Gibbs region. More specifically, such wave packets were encompassed within a regime named Lifshits region in [Kati et al., 2020] whose maximal size is defined by inequality (2.73).

In case of an out-of-phase initial excitation such that $\theta_{l+1} = \theta_l + \pi \pmod{2\pi}$, the energy of the system is given by

$$\mathcal{H}_{1D} = \sum_{l=1}^N (2 + \epsilon_l) s + \frac{\beta}{2} s^2, \quad (2.86)$$

which also depends on the disorder realization. These system states in the (x, y) parameter space lie on the curve $y(x, \epsilon_l)$ which is bounded as

$$\left(2 - \frac{W}{2} \right) x + \frac{x^2}{2} \leq y(x, \epsilon_l) \leq \left(2 + \frac{W}{2} \right) x + \frac{x^2}{2}. \quad (2.87)$$

Consequently for $x > \Delta$ all these initial wave packets belong to the Gibbs regime, while for $x < \Delta$ some of these initial excitations may lie within the non-Gibbs regime.

An important factor for our analysis is that in the Gibbs region, thermalization is well defined and therefore we expect the regimes of weak and strong chaos spreading to be located there. Let us also note that for the nonlinear frequency shift of a single oscillator we get

$$\delta_l = \beta s \approx x. \quad (2.88)$$

Therefore, we compare the value of x to the average spacing between linear frequencies d (2.16) of the initial wave packet excitation in order to delimit the various dynamical regimes. Thus for our homogeneous finite size initial wave packet of size $L = \bar{V}$, the following outcomes are expected: if $x \ll d$, the localization of the wave packet is expected to persist at least for a long time. In addition if $x \lesssim d$ a subdiffusive spreading of the wave packet in the weak chaos regime will take place, while for $x \gtrsim d$ that spreading happens in the strong chaos regime.

We now study the various locations of the selftrapping regime in the (x, y) parameter space of the 1D DDNLS model. From Eq. (2.56), depending on whether or not

$$x > \Delta, \quad (2.89)$$

the initial wave packet will be almost fully trapped. Since Eq. (2.89) does not specify conditions on y values, we loosely conclude that the selftrapping regime incorporate both Gibbs and non-Gibbs phases for large values of x (the norm) in the energy-norm parameter space. The question is to know if selftrapped wave packets also occur in the region $x < \Delta$. The first clue comes from the fact that, in the non-Gibbs region i.e. $y > x^2$, long time localized nonlinear solutions (breathers) appear in the DNLS model which may support the onset of selftrapping of wave packets in the DDNLS systems [Tsironis and Aubry, 1996; MacKay and Aubry, 1994; Flach and Willis, 1998; Rasmussen et al., 2000; Campbell et al., 2004; Johansson and Rasmussen, 2004; Kopidakis et al., 2008; Flach and Gorbach, 2008; Flach, 2016; Mithun et al., 2018]. To be more specific, based on the work of [Kopidakis et al., 2008; Skokos et al., 2009] (see Sec. 2.3.1), Eq. (2.44) gives a rough boundary above which such selftrapping regime can be seen

$$y > 2x, \quad (2.90)$$

in the thermodynamic limit. Consequently, a part of the weak and strong chaos regimes when $x \approx d$ belongs to the non-Gibbs phase as depicted in Fig. 2.6(b). The best explanation for this, so far comes from [Mithun et al., 2018] where it was suggested that once crossing the curve $y_{\bar{\nu}=0}$ the dynamics of the system do not directly becomes fully non-ergodic. Whence, spreading is still possible in that region. Here, it is easy for us to relate the ergodicity of a dynamical system's orbits in its phase space to its chaoticity. Roughly speaking, a regular orbit of the system is non-ergodic and a chaotic one is ergodic.

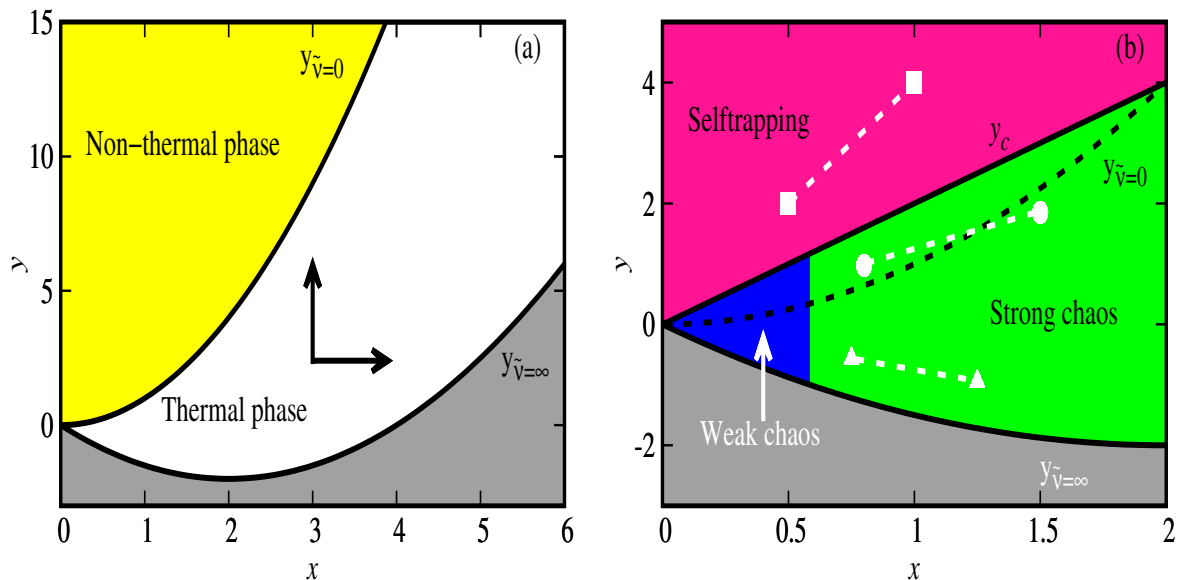


Figure 2.6: Parametric space of average norm x , vs. average energy y per site of the 1D DDNLS model (2.17) in the thermodynamics limit. (a) The bold lines $y_{\bar{\nu}=\infty} = -2x + x^2/2$ and $y_{\bar{\nu}=0} = x^2$ delimit the thermal phase in the Gibbsean sense. The arrows inside the thermal regimes report the directions toward the selftrapping regime. (b) The three colored areas represent the weak chaos [blue], strong chaos [green] and selftrapping [pink] regimes. The black bold curves $y_{\bar{\nu}=\infty} = -2x + x^2/2$ and $y_c = 2x$ denotes the limit of the spreading regimes. The black dashed curve $y_{\bar{\nu}=\infty} = x^2$ is the upper limit of thermal states in the sense of the grand-canonical distribution. The white dashed lines represent examples of trajectories followed by a system starting from the distant points when its state belong to the thermal phase with negative [triangles] and positive [circles] energies, and in the non-thermal phase [squares].

2.4.3 Wave packet evolution in the energy-norm parameter space

Let us look now at how trajectories of systems are represented in the (x, y) parameter space (see Figs. 2.6(a) and (b)). In the course of the wave packet spreading both the constant total energy and norm are shared to more sites. Therefore, we expect the coordinates $x(t)$ and $y(t)$ of the system to decrease in time $t > 0$ as the system is getting closer to the integrable limit. A way to find the rate at which this happens is via a simple algebraic manipulation based on the conservation of the integrals of motions. Indeed,

$$\mathcal{H}_{1D} = h(0)L = h(t)\Delta l(t) \quad \text{and} \quad \mathcal{S}_{1D} = s(0)L = s(t)\Delta l(t), \quad (2.91)$$

Dividing the two equations in (2.91) leads to [Flach, 2016]

$$y(t) = \frac{y_0}{x_0}x(t), \quad (2.92)$$

where in Eq. (2.92) the subscript ‘0’ means that the observable is taken at time $t = 0$. From Eq. (2.92) we see that the system’s evolution follows a line starting from (x_0, y_0) toward the origin $(0, 0)$ at a constant rate y_0/x_0 . Three arguments arise. Indeed, if the slope $y_0/x_0 \geq 2$ (see squared points in Fig. 2.6(b)) the wave packet belongs to the selftrapping regime. Further if $y_0/x_0 < 2$, two scenarios appear: for states with positive average energy per site (see circle points in Fig. 2.6(b)) launched in the Gibbs region enters the non-Gibbs region, while those with negative average energy per site (see triangle points in Fig. 2.6(b)) launched within the Gibbs region does not crossover to the non-Gibbs region as they never intersect the curve $y_{\bar{\nu}=0} = x^2$.

2.5 Characteristic measures of wave packet spreading

We now discuss some characteristics of wave packet spreading in the weak and strong chaos dynamical regimes. In what follows we present results for the DDNLS models in one and two spatial dimensions which can be easily transferred to the DKG models.

2.5.1 The 1D DDNLS model

As we have seen in Sec. 2.3, the interactions of the NMs in the 1D DDNLS system is governed by (2.31)

$$i\frac{\partial\phi_\nu}{\partial t} = E_\nu\phi_\nu + \beta \sum_{\nu_1, \nu_2, \nu_3} I_{\nu, \nu_1, \nu_2, \nu_3} \phi_{\nu_1}^* \phi_{\nu_2} \phi_{\nu_3}, \quad (2.93)$$

where we expanded the wave packet $\psi_l = \sum_\nu \phi_\nu A_{\nu, l}$ in the basis of the normal modes $A_{\nu, l} \propto \bar{\zeta}^{-1/2} \exp(-(l - l_\nu)/\bar{\zeta})$ and the prefactor $\bar{\zeta}^{-1/2}$ ensures that the NM is normalized i.e. $\sum_l A_{\nu, l}^2 = 1$. Let us simplify Eq. (2.93) in order to capture its main features. The complex overlap between modes $I_{\nu, \nu_1, \nu_2, \nu_3} = \sum_l A_{\nu, l}^* A_{\nu_1, l}^* A_{\nu_2, l} A_{\nu_3, l} \propto \bar{\zeta}^{-3/2} \sum_l A_{\nu, l}^* \propto \zeta^{-3/2}$ [Shepelyansky, 1993]. Due to the localization of NMs we expect the sum in the right hand side of Eq. (2.93) to possess approximately $\bar{\zeta}^3$ terms as we are summing over three modes whose only sites’ contribution within the localization volumes are non-negligible. Consequently the evolution of the amplitude of an exterior mode ν to the wave packet is asymptotically governed by [Shepelyansky, 1993]

$$i\frac{\partial\phi_\nu}{\partial t} \sim E_\nu\phi_\nu + \beta\phi_{\nu_1}^3. \quad (2.94)$$

From Eq. (2.94), we get

$$\left|\dot{\phi}_\nu\right|^2 \sim \beta^2 |\phi_{\nu_1}|^6. \quad (2.95)$$

which gives us an estimation of the diffusion coefficient (also called momentary diffusion rate)

$$D \sim \beta^2 |\phi_{\nu_1}|^6, \quad (2.96)$$

of influx of the norm from thermalized modes ν_1 to non-thermalized ones ν . It is worth pointing out that the diffusion coefficient D (2.96) is time dependent (i.e. $D = D(t)$) through the mode’s norm $|\phi_{\nu_1}|^2$ (see Eq. (2.95)). For the rest of our work, we will always consider that the diffusion process of the wave packet is well defined by the relation

$$m_2 = Dt, \quad (2.97)$$

with m_2 being the second moment of the wave wave packet and D its momentary diffusion rate [Shepelyansky, 1993; Pikovsky and Shepelyansky, 2008; Flach et al., 2009; Skokos et al., 2009,

2013; Senyange et al., 2018; Many Manda et al., 2020]. If we further assume that during the time for which the approximation (2.94) holds, the wave packet width is Δl such that the norm $|\phi_{\nu_1}|^2$ is more or less equally distributed among all excited modes, the normalization condition

$$\Delta l |\phi_{\nu_1}|^2 \sim 1, \quad (2.98)$$

leads to the relation $|\phi_{\nu_1}|^2 \sim 1/\Delta l$. In addition, the wave packet second moment m_2 and participation number P are related to Δl as

$$m_2 \propto (\Delta l)^2 \sim \frac{1}{|\phi_{\nu_1}|^4}, \quad P \propto \Delta l \sim \frac{1}{|\phi_{\nu_1}|^2}, \quad (2.99)$$

respectively. Consequently, the wave packet second moment is

$$m_2 = Dt \sim \frac{1}{|\phi_{\nu_1}|^4}, \quad (2.100)$$

so that

$$\frac{1}{|\phi_{\nu_1}|^4} \sim Dt \sim \beta^2 |\phi_{\nu_1}|^6 t \Rightarrow \frac{1}{|\phi_{\nu_1}|^{10}} \sim \beta^2 t \Rightarrow m_2 \sim \frac{1}{|\phi_{\nu_1}|^4} \sim \beta^{4/5} t^{2/5}. \quad (2.101)$$

Thus we obtain

$$m_2 \sim \beta^{4/5} t^{2/5}, \quad P \sim \beta^{2/5} t^{1/5}, \quad (2.102)$$

which is exactly the estimation in [Shepelyansky, 1993]. It is important to note that the result $m_2 \sim t^{2/5}$ is not in agreement with our numerical results (and many others [see e.g. Flach et al., 2009; Skokos et al., 2009; Flach, 2010; Lapyteva et al., 2010; Skokos and Flach, 2010; Ivanchenko et al., 2014; Iomin, 2017; Vakulchyk et al., 2019; Kati et al., 2020]).

The analysis presented by [Shepelyansky, 1993; Pikovsky and Shepelyansky, 2008] was improved by [Flach et al., 2009; Flach, 2010; Krimer and Flach, 2010]. Indeed, based on the Chirikov criterion, resonant modes within the wave packet behave chaotically. Thus, we can write

$$\phi_{\nu_1} = \phi_{\nu_1}^r + \phi_{\nu_1}^c, \quad (2.103)$$

with $\phi_{\nu_1}^r$ and $\phi_{\nu_1}^c$ being the regular and chaotic contributions to the wave function dynamics of mode ν_1 respectively. According to [Flach, 2010; Krimer and Flach, 2010], only the modes which possess a non-negligible chaotic contribution are resonantly interacting [Flach et al., 2009; Flach, 2010]. We note that as the wave packet spreads, $|\phi_{\nu_1}| \rightarrow 0$ taking the system toward the integrable limit as the nonlinear interaction diminishes, we expect the regular part to dominate and the chaotic contribution of resonant modes to decrease. Furthermore, the probability \mathcal{P} of a mode to be resonant depends on the nonlinear frequency shift i.e. $\mathcal{P}(\beta|\phi_{\nu_1}|^2)$. Since the \mathcal{P} value is between 0 and 1, this probability also represents the average fraction of chaotic modes within the wave packet

$$\mathcal{P}(\beta|\phi_{\nu_1}|^2) \propto \frac{|\phi_{\nu_1}^c|}{|\phi_{\nu_1}|}. \quad (2.104)$$

Consequently, we rewrite Eq. (2.94)

$$i \frac{\partial \phi_{\nu}}{\partial t} \sim E_{\nu} \phi_{\nu} + \beta \mathcal{P}(\beta|\phi_{\nu_1}|^2) \phi_{\nu_1}^3 f(t), \quad (2.105)$$

where $f(t)$ accounts for the continuous spectrum of the chaotic fraction of thermalized modes $\mathcal{P}(\beta|\phi_{\nu_1}|^2)$ and corresponds to a Gaussian white noise so that $\langle f(t), f(t') \rangle = \delta(t - t')$ (in opposition to the discrete spectrum of the linear background E_{ν}). The above equation (2.105) leads to the time-dependent norm influx from the thermalized mode ν_1 to the cold one ν

$$\left| \dot{\phi}_{\nu} \right|^2 \sim \beta^2 |\phi_{\nu_1}|^6 [\mathcal{P}(\beta|\phi_{\nu_1}|^2)]^2 \Rightarrow |\phi_{\nu}|^2 \sim \beta^2 |\phi_{\nu_1}|^6 [\mathcal{P}(\beta|\phi_{\nu_1}|^2)]^2 t. \quad (2.106)$$

Thus the mode ν reaches the same norm as mode ν_1 i.e. $|\phi_{\nu_1}|^2$ after

$$T_M \sim \left(\beta^2 |\phi_{\nu_1}|^4 [\mathcal{P}(\beta|\phi_{\nu_1}|^2)]^2 \right)^{-1}, \quad (2.107)$$

which is a characteristic timescale for the wave packet diffusion, such that its inverse defines a diffusion rate (see Secs. 3.4.1, 4.5 and 5.5 for further details)

$$T_M \sim \frac{1}{D} \Rightarrow D \sim \beta^2 |\phi_{\nu_1}|^4 [\mathcal{P}(\beta|\phi_{\nu_1}|^2)]^2, \quad (2.108)$$

which depends on the portion of chaotically resonant modes \mathcal{P} inside the wave packet.

Let us see now the result of the analysis for the strong and weak chaos spreading regimes.

- a) **Strong chaos.** As discussed in Sec. 2.3, in this case all the modes in the wave packet are chaotic, which means that $\mathcal{P} \approx 1$, we get from Eq. (2.108)

$$D \sim \beta^2 |\phi_{\nu_1}|^4. \quad (2.109)$$

Then from Eqs. (2.100) and (2.109) we obtain the estimation

$$\frac{1}{|\phi_{\nu_1}|^4} \sim Dt \sim \beta^2 |\phi_{\nu_1}|^4 t \Rightarrow \frac{1}{|\phi_{\nu_1}|^8} \sim \beta^2 t \Rightarrow m_2 \sim \frac{1}{|\phi_{\nu_1}|^4} \sim \beta t^{1/2}. \quad (2.110)$$

Thus we get $m_2 \sim \beta t^{1/2}$ and $P \sim \beta^{1/2} t^{1/4}$ found in [Flach et al., 2009; Flach, 2010; Lapyteva et al., 2010; Iomin, 2017].

- b) **Weak chaos.** In this case, not all the modes within the wave packet interact chaotically. In particular $\mathcal{P} \approx C\beta|\phi_{\nu_1}|^2$, where C is a prefactor [Flach, 2010; Krimer and Flach, 2010; Lapyteva et al., 2010]. Following a similar approach as in the above case a), we obtain the diffusion coefficient

$$D \sim C^2 \beta^4 |\phi_{\nu_1}|^8. \quad (2.111)$$

Consequently

$$\frac{1}{|\phi_{\nu_1}|^4} \sim Dt \sim C^2 \beta^4 |\phi_{\nu_1}|^8 t \Rightarrow \frac{1}{|\phi_{\nu_1}|^{12}} \sim C^2 \beta^4 t \Rightarrow m_2 \sim \frac{1}{|\phi_{\nu_1}|^4} \sim C^{2/3} \beta^{4/3} t^{1/3}. \quad (2.112)$$

Therefore $m_2 \sim t^{1/3}$ and $P \sim t^{1/6}$ exactly the estimation found in [Flach, 2010; Lapyteva et al., 2010].

- c) **Selftrapping.** In the case of selftrapping regime, a substantial part of the wave packet remain localized while the other portion spreads infinitely. Thus, we should expect the wave packet second moment to always increase as $m_2 \sim t^{a_m}$ ($0 < a_m < 1$) following the processes described above. However, when the norm of the wave packet background is small enough, the value of the participation number which indicates the number of highly excited sites saturates at a value which gives the number of sites effectively trapped P_{tr} . Therefore, we expect $P \sim P_{tr} t^0$ in the limit of very large wave packets.

2.5.2 The 2D DDNLS model

The analysis of Sec. 2.5.1 can be extended to any number of spatial dimensions, but we will consider only the 2D case [Garcia-Mata and Shepelyansky, 2009; Flach, 2010; Lapyteva et al., 2012]. Indeed, the system's wave function can be written as $\psi_{l,m} = \sum_{\nu} \phi_{\nu} A_{\nu,l,m}$ where $A_{\nu,l,m} \propto \bar{\zeta}^{-1} \exp\left(-[(l - \bar{l}_{\nu})^2 - (m - \bar{m}_{\nu})^2]^{1/2} / \bar{\zeta}\right)$ with $(\bar{l}_{\nu}, \bar{m}_{\nu})$ the spatial center of mode $\Psi_{\nu} = (A_{\nu,1,1}, A_{\nu,1,2}, \dots, A_{\nu,N,M})$ and $\bar{\zeta}$ the average localization length of NMs over modes and disorder realizations (note that in 2D the $\bar{\zeta}$ can be considered as the radius or the side of a NM's volume). Thus the evolution of the 2D DDNLS model in the NM space $A_{\nu,l,m}$ is still described by Eq. (2.93) but now the overlap-integral is $I_{\nu,\nu_1,\nu_2,\nu_3} = \sum_{l,m} A_{\nu,l,m}^* A_{\nu_1,l,m}^* A_{\nu_2,l,m} A_{\nu_3,l,m} \propto \bar{\zeta}^{-3} \sum_{l,m} A_{\nu,l,m}^* \propto \bar{\zeta}^{-3}$ and the number of terms in the sum in the right hand side of Eq. (2.31) being $\bar{\zeta}^{3 \times 2}$ due to the localization of the modes ν_1 , ν_2 and ν_3 [Garcia-Mata and Shepelyansky, 2009]. This leads again in the approximations (2.105) to (2.108).

The difference with the 1D case comes from the expression of the geometrical characteristics of the wave packet. The normalization of the system's wave packet implies $\Delta l |\phi_{\nu_1}|^2 \sim 1$ where Δl is the volume of the wave packet in 2 dimensions. We express Δl as

$$\Delta l \propto \Delta R^2, \quad (2.113)$$

where ΔR can be viewed as the side or the radius of the wave packet. The value of ΔR is related to the second moment and participation number of the wave packet by [Garcia-Mata and Shepelyansky, 2009; Flach, 2010]

$$m_2 \propto (\Delta R)^2 \sim \frac{1}{|\phi_{\nu_1}|^2}, \quad P \propto \Delta l = (\Delta R)^2 \sim \frac{1}{|\phi_{\nu_1}|^2}. \quad (2.114)$$

From Eq. (2.114), we see that the time dependence of the m_2 and P are the same in 2D lattice. So in this case, we have the following behaviors.

a) **Strong chaos.** Repeating the same process as in case a) of Sec. 2.5.1 with $D \sim \beta|\phi_{\nu_1}|^4$, we get

$$\frac{1}{|\phi_{\nu_1}|^2} \sim Dt \sim \beta^2|\phi_{\nu_1}|^4t \Rightarrow \frac{1}{|\phi_{\nu_1}|^6} \sim \beta^2t \Rightarrow m_2 \sim \frac{1}{|\phi_{\nu_1}|^2} \sim \beta^{2/3}t^{1/3}. \quad (2.115)$$

Consequently, we find the estimations $m_2 \sim t^{1/3}$ and $P \sim t^{1/3}$ of [Flach, 2010; Lapyteva et al., 2012].

b) **Weak chaos.** In analogy to case b) in Sec. 2.5.1 where $D \sim C^2\beta^4|\phi_{\nu_1}|^8$, we obtain

$$\frac{1}{|\phi_{\nu_1}|^2} \sim Dt \sim C^2\beta^4|\phi_{\nu_1}|^8t \Rightarrow \frac{1}{|\phi_{\nu_1}|^{10}} \sim C^2\beta^4t \Rightarrow m_2 \sim \frac{1}{|\phi_{\nu_1}|^2} \sim C^{2/5}\beta^{4/5}t^{1/5}. \quad (2.116)$$

Thus we get $m_2 \sim t^{1/5}$ and $P \sim t^{1/5}$ which are the estimations obtained in [Flach, 2010; Lapyteva et al., 2012].

c) **Selftrapping.** Similar arguments as in case c) of Sec. 2.5.1 hold. In addition, as the 2D NMs are more extended compared to the 1D counterpart, the spreading is faster. Whence, we expect the saturation $P \sim P_{tr}t^0$ to be reached faster in the former system.

2.6 Dynamics of extended initial wave packet

At last we would like to build a formalism for a special case of initial wave packets which proved to be very useful for numerical experiments, as it constitutes an effective way for obtaining long lasting strong chaos behavior. This is especially useful in 2D lattices where the final integration time is limited by computer capabilities and the boundaries of the strong chaos dynamical spreading regime are not very well defined [Lapyteva et al., 2012; Many Manda et al., 2020]. Indeed all the results above (see Figs. 2.6, 2.4 and 2.5 and Sec. 2.3.2) are presented for either single-site i.e. $L = 1$ or block-site excitations of about the localization volume i.e. $L \approx \bar{V}$ wave packets. Now let us ask ourselves what happens for much larger initial wave packet excitations i.e. $L \gg \bar{V}$ when selftrapping is avoided? First, if such an extended wave packet is given a large average norm s per site, we expect it to exhibit the characteristics of the strong chaos regime as the majority of the thermalized modes will chaotically interact (the effective nonlinearity per site is high). On the other hand, if s is small, both the strong and weak chaos spreading regimes are possible. More specifically, for the strong chaos spreading to be visible, the sum of the fractions of chaos within each wave packet's NMs should sum up to unity. For the 1D DDNLS model (2.17), we get

$$\sum_l C\beta s \sim 1 \Rightarrow xL \sim \frac{1}{C}, \quad (2.117)$$

where $x = \beta s$, with s being the constant norm at each excited site and the prefactor C introduces a disorder dependence on the fraction of chaotic NMs [Skokos et al., 2009; Flach, 2010]. Note that here, we assume that the number of NMs within the wave packet is approximately equal to the total number of excited sites. This leads to the estimation

$$L \sim \frac{W}{x}, \quad (2.118)$$

with $C \sim 1/W$ for the 1D DDNLS model [Krimer and Flach, 2010; Flach, 2010]. In the 2D DDNLS model (2.20), we obtain

$$\sum_{l,m} C\beta s \sim 1 \Rightarrow L^2 \sim \frac{1}{Cx}. \quad (2.119)$$

In Eq. (2.119) the dependence of C on the disorder parameter W is not known. Nevertheless, we can expect $C = C(1/W)$ similar to the 1D DDNLS model (2.118) [C decreases with increasing disorder strength]. In this context, for large enough disorder parameter W , we can loosely assume that $C \sim 1/W$.

2.7 Summary

In this chapter, we reviewed the notion of AL and analyzed both quantitatively and qualitatively its fate when nonlinearity is introduced. We focussed on the 1D and 2D DDNLS lattice models, but connections to the DKG systems were also briefly presented. When AL is destroyed, three dynamical behaviors are observed: the weak and strong chaos spreading regimes, as well as selftrapping case where a substantial part of the wave packet remains localized. The characteristics of these regimes were analyzed based on

the Chirikov criterion about the onset of chaos in nonlinear systems, as well as the study of selftrapping presented in [Kopidakis et al., 2008] and the location of these regimes in an appropriate parameter space (namely disorder strength W and average nonlinear frequency shift δ) was shown.

A further analysis based on statistical physics ideas was conducted in the parameter space of the rescaled average norm $x = \beta s$ and energy $y = \beta h$ densities where we identified the existence of Gibbs and non-Gibbs regions and their relation with the various dynamical regimes. Then, we presented the analytic derivation of the evolution of the wave packet's second moment m_2 and participation number P . In particular we have shown that

$$m_2 \sim \begin{cases} C^{2/3} \beta^{4/3} t^{1/3} \\ \beta t^{1/2} \end{cases}, \quad P \sim \begin{cases} C^{1/3} \beta^{2/3} t^{1/6} & \text{weak chaos,} \\ \beta^{1/2} t^{1/4} & \text{strong chaos,} \end{cases} \quad (2.120)$$

in the 1D case, while for its 2D counterpart, we obtained

$$m_2 = P \sim \begin{cases} C^{2/5} \beta^{4/5} t^{1/5} & \text{weak chaos,} \\ \beta^{2/3} t^{1/3} & \text{strong chaos.} \end{cases} \quad (2.121)$$

Furthermore, in the selftrapping regime of both the 1D and 2D systems, we asymptotically expect

$$m_2 \sim t^{a_m}, \quad P \sim P_{tr} t^0, \quad (2.122)$$

$$(2.123)$$

where a_m depends on the characteristics of chaos of the spreading part of the wave packet, while P_{tr} is the number of sites which remain highly thermalized (the number of sites the system's energy/norm is effectively trapped) in comparison to the wave packet's background.

Finally we also discussed the case of an initial wave packet which extends much further than the system's localization volume \bar{V} and has a small average norm s per site, showing that such an excitation can still evolve in the strong chaos regime. This result will be of practical use to us, especially when we will discuss the dynamics of the 2D DDNLS system in Chap. 5.

Chapter 3

Computational techniques

3.1 Introduction

In this chapter, we present the main numerical techniques we use in this thesis. More specifically, we discuss the wave packet's initialization and present the quantities we measure to characterize its evolution along with the system's chaoticity. A large part of this chapter is devoted to designing numerical integration schemes which efficiently follow the time evolution of wave packets. A particular emphasis is placed on a special type of numerical method called symplectic integrators (SIs) which preserve the phase space volume of conservative Hamiltonian systems, a property which is translated to the accurate conservation of the system's energy (i.e. the value of the Hamiltonian function itself) as its numerical error remains bounded for all times. This behavior makes SIs ideal numerical schemes for long time evolution of autonomous (conservative) Hamiltonian systems. In addition, the composition of simple low order SIs leads to new SIs with improved accuracy. We investigate the efficiency of these methods for the evolution of the equations of motion and the variational equations of the 1D and 2D DDNLS models. A large part of the material presented in this chapter is based on results published in [Danieli et al., 2019a].

The chapter is organized as follows: In Sec. 3.2 we define the quantities which characterize the wave packet's spatial extent, while in Sec. 3.3 we discuss how we set up the initial conditions for our numerical simulations. The framework of our numerical integration techniques along with the notions of the MLE and DVD are presented in Sec. 3.4. In Sec. 3.5, we explain the method used to obtain the power law exponents from scattered data sets. Section 3.6 is devoted to the presentation of standard integration techniques which can be used to integrate a general system of differential equations, while in Sec. 3.7 we develop various SI schemes which we implement for integrating simultaneously the equations of motion and the variational equations of both the 1D and 2D DDNLS systems. Then in Sec. 3.8 all integrators are compared and ranked according to their accuracy, efficiency and speed. Finally in Sec. 3.9 we summarize the content of this chapter.

3.2 Wave packet characterization

For the DDNLS model in one (2.17) and two (2.20) spatial dimensions, the wave packet extent is represented by the normalized norm density distribution [Flach et al., 2009; Senyange et al., 2018; Many Manda et al., 2020]

$$\xi_{\mathbf{r}} = \frac{s_{\mathbf{r}}}{\sum_{\mathbf{r}} s_{\mathbf{r}}}, \quad (3.1)$$

where $s_{\mathbf{r}} = |\psi_{\mathbf{r}}|^2$ is the local norm at site $\mathbf{r} = l$ in the 1D case, and $\mathbf{r} = (l, m)$ in the 2D lattice. If the norm is normalized so that $\sum_{\mathbf{r}} s_{\mathbf{r}} = 1$, the $\xi_{\mathbf{r}}$ and $s_{\mathbf{r}}$ are equal, meaning that the two quantities are equivalent. So in many place in this thesis we refer to $s_{\mathbf{r}}$ as simply the norm density. For the sake of completeness, let us note that for the DKG system, the normalized energy density [Skokos et al., 2009; Lptyeva et al., 2010; Senyange et al., 2018; Many Manda et al., 2020]

$$\xi_{\mathbf{r}} = \frac{h_{\mathbf{r}}}{\sum_{\mathbf{r}} h_{\mathbf{r}}}, \quad (3.2)$$

is considered, where

$$h_{\mathbf{r}} = \frac{p_{\mathbf{r}}^2}{2} + \frac{\tilde{\epsilon} q_{\mathbf{r}}^2}{2} + \frac{q_{\mathbf{r}}^4}{4} + \frac{1}{4W} \sum_{\mathbf{n}} (q_{\mathbf{n}} - q_{\mathbf{r}})^2, \quad (3.3)$$

is the local energy at site $\mathbf{r} = l$ [$\mathbf{r} = (l, m)$] in the 1D [2D] model and $\sum_{\mathbf{n}}$ represents a summation along all nearest neighbors of site \mathbf{r} .

We find the position of the center of the wave packet i.e. the first moment of the norm distribution as

$$\bar{\mathbf{r}} = \sum_{\mathbf{r}} \mathbf{r} \xi_{\mathbf{r}}, \quad (3.4)$$

while the squared distance from the center (3.4) i.e. the second moment

$$m_2 = \sum_{\mathbf{r}} \|\mathbf{r} - \bar{\mathbf{r}}\|^2 \xi_{\mathbf{r}}, \quad (3.5)$$

of the norm distribution is used to quantify the extent of the wave packet. As an alternative way to quantify the wave packet size, we also compute the so-called participation number (see also Eqs. (2.13) and (2.37) in Chap. 2)

$$P = \frac{1}{\sum_{\mathbf{r}} \xi_{\mathbf{r}}^2}, \quad (3.6)$$

which measures the number of highly excited sites.

3.3 Wave packet initialization

The fact that the DDNLS model in one and two spatial dimensions admits two integrals of motion, namely the total energy (Eqs. (2.17) and (2.20) for 1D and 2D systems respectively) and norm (Eqs. (2.19) and (2.23) for 1D and 2D systems respectively) requires some special care in setting up the the packet's initialization in order to create our initial condition at a particular point in the (x, y) plane of Figs. 2.4 and 2.6 (1D DDNLS model) and Fig. 2.5 (2D DDNLS system), where $x = \beta s$ (2.68) is the rescaled average norm density; which is equivalent to the average nonlinear frequency shift at each oscillator and $y = \beta h$ (2.68) the rescaled energy density. Let us focus on the 1D DDNLS system. In our numerical computation (and as suggested in Secs. 2.3 and 2.4), we want to initialize a wave packet of L consecutive sites with $\psi_l = \sqrt{s} \exp i\theta_l$ at the center of our lattice such that the norm (2.19) and the Hamiltonian (2.17) give

$$S_{1D} = Ls, \quad \mathcal{H}_{1D} = \sum_l \epsilon_l s + \frac{\beta}{2} s^2 - 2s \cos \Delta\theta_l, \quad (3.7)$$

with $\Delta\theta_l = \theta_{l+1} - \theta_l$ being the dephasing between adjacent sites and the summation in \mathcal{H}_{1D} counts only the L initially excited sites. In what follow, we describe two approaches in obtaining such initial states for specific x and y values.

3.3.1 Approach 1: Thermodynamical averaging

In this approach, we approximate the Hamiltonian in Eq. (3.7) in the thermodynamic limit [Flach, 2016; Kati et al., 2020], $\epsilon = \lim_{N \rightarrow \infty} N^{-1} \epsilon_l = 0$ and $\Delta\theta = \lim_{N \rightarrow \infty} (\sum_l \mathcal{P}_\theta)^{-1} \mathcal{P}_\theta \Delta\theta_l$ with \mathcal{P}_θ the probability distribution of the phases. Consequently from Eq. (3.7), we obtain

$$h = \frac{\beta}{2} s^2 - 2s \cos \Delta\theta \quad \Rightarrow \quad y = \frac{1}{2} x^2 - 2x \cos \Delta\theta. \quad (3.8)$$

In order to obtain a specific set of (x, y) values, we have to set the dephasing angle $\Delta\theta$ to the constant value

$$\Delta\theta = \arccos \left[\frac{x}{4} - \frac{y}{2x} \right]. \quad (3.9)$$

This arrangement leads to the following relation for the phases θ_l of initially excited sites

$$\theta_l \approx l\Delta\theta + \theta_0, \quad (3.10)$$

with θ_0 being the phase at the first site.

This method for setting our initial condition is quite effective for extended initial wave packet which can be considered to be close to the thermodynamic limit. For not-too-extended wave packets, we cannot neglect the contribution of the disorder parameter values at each site and the approximation of Eq. (3.8) is not very accurate. In this case, we find an initial condition leading to a point (x, y') which is close to the initially desired (x, y) . We consider different disorder realizations, i.e. different sets of ϵ_l values which generate a plethora of points (x, y') and keep in our analysis the ones which are the closest to the desired point (x, y) .

3.3.2 Approach 2: Setting specific energy per site

In order to overcome the problem of not accurately obtaining a specific (x, y) point, which as we already explained becomes more important for not very extended initial wave packets, we will take into account here the exact values of the ϵ_l and θ_l and accordingly tune the energy h_l of each site individually. For the initial block-site excitation $\psi_l = \sqrt{s} \exp i\theta_l$ of size L , described in the first lines of Sec. 3.3.1, we require the h_l values to satisfy Eq. (3.7) i.e for a given norm s per site

$$\sum_l \epsilon_l s + \frac{\beta}{2} s^2 - 2s \cos \Delta\theta_l = \sum_l h_l, \quad (3.11)$$

where again, the index l corresponds to only initially excited sites.

We can have infinitely many choices of h_l so that Eq. (3.11) is satisfied. The simplest one is to set all these values equal to a constant term i.e $h_l = h$. Inserting this choice in Eq. (3.11) and multiplying by β , we get the following set of nonlinear equations

$$\sum_l \epsilon_l x + \frac{x^2}{2} - 2x \cos(\theta_{l+1} - \theta_l) = \sum_l y. \quad (3.12)$$

Since the desired x and y values are given along with the parameters ϵ_l defining the specific disordered realization, system (3.12) corresponds to a set of L equations with L unknowns, the angles θ_l . Consequently, a root finding algorithm (e.g. Newton-Raphson) could be used to solve (3.12) in order to get the initial wave packet of the system. Since these angles appear in (3.12) only through their difference $\theta_{l+1} - \theta_l$, we have some flexibility in their determination. For example, setting θ_1 to be equal to a specific value, let's say Θ_1 , the solution of set (3.12) is straightforward

$$\begin{aligned} \theta_1 &= \Theta_1, \\ \theta_2 &= \arccos \left[\frac{x}{4} - \frac{y}{2x} + \frac{\epsilon_2}{2} \right] + \Theta_1, \\ \theta_3 &= \arccos \left[\frac{x}{4} - \frac{y}{2x} + \frac{\epsilon_3}{2} \right] + \Theta_2, \\ &\vdots \\ \theta_L &= \arccos \left[\frac{x}{4} - \frac{y}{2x} + \frac{\epsilon_L}{2} \right] + \Theta_{L-1}. \end{aligned} \quad (3.13)$$

In our computer code, we are using Eq. (3.13). In practice, we still have to iterate through several sets of disorder realizations, i.e. ϵ_l sequences, in order to find the ones which match the best with the solution (3.13). This is because the way we are treating endpoints in Eq. (3.13) matters. The difference with the previous method is the number of iterations, which appears to be drastically smaller for some types of initial conditions. This method needs still to be refined, something that we intend to do in the future.

The approach 1 in Sec. 3.3.1 can be easily translated to the 2D DDNLS system, while in the approach 2 of Sec. 3.3.2 the size of the system (3.12) increases exponentially with the initial wave packet volume and the form of the solution (3.13) is more subtle. Consequently, in most of the work performed within our simulations for the lattice initialization, we use the approach 1 of Sec. 3.3.1 for the 2D DDNLS system and the approach 2 presented in Sec. 3.3.2 in the case of the 1D DDNLS model.

3.4 Variational equations

Let us briefly discuss the time evolution of small perturbations to an orbit of a Hamiltonian system needed for the computation of various chaos indicators like the MLE that we will implement in our study. The Hamilton equations of motion, for an autonomous Hamiltonian system of N degrees of freedom have the form

$$\frac{d\mathbf{q}}{dt} = \frac{\partial \mathcal{H}}{\partial \mathbf{p}}, \quad \frac{d\mathbf{p}}{dt} = -\frac{\partial \mathcal{H}}{\partial \mathbf{q}}, \quad (3.14)$$

where $\mathcal{H} = \mathcal{H}(\mathbf{q}, \mathbf{p})$ is the system's Hamiltonian function, with $\mathbf{q} = (q_1 \ q_2 \ \dots \ q_N)^T$ and $\mathbf{p} = (p_1 \ p_2 \ \dots \ p_N)^T$ being respectively the generalized positions and momenta. Here the superscript (T) denotes the matrix transpose. The equations of motion (3.14) can be expressed in the general setting of ordinary differential equations (ODEs) as

$$\frac{dz}{dt} = \dot{z} = \mathbf{J}_{2N} \cdot \mathbf{D}_{\mathcal{H}}(\mathbf{z}(t)), \quad (3.15)$$

where $\mathbf{z} = (\mathbf{q} \ \mathbf{p})^T = (z_1 \ z_2 \ \dots \ z_N \ z_{N+1} \ \dots \ z_{2N})^T = (q_1 \ q_2 \ \dots \ q_N \ p_1 \ \dots \ p_N)^T$ is a vector representing the position of the system in its phase space and $(\dot{})$ denotes differentiation with respect to the time t . In Eq. (3.15)

$$\mathbf{J}_{2N} = \begin{pmatrix} \mathbf{O}_N & \mathbf{I}_N \\ -\mathbf{I}_N & \mathbf{O}_N \end{pmatrix}, \quad (3.16)$$

is the symplectic matrix with \mathbf{I}_N and \mathbf{O}_N being the $N \times N$ identity and null matrices respectively, and

$$\mathbf{D}_{\mathcal{H}} = \left(\frac{\partial \mathcal{H}}{\partial q_1} \ \frac{\partial \mathcal{H}}{\partial q_2} \ \dots \ \frac{\partial \mathcal{H}}{\partial q_N} \ \frac{\partial \mathcal{H}}{\partial p_1} \ \dots \ \frac{\partial \mathcal{H}}{\partial p_N} \right)^T. \quad (3.17)$$

The evolution of a small perturbation $\mathbf{w}(0) = \delta \mathbf{z}(0) = (\delta z_1(0) \ \delta z_2(0) \ \dots \ \delta z_N(0) \ \delta z_{N+1}(0) \ \dots \ \delta z_{2N}(0)) = (\delta q_1(0) \ \delta q_2(0) \ \dots \ \delta q_N(0) \ \delta p_1(0) \ \dots \ \delta p_N(0))$ which is also referred to as the deviation vector (DV) to the system's orbit $\mathbf{z}(0)$ evolves in the system's *tangent space*. The system's *tangent dynamics* describing the evolution of $\mathbf{w}(t)$ is governed by the so called variational equations (see e.g. [Skokos, 2010; Skokos and Gerlach, 2010])

$$\frac{d\mathbf{w}}{dt}(t) = \dot{\mathbf{w}}(t) = [\mathbf{J}_{2N} \cdot \mathbf{D}_{\mathcal{H}}^2(\mathbf{z}(t))] \mathbf{w}(t), \quad (3.18)$$

where

$$\mathbf{D}_{\mathcal{H}}^2(\mathbf{z}(t))_{i,j} = \left. \frac{\partial^2 \mathcal{H}}{\partial z_i \partial z_j} \right|_{\mathbf{z}(t)}, \quad (3.19)$$

is the $2N \times 2N$ Hessian matrix of the system evaluated at the phase space trajectory $\mathbf{z}(t)$. We emphasize that Eq. (3.18) is linear in $\mathbf{w}(t)$ with coefficients depending on the system's trajectory $\mathbf{z}(t)$. Therefore, one has to integrate the variational equations (3.18) along with the equations of motion (3.15) in order to follow the evolution of the DV. In practice, we create an extended vector $\mathbf{Z}(t) = (\mathbf{z}(t) \ \delta \mathbf{z}(t))^T$ and numerically solve the unified system of ODEs [Skokos and Gerlach, 2010; Gerlach and Skokos, 2011; Gerlach et al., 2012]

$$\frac{d\mathbf{Z}}{dt} = \mathbf{f}(\mathbf{z}, \delta \mathbf{z}) = \begin{pmatrix} \dot{\mathbf{z}} \\ \delta \dot{\mathbf{z}} \end{pmatrix} = \begin{pmatrix} \mathbf{J}_{2N} \cdot \mathbf{D}_{\mathcal{H}}(\mathbf{z}(t)) \\ (\mathbf{J}_{2N} \cdot \mathbf{D}_{\mathcal{H}}^2(\mathbf{z}(t)) \cdot \delta \mathbf{z}(t)) \end{pmatrix}. \quad (3.20)$$

The vector function \mathbf{f} is often called the vector field of (3.20), and is tangent at every point to the system's orbit $\mathbf{Z}(t)$ [Schroers, 2011].

3.4.1 Maximum Lyapunov exponent

The variational equations constitute a very important tool in our effort to characterize the chaoticity of Hamiltonian systems. A system's chaotic behavior is associated with an exponential rate of growth of the DV. This is quantified by computing the so-called finite time maximum Lyapunov exponent (ftMLE) [Benettin et al., 1980; Skokos, 2010; Pikovsky and Politi, 2016]

$$\Lambda(t) = \frac{1}{t} \ln \left(\frac{\|\mathbf{w}(t)\|}{\|\mathbf{w}(0)\|} \right), \quad (3.21)$$

at each time t of the evolution, with $\mathbf{w}(t)$ and $\mathbf{w}(0)$ being respectively the DV at time $t > 0$ and $t = 0$. Therefore, the MLE Λ_1 is

$$\Lambda_1 = \lim_{t \rightarrow \infty} \Lambda(t). \quad (3.22)$$

The time evolution of $\Lambda(t)$ can discriminate between regular and chaotic orbits in a rather straightforward way. Indeed, for regular orbits we expect the evolution of $\mathbf{w}(t)$ to be sub-exponential so that $\Lambda(t)$ tends to zero following a power law [Benettin et al., 1980; Skokos, 2010]

$$\Lambda(t) \propto t^{-1}, \quad (3.23)$$

otherwise the orbit is said to be chaotic. In the latter case, we can define approximately how much time the system needs to become chaotic [Skokos, 2010; Pikovsky and Politi, 2016],

$$T_L = \frac{1}{\Lambda_1}, \quad (3.24)$$

referred to as Lyapunov time.

3.4.2 Deviation vector distribution

As already mentioned, the ftMLE measures the average exponential rate of growth (or shrinking) of perturbations of an orbit and it is influenced by the global dynamics of the system. Therefore is a macroscopic observable, influenced by the overall dynamics. Trying to define a quantity which measures the local contribution of perturbations to the chaotic dynamics of the system, we compute what is called DVD [Skokos et al., 2013; Senyange et al., 2018; Hillebrand et al., 2019; Miranda Filho et al., 2019; Ngapasare et al., 2019; Many Manda et al., 2020] defined as the distribution of quantities

$$\xi_l^D = \frac{\delta q_l^2 + \delta p_l^2}{\sum_l \delta q_l^2 + \delta p_l^2}, \quad (3.25)$$

where δq_l and δp_l are the components of the deviation vector \mathbf{w} and l is the lattice's site. This distribution attains its highest values at sites which are more sensitive to small changes of initial conditions i.e. more chaotic. Consequently, it is a very useful tool to visualize the location of chaotic contributions (see the papers cited above).

Similarly to what we did for the normalized norm/energy density ξ , during our simulations we also calculate the statistical properties of the DVD ξ^D . We compute the first \bar{l}^D and second m_2^D moments which measure respectively the center's coordinates and the extent of the distribution. In addition, we also evaluate the participation number P^D of the DVD which gives the number of highly chaotic sites. It is worth noting that P^D has already been used to study the localization of chaos in the FPUT lattice [Dauxois et al., 1997] and DNA models [Barré and Dauxois, 2001; Hillebrand et al., 2019].

3.5 Numerical determination of power law exponents

As we will see in the two next chapters in several places we will need to accurately determine the power law exponent of the time evolution of dynamical quantities. Since the numerical data will not be smoothly located on a curve, we need a reliable numerical approach to determine such exponents in expected behavior of the form $Q(t) = Q_0 t^{\alpha_Q}$. The methodology we briefly describe here has been implemented successfully in many studies [Laptyeva et al., 2010; Bodyfelt et al., 2011a,b; Laptyeva et al., 2012; Laptyeva, 2013; Skokos et al., 2013; Laptyeva et al., 2014; Yusipov et al., 2017; Senyange et al., 2018; Vakulchuk et al., 2019; Many Manda et al., 2020].

Let us present the whole process by considering that our observable Q grows as $Q(t) = t^{2/5}$. As mentioned, the raw data obtained from the numerical simulations are not smooth. In order to mimic this behavior in this simple example, we create a time series of data by introducing a random noise to the exact values obtained by the law $t^{2/5}$ whose magnitude depends on the expected Q values. Fig. 3.1 presents

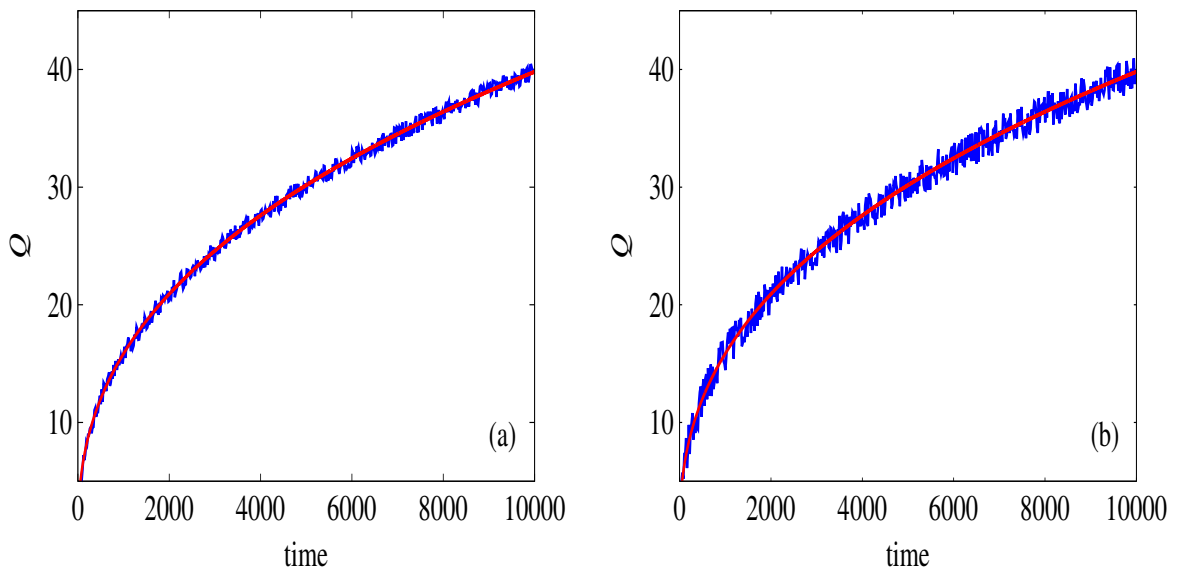


Figure 3.1: Randomly created values [(b)lue line connected points] around an artificial function $Q(t) = t^{2/5}$ [(r)ed curves]. The amplitude of the randomness is $\frac{1}{50}Q(t)$ (a) and $\frac{1}{25}Q(t)$ (b).

the evolution of such noisy outcome of $Q(t)$ for two different amplitudes of the noise. For example, in

Fig. 3.1 we see such a data set created by random additions (or subtractions) to the $Q(t) = t^{2/5}$ values when the magnitude of this randomness is $\frac{1}{50}Q(t)$ [panel (a)] and $\frac{1}{25}Q(t)$ [panel (b)]. Now, the question is how can we obtain the correct exponent ($2/5$ in our simple example) from the randomly scattered points.

More generally, if we want to estimate the exponent α_Q of the expression $Q(t) = Q_0 t^{\alpha_Q}$, it is better to see this law in the log – log scale as

$$\log_{10} Q = \alpha_Q \log_{10} t + \log_{10} Q_0, \quad (3.26)$$

and determine α_Q as

$$\alpha_Q = \frac{d \log_{10} Q}{d \log_{10} t}. \quad (3.27)$$

Since by line connecting the noisy data of Fig. 3.1 we do not get a differentiable curve, we first need to smooth the raw data. We do so by applying a locally weighted regression method developed in [Cleveland and Devlin, 1988], then use finite difference methods to evaluate the slope (3.27) [Fornberg, 1988, 1998]. More specifically in this work, we adapt the computer codes developed by Hilboll [Hilboll, 2007] for the regression process and by Xavier [Xavier, 2019] for the finite difference techniques.

We present in Fig. 3.2 the results of the smoothing procedure for the data of Fig. 3.1 [(b)lue line connected points] along with original function $Q = t^{2/5}$ [(r)ed curves]. There is a good agreement between the two, further supported by the value of the numerically computed exponent α_Q of the smoothed data presented in the insets of Fig. 3.2 whose values are very close to $2/5$. Obviously, the deviation from the ‘actual’ value $\alpha_Q = 2/5 = 0.4$ is larger in the case of the more noisy points (Fig. 3.2(b)).

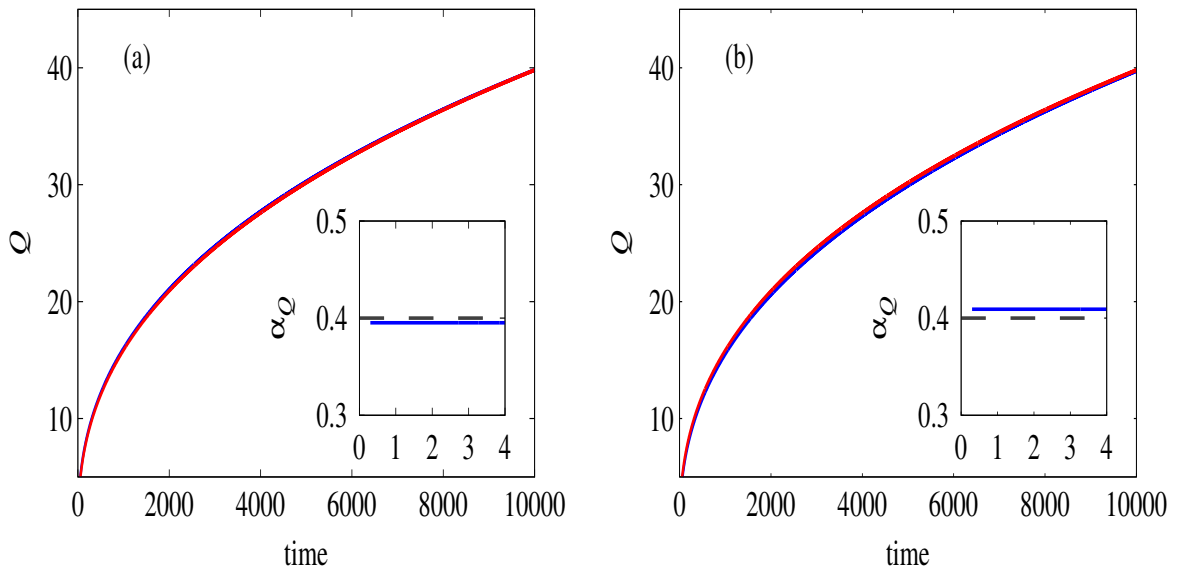


Figure 3.2: The smoothed data [(b)lue line connected points] of Fig. 3.1 along with the function $Q = t^{2/5}$ [(g)reen curves]. The insets show the time dependence in semi-log scale of the value of the numerically obtained exponent α_Q (3.27) for the smoothed data [(b)lue curves]. The thick dashed lines denote the value 0.4.

3.6 General purpose integration schemes

Let us now briefly present some possible ways to numerically integrate the system of ODEs (3.20). We will first discuss some general purpose integrators.

3.6.1 The explicit Euler method

Let us first describe the so-called explicit Euler method which is a basic numerical technique for solving system (3.20). So, starting with the initial condition, $\mathbf{Z}(t)$ at $t \geq 0$, we propagate the Hamiltonian flow and the variational equations to $t + \tau$ using a linear interpolation

$$\mathbf{Z}(t + \tau) = \mathbf{Z}(t) + \tau \mathbf{f}(\mathbf{Z}(t), t), \quad (3.28)$$

where τ is the integration time increment. In what follows we will occasionally use \mathbf{Z}' to denote $\mathbf{Z}(t + \tau)$ and \mathbf{Z} for $\mathbf{Z}(t)$. Following the process of [Yoshida, 1993], in order to illustrate the applicability and the limitations of this method, let us use as a ‘toy model’ the Hamiltonian of a single harmonic oscillator

$$\mathcal{H} = \frac{\varepsilon}{2} (q^2 + p^2), \quad (3.29)$$

where q and p are the canonical generalized position and momentum respectively and ε is the proper frequency of the oscillator. Its tangent dynamics is described by the Hamiltonian function of the form [Skokos and Gerlach, 2010]

$$\mathcal{H}_V = \varepsilon (q\delta q + p\delta p), \quad (3.30)$$

with canonical coordinates δp and δq . \mathcal{H}_V depends explicitly on time t through the presence of $q(t)$ and $p(t)$. In this case Eq. (3.20) take the form

$$\begin{pmatrix} \dot{q} \\ \dot{p} \\ \dot{\delta q} \\ \dot{\delta p} \end{pmatrix} = \mathbf{f}(q, p, \delta q, \delta p) = \begin{pmatrix} \varepsilon p \\ -\varepsilon q \\ \varepsilon \delta p \\ -\varepsilon \delta q \end{pmatrix}. \quad (3.31)$$

Consequently, the explicit Euler scheme (3.28) evolves Hamiltonians (3.29) and (3.30) through

$$\begin{pmatrix} q' \\ p' \\ \delta q' \\ \delta p' \end{pmatrix} = \begin{pmatrix} 1 & \varepsilon\tau & 0 & 0 \\ -\varepsilon\tau & 1 & 0 & 0 \\ 0 & 0 & 1 & \varepsilon\tau \\ 0 & 0 & -\varepsilon\tau & 1 \end{pmatrix} \begin{pmatrix} q \\ p \\ \delta q \\ \delta p \end{pmatrix}. \quad (3.32)$$

Let us now, compute these Hamiltonian functions after one integration step τ , getting

$$\mathcal{H}' = \frac{\varepsilon}{2} (q'^2 + p'^2) = \frac{\varepsilon}{2} (1 + \varepsilon^2\tau^2) (q^2 + p^2), \quad (3.33)$$

and

$$\mathcal{H}'_V = \varepsilon (q'\delta q' + p'\delta p') = \varepsilon (1 + \varepsilon^2\tau^2) (q\delta q + p\delta p). \quad (3.34)$$

We see that the new Hamiltonians for both the phase space orbit and the related deviation vector have some additional terms as they now have the form $\mathcal{H}' = \mathcal{H} + \varepsilon^2\tau^2\mathcal{H}$ and $\mathcal{H}'_V = \mathcal{H}_V + \varepsilon^2\tau^2\mathcal{H}_V$. This means that, an artificial drifting force proportional to τ^2 has been introduced introduced to the system whose origin is purely numerical. Furthermore at each iteration, the cumulative drift from the initial Hamiltonian will become larger up to the point where it could not be anymore neglected in comparison to the original system. This deviation could lead to the appearance of an artificial chaotic behavior. A common practice to try to address this problem is the use of small integration time steps τ along with the development of time adaptative step size integrators, which is not very efficient for very long time integrations as the ones needed for our study.

3.6.2 The Taylor/Lie series method

In general, the solution of Eq. (3.20) $\mathbf{Z}(t + \tau)$ at time $t + \tau$ can be expressed as a Taylor series of $\mathbf{Z}(t)$

$$\mathbf{Z}(t + \tau) = \mathbf{Z}(t) + \tau \frac{d\mathbf{Z}(t)}{dt} + \frac{\tau^2}{2} \frac{d^2\mathbf{Z}(t)}{dt^2} + \dots + \frac{\tau^n}{n!} \frac{d^n\mathbf{Z}(t)}{dt^n} + \mathcal{O}\left(\frac{\tau^{n+1}}{(n+1)!} \frac{d^{n+1}\mathbf{Z}(t)}{dt^{n+1}}\right). \quad (3.35)$$

If we consider the first two terms, we obtain the explicit Euler method presented in Sec. 3.6.1. Thus an artificial drift from the primary system’s dynamics is also present. Obviously, increasing the number of terms considered in the expansion (3.35) this artificial drift reduces. The scheme presented in Eq. (3.35) where the first n terms of the expansion are used is said to be of order n . Further information about this method is presented in [Hairer et al., 1993, Sec. I.8] and references therein, while a detailed discussion of the performances of this technique in the present context can be found for example in [Gerlach et al., 2012; Danieli et al., 2019a].

Following [Gröbner, 1967; Hanslmeier and Dvorak, 1984; Ettl and Dvorak, 2010; Blanes and Casas, 2016], we will discuss an elegant way to present the Taylor series using Lie algebra. Indeed, Eq. (3.20) can be written in terms of Lie operators as

$$\frac{d\mathbf{Z}(t)}{dt} = \mathbf{L}_{\mathcal{H}_V} \mathbf{Z}(t), \quad (3.36)$$

where the Lie operator $L_{\mathcal{H}_V}$ is defined as

$$L_{\mathcal{H}_V} = \sum_{i=1}^{2N} f_i \frac{\partial}{\partial z_i} + f_{i+2N} \frac{\partial}{\partial \delta z_i}. \quad (3.37)$$

Then the solution of Eq. (3.36) can be formally written as

$$\mathbf{Z}(t + \tau) = e^{\tau L_{\mathcal{H}_V}} \mathbf{Z}(t), \quad (3.38)$$

where the exponential differential operator $e^{\tau L_{\mathcal{H}_V}}$ plays the role of the propagator of the solution as its application on the initial state $\mathbf{Z}(t)$ advances the solution by time step τ i.e. to $\mathbf{Z}(t + \tau)$. In the case of integrable systems, such operators represent the exact solution of the equations of motion and the variational equations. However in the case of non-integrable systems, the Lie series integrator approximates the solution through a series expansion of the operator $L_{\mathcal{H}_V}$

$$\mathbf{Z}(t + \tau) = L_{\mathcal{H}_V}^0 \mathbf{Z}(t) + \tau L_{\mathcal{H}_V} \mathbf{Z}(t) + \frac{\tau^2}{2} L_{\mathcal{H}_V}^2 \mathbf{Z}(t) + \dots + \frac{\tau^n}{n!} L_{\mathcal{H}_V}^n \mathbf{Z}(t) + \mathcal{O}\left(\frac{\tau^{n+1}}{(n+1)!} L_{\mathcal{H}_V}^{n+1} \mathbf{Z}(t)\right). \quad (3.39)$$

The next step in order to practically implement Eq. (3.39) is to find an analytical expression for the action of $L_{\mathcal{H}_V}$ and its powers $L_{\mathcal{H}_V}^n$ on the system state \mathbf{Z} at time t . Equation (3.39) corresponds to the Lie series method of order n and is equivalent to expression (3.35) by considering $L_{\mathcal{H}_V}^0 \mathbf{Z} = \mathbf{Z}$, $L_{\mathcal{H}_V} \mathbf{Z} = \frac{d\mathbf{Z}}{dt}$, $L_{\mathcal{H}_V}^2 \mathbf{Z} = \frac{d^2\mathbf{Z}}{dt^2}$ etc.

Actually, the determination of an analytical closed form of $L_{\mathcal{H}_V}^n \mathbf{Z}$ is a very challenging task even for systems with few degrees of freedom [Eggl and Dvorak, 2010], and becoming almost impossible for multidimensional systems. Nevertheless the application of modern computer algebra softwares, can automate successive differentiations of the force field vector \mathbf{f} (see e.g. [Barrio, 2005]). This approach has been followed for instance using the software *Mathematica*¹ in the freely available package called *TIDES* [Abad et al., 2014]. The *TIDES* package has already been used in several investigations of dynamical systems (see e.g. [Barrio and Shilnikov, 2011; Gerlach et al., 2012; Barrio et al., 2015; Wilczak et al., 2016; Danieli et al., 2019a]). It requires as input the set of differential equations to be integrated along with a set of initial conditions, as well as the final time of integration. It creates internally a Fortran77 or C code which is immediately compiled producing an executable program which generates the numerical solution. The accuracy of the performed integration does not only depend on the integration time step τ but also on a parameter (denoted as δ_a) defining the integrator's single step precision. As a consequence, the *TIDES* package creates an adaptive step size integrator.

3.6.3 The General purpose DOP853 Runge-Kutta integrator

The Runge-Kutta (RK) numerical integration methods are some of the most used numerical schemes. Their simplicity and robustness make them widely used in several scientific fields such as physics, astrophysics, population dynamics, etc. Details on this family of integrators can be found in [Hairer et al., 1993, 2006; Eggl and Dvorak, 2010]. A p -stage RK method for Eq. (3.20), is described by the scheme

$$\mathbf{Z}(t + \tau) = \mathbf{Z}(t) + \tau \sum_{i=1}^p b_i \mathbf{k}_i, \quad \text{with} \quad (3.40)$$

$$\mathbf{k}_i = \mathbf{f} \left(t + c_i \tau, \mathbf{Z}(t) + \tau \sum_{j=1}^{p-1} a_{ij} \mathbf{k}_j \right), \quad (3.41)$$

where the values of the coefficients $a_{i,j}$, b_i and c_i depend on the desired accuracy. In order to obtain numerical values for these coefficients, one has to perform Taylor series expansions and deduce order conditions which are algebraic equations on a_{ij} , b_i and c_i . As seen previously, Taylor series expansions introduce an artificial drift which is also expected to appear for this method.

In the rest of this thesis, unless otherwise state, we implement a 12-stage explicit RK algorithm called DOP853 which is freely available online [Hairer, 2009] and is based on the Dormand and Prince method [Hairer et al., 1993]. The DOP853 has already been extensively used in lattice dynamics (see e.g. [Mulansky et al., 2009; Sales et al., 2018]).

¹Wolfram Mathematica: Modern technical computing. <https://www.wolfram.com/mathematica/>.

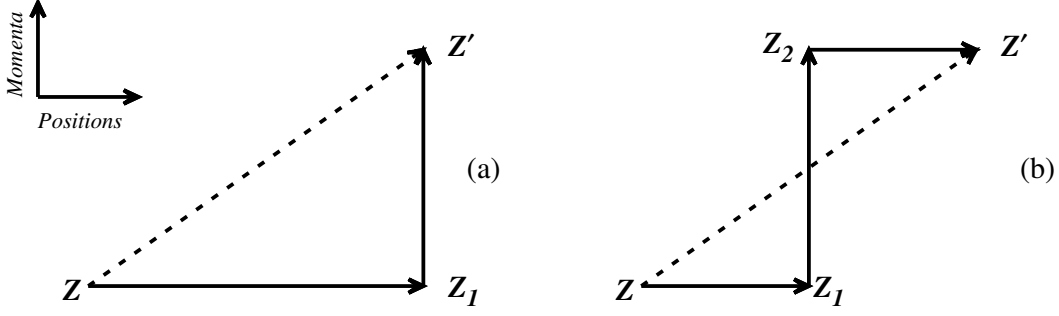


Figure 3.3: Geometric representations of the symplectic explicit Euler (3.28) (a) and leapfrog (LF) (3.55) (b) methods. The bold arrows represent the paths followed by the successive steps within the numerical scheme and the dashed arrows joins the initial and final integration points. In (a) $\mathbf{Z}_1 = e^{\tau \mathbf{L}_{A_V}} \mathbf{Z}$ and $\mathbf{Z}' = e^{\tau \mathbf{L}_{B_V}} \mathbf{Z}_1$ respectively, giving a 2 step SI. In (b) $\mathbf{Z}_1 = e^{\tau \mathbf{L}_{A_V}/2} \mathbf{Z}$, $\mathbf{Z}_2 = e^{\tau \mathbf{L}_{B_V}} \mathbf{Z}_1$ and $\mathbf{Z}' = e^{\tau \mathbf{L}_{A_V}/2} \mathbf{Z}_2$ such that the LF corresponds to a 3 step SI.

3.7 Symplectic integrators

Based on the nature of the physical phenomena they describe, Hamiltonian models should conserve certain macroscopic observables such as mass, energy and number of particles. These constants are called *integrals of motion* and, in principle, described by analytical functions whose values remain constant throughout the system's evolution. Since the basic principle of finding accurate numerical solutions is to get as close as possible to the properties of the real analytical solutions, finding numerical integration schemes which preserve the integrals of motion is highly desirable. SIs are numerical integration schemes specifically designed for autonomous Hamiltonian systems as they preserve by default the system's phase space volume $d\mathfrak{V} = d\mathbf{q} \wedge d\mathbf{p}$. The numerical schemes presented in Secs. 3.6.2 and 3.6.3 were losing the preservation of symplecticity once we considered that the action of the operator $e^{\mathbf{L}_{\mathcal{H}_V}}$ was approximated by a truncated Taylor series expansion (3.39) (see for example Sec. 3.6.1). Let us consider a particular class of Hamiltonian functions which is encountered in many applications, systems whose Hamiltonian can be expressed as a sum of a *kinetic* energy $A(\mathbf{p})$ depending only on the momentum variables \mathbf{p} and a *potential* energy $B(\mathbf{q})$ term depending only on the position variables \mathbf{q}

$$\mathcal{H}(\mathbf{q}, \mathbf{p}) = A(\mathbf{p}) + B(\mathbf{q}). \quad (3.42)$$

The formal solution of Eq (3.20) (see (3.38)) becomes

$$\mathbf{Z}(t + \tau) = e^{\tau(\mathbf{L}_{A_V} + \mathbf{L}_{B_V})} \mathbf{Z}(t). \quad (3.43)$$

Since each part $A(\mathbf{p})$ and $B(\mathbf{q})$ possess N cyclic coordinates which act as integrals of motion, the analytical forms of the operators $e^{\tau \mathbf{L}_{A_V}}$ and $e^{\tau \mathbf{L}_{B_V}}$ are explicitly known. These operators represent the exact solutions of the equations of motion and the related variational equations of the respectively simple Hamiltonian functions $A(\mathbf{p})$ and $B(\mathbf{q})$

$$e^{\tau \mathbf{L}_{A_V}} : \begin{cases} \mathbf{q}' &= \mathbf{q} + \tau \left. \frac{\partial A}{\partial \mathbf{p}} \right|_{\substack{\mathbf{p}=\mathbf{p} \\ \delta \mathbf{p}=\delta \mathbf{p}}} \\ \delta \mathbf{q}' &= \delta \mathbf{q} + \tau \left[\delta \mathbf{p} \cdot \mathbf{D}^2 A \right]_{\substack{\mathbf{p}=\mathbf{p} \\ \delta \mathbf{p}=\delta \mathbf{p}}} \end{cases}, \quad e^{\tau \mathbf{L}_{B_V}} : \begin{cases} \mathbf{p}' &= \mathbf{p} - \tau \left. \frac{\partial B}{\partial \mathbf{q}} \right|_{\substack{\mathbf{q}=\mathbf{q} \\ \delta \mathbf{q}=\delta \mathbf{q}}} \\ \delta \mathbf{p}' &= \delta \mathbf{p} - \tau \left[\delta \mathbf{q} \cdot \mathbf{D}^2 B \right]_{\substack{\mathbf{q}=\mathbf{q} \\ \delta \mathbf{q}=\delta \mathbf{q}}} \end{cases}. \quad (3.44)$$

Here \mathbf{D}^2 represents a multi-variable derivative operator of order two with respect to the momenta ($\mathbf{D}^2 A$ in $e^{\tau \mathbf{L}_{A_V}}$) or the positions ($\mathbf{D}^2 B$ in $e^{\tau \mathbf{L}_{B_V}}$). Further assuming that \mathbf{L}_{A_V} and \mathbf{L}_{B_V} commute (something which is generally not true), we can write

$$e^{\tau \mathbf{L}_{\mathcal{H}_V}} = e^{\tau \mathbf{L}_{B_V}} e^{\tau \mathbf{L}_{A_V}}, \quad (3.45)$$

such that

$$\mathbf{Z}(t + \tau) = e^{\tau \mathbf{L}_{B_V}} e^{\tau \mathbf{L}_{A_V}} \mathbf{Z}(t). \quad (3.46)$$

The geometrical representation of Eq. (3.46) is presented in Fig. 3.3(a). We see that \mathbf{Z} and \mathbf{Z}' are related through the application of a two step process involving two perpendicular mappings. Thus using Eq. (3.45), we approximate the exact solution described by $e^{\tau \mathbf{L}_{\mathcal{H}_V}}$, by the composition of two operators

$e^{\tau \mathbf{L}_{AV}}$ and $e^{\tau \mathbf{L}_{BV}}$. Since each operator is symplectic, so is the composition. Thus we have constructed a very simple SI

$$S_1(\tau) = e^{\tau \mathbf{L}_{BV}} e^{\tau \mathbf{L}_{AV}}, \quad (3.47)$$

which is called the *symplectic explicit Euler method*.

For the sake of completeness, let us apply the SI (3.47) to the single harmonic oscillator (3.29) as done in [Yoshida, 1993]. Indeed, Hamiltonian (3.29) can be splitted in two parts $A(p) = \varepsilon p^2/2$ and $B(q) = \varepsilon q^2/2$. Thus Eq. (3.44), gives

$$e^{\mathbf{L}_{AV}} \mathbf{Z}(t): \begin{cases} q' &= q + \tau \varepsilon p \\ p' &= p \\ \delta q' &= \delta q + \tau \varepsilon \delta p \\ \delta p' &= \delta p \end{cases}, \quad \text{and} \quad e^{\mathbf{L}_{BV}} \mathbf{Z}(t): \begin{cases} q' &= q \\ p' &= p - \tau \varepsilon p \\ \delta q' &= \delta q \\ \delta p' &= \delta p - \tau \varepsilon \delta p \end{cases}, \quad (3.48)$$

such that the numerical scheme $S_1(\tau)$ (3.47) gives

$$\begin{pmatrix} q' \\ p' \\ \delta q' \\ \delta p' \end{pmatrix} = \begin{pmatrix} 1 & \varepsilon \tau & 0 & 0 \\ -\varepsilon \tau & 1 - \varepsilon^2 \tau^2 & 0 & 0 \\ 0 & 0 & 1 & \varepsilon \tau \\ 0 & 0 & -\varepsilon \tau & 1 - \varepsilon^2 \tau^2 \end{pmatrix} \begin{pmatrix} q \\ p \\ \delta q \\ \delta p \end{pmatrix}. \quad (3.49)$$

The computation of the energy (3.29) after one time step τ

$$\mathcal{H}' = \mathcal{H} + \tau^2 \frac{\varepsilon^3}{2} (q^2 - p^2) + \tau^3 \frac{\varepsilon^4}{2} qp + \tau^4 \frac{\varepsilon^5}{2} p^2, \quad (3.50)$$

depicts a non-conserved total energy of the system. Nevertheless, the presence of a negative term in τ^2 , ensures that there is no monotonic increase of the energy error which is bounded by $\mathcal{O}(\tau)$. This observation is further explained by the fact the mapping (3.49) has an integral of motion [Yoshida, 1993]

$$\frac{\varepsilon}{2} (q^2 + p^2) + \frac{\tau}{2} \varepsilon qp = \text{const.} \quad (3.51)$$

Indeed, if we start with a natural initial condition $(0, 1)$, all the points generated iterating the mapping (3.49) lie on the conic section $q^2 + p^2 + \tau qp = 1$, which deviates from the exact orbit $q^2 + p^2 = 1$ by a term of the order of τ . Consequently the error in energy in (3.50) cannot grow in time. Further, for small enough values of τ , the orbit of the system's perturbed trajectory also takes the form (3.51), meaning that no exponential growth of the DV is possible. Thus, the system's MLE will always exhibit a regular behavior $\Lambda \propto t^{-1}$ as expected from the harmonic oscillator (3.29). Obviously, the computer precision also has to be taken into account on the above argumentation.

In general, any composition of the operators $e^{\tau \mathbf{L}_{AV}}$ and $e^{\tau \mathbf{L}_{BV}}$ leads to a symplectic numerical scheme. A SI of order n is

$$S_n(\tau) = \prod_{i=1}^k e^{\tau c_i \mathbf{L}_{AV}} e^{\tau d_i \mathbf{L}_{BV}} + \mathcal{O}(\tau^{n+1}). \quad (3.52)$$

We note that the SI (3.47) is of order 1 as it is indicated by the subscript '1' in S_1 . The problem of constructing the SIs in (3.52) is reduced in finding the coefficients c_i and d_i with $i = 1, 2, \dots, k \leq n$ such that Eq. (3.52) approximates $e^{\tau(\mathbf{L}_{AV} + \mathbf{L}_{BV})}$ up to a certain order of precision. This problem, was initially set and tackled in several pioneering papers [Neri, preprint, 1988; Suzuki, 1990; Yoshida, 1990; Suzuki, 1991].

From Eqs (3.47) and (3.52) we see that the symplectic explicit Euler method corresponds to $n = 1$ and $k = 1$ which leads to the trivial values of the coefficients $c_1 = 1$ and $d_1 = 1$. For $n = 2$ and $k = 2$ we get the second order SI [Hairer et al., 1993, 2006; Blanes and Casas, 2016]

$$S_2(\tau) = e^{\tau c_1 \mathbf{L}_{AV}} e^{\tau d_1 \mathbf{L}_{BV}} e^{\tau c_2 \mathbf{L}_{AV}} e^{\tau d_2 \mathbf{L}_{BV}}. \quad (3.53)$$

For this scheme the coefficients c_1, c_2, d_1 and d_2 should satisfy the order conditions

$$\begin{cases} c_1 + c_2 = 1 \\ d_1 + d_2 = 1 \end{cases}, \quad (3.54)$$

whose solution is not uniquely determined. For example the choice

$$c_1 = c_2 = \frac{1}{2}, \quad d_1 = 1 \quad \text{and} \quad d_2 = 0,$$

satisfies the order conditions (3.54), leading to the SI

$$S_2^{[1]}(\tau) = e^{\tau \frac{1}{2} \mathbf{L}_{A_V}} e^{\tau \mathbf{L}_{B_V}} e^{\tau \frac{1}{2} \mathbf{L}_{A_V}} + \mathcal{O}(\tau^3). \quad (3.55)$$

This integrator is the symplectic *leapfrog* or *Störmer-Verlet* scheme [Hairer et al., 1993]. The geometrical interpretation of the leapfrog scheme (3.55) is depicted in Fig. 3.3 (b). We see that \mathbf{Z}' and \mathbf{Z} are related through 3 different steps each conserving the local constants of motion. It is worth mentioning that not all choices of the parameters c_1 , c_2 , d_1 and d_2 satisfying the order conditions (3.54) lead to SIs. For example, the choice

$$c_1 = c_2 = d_1 = d_2 = \frac{1}{2},$$

leads to the numerical scheme

$$S_2^{[2]}(\tau) = e^{\tau \frac{1}{2} \mathbf{L}_{A_V}} e^{\tau \frac{1}{2} \mathbf{L}_{B_V}} e^{\tau \frac{1}{2} \mathbf{L}_{A_V}} e^{\tau \frac{1}{2} \mathbf{L}_{B_V}} + \mathcal{O}(\tau^3). \quad (3.56)$$

Although this integrator is also symplectic, it is not *time reversible* as is the leapfrog method $S_2^{[1]}$ (3.55). This means that making a time step τ with this integrator followed by another step $-\tau$ i.e. going back and forth (and vice versa) in time for one time step will not lead us to our initial state:

$$S_2^{[2]}(\tau) S_2^{[2]}(-\tau) \mathbf{Z}(t) \neq S_2^{[2]}(-\tau) S_2^{[2]}(\tau) \mathbf{Z}(t) \neq \mathbf{Z}(t). \quad (3.57)$$

Since the property of time reversibility is quite natural, we will restrict our study only to SIs which have this property.

3.7.1 The Baker-Campbell-Hausdorff formula

Let us now see how we can use the Baker-Campbell-Hausdorff (BCH) formula to obtain SIs. The BCH formula gives the solution for operator W_1 in the equation

$$e^X e^Y = e^{W_1}, \quad (3.58)$$

when X and Y are non-commutative elements. In particular, we get

$$W_1 = X + Y + \frac{1}{2}[X, Y] + \frac{1}{12}([X, X, Y] + [Y, Y, X]) + \frac{1}{24}[X, Y, Y, X] + \dots \quad (3.59)$$

where $[\cdot, \cdot]$ and $[\cdot, \cdot, \cdot]$ are commutators such that $[X, Y] = XY - YX$, $[X, X, Y] = [X, [X, Y]]$ etc.

Setting $X = \tau \mathbf{L}_{A_V}$ and $Y = \tau \mathbf{L}_{B_V}$ in (3.58) and (3.59), we obtain

$$\begin{aligned} W_1 &= \tau \mathbf{L}_{A_V} + \tau \mathbf{L}_{B_V} + \frac{1}{2}[\tau \mathbf{L}_{A_V}, \tau \mathbf{L}_{B_V}] + \frac{1}{12}([\tau \mathbf{L}_{A_V}, \tau \mathbf{L}_{A_V}, \tau \mathbf{L}_{B_V}] + [\tau \mathbf{L}_{B_V}, \tau \mathbf{L}_{B_V}, \tau \mathbf{L}_{A_V}]) + \dots, \\ &= \tau \mathbf{L}_{\mathcal{H}_V} + \frac{\tau^2}{2}[\mathbf{L}_{A_V}, \mathbf{L}_{B_V}] + \frac{\tau^3}{12}([\mathbf{L}_{A_V}, \mathbf{L}_{A_V}, \mathbf{L}_{B_V}] + [\mathbf{L}_{B_V}, \mathbf{L}_{B_V}, \mathbf{L}_{A_V}]) + \dots \end{aligned} \quad (3.60)$$

So neglecting the terms of order 2 and above in τ , we obtain the symplectic explicit Euler integrator of Eq. (3.47)

$$S_1(\tau) = e^{\tau \mathbf{L}_{A_V}} e^{\tau \mathbf{L}_{B_V}} \approx e^{\tau \mathbf{L}_{\mathcal{H}_V}}. \quad (3.61)$$

Let us now implement the BCH formula in order to obtain the leapfrog integrator of Eq. (3.55), setting

$$e^X e^Y e^X = e^{W_1} e^X = e^{W_2}, \quad (3.62)$$

and applying again (3.59), we get

$$\begin{aligned} W_2 &= 2\frac{\tau}{2}\mathbf{L}_{A_V} + \tau \mathbf{L}_{B_V} + \frac{1}{6} \left([\tau \mathbf{L}_{B_V}, \tau \mathbf{L}_{B_V}, \frac{\tau}{2} \mathbf{L}_{A_V}] - \left[\frac{\tau}{2} \mathbf{L}_{A_V}, \frac{\tau}{2} \mathbf{L}_{A_V}, \tau \mathbf{L}_{B_V} \right] \right) + \dots, \\ &= \tau \mathbf{L}_{\mathcal{H}_V} + \frac{\tau^3}{12} \left([\mathbf{L}_{B_V}, \mathbf{L}_{B_V}, \mathbf{L}_{A_V}] - \frac{1}{2} [\mathbf{L}_{A_V}, \mathbf{L}_{A_V}, \mathbf{L}_{B_V}] \right) + \dots \end{aligned} \quad (3.63)$$

So neglecting terms of order 3 and above in τ we obtain the leapfrog integrator of Eq. (3.55)

$$S_2(\tau) = e^{\frac{1}{2}\tau \mathbf{L}_{A_V}} e^{\tau \mathbf{L}_{B_V}} e^{\frac{1}{2}\tau \mathbf{L}_{A_V}} \approx e^{\tau \mathbf{L}_{\mathcal{H}_V}}. \quad (3.64)$$

This process can be followed in order to build higher order SIs. The error of such integrator is defined by the power of the integration time step τ encountered in the first nonlinear term. For Eq. (3.60), we see that this term is τ^2 for the symplectic explicit Euler method, which according to (3.52) means that this integrator is of order 1, while Eq. (3.63) denotes that the leapfrog integrator is of order 2. The approach describes here is based on Lie algebra concepts and is more complex as we go to higher order integrators. The interested reader can get a very concise and complete overview on these method in [Hairer et al., 2006; Blanes and Casas, 2016].

3.7.2 The Yoshida composition technique

Let us now see how we can use these ideas in order to build higher order methods in a repeatable way. Let us rewrite Eq. (3.63) as

$$W_2 = \tau\alpha_1 + \tau^3\alpha_3 + \tau^5\alpha_5 + \dots, \quad (3.65)$$

with $\alpha_1 = \mathbf{L}_{A_V} + \mathbf{L}_{B_V}$, $\alpha_3 = \frac{1}{12}[\mathbf{L}_{B_V}, \mathbf{L}_{B_V}, \mathbf{L}_{A_V}] - \frac{1}{24}[\mathbf{L}_{A_V}, \mathbf{L}_{A_V}, \mathbf{L}_{B_V}]$, etc. Expression (3.65) stands at the basis of what is called *Yoshida composition* technique [Yoshida, 1990]. According to that technique, we can build higher order *symmetric* SIs using *palindromic* composition of lower order SIs. For instance, let us try to construct a SI of order 4 of the form

$$S_4(\tau) = S_2(x_1\tau)S_2(x_0\tau)S_2(x_1\tau), \quad (3.66)$$

where x_0, x_1 are real coefficients we have to define. We get from (3.65)

$$W_2 = \tau(x_0 + 2x_1)\alpha_1 + \tau^3(x_0^3 + 2x_1^3)\alpha_3 + \tau^5(x_0^5 + 2x_1^5)\alpha_5 + \dots \quad (3.67)$$

In order to achieve the desired order 4, we want the first nonlinear term in τ we encounter in (3.67) to be τ^5 . This means that we want to kill the order 3 term by setting $x_0^3 + 2x_1^3 = 0$ and at the same time keeping the $\alpha_1 = \mathbf{L}_{\mathcal{H}_V}$ term by setting $x_0 + 2x_1 = 1$. Thus we obtain the conditions

$$\begin{cases} x_0 + 2x_1 = 1 \\ x_0^3 + 2x_1^3 = 0 \end{cases}, \quad (3.68)$$

which can be solved analytically to give [Yoshida, 1990]

$$x_0 = -\frac{2^{1/3}}{2 - 2^{1/3}}, \quad x_1 = \frac{1}{2 - 2^{1/3}}. \quad (3.69)$$

In fact this process can be repeated over and over again in order to create higher order SIs. Its generalization states that from any symmetric n th order SI we build a $(n + 2)$ th scheme using the composition (see also [Iserles and Quispel, 2018] and references therein)

$$S_{n+2}(\tau) = S_n(x_1\tau)S_n(x_0\tau)S_n(x_1\tau), \quad (3.70)$$

with coefficients

$$x_0 = -\frac{2^{1/(2n+1)}}{2 - 2^{1/(2n+1)}}, \quad x_1 = \frac{1}{2 - 2^{1/(2n+1)}}. \quad (3.71)$$

Equation (3.70) is usually referred to as the *Yoshida composition*. Let us make an additional remark here. The palindromic composition as in (3.70) ensures that the SIs built using the Yoshida composition technique are always time reversible. It is worth noting that there also exist other composition schemes which follow the same basic principle of Yoshida's method having some differences on the way the Lie algebra is applied (see e.g. [Suzuki, 1991]), based sometimes on the particular type of physical problem they were initially created to solve (see e.g. [Ruth, 1983; Laskar and Robutel, 2001; Laskar and Vaillant, 2019]).

3.7.3 Two-part split symplectic integrators

In this section we present several two-part split SIs i.e. schemes which can be used in case the Hamiltonian function can be split into two integrable parts like in Eq. (3.42), which have been recently used in studies of multidimensional Hamiltonian models. These studies considered for example models such as the DKG chain of anharmonic oscillators [Skokos et al., 2013; Danieli et al., 2017; Senyange et al., 2018; Many Manda et al., 2020], the DDNLS system in one [Gerlach et al., 2016; Mithun et al., 2018; Mallick et al., 2020] and two [Many Manda et al., 2020] spatial dimensions, the Josephson junction chain [Mithun et al., 2019], the FPUT system [Danieli et al., 2017, 2019a], the Peyrard-Bishop-Dauxois model of the DNA [Hillebrand et al., 2019], as well as graphene models [Bountis et al., 2020; Hillebrand et al., 2020] to name a few.

Symplectic integrators of order two.

The leapfrog (LF) method. We explicitly presented this scheme in Sec. 3.7.1. More details about the LF scheme can be found in [Ruth, 1983] and [Hairer et al., 2006, Sect. VI.3]. This integrator has 3 individual steps i.e. the number of applications of simple operators $e^{\tau\mathbf{L}_{A_V}}$, $e^{\tau\mathbf{L}_{B_V}}$ (see also Fig. 3.3(b)) and is given by the relation

$$LF(\tau) = e^{a_1\tau\mathbf{L}_{A_V}}e^{b_1\tau\mathbf{L}_{B_V}}e^{a_1\tau\mathbf{L}_{A_V}}, \quad (3.72)$$

with $a_1 = \frac{1}{2}$ and $b_1 = 1$.

The $SABA_2/SBAB_2$ integrators. These SIs possess 5 individual steps and have the following expressions

$$SABA_2(\tau) = e^{a_1\tau L_{AV}} e^{b_1\tau L_{BV}} e^{a_2\tau L_{AV}} e^{b_1\tau L_{BV}} e^{a_1\tau L_{AV}}, \quad (3.73)$$

with $a_1 = \frac{1}{2} - \frac{1}{2\sqrt{3}}$, $a_2 = \frac{1}{\sqrt{3}}$ and $b_1 = \frac{1}{2}$, and

$$SBAB_2(\tau) = e^{b_1\tau L_{BV}} e^{a_1\tau L_{AV}} e^{b_2\tau L_{BV}} e^{a_1\tau L_{AV}} e^{b_1\tau L_{BV}}, \quad (3.74)$$

with $a_1 = \frac{1}{2}$, $b_1 = \frac{1}{6}$ and $b_2 = \frac{2}{3}$. This class of schemes was studied in [McLachlan, 1995], where they were referred to as the (4, 2) methods. In addition, they have been employed in [Laskar and Robutel, 2001] to study Hamiltonian functions of the form $A(\mathbf{p}) + \varrho B(\mathbf{q})$ or $A(\mathbf{q}, \mathbf{p}) + \varrho B(\mathbf{q}, \mathbf{p})$, where the contribution ϱB was considered small since $\varrho \ll 1$. Nevertheless these integrators have shown good performance also for cases $\varrho = 1$ (see e.g. [Skokos et al., 2009; Veksler et al., 2009; Danieli et al., 2017; Mithun et al., 2018; Kati et al., 2020; Mallick et al., 2020]).

The $ABA82$ scheme. This integrator is given by [McLachlan, 1995; Farrés et al., 2013]

$$ABA82(\tau) = e^{a_1\tau L_{AV}} e^{b_1\tau L_{BV}} e^{a_2\tau L_{AV}} e^{b_2\tau L_{BV}} e^{a_3\tau L_{AV}} e^{b_2\tau L_{BV}} e^{a_2\tau L_{AV}} e^{b_1\tau L_{BV}} e^{a_1\tau L_{AV}}, \quad (3.75)$$

and has 9 individual steps. The values of the coefficients $a_i, b_i, i = 1, 2, 3$ in Eq. (3.75) are given in Table 2 of [Farrés et al., 2013]. It is worth mentioning that the $ABA82$ SI was also used in [Laskar and Robutel, 2001] where it was named $SABA_4$.

Symplectic integrators of order four.

The $ABA864/ABAH864$ integrators. These SIs were introduced in [Blanes et al., 2013; Farrés et al., 2013]. The first scheme has the form

$$\begin{aligned} ABA864(\tau) = & e^{a_1\tau L_{AV}} e^{b_1\tau L_{BV}} e^{a_2\tau L_{AV}} e^{b_2\tau L_{BV}} e^{a_3\tau L_{AV}} e^{b_3\tau L_{BV}} e^{a_4\tau L_{AV}} \\ & \times e^{b_4\tau L_{BV}} e^{a_4\tau L_{AV}} e^{b_3\tau L_{BV}} e^{a_3\tau L_{AV}} e^{b_2\tau L_{BV}} e^{a_2\tau L_{AV}} e^{b_1\tau L_{BV}} e^{a_1\tau L_{AV}}, \end{aligned} \quad (3.76)$$

and includes 15 individual steps. The coefficients $a_i, b_i, i = 1, 2, 3, 4$ of Eq. (3.76) are listed in Table 3 of [Blanes et al., 2013]. The form of the second SI is

$$\begin{aligned} ABAH864(\tau) = & e^{a_1\tau L_{AV}} e^{b_1\tau L_{BV}} e^{a_2\tau L_{AV}} e^{b_2\tau L_{BV}} e^{a_3\tau L_{AV}} e^{b_3\tau L_{BV}} e^{a_4\tau L_{AV}} e^{b_4\tau L_{BV}} e^{a_5\tau L_{AV}} \\ & \times e^{b_4\tau L_{BV}} e^{a_4\tau L_{AV}} e^{b_3\tau L_{BV}} e^{a_3\tau L_{AV}} e^{b_2\tau L_{BV}} e^{a_2\tau L_{AV}} e^{b_1\tau L_{BV}} e^{a_1\tau L_{AV}}. \end{aligned} \quad (3.77)$$

This integrator has 17 steps and its constants $a_i, b_i, i = 1, 2, 3, 4, 5$ are presented in Table 4 of [Blanes et al., 2013]. The main difference between the two schemes (3.76) and (3.77) is the fact that the $ABAH864$ integrator was constructed for Hamiltonians for which one of their parts A or B is not directly integrable and its action can be approximated by an order two SI. Thus it can be considered as a two, or a three-part split SI.

Symplectic integrators of order six.

The $SABA_2Y6$ integrator. As mentioned earlier in Sec. 3.7.2, apart from the Yoshida composition technique (3.70), there exist other composition techniques leading to higher order SIs. A composition method for creating a sixth order SI, starting from a second order scheme S_2 was presented in [Yoshida, 1990] having the form

$$S_6(\tau) = S_2(w_3\tau)S_2(w_2\tau)S_2(w_1\tau)S_2(w_0\tau)S_2(w_1\tau)S_2(w_2\tau)S_2(w_3\tau). \quad (3.78)$$

It is worth mentioning that the numerical scheme (3.78) was also presented in [Kahan and Li, 1997] where it was called the *s6odr6* method. The constants $w_i, i = 0, 1, 2, 3$ of (3.78) are listed in Table 1 of [Yoshida, 1990] corresponding to the so-called ‘solution A’ of that table. Using Eq. (3.78) with the $SABA_2$ (3.73) SI in the place of $S_2(\tau)$, we construct the order 6 SI $SABA_2Y6$ having 29 steps.

The $ABA864Y6$ scheme. Implementing the composition method (3.70) for $n = 4$, with the $ABA864$ (3.77) in the role of $S_4(\tau)$, we construct the order 6 integrator $ABA864Y6$, possessing 43 steps. This integrator was used in [Senyange and Skokos, 2018].

The $s9SABA_26$ integrator. We also consider the composition technique [Kahan and Li, 1997]

$$s9odr6b(\tau) = S_2(\delta_1\tau)S_2(\delta_2\tau)S_2(\delta_3\tau)S_2(\delta_4\tau)S_2(\delta_5\tau)S_2(\delta_4\tau)S_2(\delta_3\tau)S_2(\delta_2\tau)S_2(\delta_1\tau), \quad (3.79)$$

with the values of the coefficients $\delta_i, i = 1, 2, 3, 4, 5$ given in the Appendix A of [Kahan and Li, 1997]. Implementing the composition method (3.79) using the SI $SABA_2$ (3.73) in place of $S_2(\tau)$, we build the $s9SABA_26$ order 6 integrator, having 37 steps.

3.7.4 Three-part split symplectic integrators

For some models such as the 1D and 2D DDNLS systems [Senyange et al., 2018; Many Manda et al., 2020; Sun and Yu, 2020] studied here, it is preferable (or even necessary) to split the Hamiltonian in more than two integrable parts [Skokos et al., 2014; Gerlach et al., 2016; Laskar and Vaillant, 2019; Casas and Escorihuela-Tomàs, 2020]. Here, we construct some basic SIs for such systems, i.e. for Hamiltonian functions which split in three integrable parts as

$$\mathcal{H} = \mathcal{A} + \mathcal{B} + \mathcal{C}. \quad (3.80)$$

In this case, we are looking for appropriate coefficients c_i , d_i and e_i in order to obtain the approximation

$$e^{\tau(L_{\mathcal{A}_V} + L_{\mathcal{B}_V} + L_{\mathcal{C}_V})} = \prod_{i=1}^k e^{\tau a_i L_{\mathcal{A}_V}} e^{\tau b_i L_{\mathcal{B}_V}} e^{\tau c_i L_{\mathcal{C}_V}} + \mathcal{O}(\tau^{n+1}). \quad (3.81)$$

Before proceeding, it is worth mentioning that some additional well-performing three-part split schemes were proposed recently in [Casas and Escorihuela-Tomàs, 2020] which were also implemented for the 1D DDNLS model.

Symplectic integrators of order two.

The $ABC2$ integrator. The simplest possible scheme of this type is

$$ABC2(\tau) = e^{a_1 \tau L_{\mathcal{A}_V}} e^{b_1 \tau L_{\mathcal{B}_V}} e^{c_1 \tau L_{\mathcal{C}_V}} e^{b_1 \tau L_{\mathcal{B}_V}} e^{a_1 \tau L_{\mathcal{A}_V}}, \quad (3.82)$$

with $a_1 = b_1 = 1/2$ and $c_1 = 1$, which is in some sense the equivalent to the LF (3.72) we saw in the case of two-part split. This integrator has 5 steps and is of order 2. Equation (3.82) can be considered as the outcome of two successive applications of the LF (3.72), first to the Hamiltonian $\mathcal{H} = \mathcal{A} + \mathcal{B}$ and then to the Hamiltonian $\mathcal{B} + \mathcal{C}$, considering it to be split into two parts. This scheme has already been used in several studies (see for example [Koseleff, 1996; Chambers, 1999; Goździewski et al., 2008; Chambers, 2010; Quinn et al., 2010; Sun and Yu, 2020]). As in the case of two-part split SIs we can construct higher order schemes based on composition methods. Some integrators constructed this way are reported in the rest of this section.

Symplectic integrators of order four.

The $ABCY4$ scheme. Implementing the Yoshida composition technique (3.70) for $n = 2$ with $ABC2$ (3.82) in the place of the second order SI $S_2(\tau)$, we obtain the SI $ABCY4(\tau)$ [Koseleff, 1996] having 13 steps. This integrator has already been used by [Gerlach et al., 2016] for studying multidimensional Hamiltonian systems. In that work, the integrator was named $ABC_{[Y]}^4$.

The $ABCS4$ integrator. Implementing the composition technique proposed in [Suzuki, 1990], we build the fourth order SI

$$ABCS4(\tau) = ABC2(p_2 \tau) ABC2(p_2 \tau) ABC2((1 - 4p_2)\tau) ABC2(p_2 \tau) ABC2(p_2 \tau), \quad (3.83)$$

with $p_2 = \frac{1}{4-4^{1/3}}$ and $1 - 4p_2 = \frac{-4^{1/3}}{4-4^{1/3}}$. This integrator has 21 individual steps. The $ABCS4$ SI was also considered in [Kahan and Li, 1997] where it was denoted as the *s5odr4* method. In addition, it was also used in [Gerlach et al., 2016] where it was called $ABC_{[S]}^4$.

The $SS864S$ scheme. As we mentioned in Sec. 3.7.3, the $ABAH864$ (3.77) SI was initially designed for Hamiltonians which can be split in three integrable parts and for which the numerical evolution of two of these parts (say $\mathcal{B} + \mathcal{C}$ in (3.80)) is approximated by the application of a second order two-part split SI. Using the $SABA_2$ (3.73) SI for the integration of the $\mathcal{B} + \mathcal{C}$ (3.80) part, the application of the $ABAH864$ (3.77) SI results in a method having 49 steps which we name $SS864S$. This integrator was called SS_{864}^4 in [Skokos et al., 2014].

Symplectic integrators of order six.

The $ABCY4Y6/ABCS4Y6$ integrators. Implementing the Yoshida composition technique (3.70) for $n = 4$, with the $ABCY4$ and $ABCS4$ (3.83) methods in the place of $S_4(\tau)$, we respectively construct the $ABCY4Y6$ and $ABCS4Y6$ schemes having 37 and 49 steps.

The $ABCY6_A$ scheme. Applying the composition technique (3.78) with $ABC2$ (3.82) in the role of $S_2(\tau)$, we create the $ABCY6_A(\tau)$ integrator with 29 steps. This SI has already been implemented in [Skokos et al., 2014; Gerlach et al., 2016], where it was referred to as $ABC_{[Y]}^6$.

The $s9ABC6$ integrator. Implementing the composition technique (3.79), with $ABC2$ (3.82) in the place of $S_2(\tau)$, we build the SI $s9ABC6(\tau)$ which has 37 steps. This integrator was also studied in [Skokos et al., 2014; Gerlach et al., 2016] where it was named $ABC_{[KL]}^6$.

The $s11ABC6$ scheme. The application of the composition technique [Sofroniou and Spaletta, 2005]

$$s11odr6(\tau) = S_2(\gamma_1\tau)S_2(\gamma_2\tau)S_2(\gamma_3\tau)S_2(\gamma_4\tau)S_2(\gamma_5\tau)S_2(\gamma_6\tau)S_2(\gamma_5\tau) \\ \times S_2(\gamma_4\tau)S_2(\gamma_3\tau)S_2(\gamma_2\tau)S_2(\gamma_1\tau), \quad (3.84)$$

with $ABC2$ (3.82) in the role of $S_2(\tau)$, leads to the scheme $s11ABC6(\tau)$ which has 45 steps. The values of the coefficients γ_i , $i = 1, 2, \dots, 6$ of (3.84) are given in section 4.2 of [Sofroniou and Spaletta, 2005]. The $s11ABC6$ SI was called $ABC_{[SS]}^6$ in [Skokos et al., 2014; Gerlach et al., 2016].

Symplectic integrators of order eight.

The $ABCY8_A/ABCY8_D$ schemes. Implementing the composition technique [Yoshida, 1990]

$$S_8(\tau) = S_2(w_7\tau)S_2(w_6\tau)S_2(w_5\tau)S_2(w_4\tau)S_2(w_3\tau)S_2(w_2\tau)S_2(w_1\tau)S_2(w_0\tau)S_2(w_1\tau)S_2(w_2\tau) \\ \times S_2(w_3\tau)S_4(w_4\tau)S_2(w_5\tau)S_2(w_6\tau)S_2(w_7\tau), \quad (3.85)$$

with the $ABC2$ (3.82) in the role of $S_2(\tau)$, we build an order 8 SI $ABCY8$ which has 61 steps. For this scheme, we use two sets of coefficient values w_i , $i = 0, \dots, 7$ corresponding to the so-called ‘solution A’ and ‘solution D’ in [Yoshida, 1990]. The particular sets of these values can be found in Table 2 of [Yoshida, 1990]. Here, we generate the SI $ABCY8_A(\tau)$ [$ABCY8_D(\tau)$] using the coefficient values of ‘solution A’ [‘solution D’].

The $s17ABC8$ integrator. Implementing the composition technique [Kahan and Li, 1997]

$$s17odr8b(\tau) = S_2(\delta_1\tau)S_2(\delta_2\tau) \times \dots \times S_2(\delta_8\tau)S_2(\delta_9\tau)S_2(\delta_8\tau) \dots \times S_2(\delta_2\tau)S_2(\delta_1\tau), \quad (3.86)$$

with the $ABC2$ (3.82) SI playing the role of the second order SI $S_2(\tau)$, we create the scheme $s17ABC8$ having 69 steps. The coefficient values δ_i , $i = 1, 2, \dots, 9$ are given in Appendix A of [Kahan and Li, 1997]. The $s17ABC8$ integrator was named $ABC_{[KL]}^8$ in [Skokos et al., 2014; Gerlach et al., 2016].

The $s19ABC8$ scheme. Implementing the composition technique [Sofroniou and Spaletta, 2005]

$$s19odr8b(\tau) = S_2(\gamma_1\tau)ABC2(\gamma_2\tau) \times \dots \times S_2(\gamma_8\tau)S_2(\gamma_9\tau)S_2(\gamma_8\tau) \dots \times S_2(\gamma_2\tau)S_2(\gamma_1\tau), \quad (3.87)$$

with the $ABC2$ (3.82) integrator being the required second order SI $S_2(\tau)$, we obtain the scheme $s19ABC8$ having 72 steps. In [Sofroniou and Spaletta, 2005], the values of the coefficients γ_i , $i = 1, 2, \dots, 9$ are listed in equation (13). The $s19ABC8$ SI was called $ABC_{[SS]}^8$ in [Skokos et al., 2014; Gerlach et al., 2016].

3.8 Efficient integration of the 1D and 2D DDNLS systems

We will compare the numerical efficiency of several of the integration schemes presented in Secs. 3.7.3 and 3.7.4 for studying the DDNLS model in one (2.17) and two (2.20) spatial dimensions. In particular, we will compute the time evolution of initial excitations by solving the system’s equations of motion and variational equations through numerical integration. The efficiency of the integration methods will be judged by their ability to correctly reproduce the system’s dynamical behaviors in the least possible needed central processing unit (CPU) time. Since our focus is on the implementation of SIs for these tasks, our results will be presented mainly in relation to such integration techniques.

3.8.1 Two-part split symplectic integrators

Two-part split SIs can be used for the Hamiltonian functions \mathcal{H}_{1D} (2.17) and \mathcal{H}_{2D} (2.20) of the 1D and 2D DDNLS models, although as we will discuss below this is not the best approach in integrating such systems if the number of sites is large. Let us discuss in more detail the case of the 1D DDNLS model (2.17). Its Hamiltonian function splits into two integrable parts $\mathcal{H}_{1D} = A + B$ as

$$A = \sum_l \epsilon_l |\psi_l|^2 + \frac{\beta}{2} |\psi_l|^4, \quad (3.88)$$

possessing N integrals of motion, namely the quantities $s_l = |\psi_l|^2$, and

$$B = - \sum_l \psi_{l+1}^* \psi_l + \psi_{l+1} \psi_l^*, \quad (3.89)$$

where ψ_l is a complex valued quantity representing the wave packet's state at site l . Following [Skokos et al., 2014; Gerlach et al., 2016], we introduce real phase space variables

$$\psi_l = \frac{1}{\sqrt{2}} (q_l + ip_l), \quad \psi_l^* = \frac{1}{\sqrt{2}} (q_l - ip_l), \quad (3.90)$$

with q_l and p_l respectively being the generalized position and momentum of the system at site l . This transformation brings the A (3.88) and B (3.89) parts of the \mathcal{H}_{1D} (2.17) Hamiltonian to

$$A = \sum_l \frac{\epsilon_l}{2} (q_l^2 + p_l^2) + \frac{\beta}{8} (q_l^2 + p_l^2)^4, \quad B = \sum_l -p_{l+1} p_l - q_{l+1} q_l. \quad (3.91)$$

In [Gerlach et al., 2016], the efficiency of several two-part split SIs (in particular the LF (3.72), $SABA_2$ (3.73), $ABA864$ (3.76) and $SABA_2Y6$ (3.78)) were tested mainly in comparison with three-part split schemes. In that work, the ability of the integrator to accurately reproduce the correct system's dynamics in the least CPU time was investigated primarily through the computation of the wave packet's second moment (3.5) and participation number (3.6). As the 1D DDNLS possesses two integrals of motion, namely the total norm \mathcal{S}_{1D} (2.19) and energy \mathcal{H}_{1D} (2.17), the accuracy of the integration of the equations of motion was checked via the computation of the *relative energy error*

$$E_r(t) = \left| \frac{\mathcal{H}_{1D}(t) - \mathcal{H}_{1D}(0)}{\mathcal{H}_{1D}(0)} \right|, \quad (3.92)$$

and *relative norm error*

$$S_r(t) = \left| \frac{\mathcal{S}_{1D}(t) - \mathcal{S}_{1D}(0)}{\mathcal{S}_{1D}(0)} \right|. \quad (3.93)$$

The main outcome of that study was that for large 1D DDNLS systems having $N \gtrsim 70$ lattice sites, three-part split SIs (whose efficiency will be discussed below) have to be preferred over two-part split schemes. Although the investigation in [Gerlach et al., 2016] was limited to the numerical integration of the system's equations of motion it is reasonable to assume that the simultaneous integration of the variational equations (needed for the computation of chaos indicators like the MLE) will not change the superiority of three-part split methods for large systems. Since in our work, we always consider systems with $N > 70$ sites, typically N is of the order of several hundreds, we will not use two-part split SIs. Nevertheless, for the sake of completeness, we present in Sec. D.1 of Appendix D the explicit expression of the operators appearing in SI implementations for solving both the equations of motion and the variational equations of the 1D DDNLS system (2.17). Due to the inefficiency of two-part split SIs for the 1D DDNLS system, such SI were not also considered for the 2D DDNLS model.

As a final remark, let us note that the two-part split SIs are adequate for computing the dynamics (integration of the equations of motion) and tangent dynamics (integration of the variational equations) for several many body systems like the 1D (2.24) and 2D (2.27) DKG models (see [Skokos et al., 2013; Danieli et al., 2017]), the FPUT model and the XY model of Josephson junction array [Danieli et al., 2017; Mithun et al., 2019]. The performance of several such schemes were studied in detail in [Senyange and Skokos, 2018; Danieli et al., 2019a]. There, it was found that the integrators $ABA864$ (3.76), $ABA864$ (3.77) of order 4 and the $SABA_2Y6$ (3.78), $s9SABA_26$ (3.79) and $ABA864Y6$ (3.70) SIs of order 6 exhibited the best performance when a moderate energy conservation ($E_r \approx 10^{-5}$) was required.

3.8.2 Three-part split symplectic integrators

Let us now consider the case of SIs for Hamiltonian systems which can be split in three integrable parts. Example cases of such Hamiltonian functions include the 1D (2.17) and 2D (2.20) DDNLS models [Skokos et al., 2014; Gerlach et al., 2016; Danieli et al., 2019a], system's describing the motion of a rotating body [Laskar and Vaillant, 2019] and of charged particles under Lorentz force fields [He et al., 2015, 2016; Casas and Escorihuela-Tomás, 2020].

The 1D DDNLS Hamiltonian (2.17) can be split in three integrable parts

$$\mathcal{A} = \sum_l \frac{\epsilon_l}{2} (q_l^2 + p_l^2) + \frac{\beta}{8} (q_l^2 + p_l^2)^2, \quad \mathcal{B} = - \sum_l p_{l+1} p_l, \quad \mathcal{C} = - \sum_l q_{l+1} q_l, \quad (3.94)$$

where obviously $\mathcal{A} = A$ (3.88). Similarly, the Hamiltonian function of the 2D DDNLS system (2.20) can be split as

$$\begin{aligned} A &= \sum_{l,m} \frac{\epsilon_{l,m}}{2} (q_{l,m}^2 + p_{l,m}^2) + \frac{\beta}{8} (q_{l,m}^2 + p_{l,m}^2)^2, & B &= - \sum_{l,m} p_{l+1,m} p_{l,m} + p_{l,m+1} p_{l,m}, \\ C &= - \sum_{l,m} q_{l+1,m} q_{l,m} + q_{l,m+1} q_{l,m}. \end{aligned} \quad (3.95)$$

The explicit expressions of the operators needed for the application of three-part split SIs for these two systems are respectively given in sections D.2.1 and D.2.2 of Appendix D.

Let us first focus on the 1D DDNLS system (3.94) and check the ability of the various integration schemes to accurately reproduce the system's evolution in its phase space, as well as its tangent dynamics. To that end, we monitor the time evolution of the energy $E_r(t)$ (3.92) and norm $S_r(t)$ (3.93) errors along with a basic observable like the wave packet's second moment $m_2(t)$ (3.5). For monitoring the accurate description of the system's the tangent dynamics we compute the motion's ftMLE (3.21). We consider two

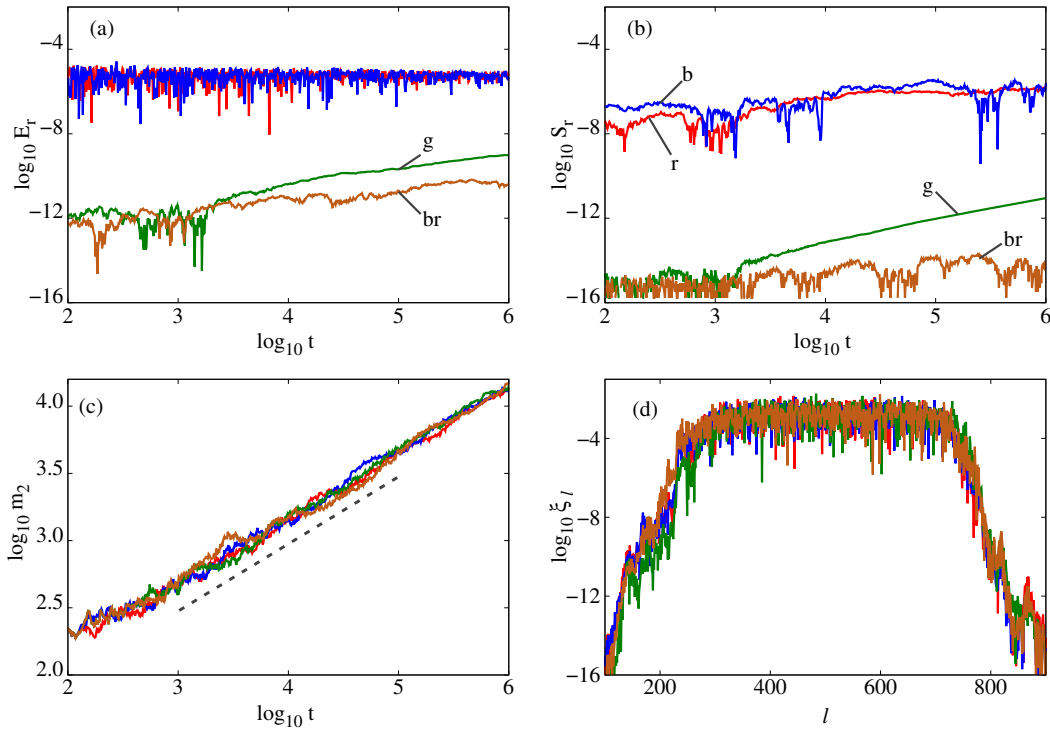


Figure 3.4: Results for the numerical integration of case A1 (see text for details) of the 1D DDNLS system (2.17) by the second order SI $\mathcal{ABC}2$ (3.82) for $\tau = 0.0002$ [(r)ed curves], the fourth order SI $\mathcal{ABCY}4$ (3.7.4) for $\tau = 0.0125$ [(b)lue curves] and the non-symplectic schemes $DOP853$ (Sec. 3.6.3) [(g)reen curves] and $TIDES$ (Sec. 3.6.2) [(br)own curves]. The time evolution of (a) the relative energy error $E_r(t)$ (3.92), (b) the relative norm error $S_r(t)$ (3.93) and (c) the second moment $m_2(t)$ (3.5) of the wave packet. In (d) the norm density distribution ξ_l (3.1) at time $t_f = 10^6$ is shown. The dashed line in (c) guides the eye for slope 1/2 (from [Danieli et al., 2019a]).

cases belonging respectively to the strong and weak chaos spreading regimes, which were also investigated in [Senyange et al., 2018]:

- **Case A1.** We excite $L = 21$ central sites, with a constant norm per site $s = 1$. In addition, the parameters $W = 3.5$ and $\beta = 0.62$ were chosen for the \mathcal{H}_{1D} (2.17) such that its value is approximately 0.0212 for the disorder realization we are using.
- **Case A2.** Here, we consider a similar setup as in case A1, but the parameters of the \mathcal{H}_{1D} (2.17) are $W = 3$ and $\beta = 0.03$, giving for the disorder realization we selected $\mathcal{H}_{1D} \approx 3.444$.

In both cases, the total size of the lattice is $N = 1024$ sites and the initial DV needed for the computation of the MLE is chosen such that only one site at the center of the lattice has non zero δq_l and δp_l values, while its other components are set to zero. As usual, the initial DV was normalized so that $\|\mathbf{w}(0)\| = 1$.

Some of the result of our analysis for the case A1 are presented in Fig. 3.4. In particular, we depict the evolution in time of the energy error $E_r(t)$ (3.92) in Fig. 3.4(a), the norm error $S_r(t)$ (3.93) in

Fig. 3.4(b), and the $m_2(t)$ (3.5) in Fig. 3.4(c), while in Fig. 3.4(d) we plot the norm profile at the end of our integration. We see that the used SIs: namely the $\mathcal{ABC}2$ [(r)ed curves] and $\mathcal{ABCY}4$ [(b)lue curves] schemes conserve quite well the value of the computed energy as the relevant error is bounded from above by $E_r \approx 10^{-5}$ [Fig. 3.4(a)]. On the other hand, the general purpose integrators (non-symplectic schemes): $DOP853$ [(g)reen curves] and $TIDES$ [(br)own curves] integrators although having $E_r(t)$ values much smaller than that of the SIs, their errors are increasing in time. From the results of Fig. 3.4 we see that the value of $S_r(t)$ grows in time for all the used integrators, with $TIDES$ showing the best behavior as its S_r values are the smallest and show a mild increase up to the maximum considered time $t_f = 10^6$. We see that the SIs do not conserve the second integral of motion i.e. the system's norm, although the increase of the related error $S_r(t)$ is in general slower than the ones observed for the non-symplectic methods. We emphasize that all the used schemes accurately reproduce the system's dynamics as the evolution of the wave packet's m_2 [Fig. 3.4(c)] and its profile [Fig. 3.4(d)] are correctly captured by all methods. We also note that similar behaviors are seen for case A2, although we do not report these results here in order to avoid repetition of similar outcomes.

The performance of seven three-part split SIs along with non-symplectic schemes for the integration of the equations of motion of the 1D DDNLS system was also investigated in [Skokos et al., 2014; Gerlach et al., 2016]. Here, we want to go one step further and investigate the ability of three-part split SIs to efficiently integrate the system's variational equations through the application of the 'tangent map' method. In Figs. 3.5(a) and (c), we present the evolution of the ftMLEs, computed through the numerical solution of the variational equations and see that for both sets of conditions considered here, all schemes practically reproduce similar results. In Fig. 3.5(b) and (d) we show the required CPU time T_C for these computations and see that the best performing integrator among the ones presented in Fig. 3.4 is the $\mathcal{ABCY}4$ scheme.

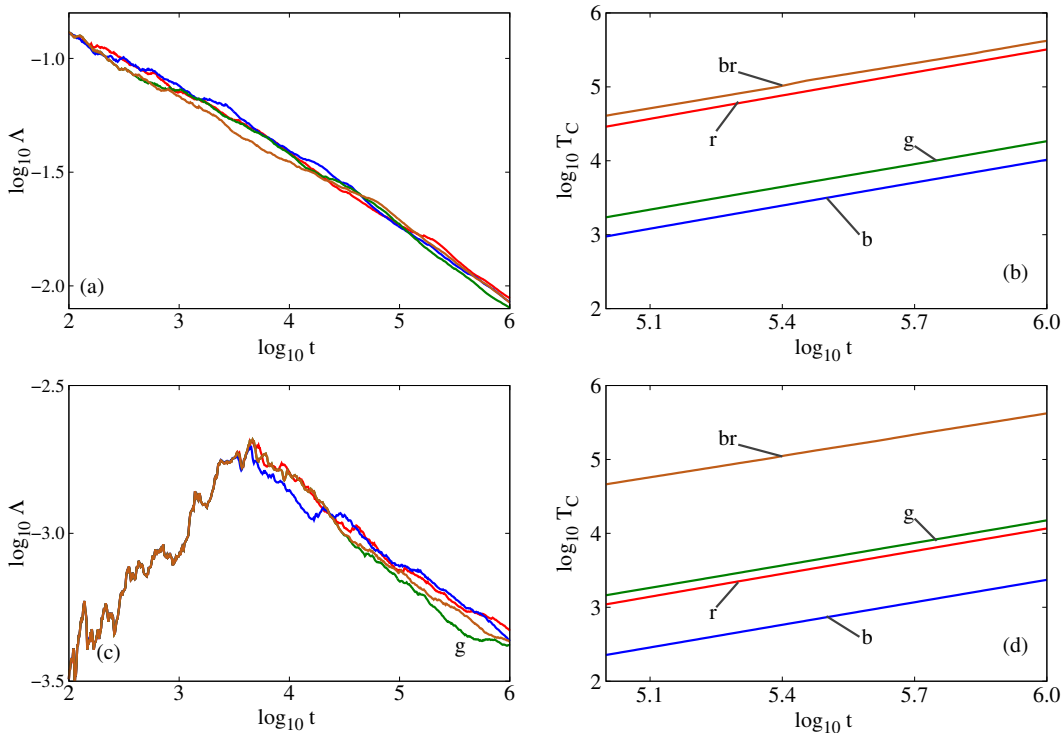


Figure 3.5: Results obtained by the numerical integration of the variational equations of the 1D DDNLS Hamiltonian (2.17) for the initial conditions described in cases A1 [panels (a) and (b)] and A2 [panels (c) and (d)] (see text for details). The time evolution of, (a) and (c) the ftMLE $\Lambda(t)$ (3.21), and (b) and (d) the required CPU time T_C in seconds. The integrators and the curves' colors are the ones used in Fig. 3.4.

In Figs. 3.4 and 3.5, we showed some representative results of only four integration schemes, although we performed a more detailed study by repeating the same simulations with several integrators. The obtained results for cases A1 and A2 are respectively presented in Tables 3.1 and 3.2. In these Tables accurate simulations with $E_r \lesssim 10^{-9}$ are also considered. We see that overall, both tables give qualitatively the same information. The best performing integrators for moderate accuracy ($E_r \lesssim 10^{-5}$) are the $s11\mathcal{ABC}6$ and $s9\mathcal{ABC}6$ SIs, while for higher accuracies ($E_r \lesssim 10^{-9}$), the $s19\mathcal{ABC}8$ and $s17\mathcal{ABC}8$ schemes are behaving better. Consequently, we conclude that the $s11\mathcal{ABC}6$ and $s9\mathcal{ABC}6$ SIs

are particularly well suited for the integration of the 1D DDNLS for moderate accuracies that are typically required in dynamical studies of this model [Skokos et al., 2009; Bodyfelt et al., 2011a; Danieli et al., 2017, 2019b; Senyange et al., 2018; Many Manda et al., 2020].

Table 3.1: Information on the performance of the numerical schemes used for the integration of the equations of motion and the variational equations of the 1D DDNLS system (2.17) up to final time of $t_f = 10^6$ time units for the case A1 (see text for details). The order n , the number of ‘Steps’ of each SI along with the required CPU time T_C in seconds are reported. The integration time step τ used for each integrator fixes the relative energy error $E_r(t) \lesssim 10^{-5}$ and $E_r(t) \lesssim 10^{-9}$. All simulations were performed on a workstation using 3.00 GHz Intel Xeon E5 – 2623 processors. All codes were written in Fortran90 language and were compiled by using the gfortran compiler (<https://gcc.gnu.org/>) with `-O3` optimization flag. No advanced vectorization mode has been implemented.

$E_r \approx 10^{-5}$					$E_r \approx 10^{-9}$				
Integrator	n	Steps	τ	T_C	Integrator	n	Steps	τ	T_C
<i>s11ABC6</i>	6	45	0.115	3395	<i>s19ABC8</i>	8	77	0.09	7242
<i>s9ABC6</i>	6	37	0.095	3425	<i>s17ABC8</i>	8	69	0.08	7301
<i>ABCY6_A</i>	6	29	0.07	3720	<i>s11ABC6</i>	6	45	0.025	15692
<i>SS864S</i>	4	17	0.05	6432	<i>s9ABC6</i>	6	37	0.02	16098
<i>ABCY4</i>	4	13	0.0125	10317	<i>DOP853</i>	8	$\delta_a = 10^{-16}$	0.05	18408
<i>ABCS4Y6</i>	6	49	0.015	35417	<i>ABCY8_D</i>	8	61	0.002	258891
<i>ABCY4Y6</i>	6	37	0.008	40109	<i>TIDES</i>	–	$\delta_a = 10^{-16}$	0.05	419958
<i>ABCS4</i>	4	21	0.00085	267911					
<i>ABC2</i>	2	5	0.0002	320581					

Table 3.2: Similar to Table 3.1 but for case A2 (see text for details) of the 1D DDNLS system (2.17)

$E_r \approx 10^{-5}$					$E_r \approx 10^{-9}$				
Integrator	n	Steps	τ	T_C	Integrator	n	Steps	τ	T_C
<i>s11ABC6</i>	6	45	0.4	1132	<i>s19ABC8</i>	8	77	0.3	2184
<i>s9ABC6</i>	6	37	0.285	1147	<i>s17ABC8</i>	8	69	0.225	2632
<i>ABCY6_A</i>	6	29	0.2	1308	<i>s11ABC6</i>	6	45	0.1	4137
<i>SS864S</i>	4	17	0.265	1365	<i>s9ABC6</i>	6	37	0.075	4462
<i>ABCY4</i>	4	13	0.055	2354	<i>ABCY8_D</i>	8	61	0.065	8528
<i>ABCS4Y6</i>	6	49	0.105	4965	<i>DOP853</i>	8	$\delta_a = 10^{-16}$	0.05	14998
<i>ABCY4Y6</i>	6	37	0.04	8091	<i>TIDES</i>	–	$\delta_a = 10^{-16}$	0.05	420050
<i>ABCS4</i>	4	21	0.02	9774					
<i>ABC2</i>	2	5	0.0055	11700					

Let us now perform similar computations for the 2D DDNLS system (2.20) and in particular for two typical particular setups.

- **Case B1.** The initial wave packet is located at $L \times L = 7 \times 7$ central sites having a uniformly distributed norm per site $s_{l,m} = 1/6$. The disorder strength is set at $W = 15$, the nonlinear coefficient $\beta = 6$ and the specific disorder realization gives $\mathcal{H}_{2D} \approx 1.96$ (2.20).
- **Case B2.** An initial wave packet of size $L \times L = 1$ at the central site with a unit norm i.e. $s_{l,m} = 1$ per site for $W = 16$ and $\beta = 1.25$. The specific realization of disorder parameters sets up $\mathcal{H}_{2D} \approx 0.625$.

In both cases, a lattice of 200×200 sites was considered and the initial DV needed for the variational equations has non zero components chosen from a random uniform distribution for only the initially excited sites and its norm was set to unity i.e. $\|\mathbf{w}(0)\| = 1$. The obtained classifications for the performance of several integration schemes are shown in Tables 3.3 and 3.4 respectively for cases B1 and B2. From these tables, we see again that for moderate energy accuracy ($E_r \lesssim 10^{-5}$) the *s9ABC6* and *s11ABC6* SIs have the best performance, while at higher energy accuracy ($E_r \lesssim 10^{-9}$) both the *s19ABC8* and *s17ABC8* SIs exhibit the best performance.

Let us also stress a point which we consider important. Although the results presented in this section suggest that the *DOP853* and *TIDES* schemes are not well suited for very long time integrations as they require a lot of CPU time, they are nevertheless extremely versatile and perform quite well for

Table 3.3: Similar to Table 3.1 but for the case B1 of the 2D DDNLS model (2.20).

$E_r \approx 10^{-5}$					$E_r \approx 10^{-9}$				
Integrator	n	Steps	τ	T_C	Integrator	n	Steps	τ	T_C
<i>s9ABC6</i>	6	45	0.105	13914	<i>s17ABC8</i>	8	77	0.075	36528
<i>s11ABC6</i>	6	37	0.125	14000	<i>s19ABC8</i>	8	69	0.08	38270
<i>ABCY6_A</i>	6	29	0.08	15344	<i>s9ABC6</i>	6	45	0.0235	65287
<i>ABCY4</i>	4	13	0.025	23030	<i>s11ABC6</i>	6	37	0.0275	67314
<i>SS864S</i>	4	17	0.085	23887	<i>ABCY8_D</i>	8	61	0.008	140506
<i>ABCS4Y6</i>	6	49	0.03	77424	<i>DOP853</i>	8	$\delta_a = 10^{-16}$	0.05	218704
<i>ABCY4Y6</i>	6	37	0.0165	87902					
<i>ABCS4</i>	4	21	0.0065	132713					
<i>ABC2</i>	2	5	0.005	157694					

Table 3.4: Similar to Table 3.1 but for the case B2 of the 2D DDNLS model (2.20)

$E_r \approx 10^{-5}$					$E_r \approx 10^{-9}$				
Integrator	n	Steps	τ	T_C	Integrator	n	Steps	τ	T_C
<i>s11ABC6</i>	6	45	0.1515	11443	<i>s19ABC8</i>	8	77	0.135	20952
<i>s9ABC6</i>	6	37	0.11	13408	<i>s17ABC8</i>	8	69	0.0875	28966
<i>ABCY6_A</i>	6	29	0.0775	14607	<i>s11ABC6</i>	6	45	0.0335	50301
<i>SS864S</i>	4	17	0.0915	15564	<i>s9ABC6</i>	6	37	0.024	58187
<i>ABCY4</i>	4	13	0.0215	25898	<i>ABCY8_D</i>	8	61	0.009	150045
<i>ABCS4Y6</i>	6	49	0.035	64423	<i>DOP853</i>	8	$\delta_a = 10^{-16}$	0.05	166145
<i>ABCY4Y6</i>	6	37	0.01375	102580					
<i>ABCS4</i>	4	21	0.005	185615					
<i>ABC2</i>	2	5	0.00155	198534					

several tasks we expect an integrator to do. This fact is emphasized in Fig. 4.2 of [Hairer et al., 1993] and in the related discussion where the *DOP853* scheme proved to be the best performing integrator among the ones considered there. In the same spirit, the advantages of the *TIDES* package were discussed in [Barrio, 2005; Abad et al., 2012].

3.9 Summary

In this chapter, we presented the numerical methods we use in our study. Particular emphasis was given to a plethora of SIs developed for the integration of the equations of motion and the variational equations of the 1D and 2D DDNLS systems. For the 1D DDNLS model, we considered symplectic schemes based on splitting the system's Hamiltonian into two and three integrable parts, while for the 2D DDNLS model, only the three-part split of the Hamiltonian function was explored. We studied the performance of the obtained numerical SIs by comparing their efficiency to some commonly used integrators: The RK scheme of order 8 based on the Dormand-Prince method *DOP853* and the *TIDES* package which is extracted from Taylors/Lie series expansions of the system's vector field. Our results suggest that SIs should be preferred for very long time integrations as they need less CPU time to achieve a certain level of accuracy. In the case of three-part split methods, the *s11ABC6* and *s9ABC6* as well as the *s19ABC8* and *s17ABC8* SIs proved to be the most efficient ones for moderate and high accuracy respectively. In addition, the three-part split approach leads to SIs which are faster than those produced by the two-part split method for large system sizes. This result justifies our choice of the former approach as our used integration techniques.

The proper selection of initial excitations of the DDNLS models has been discussed in [Kati et al., 2020] as one has to take into account the values of both integrals of motion i.e. the total energy and total norm. Therefore, numerical approaches for designing initial conditions for these systems in order to obtain specific energy and norm values were also presented in detail. We further outlined other numerical techniques we use in our study, such as the determination of the power law exponents from non smooth numerical data sets, the numerical characterization of the wave packet as well as the numerical calculations of its extent through definitions of the first and second moments, and the participation number. Furthermore, we introduced the notion of tangent space of a trajectory in the phase space and

presented numerical techniques for the computation of observables of the orbit's dynamics like the MLE and the DVD.

So far we have discussed and presented the analytical approaches, as well as numerical techniques we are using in our work. The two next chapters will be devoted on the application of these techniques in order to investigate in detail the characteristics of chaos of the 1D and 2D DDNLS systems.

Chapter 4

Chaotic dynamics of wave packet spreading in the one-dimensional disordered nonlinear Schrödinger equation

4.1 Introduction

In this chapter we turn the focus to one of the main objectives of this thesis, namely the investigation of the chaotic dynamics of wave packet spreading in the 1D DDNLS model (2.17). Although this subject has been considered in the past [see e.g. [Mulansky et al., 2009](#); [Skokos et al., 2013](#); [Antonopoulos et al., 2014, 2016, 2017](#)], the detailed investigation of the asymptotic behavior of chaos for the different dynamical regimes in the 1D DDNLS system is still incomplete. Due to both the presence of disorder in the equations of motion (2.18) and the stochastic nature of the tangent dynamics, visible for example if we consider a small perturbation in the reduced nonlinear stochastic ODE (2.105) approximating the system's dynamics in the limit of small amplitude wave packet spreading, the analytical study of the system chaotic dynamics is very difficult. Thus, we rely on numerical simulations for our investigations.

The chapter is organized as follows: In Sec. 4.2, we discuss some of the computational issues mainly related to the integration of the model's variational equations. Section 4.3 is devoted to presenting our computations of the MLE for the AL, weak chaos, and strong chaos dynamical regimes. In Sec. 4.4 we analyse the local characteristics of chaos. We investigate how the DVD behaves in the linear regime and discuss the idea of the presence of chaotic hotspots within the wave packet interior as a mechanism for promoting spreading in the weak and strong chaos regimes. In Sec. 4.5 we discuss our findings. More specifically, we discuss the implication of the wave packet chaoticity for its spreading dynamics in the weak and strong chaos cases. The results of this chapter are heavily based on findings in [[Senyange et al., 2018](#)].

4.2 Some aspects related to our numerical simulations

4.2.1 Choice of the initial deviation vector

Let us now look more closely at the numerical aspect of the DV in our simulations. In general the choice of the DVs is of practical importance for the computation of the Lyapunov exponents [[Skokos, 2010](#)]. The most commonly suggested option being initial DVs having randomly selected elements in order to avoid any linear dependence between the coordinates of the DVs. As the computation of the MLE only requires a single DV the practice above is not absolutely necessary. However, most papers suggest it as good choice of DV [see e.g. [Skokos, 2010](#)]. For low degrees of freedom Hamiltonian models such as the ones seen in pioneering fields of chaos theory like celestial mechanics [[Hénon and Heiles, 1964](#); [Froeschlé, 1972](#); [Skokos, 2001](#)] or plasma physics [[Chirikov, 1971](#); [Wingen et al., 2005](#); [Kominis et al., 2008](#); [White, 2013](#)], the dynamics of the system takes place in a rather 'small' phase space such that if the system's orbit is chaotic, all choices of DVs for the computation of the ftMLE converge to the MLE practically at the same rate. In systems with many more degrees of freedom, especially the ones we are working in this thesis which have in theory an infinite phase space dimension, the system's dynamics in the phase space take place in 'tiny' regions compared to the overall size of the system's phase space. Thus, one has

to carefully select the type of DVs in order to correctly capture the dynamics.

To better understand this let us consider the example in Figs. 4.1 and 4.2(a), where we initially excite in a lattice of $N = 1021$ sites the q_l and p_l coordinates of $L = 21$ central sites with a uniformly distributed norm per site $s = 0.3$, such that the total norm (2.19) is $\mathcal{S}_{1D} = 6.3$. Moreover, the nonlinear coefficient $\beta = 1$, the disordered strength $W = 4$ and the random values ϵ_l are chosen such that the total energy (2.17) $\mathcal{H}_{1D} \approx 1.05$ is uniformly distributed among all the excited sites with an energy per site $h \approx 0.05$. This initial wave packet belongs to the weak chaos regime of the 1D DDNLS model (2.17) according to the parameter spaces of Figs. 2.4 and 2.6. We integrate the system's equations of motion and variational equations using the *s11ABC6* scheme (3.84) up to $t_f = 10^6$, fixing the integration time step $\tau = 0.15$ which leads to a maximal relative energy error (3.92) $E_r(t) \lesssim 10^{-6}$ and relative norm error (3.92) $S_r(t) \lesssim 10^{-4}$. For the initial DV, we use four cases:

Case DV₁. We give random values to δq_l and δp_l of only the central site of the lattice. This leads to the spatial distribution of the DVD ξ_l^D (3.25) as shown in upper left panel of Fig. 4.2(a).

Case DV₂. We randomly excite the δq_l and δp_l coordinates of $L = 21$ central sites i.e. the DVD ξ_l^D (3.25) has non-zero elements only in the lattice's initially excited region as shown in the upper right panel of Fig. 4.2(a).

Case DV₃. We give to the δq_l and δp_l coordinates of the $L = 21$ sites at either end of the lattice, randomly chosen values, which corresponds to the DVD ξ_l^D (3.25) depicted in the lower left panel of Fig. 4.2(a).

Case DV₄. We excite all the elements of the DV with values drawn from a random uniform distribution. This results to a DVD ξ_l^D (3.25) having non-zero elements at all lattice sites as shown in the lower right panel of Fig. 4.2(a).

In Fig. 4.1 we present the spatiotemporal evolution of the DVD, ξ_l^D (3.25), for the cases DV₁ in Fig. 4.1(a), DV₂ in Fig. 4.1(b), DV₃ in Fig. 4.1(c) and DV₄ in Fig. 4.1(d). A transient time where the dynamical behaviors of each DVD differs is clearly visible. For DV₁ and DV₂, a timid expansion of the DVD is observed which do not spread over the whole lattice, but always remain within the area of the wave packet extent where the dynamics of the system take place. This is further supported by the observations of the spatiotemporal evolution of DV₃ and DV₄, where the tangent dynamics has a tendency to enhance the magnitude of the coordinates of the DV inside the region where the motion of the wave packet occurs and the values of the coordinates of the DV outside the wave packet die out. In the case of DV₃, this transition happens around $\log_{10} t \approx 3.5$ [see Fig. 4.1(c)], while for the case DV₄ it happens at $\log_{10} t \approx 2$ [see Fig. 4.1(d)].

During these transient times, the ftMLEs in each DV case show different evolutions as seen in Fig. 4.2(b). Indeed, the ftMLEs obtained with DV₁ and DV₂ display larger values compared to the other DVs (DV₃ and DV₄). This is due to the fact that these DVs evolve within the active domain, whose evolution is controlled by nonlinear deterministic equations (2.18). Consequently, a deterministic chaotic dynamics is visible from the beginning of their evolutions which explain the large values of the ftMLEs. Next is the ftMLE of DV₄ which is at its peak two order of magnitudes smaller than the values observed for the ftMLEs of DV₁ and DV₂. The reason for such a measurement is the following: For time t such that $\log_{10} t \lesssim 2$ in the early evolution of DV₄, a large part of the DV coordinates evolve in the regular background outside the system's excited region. Thus the contribution of the regular part is non-negligible compared to the contribution of the excited region of the lattice which is chaotic. This leads to the smaller value of the ftMLE observed in Fig. 4.2(b) compared to the ones obtained from DV₁ and DV₂. In the case of DV₃, when $\log_{10} t \lesssim 3.5$, all the non-zero coordinates of the DV evolve only into the regular part of the lattice which therefore solely contribute to the value of the ftMLE which indicates $\Lambda(t) \approx 10^{-10}$ at its lowest pick i.e. an almost zero ftMLE.

For longer times, well above the largest transient time of DV₃, all the DVs converge to a consistent behavior as all the asymptotic spatiotemporal evolution of the DVDs ξ_l^D (3.25) are practically the same in Fig. 4.2. According to the theory of chaos [see e.g. Skokos, 2010; Skokos and Manos, 2016], this asymptotic behavior of the DVs in Fig. 4.1 corresponds to the spatial alignment of the tangent dynamics along the most chaotic direction of the system's reference orbit. Thus, the average exponential rate of growth (or shrinking) of the magnitude of this DV measures the system's MLE. This is what is observed in Fig. 4.2(b), where for time t above the transient time, all the ftMLEs practically indicate the same value.

Based on this experiment, we can decide which type of DVs is the best from a practical point of view. Indeed, our objective is to be able to retrieve the asymptotic behavior of the tangent dynamics as fast as possible since we are constrained by computational time limitations. Thus, DV₃ and DV₄, which possess the largest transient times are bad choices for our purpose. This is worsened by the

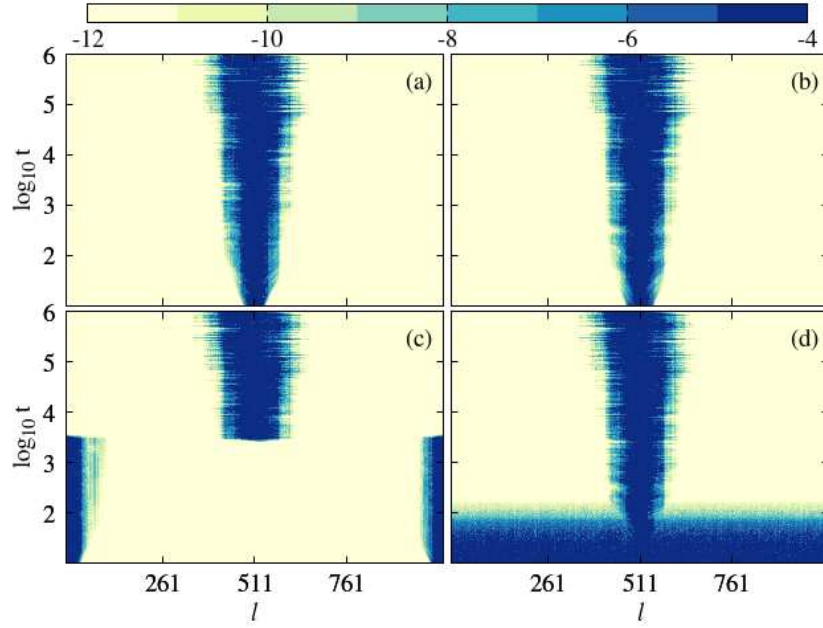


Figure 4.1: Spatiotemporal evolution of the DVD ξ_l^D (3.25) profile for different initial DVs. The panel (a) corresponds to DV_1 , the panel (b) to DV_2 , the panel (c) to DV_3 and the panel (d) to DV_4 (see text for details). The color scales at the top of the figure are used for coloring the lattice sites according to their $\log_{10} \xi_l^D$ values.

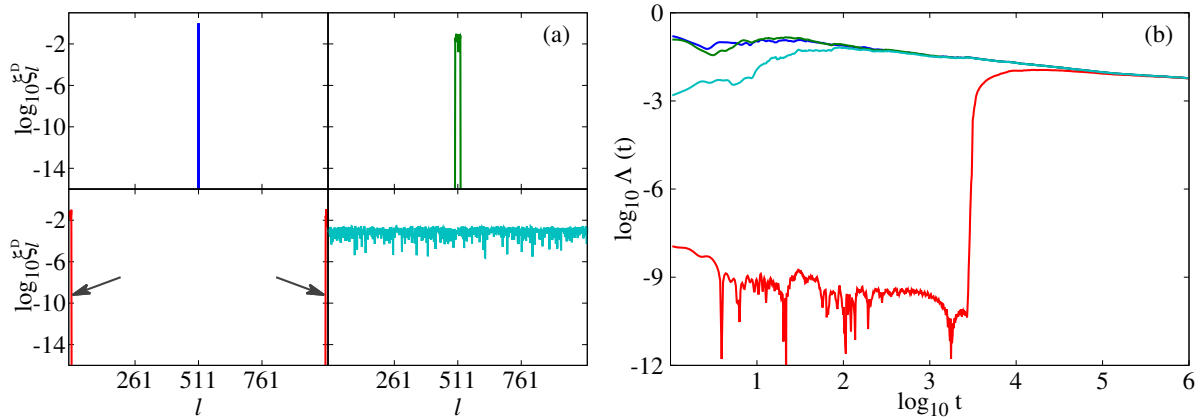


Figure 4.2: (a) Initial profiles ξ_l^D (3.1) of the DVDs used for obtaining the results of Fig. 4.1. The positions of each panel corresponds to the arrangement seen in Fig. 4.1. (b) Time evolution of the ftMLE, $\Lambda(t)$ (3.21) for the DVs of panel (a). The colors of the curves correspond to the ones in panel (a).

fact that for lattice size $N > 1021$ (with the size of the excited region L almost constant), the regular background outside the excited central part of the lattice becomes larger, therefore longer transient times are expected for the DVs similar to DV_3 and DV_4 as the elements of the tangent dynamics outside the wave packet evolution take larger times to vanish (only the elements of the DV inside the lattice's excited part contribute to the MLE). On the other hand the cases DV_1 and DV_2 are good choices since they are located inside the central excited part of the lattice where the dynamics take place. Consequently, they take less time to converge to the most chaotic direction whose non zero elements of the DV are always located inside the wave packet as indicated by the evolution of the DVDs in Fig. 4.1. For the rest of this chapter, unless otherwise stated, our default initial DV is the DV_1 .

4.2.2 The dynamic lattice expansion

Because the initially excited sites are located at the central part of a lattice of large size, in our simulations we can consider a smaller subset of the lattice at the beginning of our simulations and expand it when ever it is necessary. We refer to this approach as the *dynamic lattice simulation* which has been successfully implemented for both the 1D (2.17) and 2D (2.20) DDNLS models and DKG systems (Eqs. (2.24) and (2.27)) in [Senyange et al., 2018; Many Manda et al., 2020] in contrast to the *fixed lattice method*

used in several studies on the subject [Flach et al., 2009; Skokos and Flach, 2010; Lapyteva et al., 2010, 2012; Kati et al., 2020]. Let us note that this is not particularly unusual as even in the theory (see Chap. 2 and references therein), the infinite lattice size i.e. $N \rightarrow \infty$ in \mathcal{H}_{1D} (2.17) is often substituted by a large but finite value of N . Then, we have to define a condition which controls our lattice expansion. For the 1D DDNLS model (2.17), we monitor the value of the average norm per site $\sum_{l \in \mathcal{D}} s_l / \mathcal{D}$ of the last \mathcal{D} sites at both edges of the ‘active’ (dynamic) lattice with size $N_{\mathcal{D}, \delta_{\mathcal{D}}}$ sites. Then, whenever

$$\frac{1}{\mathcal{D}_L} \sum_{l \in \mathcal{D}_L} s_l > \delta_{\mathcal{D}_L}, \text{ or } \frac{1}{\mathcal{D}_R} \sum_{l \in \mathcal{D}_R} s_l > \delta_{\mathcal{D}_R}, \quad (4.1)$$

the lattice is expanded at both ends (in order to maintain the symmetry with respect to the initial central excitation) by \mathcal{N} sites. Note that in Eq. (4.1), \mathcal{D}_L and \mathcal{D}_R describe the number of sites at the left and right edges respectively (we often assume $\mathcal{D}_L = \mathcal{D}_R = \mathcal{D}$). In addition, $\delta_{\mathcal{D}_L} = \delta_{\mathcal{D}_R} = \delta_{\mathcal{D}}$ is the threshold above which we expand our current dynamic lattice at the edges. It is worth mentioning that $\mathcal{N} > \mathcal{D}$.

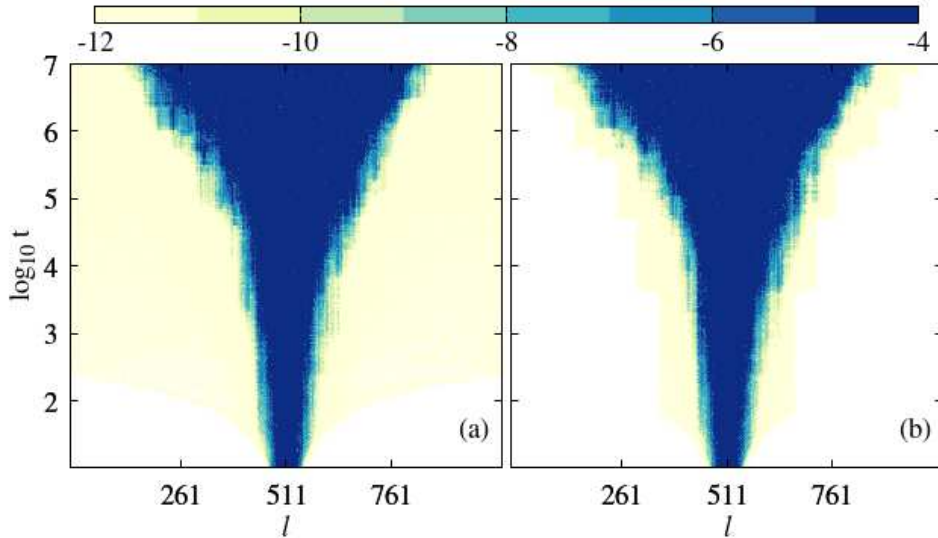


Figure 4.3: Heatmaps of the spatiotemporal evolutions of the normalized norm distribution ξ_l (3.25) for an initial condition belonging to the strong chaos spreading regime (see text for details). We excited $L = 21$ central sites on a lattice of $N = 1021$ sites with the same norm per site $s = 1$ so that the total norm (2.19) $\mathcal{S}_{1D} = 21$. The random values ϵ_l , $1 \leq l \leq N$, give a total energy (2.17) $\mathcal{H}_{1D} \approx 3.21$, using the parameters $W = 4$ and $\beta = 0.72$. The panel (a) corresponds to the fixed lattice size as we see the residual norm i.e. $s \sim 10^{-12}$ (light yellow in the heatmap) spreads over the entire lattice. The panel (b) corresponds to the lattice expansion approach as the residual norm is concentrated around the wave packet (darker region in the heatmap). The white area, corresponds to (empty) lattice sites with no norm s . The color scales at the top of the figure are used for coloring the lattice sites according to the magnitude of their $\log_{10} \xi_l$ values.

To be more specific, in Fig. 4.3, we plot the evolution of the normalized norm distribution ξ_l (3.1) on a lattice of $N = 1021$ sites using at time $t = 0$, $L = 21$ centrally excited sites such that each site receives the same constant norm per site $s = 1$, leading to the total norm (2.19) $\mathcal{S}_{1D} = 21$. Further, the values of ϵ_l are chosen in a way that the Hamiltonian (2.17) $\mathcal{H}_{1D} \approx 3.21$, with parameters $W = 4$ and $\beta = 0.72$. This initial condition belongs to the strong chaos spreading regime according to Figs. 2.4 and 2.6 of Chap. 2. We integrate the system’s phase space and tangent dynamics using the *s11ABC6* SI (3.84), with time step $\tau = 0.2$ up to the final integration time $t_f = 10^7$. In doing so, we obtain a relative energy error (3.92) $E_r(t) \lesssim 10^{-5}$ and a relative norm error (3.93) $S_r(t) \lesssim 10^{-3}$. In Fig. 4.3(a), we plot the spatiotemporal wave packet evolution $\xi_l(t)$ for the fixed lattice size system, along with the one of the dynamic lattice implementation [see Fig. 4.3(b)], starting from $N_{\mathcal{D}, \delta_{\mathcal{D}}} = 321$ at time $t = 0$. In addition, we used as threshold $\delta_{\mathcal{D}} = 10^{-12}$. We monitor $\mathcal{D} = 10$ points at the edges and increase each edges by $\mathcal{N} = 50$ sites each time that the wave packet has reached the borders of the lattice i.e. whether the condition (4.1) is verified.

In Fig. 4.3(b), the dynamic lattice size $N_{\mathcal{D}, \delta_{\mathcal{D}}} = 321$ sites at time $t = 0$, was increased by $2\mathcal{N} = 100$ at time $\log_{10} t \approx 3.64$ to $N_{\mathcal{D}, \delta_{\mathcal{D}}} = 421$ sites, at $\log_{10} t \approx 4.72$ to $N_{\mathcal{D}, \delta_{\mathcal{D}}} = 521$ sites, at $\log_{10} t \approx 5.57$ to $N_{\mathcal{D}, \delta_{\mathcal{D}}} = 621$ sites, at $\log_{10} t \approx 5.75$ to $N_{\mathcal{D}, \delta_{\mathcal{D}}} = 721$ sites, at $\log_{10} t \approx 6.34$ to $N_{\mathcal{D}, \delta_{\mathcal{D}}} = 821$ sites, and at time $\log_{10} t \approx 6.86$ reaching a total lattice size at the final time $t_f = 10^7$ of the integration $N_{\mathcal{D}, \delta_{\mathcal{D}}} = 921$ sites. Consequently, after increasing the dynamic lattice 6 times, we obtain the results

shown in Fig. 4.3(b) where the white areas at the edges indicate empty space i.e. lattice sites with norm per site $s = 0$. Further, it clearly appears from Figs. 4.3(a) and (b) that the spatiotemporal evolutions of the normalized norm distribution $\xi_l(t)$ (3.1) are practically the same. It is worth mentioning that the initial lattice size $N_{\mathcal{D},\delta_{\mathcal{D}}} = 321$ is much larger than the NM average localization volume (2.61) $\bar{V} \approx 21$ sites in this context.

In order to quantify the qualitative observations of the evolution of the norm distribution ξ_l (3.1) in Fig. 4.3, we plot the time evolution of the $m_2(t)$ (3.5) [panel (a) of Fig. 4.4] and $P(t)$ (3.6) [inset of panel (a) in Fig. 4.4] of ξ_l (3.1) for the fixed [(g)reen curve] and dynamic [(b)lue curves] lattice simulations. Both the m_2 and P of ξ_l are practically overlapping up to the largest simulation time $t_f = 10^7$. As in this work we are also interested in the evolution of the variational equations, we depict the time evolution of the second moment $m_2^D(t)$ (3.5) and participation number $P^D(t)$ (3.6) of the DVD ξ_l^D (3.25) as well as the values of the ftMLE $\Lambda(t)$ (3.21) in Figs. 4.4(b-c) for both the fixed [(g)reen curves] and dynamic [(b)lue curves] lattices computations of Fig. 4.3. We notice a good correspondence in magnitude of the values of the m_2^D and P^D between the two lattice types as they are randomly oscillating in the same range of m_2^D and P^D values. Further, the chaoticity of the reference orbit depicted in the initial condition used in Fig. 4.3 is well reported by the two type of simulations as the curves of the ftMLEs practically overlap. Finally, we analyze the CPU time T_C necessary to reach the final time of integration $t_f = 10^7$ [Fig. 4.4(d)]. Clearly, the dynamic lattice appears advantageous as the final CPU time is noticeably smaller on the logarithmic scale. More specifically, we calculate the gain factor

$$g = \frac{T_C^{(F)} - T_C^{(D)}}{T_C^{(F)}}, \quad (4.2)$$

with $T_C^{(F)}$ and $T_C^{(D)}$ being respectively the CPU time needed for the fixed and dynamics lattice simulations. In the example above, we obtain an improvement of approximately 20%, using $T_C^{(F)} \approx 5.5$ hours and $T_C^{(D)} \approx 4.43$ hours.

It is worth commenting a bit more on the bent nature of the curve of the CPU time for the dynamic lattice simulation. For the fixed lattice simulation, a fairly straight line is seen on the dependence of $\log_{10} T_C$ on the logarithmic time i.e. $\log_{10} t$. This is due to the fact that the lattice size remains fixed along the integration of the system's orbit. Thus the number of basic computer operations (addition, multiplication, and so on) necessary to evolve the equations of motion and the variational equations, as well as to compute all the observables of the phase space and tangent dynamics, remains constant for each integration time step τ . So the constant CPU time necessary for a single integration time step τ evolution adds up to the cumulative CPU time $\log_{10} T_C$ in the constant rate (or slope) seen on the (g)reen curve of Fig. 4.4(d). This is not the case for the dynamic lattice simulation. Indeed, the number of lattice sites is constantly increased, leading to an augmentation of the number of basic computer operations for the time evolution of the equations of motion and variational equations along with the calculation of observables of the phase space and tangent dynamics. Consequently, the CPU time needed for a single integration time step τ increases in time leading to a constant increase of the slope of the (b)lue curve in Fig. 4.4(d) which create the bending effects of the $\log_{10} T_C$ curve. Ultimately, there exists a time t where the CPU time of both lattice simulations overlap and no gain from using the dynamic lattice is visible.

Let us now discuss what happens when we change the value of the threshold $\delta_{\mathcal{D}}$ in Eq. (4.1). In Fig. 4.5, we perform simulations with the initial condition used in the example of Fig. 4.3. We use different parameter values of the norm per site threshold at the edge points $\delta_{\mathcal{D}}$ ranging from 10^{-8} to 10^{-12} . The result is depicted in Fig. 4.5. There, we plot the time evolution of $m_2(t)$ (3.5) of ξ_l (3.1) as observable of the evolution of the equations of motion [see Fig. 4.5(a)] and the ftMLE $\Lambda(t)$ (3.21) [see inset of Fig. 4.5(a)] for of the tangent dynamics with $\delta_{\mathcal{D}} = 10^{-8}$ [(b)lue curves], $\delta_{\mathcal{D}} = 10^{-10}$ [(g)reen curves], $\delta_{\mathcal{D}} = 10^{-12}$ [(r)ed curves] and the fixed lattice computation [(c)yan curves]. The evolutions of the $m_2(t)$ (3.5) and the $\Lambda(t)$ (3.21) practically overlap in all used cases, indicating a tendency to follow the same power law behaviors. In Fig. 4.5 (b), we depict the time evolution of the CPU time T_C needed for these simulations. Once again the fixed lattice takes a longer time to complete the integration compared to the dynamic lattice. In addition, dynamic lattice simulations with larger norm per site threshold $\delta_{\mathcal{D}}$ for the control of the endpoints take less time. Overall, a gain of $g \approx 27\%$, 24% , 15% respectively when $\delta_{\mathcal{D}} = 10^{-8}$, 10^{-10} and 10^{-12} are observed. The closeness of the gains in the case $\delta_{\mathcal{D}} = 10^{-8}$ and $\delta_{\mathcal{D}} = 10^{-10}$ is explained by the fact that the norm flows rather quickly at the boundaries, as the case used here belongs to the strong chaos spreading regime. A larger difference appears between the different $\delta_{\mathcal{D}}$ values when initial conditions are taken from the weak chaos spreading regime.

From what has been observed above, the overall idea of the dynamic lattices is to find the optimal lattice size for the numerical evolution of the Hamiltonian models (in the present context \mathcal{H}_{1D} (2.17) and \mathcal{H}_{2D} (2.20)) for a specific set of parameter values W , β , \mathcal{H}_{1D} (2.17), and \mathcal{S}_{1D} (3.1) realizing a specific level of accuracy $\delta_{\mathcal{D}}$ in capturing the evolution of a central initial wave packet excitation. Of course, the

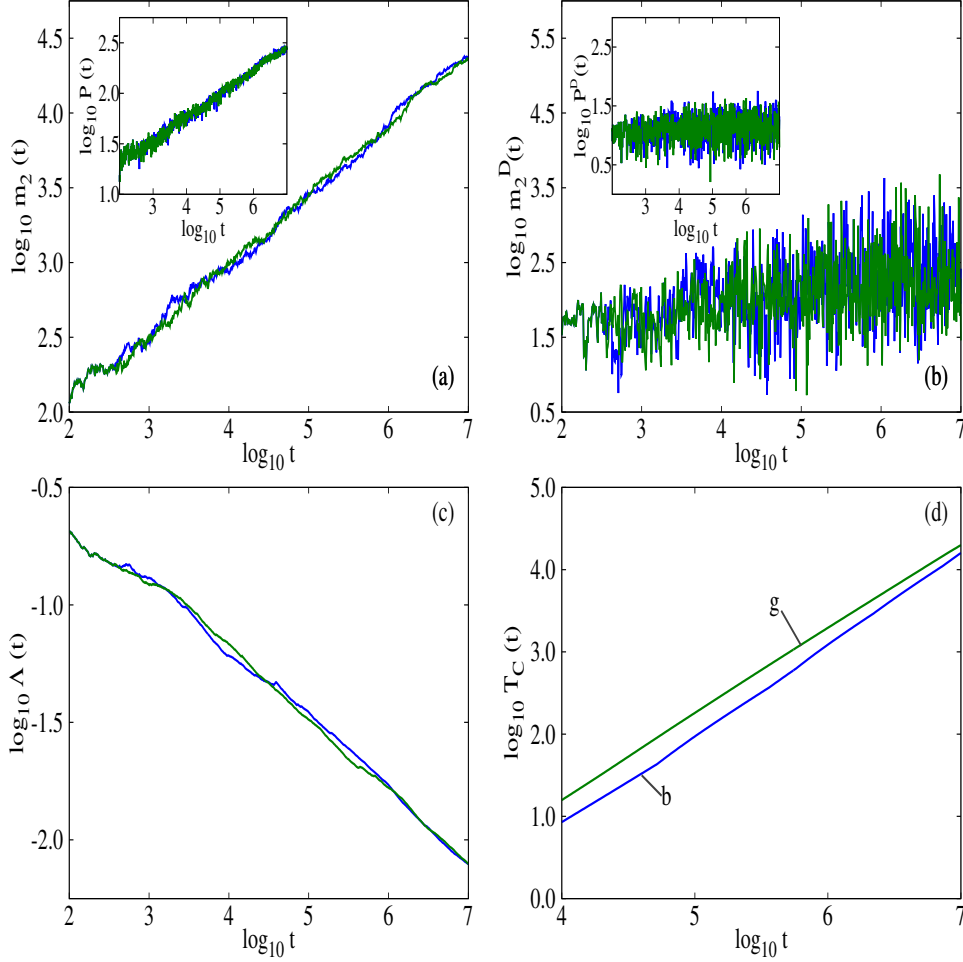


Figure 4.4: Results of the time evolution of the observables of the phase space and tangent dynamics of the case used in Fig. 4.3. The panel (a) presents the second moment $m_2(t)$ (3.5) and the participation number $P(t)$ (3.6) [inset of panel (a)] of the norm distribution ξ_l (3.1). The panel (b) shows the second moment $m_2^D(t)$ and participation number $P^D(t)$ [inset of panel (b)] of the DVD ξ_l^D (3.25). In panel (c) we see the ftMLEs $\Lambda(t)$ (3.21) and in panel (d) the required CPU time. The (g)reen curves are for the fixed and the (b)lue curves the dynamic lattice simulations.

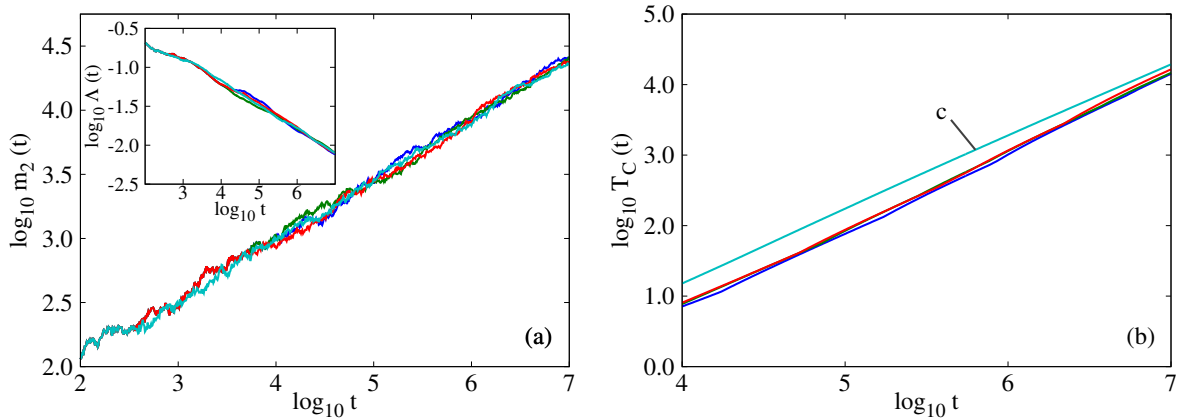


Figure 4.5: Similar to Fig. 4.4, but only the $m_2(t)$ (3.5) [panel (a)], the ftMLE $\Lambda(t)$ (3.21) [inset of panel (a)] and the CPU time $T_C(t)$ [panel (b)] are reported. The curve coloring corresponds to $\delta_{\mathcal{D}} = 10^{-8}$ [(b)lue], $\delta_{\mathcal{D}} = 10^{-10}$ [(g)reen], $\delta_{\mathcal{D}} = 10^{-12}$ [(r)ed] and the fixed lattice simulation [(c)yan]. See text for details.

smaller $\delta_{\mathcal{D}}$ is the larger lattice size we are going to need. In practice, our choice of $\delta_{\mathcal{D}}$ depends on the final values of the average norm per site attained in our longest simulations. In the case of the 1D DDNLS model, we are reaching a wave packet width $P_w \propto 10^3$ sites. Since the constant total norm $\mathcal{S}_{1D} \propto 10$ is shared among all the excited sites, the final average norm per site

$$s_f \propto \frac{\mathcal{S}_{1D}}{P_w} \sim 10^{-2} - 10^{-3}, \quad (4.3)$$

such that using

$$\delta_{\mathcal{D}} \sim 10^{-8}, \quad (4.4)$$

we capture the wave packet evolution with a rather good accuracy as shown in Fig. (4.4) up to our largest simulation time $t_f = 10^8$.

In order to avoid repetition, in all our numerical simulations, we consider for the 1D DDNLS system (2.17) initially localized wave packet excitations of size L at the center of a lattice whose maximal size reach in some cases $N \approx 5000$ sites in order to exclude effects from the lattice edges (i.e. in order to secure that the evolved wave packet does not reach the fixed edges). We give to each excited site a single oscillator frequency shift (or rescaled norm per site) $x = \beta s$ (2.68), where s is the constant norm at each site so that the total norm (2.19) is $\mathcal{S}_{1D} = \sum_{l \in L} s = Ls$ (or $\mathcal{S}_{1D} = Lx/\beta$, β being the nonlinear coefficient of the Hamiltonian \mathcal{H}_{1D} (2.17)). As mentioned in Sec. (4.2.1), for the initial DV $\mathbf{w}(0)$, we choose to excite only the δq_l and δp_l values of the site at the centre the lattice (it corresponds to DV₁ in Sec. 4.2.1) and ensure that the norm $\|\mathbf{w}(0)\| = 1$. Further we integrate the equations of motion and the variational equations using the SI *s11.ABC6* (3.84) of order 6 with an integration time step $\tau \approx 0.15 - 0.25$, always ensuring that the maximal relative energy (3.92) E_r and norm (3.1) S_r errors remain below 10^{-3} . Our typical final integration time is $t_f \approx 10^7 - 10^8$ time units. For all the considered realizations with $\beta > 0$ in the \mathcal{H}_{1D} (2.17), we set the same random parameter $\epsilon_l = 0$ at the lattice's centre. This ensures that all simulations of single (the central) site excitation ($L = 1$) results in the same energy value for the same initial norm per site s_l . On the other hand, in case of multi-site ($L > 1$) initial excitation, all the active sites receive the same value of the norm per site s_l (2.84) and we take particular care so the value of the corresponding \mathcal{H}_{1D} (2.17) is in a region belonging to the system's thermal phase [Flach, 2016; Kati et al., 2020] (see also Sec. 3.3).

4.3 The maximum Lyapunov exponent

4.3.1 The linear regime

Here, we look at the linear regime in the 1D DDNLS model (2.17). Its Hamiltonian corresponds to \mathcal{H}_L (2.1), or equivalently \mathcal{H}_{1D} (2.17) with the nonlinear coefficient $\beta = 0$. The theory in Sec. 2.1 tells us that no diffusion of initially localized excitations is present as AL prevails. In this situation, a saturation of the m_2 and P is observed once the wave packet extent reaches the border of the localization volume \bar{V} (2.14). This corresponds to equilibrium non-ergodic (regular) dynamics in the system's phase space where the trajectories belong to a torus associated with energy level E of the periodic motion $\psi_l = A_l e^{-iEt}$ at each site l (2.4) of the chain of oscillators. Thus no chaos is present and one expects the ftMLE $\Lambda(t) \propto t^{-1}$.

In Fig. 4.6, we plot the results of the time evolution of the $m_2(t)$ (3.5) and $P(t)$ (3.6) of the norm distribution ξ_l (3.1) as observables of the evolution of the equations of motion, and the ftMLE $\Lambda(t)$ (3.21) for the variational equations for a single site $L = 1$ excitation (we label this as case A1_{1D} for future reference) with a unit norm per site i.e. $s = 1$ at the center of a lattice of size $N = 1021$ sites. The energy $\mathcal{H}_{1D} = 1$ is obtained from the disorder realization we used, with parameters $W = 4$ and $\beta = 0$. In panel (a) of Fig. 4.6, we depict the obtained evolution of $m_2(t)$ (3.5) [(blue) curve], and $P(t)$ (3.6) [(green) curve]. We see that the $m_2(t)$ and $P(t)$ saturate as their values randomly oscillate around their the means $\bar{m}_2 \approx 32$ [upper black line in Fig. 4.6(a)] and $\bar{P} \approx 8$ [lower black line in Fig. 4.6(a)] rather quickly ($\log_{10} t \approx 1$). In panel (b) of Fig. 4.6, we show the evolution of the ftMLE $\Lambda(t)$ (3.21). A clear behavior $\Lambda(t) \propto t^{-1}$ is visible as the (blue) curve in Fig. 4.6(b) has the tendency to lay along the black straight line whose slope is -1 . This was also reported for the DKG of harmonic oscillators [see e. g. Skokos et al., 2013]. Next, we inch up the nonlinearity β in \mathcal{H}_{1D} (2.17) and numerically investigate the fate of the wave packet's localization.

4.3.2 The weak chaos regime

So far, the results predicted in Chap. 2 regarding the spreading of a nonlinear localized excitation in the 1D DDNLS model (2.17) appear to be accurately reproduced by numerical simulations. Indeed, the

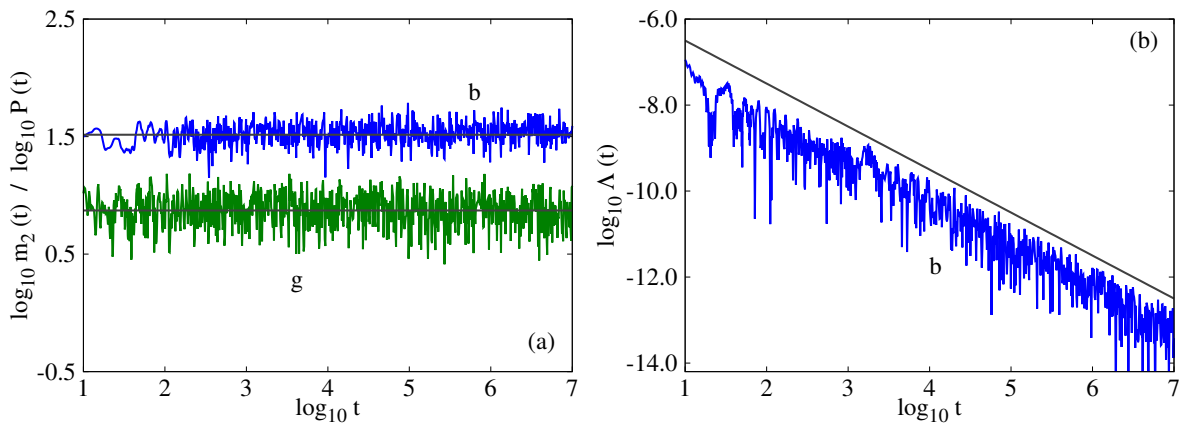


Figure 4.6: The time evolution of the second moment $m_2(t)$ (3.5) [(b)lue curve in panel (a)], the participation number $P(t)$ (3.6) [(g)reen curve in panel (a)] of the norm density distribution ξ_l (3.1). The related ftMLE $\Lambda(t)$ is shown in panel (b) for a representative of case $A1_{1D}$ (see text for details). The black lines in panel (a) guide the eye for zero slopes along the observable's mean values ≈ 32 for the m_2 [upper black line] and ≈ 8 [lower black line] for P respectively. In addition, the one in panel (b) guides the eye for slope -1 .

first numerical experiments performed in [Flach et al., 2009] were a complete success in confirming these predictions. Furthermore, the observation of two distinct power laws of wave packet expansion during the spreading was extensively studied in [Skokos et al., 2009; Flach, 2010; Lapyteva et al., 2010; Bodyfelt et al., 2011a,b; Lapyteva, 2013] with the crossover from the strong to weak chaos spreading characteristics also reported in [Lapyteva et al., 2010]. Here we present the results of the numerical investigation of the chaotic dynamics of the wave packet spreading within the weak chaos regime. In particular we focus on the following cases:

- **Case $W1_{1D}$.** $W = 3$, $\beta = 0.03$, $L = 21$ and $x = 0.03$.
- **Case $W2_{1D}$.** $W = 3$, $\beta = 0.6$, $L = 1$ and $x = 0.6$.
- **Case $W3_{1D}$.** $W = 4$, $\beta = 1$, $L = 1$ and $x = 1$.
- **Case $W4_{1D}$.** $W = 4$, $\beta = 0.04$, $L = 21$ and $x = 0.04$.

We can justify the choice of these parameters based on the first condition of Eq. (2.56). Indeed, a multisite excitation is expected to evolve in the the weak chaos regime whenever

$$x \frac{L}{\bar{V}} < d. \quad (4.5)$$

where $x = \beta s$ (2.68) is the rescaled average norm per site, \bar{V} (2.14) is the average localization volume and d (2.16) is the average spacing between frequencies in a NM volume. In Table 4.1, we give the various values of d (2.16), \bar{V} (2.14), and Δ (2.15) the frequency bandwidth of NMs for the different disorder strength W values of the 1D DDNLS Hamiltonian model \mathcal{H}_{1D} (2.17) we are using in this chapter. Applying the condition (4.5) in case $W1_{1D}$, we see that $xL/\bar{V} = 0.03 \cdot 21/37 \approx 0.017$ which is one order of magnitude smaller than the value of $d = 0.2$ indicated in Table 4.1. For the case $W4_{1D}$, the same calculation leads to the number $0.04 \cdot 21/21$ which is again much smaller than $d = 0.39$ of $W = 4$ in Table 4.1. In the case of single excitation wave packet, it is the first condition of inequality (2.57)

$$x < \Delta, \quad (4.6)$$

which governs the weak chaos spreading dynamics appearance. For the case $W2_{1D}$ the inequality (4.6) gives $0.6 < 7$, while in the case $W3_{1D}$ we obtain $1 < 8$, both of which are true. It is worth mentioning that the cases $W1_{1D}$, $W2_{1D}$, $W3_{1D}$ and $W4_{1D}$ have already been used in several works [Lapyteva et al., 2010; Bodyfelt et al., 2011a; Senyange and Skokos, 2018; Senyange et al., 2018]. In all the cases, we are averaging our observables of the phase space and tangent dynamics over 100 disorder realizations in order to obtain a robust representation of the system's dynamical behavior which takes into account several trajectories of the same total norm \mathcal{S}_{1D} (3.1).

The fact that all these cases belong to weak chaos becomes evident in Fig. 4.7(a) and (b), where we plot the time evolution of the second moment $m_2(t)$ (3.5) and the participation number $P(t)$ (3.6) of the norm density distribution ξ_l (3.1) respectively. For both quantities, a subdiffusive spreading is

NM properties	$W = 3$	$W = 3.5$	$W = 4$
\bar{V}	37	27	21
Δ	7	7.5	8
$d = \Delta/\bar{V}$	0.2	0.28	0.39

Table 4.1: Average localization volume \bar{V} (2.14), frequency bandwidth Δ (2.15) and average spacing between NM d (2.16) in case of a multisite excitation of width $L = \bar{V}$ sites at the center of the 1D DDNLS lattice system (2.17).

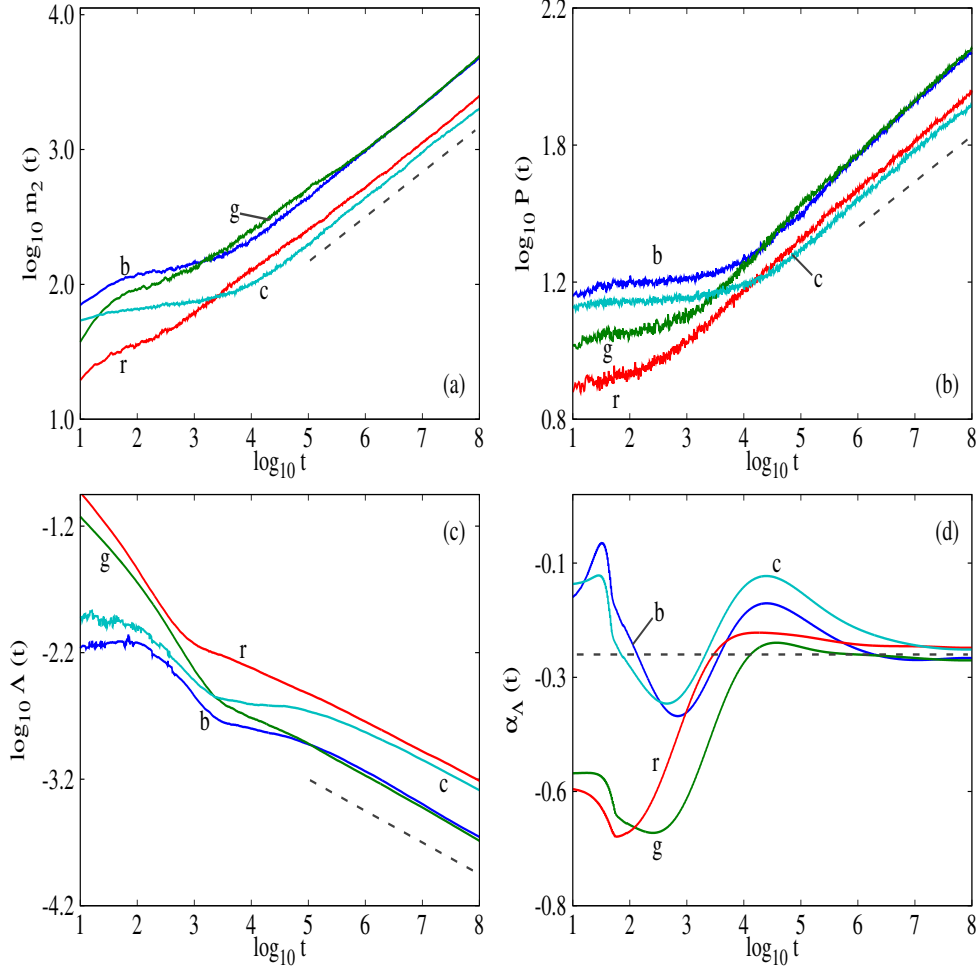


Figure 4.7: Time dependence of the second moment $m_2(t)$ (3.5) [panel (a)], the participation number $P(t)$ (3.6) [panel (b)] of ξ_l (3.1), the ftMLE $\Lambda(t)$ (3.21) (c) and $\alpha_\Lambda(t)$ (3.27) [panel (d)] for the weak chaos cases W_{1D} [(b)lue], W_{2D} [(g)reen], W_{3D} [(r)ed] and W_{4D} [(c)yan] (see text for details). The black dashed lines guide the eye for slopes $1/3$ [panel (a)], $1/6$ [panel (b)] and -0.25 [panel (c)]. The horizontal dashed black line in panel (d) indicates the value $\alpha_\Lambda = -0.25$.

noticeably well fitted by the monotonic asymptotic power laws $m_2(t) \propto t^{\alpha_m}$ [see black line in Fig. 4.7(a)] with $\alpha_m = \frac{1}{3}$ and $P(t) \propto t^{\alpha_P}$ [see black line in Fig. 4.7(b)] where $\alpha_P = \frac{1}{6}$ in agreement with previous works [Flach et al., 2009; Skokos et al., 2009; Lapyteva et al., 2010; Flach, 2010; Bodyfelt et al., 2011a]. Further, in Fig. 4.7(c) we present the time evolution of the ftMLE, $\Lambda(t)$ (3.21) which is the primary quantity of our interest. An asymptotic decay following the power law $\Lambda \propto t^{\alpha_\Lambda}$ ($\alpha_\Lambda < 0$) is observed for all cases. In Fig. 4.7(d), we present the time evolution of the related power law exponent $\alpha_\Lambda(t)$ computed following the techniques presented in Sec. 3.5. The dependence on time of the power law exponent values $\alpha_\Lambda(t)$ shows a clear tendency to saturate at $\alpha_\Lambda \approx -0.25$ in agreement with [Skokos et al., 2013; Senyange et al., 2018]. This number is retrieved in this work taking the average value of all the cases in the last decade of the evolution of $\alpha_\Lambda(t)$. These results are not only specific to the 1D DDNLS model, as they have also been found for the 1D DKG model of anharmonic oscillators (2.24) in [Skokos et al., 2013; Senyange et al., 2018].

4.3.3 The strong chaos regime

We also examine the strong chaos regime of the 1D DDNLS system (2.17). We use the following initial localized wave packet excitations:

- **Case S1_{1D}**. $W = 3$, $\beta = 1$, $L = 37$ and $x = 0.3$.
- **Case S2_{1D}**. $W = 3.5$, $\beta = 0.62$, $L = 21$ and $x = 0.62$.
- **Case S3_{1D}**. $W = 3.5$, $\beta = 0.72$, $L = 21$ and $x = 0.72$.
- **Case S4_{1D}**. $W = 3.5$, $\beta = 1$, $L = 27$ and $x = 0.525$.

Again, we justify the clustering of these initial parameter in the strong chaos spreading regime applying the second condition in Eq. (2.56). It states that if

$$x \frac{L}{V} > d, \quad (4.7)$$

the initial wave packet excitation will evolve for a finite amount of time within the strong chaos region of Fig. 2.6. As we did in the case of weak chaos, we numerically check the condition (4.7) on the parameter values above. For the case S1_{1D} the left hand side of inequality (4.7) results in $0.3 \cdot 37/37 = 0.3$, which is larger than $d = 0.2$ of $W = 3$. For the cases S2_{1D}, S3_{1D} and S4_{1D} which all use the value $W = 3.5$, we calculate the left hand side of Eq. (4.7) as $0.62 \cdot 21/27 \approx 0.482$, $0.72 \cdot 21/27 = 0.56$ and $0.525 \cdot 27/27 = 0.525$ respectively which are all greater than $d = 0.28$ in Table 4.1. Thus all the cases above belong to the strong chaos regimes according to the theory of Chap. 2. Note that the cases S2_{1D} and S3_{1D} were used in [Senyange et al., 2018], while we introduce the cases S1_{1D} and S4_{1D} in order to investigate other initial conditions than the ones already presented in the literature [Laptyeva et al., 2010; Bodyfelt et al., 2011a; Senyange et al., 2018]. Like for the weak chaos regime, we average our observables of the phases space and tangent dynamics over 100 disorder realizations in order to ensure the mixing of several different trajectories with constant \mathcal{S}_{1D} values in the system's phase space in order to ensure the robustness of our computations.

The panels of Figs. 4.8(a) and (b) depict the evolution of the wave packet second moment $m_2(t)$ (3.5) and participation number $P(t)$ (3.6) respectively. Again, a subdiffusive spreading of the wave packet initial excitation following the power laws $m_2(t) \propto t^{\alpha_m}$ and $P(t) \propto t^{\alpha_P}$ with $\alpha_m, \alpha_P < 1$ is clearly visible. This time the growth rates are well fitted by $\alpha_m = \frac{1}{2}$ [see black curve in Fig. 4.8(a)] and $\alpha_P = \frac{1}{4}$ [see black curve in Fig. 4.8(b)] in a region of around the early stages of the time evolution i.e. $\log_{10} t \approx 10^3 - 10^6$. This numerically confirms our choice of these cases as strong chaos ones. We can therefore compute the ftMLEs of all these strong chaos cases in Fig. 4.8(c). There, a similar tendency $\Lambda(t) \propto t^{\alpha_\Lambda}$ ($\alpha_\Lambda < 0$) to the one noticed for the weak chaos cases is seen for all the used cases. Nevertheless, the $\alpha_\Lambda(t)$ values tend to saturate at $\alpha_\Lambda \approx -0.3$ as shown in Fig. 4.8(d). Again, this value is obtained averaging the data of the time evolution of $\alpha_\Lambda(t)$ in the last decade of the evolution where the saturation is observed. It is worth mentioning that once again the same results have also been found for the 1D DKG model (2.24) [Senyange et al., 2018] underlining the generality of this power exponent.

4.4 The deviation vector distribution

There is a need of a second ingredient, a non-correlated spatiotemporal force $f(t)$ acting on the chaotic fraction of the system's NMs evolution as seen in Eq. (2.105) in order to obtain the chaotic spreading of the wave packet. These random fluctuations of chaotic seeds are known to support the subdiffusive spreading of the lattice's excited part [Flach et al., 2009; Skokos et al., 2013]. We have been stressing in Sec. 3.4.2 and in the first part of this chapter that the DV used for the computation of the MLE aligns with the most chaotic direction intrinsic to a system's orbit in its phase space. Therefore, the DVD (3.25)

$$\xi_l^D(t) = \frac{\delta q_l^2(t) + \delta p_l^2(t)}{\sum_l \delta q_l^2(t) + \delta p_l^2(t)}, \quad (4.8)$$

can be used to represent sites which are more sensitive to perturbation at time $t > 0$. Consequently, it can be used to visualize the motion of chaotic seeds [Oganesyan et al., 2009; Basko, 2011, 2012; Mulansky, 2014; Skokos et al., 2013; Senyange et al., 2018; Many Manda et al., 2020]. In this section, we analyse in depth the dynamical behavior of the DVD in the AL, weak chaos and strong chaos regimes of the initially localized wave packet excitation in the 1D DDNLS lattice system (2.17).

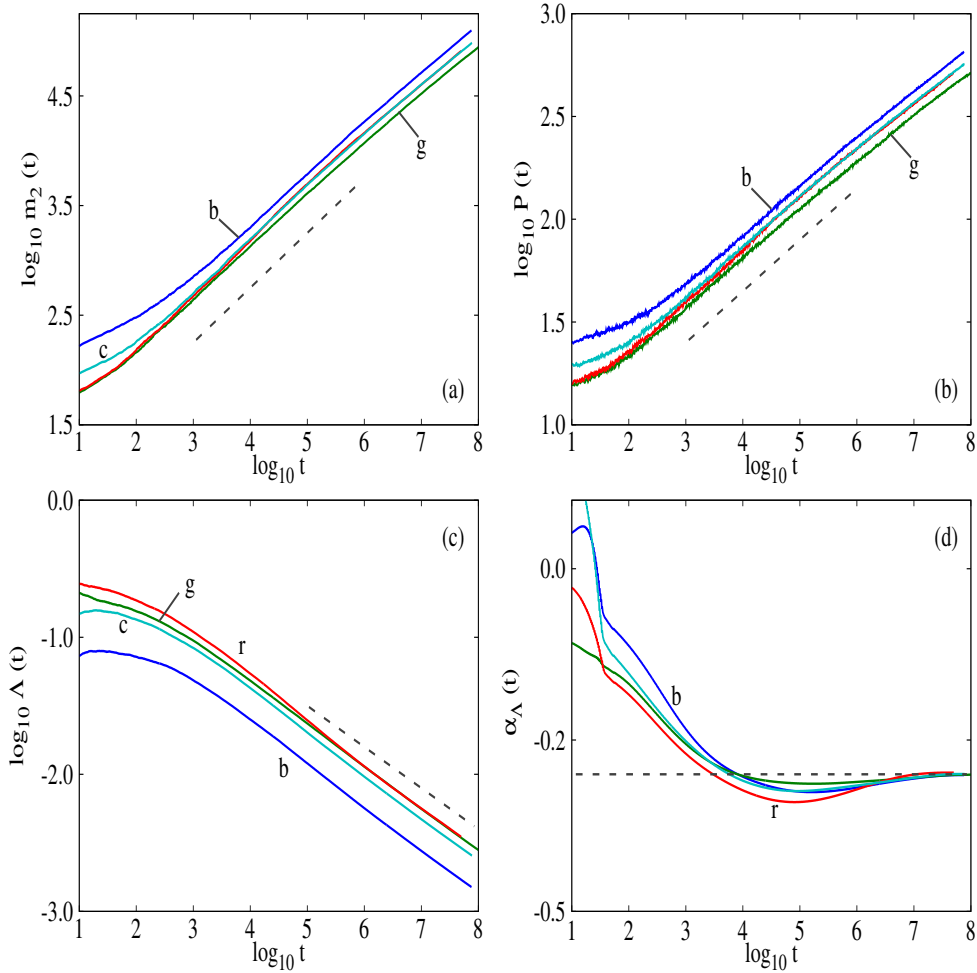


Figure 4.8: Similar to Fig. 4.7 but for strong chaos regime. The coloring corresponds to the cases $S1_{1D}$ [(b)lue], $S2_{1D}$ [(g)reen], $S3_{1D}$ [(r)ed] and $S4_{1D}$ [(c)yan] (see text for details). The straight lines guide the eye for slopes $\frac{1}{2}$ [panel (a)], $\frac{1}{4}$ [panel (b)] and -0.3 [panel (c)]. The horizontal dashed line in panel (d) indicates the value $\alpha_\Lambda = -0.3$.

4.4.1 The linear regime

Let us first look more closely to the behavior of the norm density distribution $\xi_l(t) = s_l(t)/\sum_l s_l(t)$ (3.1) with $s_l = (q_l^2 + p_l^2)/2$ and the DVD ξ_l^D (3.25) generated during the computation of the ftMLE $\Lambda(t)$ (3.22) when nonlinearity is absent from the system's dynamical equations i.e. $\beta = 0$ in \mathcal{H}_{1D} (2.17). We use the case $A1_{1D}$ of Fig. 4.6. For this case, we compute the spatiotemporal evolution of the norm distribution $\xi_l(t)$ and the DVD $\xi_l^D(t)$ in Figs. 4.9(a) and (b) respectively. For both distributions, snapshots at specific times $\log_{10} t \approx 5.6$ [(b)lue dashed line in Figs. 4.9(a) and (b)], $\log_{10} t \approx 6.65$ [(g)reen dashed line in Figs. 4.9(a) and (b)] and $\log_{10} t \approx 7$ [(r)ed dashed line in Figs. 4.9(a) and (b)] are displayed in Figs. 4.9(c) and (d) respectively for the ξ_l and ξ_l^D .

With $\xi_l(t)$ (3.1), a clear spatial saturation of the wave packet extents appears in Figs. 4.9(a) and (c), in agreement with the saturation of the wave packet $m_2(t)$ and $P(t)$ noticed in Fig. 4.6(a). For ξ_l^D (3.25) in Figs. 4.9(b) and (d) a saturation of its spatial evolution is also present. Further, a striking resemblance between the distributions ξ_l and ξ_l^D in Fig. 4.9 is visible. This is explained by the fact that if one computes the variational equations of the 1D DDLS model (2.1), we obtain

$$i\delta\dot{\psi}_l = \epsilon_l\delta\psi_l - (\delta\psi_{l-1} + \delta\psi_{l+1}), \quad (4.9)$$

whose solutions are oscillatory motion of the form $\delta\psi_l = \delta A_l \exp iEt$ which oscillates in the same manner as the system's reference orbit $\psi_l = A_l \exp iEt$ which resolves the equations of motion of \mathcal{H}_L (2.1) having the same form to (4.9). Consequently, both the $\xi_l(t)$ and $\xi_l^D(t)$, are expected to depict qualitatively the same spatiotemporal dynamics. These properties are expressions of the regularity (non-ergodicity) of the system's phase space in the linear regime and tell us that an initial condition taken a bit further away from the system's reference orbit will also experience AL as seen in Sec. 2.1.

Our observations, on the spatial evolution of the DVD (3.25) are confirmed in Fig. 4.10(a) and (b) where we plot the time evolution of the DVD's second moment $m_2^D(t)$ [see Fig. 4.10(a)] and participation

number $P^D(t)$ [see Fig. 4.10(b)] of ξ_l^D (3.25). Indeed, a clear saturation of the m_2^D [panel (a) of Fig. 4.10] and the P^D [panel (b) of Fig. 4.10] is seen, indicative of a halt of the DVD $\xi_l^D(t)$ (4.8). Note that in Fig. 4.10 the (b)lue curves corresponds to the case A1_{1D} of Figs. 4.6 and 4.9, while the (g)reen one (Case A2_{1D}) is the same condition but this time obtained with $W = 3$ in order to stress the general nature of these findings. The curves represent averages over 48 disorder realizations in order to obtain a robust representation of the behavior of the tangent dynamics in case of regular motion (we do this because of the stochasticity of the random disorder parameters).

In [Skokos et al., 2013], it was shown that the DVD oscillates inside the wave packet extent with increasing amplitudes. In order to capture this dynamical behavior, in this work we also investigate the spatiotemporal evolution of the center $\bar{l}^D(t) = \sum_l l \xi_l^D(t)$ of the DVD (3.25) by computing

$$R(t) = \max_{[0,t]} \{\bar{l}^D(t)\} - \min_{[0,t]} \{\bar{l}^D(t)\}, \quad (4.10)$$

which measures the distance between the two extreme positions reached by $\bar{l}^D(t)$ at time $t > 0$. Thus, $R(t)$ (4.10) measures the total size of the region visited by the DVD's center along its evolution. If the \bar{l}^D is fixed in time then $\max_{[0,t]} \{\bar{l}^D(t)\} = \min_{[0,t]} \{\bar{l}^D(t)\}$, so that

$$R(t) = 0. \quad (4.11)$$

This situation is highly improbable as small oscillations of the DVD center can appear due to numerical fluctuations. In the present case, we say that whether the $R(t)$ has a tendency to saturate to values smaller or comparable to the localization volume \bar{V} (2.14) i.e.

$$R \lesssim \bar{V}, \quad R(t) \sim t^0, \quad (4.12)$$

we conclude that the DVD center $\bar{l}^D(t)$ is practically fixed in time. Notice that Eq. (4.12) implies that no motion of the DVD center outside the initially excited region is observed, leading to no thermalization of more lattice's sites (or modes). On the other hand, if

$$R(t) > \bar{V}, \quad (4.13)$$

after a certain time t , then we can distinguish between two cases. (i) A saturation of the values of R take place i.e. $R(t) \sim t^0$, or (ii) we observe a consistent monotonic increasing tendency of $R(t)$ such that after

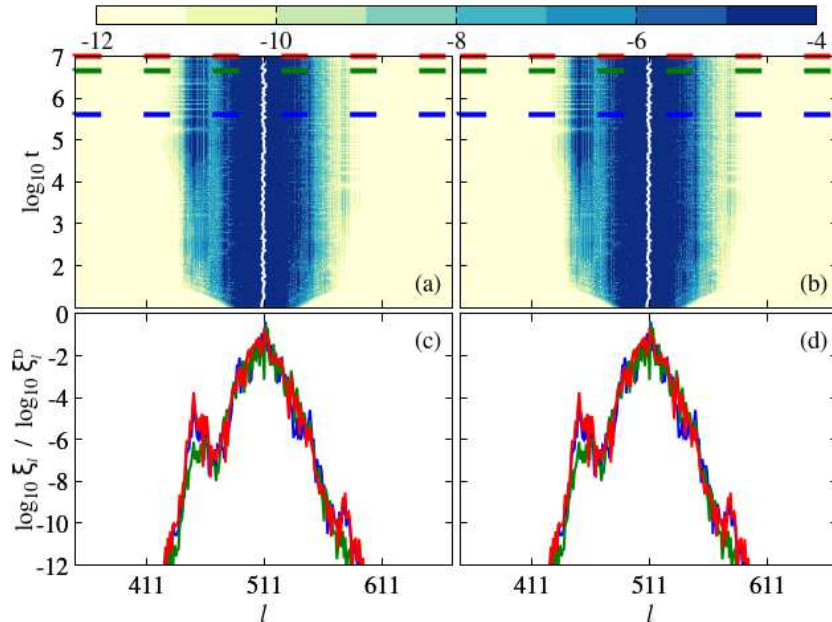


Figure 4.9: Spatiotemporal dependence of the norm density distribution ξ_l (3.1) and DVD ξ_l^D (4.8) for a representative case A1_{1D} (see text for details) of the linear regime. The color scales at the top of the figure are used for coloring the lattice sites according to their $\log_{10} \xi_l$ [panel (a)] and $\log_{10} \xi_l^D$ [panel (b)] values. In both panels, the white curves represent the motion of the distribution's centers. The panels (c) and (d) show snapshots of the spatial dependence of the distributions ξ_l and ξ_l^D respectively at times $\log_{10} t \approx 5.6$ [(b)lue curves], $\log_{10} t \approx 6.65$ [(g)reen curves] and $\log_{10} t \approx 7$ [(r)ed curves]. These times are also indicated using the same coloring for the dashed horizontal lines in panels (a) and (b).

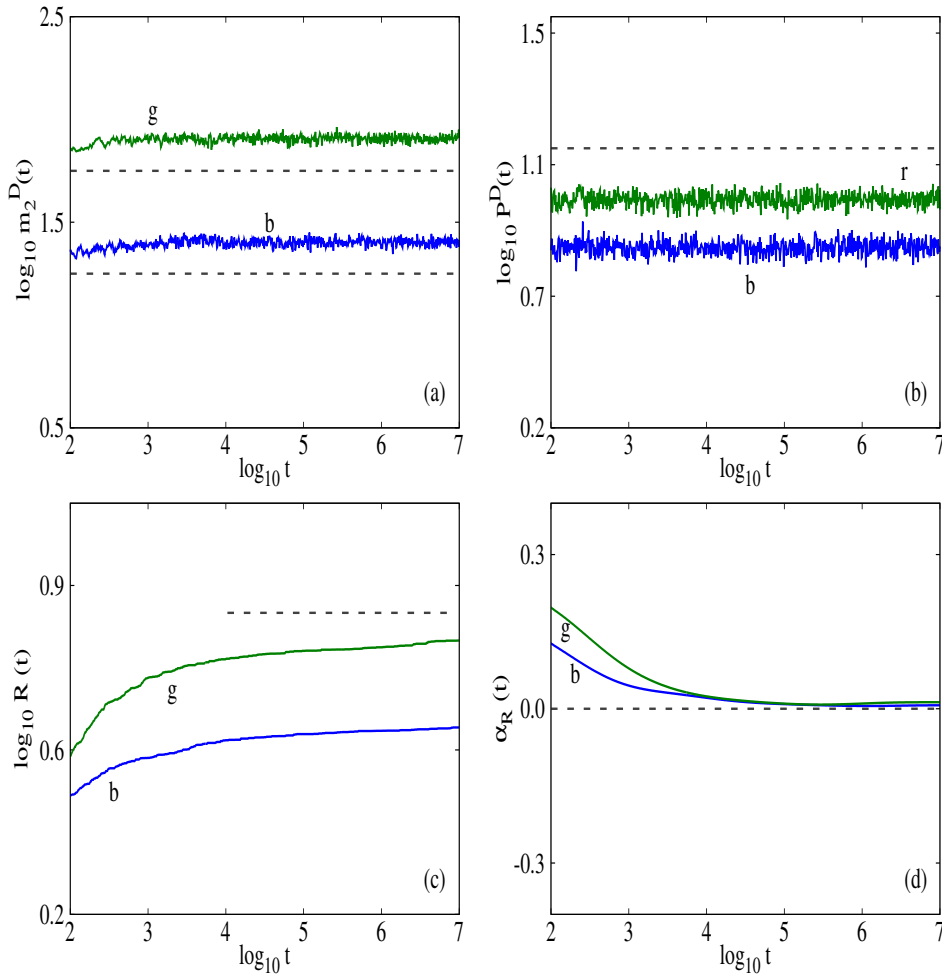


Figure 4.10: Time dependence of the second moment $m_2^D(t)$ (3.5) in panel (a), participation number $P^D(t)$ (3.6) in panel (b) of ξ_l^D (3.25). In panel (c) we plot the length covered by the distribution's center $R(t)$ (4.10), while in panel (d) we show the related power law exponent α_R when R is fitted by $R \propto t^{\alpha_R}$ at every point of its evolution. The (b)lue curves correspond to case $A1_{1D}$ and the (g)reen ones to case $A2_{1D}$ of the linear regime (see text for details). The horizontal lines in panels (a), (b) and (c) guide the eye for slope 0. Similarly, the horizontal dashed line in panel (d) indicates the value $\alpha_R = 0$. The results of panels (a), (b) and (c) are averaged over 48 disorder realizations.

a certain time $R \gg \bar{V}$. In the case (i) the DVD visited the neighboring modes of the initially excited one, therefore a wave packet expansion takes place in one of the regimes mentioned above and then slow down up to a complete halt after a certain amount of time, restoring the AL into the system. This situation, corresponds to the predictions of [Johansson et al., 2010; Aubry, 2011; Mulansky et al., 2011; Pikovsky and Fishman, 2011]. On another hand, the case (ii) means that the DVD's center is visiting sites far from the initially excited ones. This is the indication of an infinite spreading of the wave packet into the system and corresponds to situations mentioned in [Shepelyansky, 1993; Pikovsky and Shepelyansky, 2008; Flach, 2010; Lapyteva et al., 2010, 2012].

Figure 4.10(c) shows the evolution of the $R(t)$ (4.10) of the center of the DVD \bar{l}^D for the initial conditions $A1_{1D}$ [(b)lue curve] and $A2_{1D}$ [(g)reen curve] used above. A clear tendency to saturate a value $R(t) \approx 3$ for the case $A1_{1D}$ and $R(t) \approx 5$ in case of $A2_{1D}$ is seen. These values are much smaller than the localization volume $\bar{V} = 21$ and 37 respectively for the values $W = 4$ and $W = 3$. Further, we assumed that the behavior of $R(t)$ can be fitted with a functional form

$$R(t) \propto t^{\alpha_R}, \quad (4.14)$$

and plotted the time evolution of the power law exponent $\alpha_R(t)$ in Fig. 4.10(d), where a clear tendency to converge to values $\alpha_R \approx 0$ is seen, supporting the fact that the center of the DVD [see white curve in Fig. 4.9(b)] remains practically fixed in Figs. 4.9(b) and (d). Therefore, no modes' chaotic heating take place as expected in the linear regime of disordered systems. Note that the value $\alpha_R \approx 0$ was calculated averaging the slopes $\alpha_R(t)$ of the cases $A1_{1D}$ and $A2_{1D}$ over the last decade of evolution.

4.4.2 The weak chaos regime

Let us now look at the dynamical behavior of the DVD (3.25) in the case $\beta > 0$ for the 1D DDNLS model with Hamiltonian \mathcal{H}_{1D} (2.17). In Fig. 4.11(a), we sketch the time evolution of the norm density distribution ξ_l (3.1) along with its related DVD ξ_l^D (4.8) in Fig. 4.11(b) for an individual realization of the weak chaos case $W_{4_{1D}}$. Snapshots of these distributions are presented at times $\log_{10} t \approx 4.8$ [(b)lue dashed horizontal line] $\log_{10} t \approx 6.82$ [(g)reen horizontal dashed line] and $\log_{10} t \approx 7.94$ [(r)ed dashed horizontal line] in Figs. 4.11(c) and (d).

From Figs. 4.11(a) and (c), we see that the norm density ξ_l is expanding smoothly and in a more or less symmetric way about the distribution center which remains (almost) fix at the position of the initial excitation [see white curve in Fig. 2.2(a)]. On the other hand, the DVD ξ_l^D (4.8) in Figs. 4.11(b) and (d) retains a rather localized character, especially compared to the norm extent. In addition, its centre \bar{l}^D [see the white curve in Figs. 4.11(b) and (d)] is randomly wandering inside the lattice excited part as suggested by the fuzziness of the white curve in Fig. 4.11(b). These random fluctuations increase in amplitude with time which becomes evident for $\log_{10} t \gtrsim 6$ where large excursions of the ξ_l^D centre are clearly visible.

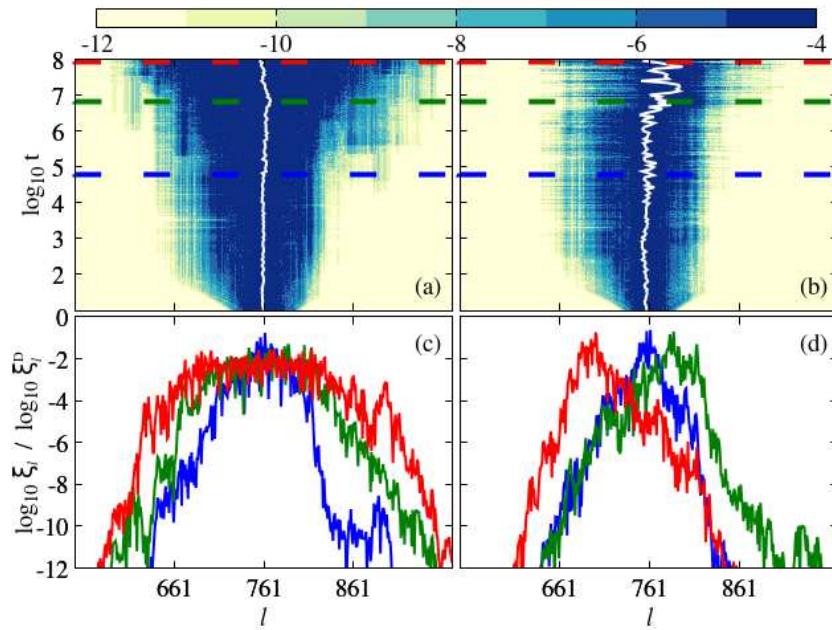


Figure 4.11: Spatiotemporal dependence of the norm density distribution ξ_l (3.1) and DVD ξ_l^D (4.8) for the representative case $W_{4_{1D}}$ (see text for details) of the weak chaos regime. The color scales at the top of the figure are used for coloring the lattice sites according to their $\log_{10} \xi_l$ [panel (a)] and $\log_{10} \xi_l^D$ [panel (b)] values. In both panels, the white curves represent the motion of the distribution's center. The panels (c) and (d) show snapshots of the spatial dependence of the distributions ξ_l and ξ_l^D respectively at times $\log_{10} t \approx 4.8$ [(b)lue curves], $\log_{10} t \approx 6.82$ [(g)reen curves] and $\log_{10} t \approx 7.94$ [(r)ed curves]. These times are also indicated using similar colors for the dashed horizontal lines in panels (a) and (b).

In order to validate our observations, we compute the evolution of the DVD's (3.25) second moment $m_2^D(t)$ (3.5) (see Fig. 4.12(a)) and participation number $P^D(t)$ (3.6) (see Fig. 4.12(b)) for all the weak chaos cases of Sec. 4.3.2. A growth of the $m_2^D(t)$ well fitted by the power law $m_2^D \propto t^{0.14}$ (see black line in Fig. 4.12(a)) is observed smaller than the $m_2(t) \propto t^{1/3}$ in the case of the ξ_l (3.1). In addition, the $P^D(t)$ slowly increases in all the studied cases following a timid power law $P^D \propto t^{0.04}$ in Fig. 4.12(b) and reaching values similar to the mode's localization volume \bar{V} (2.14) (in the cases $W_{1_{1D}}$ [(b)lue] and $W_{2_{1D}}$ [(g)reen] $P^D \approx 10^{1.3} \approx 20$) before showing a tendency to saturate at the last stages of the evolution in accordance to the localized character of the DVD observed in Figs. 4.11(b) and (d).

We also compute the size $R(t)$ (4.10) of the region visited by the centre of the DVD $\bar{l}^D(t) = \sum_l l \xi_l^D(t)$. The result is depicted in Fig. 4.12(c), where a monotonic increase of R with time is seen which attains values $R(t) \approx 10^2$, much larger than the NM localization volume. This increase is well fitted by an asymptotic power law $R \propto t^{\alpha_R}$ ($\alpha_R > 0$) where the evolution of $\alpha_R(t)$ is shown in Fig. 4.12(d). There, all the curves of the power law exponent $\alpha_R(t)$ exhibit a tendency to saturate to an estimated exponent $\alpha_R \approx 0.24$ (we averaged the $\alpha_R(t)$ of all the studied cases in the two last decades of their evolutions to obtain this value). This asymptotic value of the variations is reached at an early stage

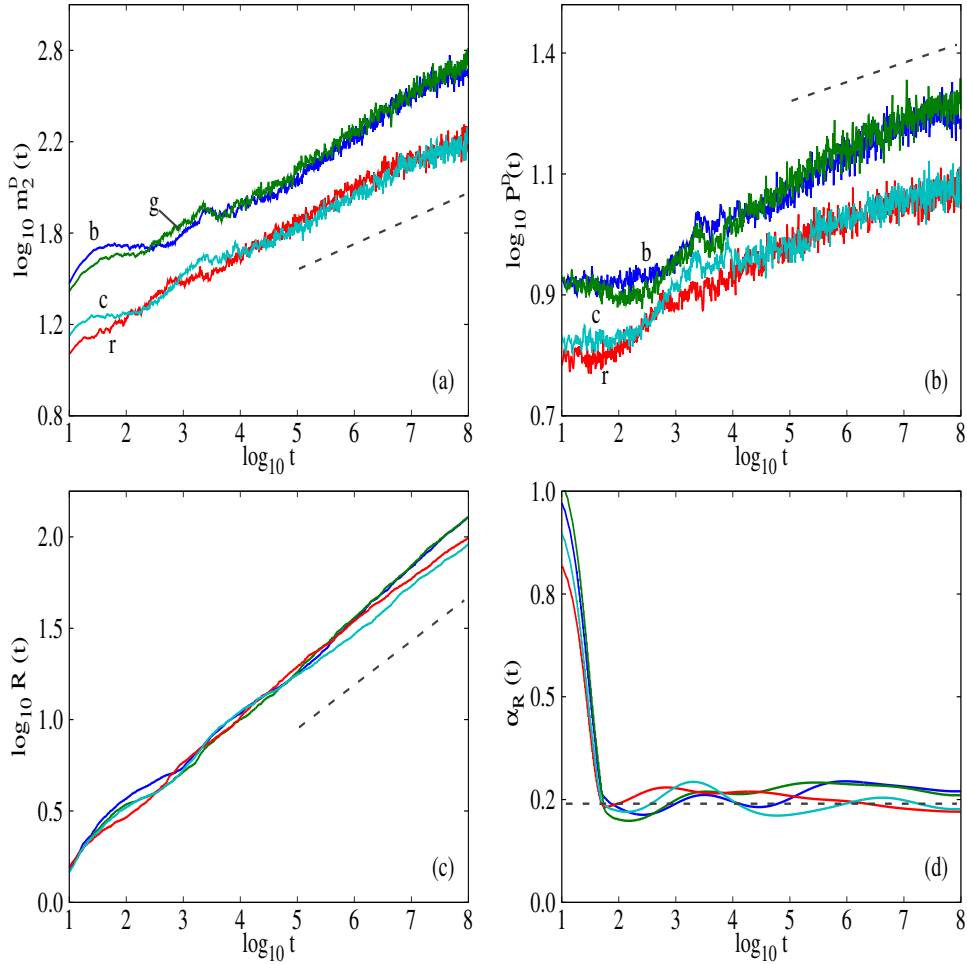


Figure 4.12: Results of the temporal dependence of the DVD's ξ_l^D (4.8) second moment m_2^D (3.5) in panel (a) and participation number P^D (3.6) in panel (b). Panel (c) shows the region R (4.10) visited by the distribution's center and in panel (d) we depict the power exponent α_R when the values of $R(t)$ are fitted with t^{α_R} . All results corresponds to the weak chaos regime of the 1D DDNLS system (2.17). The used initial wave packet parameters are for cases W_{1D} [(b)lue], W_{2D} [(g)reen], W_{3D} [(r)ed] and W_{4D} [(c)yan] (see text for details). The black lines in the panels (a), (b) and (c) guide the eye along the slopes 0.14, 0.04 and 0.24. The horizontal line in panel (d) indicates the value $\alpha_R = 0.24$ obtained averaging the two last decades of the evolution of $\alpha_R(t)$ for all the cases. The curves presented in panels (a), (b) and (c) show average results over 100 disorder realizations.

($\log_{10} t \approx 2$) of the evolution and persists for the remaining 6 decades of our numerical integration of the phase space and tangent space trajectories. Consequently, the fluctuations of the chaotic seeds exist from near the beginning of the evolution and sustain their growth along with the wave packet expansion. It is worth mentioning that the same results were found also for the 1D DKG model of anharmonic oscillators (2.24) in [Senyange et al., 2018].

4.4.3 The strong chaos regime

We also investigate the dynamical behavior of the DVD ξ_l^D (4.8) in the strong chaos region of Fig. 2.4 and 2.6. Here, we use a realization of the S_{3D} case as a representative of the strong chaos region dynamical behavior in Fig. 4.13. We plot the evolution of the norm density ξ_l (3.1) (see Fig. 4.13(a)), and its related DVD ξ_l^D (see Fig. 4.13(b)) along with snapshots of these distributions at specific times (see Figs. 4.13(c) and (d)) namely $\log_{10} t \approx 6$ [(b)lue horizontal lines], $\log_{10} t \approx 6.54$ [(g)reen horizontal lines] and $\log_{10} t \approx 7.24$ [(r)ed horizontal lines] in Figs. 4.13(a) and (b). Similar to what was observed for the weak chaos case in Fig. 4.11, the norm distribution expands rather smoothly and symmetrically around its center [the white curve in Fig. 4.13(a)]. The ξ_l spreads more widely compared to the weak chaos case in Fig. 4.11(a) as in this regime the wave packet spreads faster. On the other hand, the ξ_l^D exhibits a localized character [see Fig. 4.13(b)], with the distribution profile retaining a confined 'pointy' shape [see Fig. 4.13(d)]. In addition, we see that the centre of ξ_l^D randomly oscillates inside the wave

packet width [see the fuzziness of the white curve of Fig. 4.13(b) and the profile positions in (d)] with increasing amplitudes, moving faster and wider than in the weak chaos regime [see Figs. 4.11(b) and (d)].

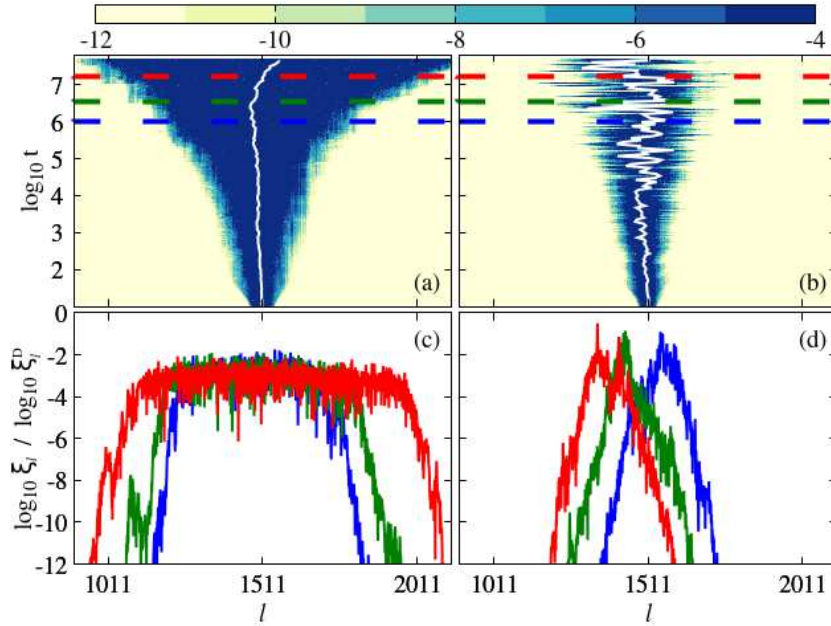


Figure 4.13: Spatiotemporal dependence of the norm density distribution ξ_l (3.1) and DVD ξ_l^D (4.8) for the representative case $S3_{1D}$ (see text for details) of the strong chaos regime. The color scales at the top of the figure are used for coloring the lattice sites according to their $\log_{10} \xi_l$ [panel (a)] and $\log_{10} \xi_l^D$ [panel (b)] values. In both panels, the white curves represent the motion of the center's distributions. The panels (c) and (d) show snapshots of the spatial dependence of the distributions ξ_l and ξ_l^D respectively at times $\log_{10} t \approx 6.0$ [(b) blue curves], $\log_{10} t \approx 6.53$ [(g) green curves] and $\log_{10} t \approx 7.23$ [(r) red curves]. These times are also indicated using similar colors for the dashed horizontal lines in panels (a) and (b).

We quantify these observations by computing the DVD's ξ_l^D (4.8) second moment $m_2^D(t)$ (3.5) [see panel (a) of Fig. 4.14] and participation number $P^D(t)$ [see panel (b) of Fig. 4.14] for all the strong chaos cases of Sec. 4.3.3. After a fast growth of the m_2^D and P^D values at the early stage of the evolution ($\log_{10} t \lesssim 5$), a tendency to saturate to a constant value is clearly visible for both quantities. For instance, we have fitted the last decades of evolution of the $P^D(t)$ with a power law $P^D(t) \propto t^a$ and obtained $a \approx 0$. It is worth mentioning that the number of highly excited sites reached by the ξ_l^D is $P^D \approx \bar{V}$ (for example $W1_{1D}$ gives $P^D \approx 10^{1.4} \approx 25$) which suggests that the DVD always remains confined in a single mode's localization volume at a time while moving around from site to site. These results support the pointy and concentrated profile seen in Figs. 4.13(b) and (d).

The evolution of the size $R(t)$ (4.10) of the region visited by the DVD center \bar{l}^D is depicted in Fig. 4.14(c). A clear monotonic increase is visible from the early stage of the evolution with $R(t)$ values reaching up to $R \approx 10^{2.8} \approx 700$ sites at the final time of the integration, several times larger than the average localization volume \bar{V} of a NM. The dependence of $R(t)$ on time can be fitted with a power law $R \propto t^{\alpha_R}$ with $\alpha_R > 0$. In Fig. 4.14(d), the evolution of the power law exponent $\alpha_R(t)$ is shown. We see that, in a large part of the dynamical evolution, the value of $\alpha_R(t)$ is always well above the ones observed for the weak chaos regime [black horizontal dashed line in Fig. 4.14 (d)]. Then, at later stages of the evolution ($\log_{10} t > 7$), the $\alpha_R(t)$ asymptotically converges to values $\alpha_R \approx 0.24$ seen in the weak chaos regime.

This transitional behavior is well in agreement with previous works [see e.g. Flach, 2010; Lapyteva et al., 2010; Skokos and Flach, 2010; Bodyfelt et al., 2011a]. Indeed, the fact that the R values reached in the weak chaos regime ($R \approx 10^2$) are smaller than the ones observed in the strong chaos case ($R \approx 10^3$) at the final time of our numerical integration is likely explained by the fact that the faster spreading in the strong chaos regime implies faster and wider wandering of chaotic seeds as a more rapid randomization and thermalization are required. In addition, because the strong chaos is a transient regime, an asymptotic crossover of the wave packet dynamics to the weak chaos regime should take place. This is what we see in Fig. 4.14(d) for example since the rate of growth of $R(t) \propto t^{\alpha_R}$ i.e. α_R is always larger for the strong chaos regime and converge to the α_R values seen in the weak chaos dynamical behavior at later stages. This numerically demonstrates that the nature of the chaotic dynamics cross over well before the wave

packet dynamics itself for which up to now a complete crossover of a strong chaos initial condition has never been reported in the literature [see e.g. [Laptyeva et al., 2010](#)]. It is worth noticing that the same behavior of the DVD in the strong chaos regime was retrieved also for the 1D DKG model in [[Senyange et al., 2018](#)].

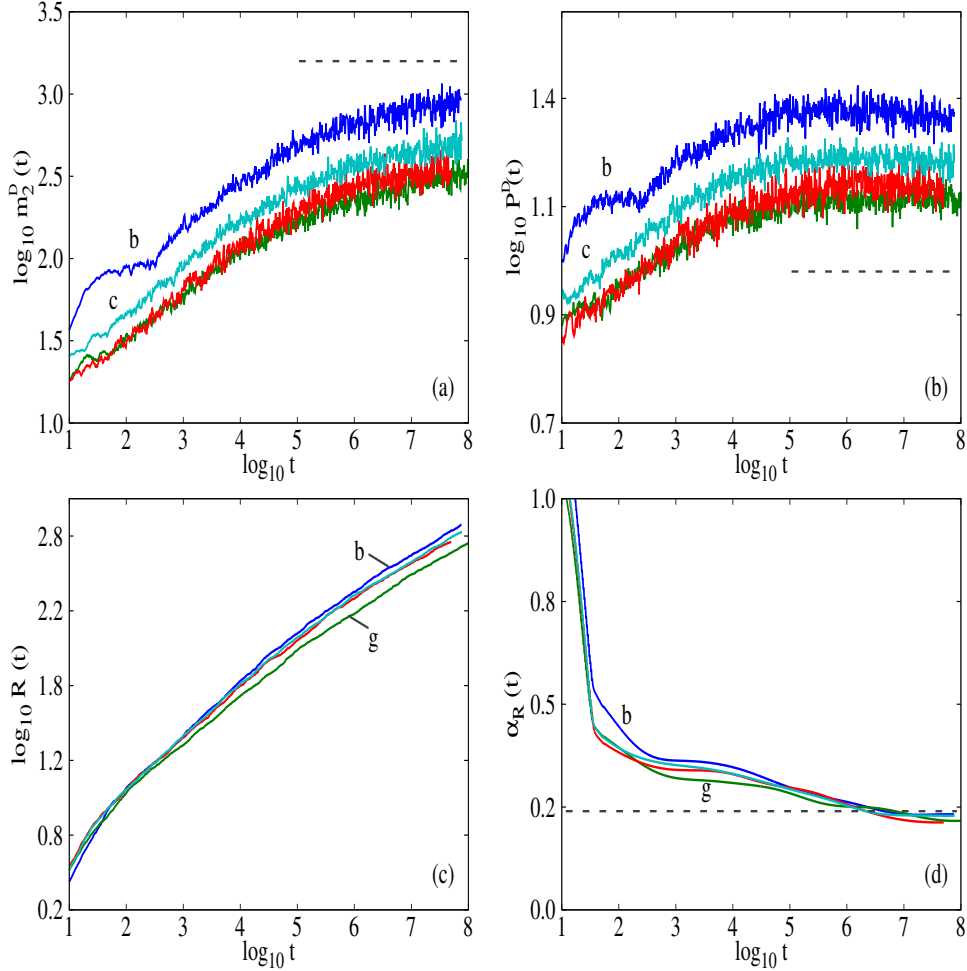


Figure 4.14: Results of the time dependence of the second moment m_2^D (3.5) in panel (a) and the participation number P^D (3.6) in panel (b) of the DVD ξ_t^D (4.8). The region visited by the distribution's center R (4.10) is in panel (c) and the power exponent α_R in panel (d) when the values of $R(t)$ are fitted with the relation t^{α_R} for the strong chaos regime. The used initial wave packet parameters are for cases S_{1D} [(b)lue], S_{2D} [(g)reen], S_{3D} [(r)ed] and S_{4D} [(c)yan] (see text for details). The black lines in the panels (a), (b) guide the eye for slope 0.0. The horizontal dashed line in panel (d) indicates the value $\alpha_R = 0.24$. The curves presented in panels (a), (b) and (c) show average results over 100 disorder realizations.

4.5 Discussion and summary

Let us now discuss the main implications of our results in this chapter. The outputs of the computation of the ftMLE $\Lambda \propto t^{-0.25}$ for the weak and $\Lambda \propto t^{-0.3}$ for the strong chaos spreading regimes are quite interesting. In studies of finite size multidimensional dynamical systems the chaotic dynamics show a plateau of the $\Lambda(t)$ values for chaotic trajectories (see e.g. [[Benettin et al., 1980](#); [Mithun et al., 2018](#); [Benettin et al., 2018](#); [Hillebrand et al., 2019](#); [Mithun et al., 2018](#); [Hillebrand et al., 2020](#)]), while quasi-periodic trajectories reveal a $\Lambda(t) \propto t^{-1}$ tendency [[Benettin et al., 1980](#); [Skokos, 2010](#)]. The results we are obtaining here can be interpreted in the following way. As the constant total norm S_{1D} (3.1) (energy \mathcal{H}_{1K} (2.24) for the 1D DKG model) is shared among more and more thermalized sites as additional degrees of freedom get activated, the average norm per site s (2.68) of the excited part decreases in time. Therefore both the single oscillator nonlinear frequency shift $\delta \propto \beta s$ [used for example in the the Chirikov criterion 2.34] and the *effective* nonlinear strength $\propto \beta s^2$ [present for example in the equations of motion (2.18) and (2.105)] decay in time, taking the system closer to the integrable limit. While one may expect a cross over to quasi-periodic (regular) motion as speculated in [[Johansson et al.,](#)

2010; Aubry, 2011], this is never the case, as the exponents of the power law $\Lambda \propto t^{\alpha_\Lambda}$ with $\alpha_\Lambda < 0$ are $\alpha_\Lambda = -0.25$ (weak chaos) and $\alpha_\Lambda = -0.3$ (strong chaos) which are different from the value $\alpha_\Lambda = -1$ seen in the case of regular motion [see for example Fig. 4.6(b)]. Thus, our results suggest that the system always remains chaotic although its chaoticity decreases in time.

Further, the fact that the exponent of the strong chaos regime $\alpha_\Lambda = -0.3$ is smaller than the one in the weak chaos case $\alpha_\Lambda = -0.25$ is explained by the fact that the wave packet spreads faster in the strong chaos regime where $m_2(t) \propto t^{1/2}$ is observed than in the weak chaos region where $m_2(t) \propto t^{1/3}$, so that the average norm per site s within the wave packet excited part and the related effective nonlinearity βs^2 of the system decrease faster in the strong chaos case. Thus orbits in the parameter spaces of the 1D DDNLS model (2.17) in the strong chaos region move faster toward the integrable limit than in the weak chaos region. This means that the value of the exponent in the power law $\Lambda \propto t^{\alpha_\Lambda}$ in the strong chaos case is closer to the -1 value observed in the integrable limit compared to the weak chaos case (indeed we see that $-1 < -0.3 < -0.25$).

Since the wave packet chaoticity is decreasing, an important aspect is to know whether the wave packet chaotic dynamics will always be able to support the subdiffusive spreading. In order to analyze that point, we compare the system's timescales. This was first done by [Skokos et al., 2013] for the weak chaos regime of the 1D DKG model (2.24). Here, we extend this analysis to the weak and strong chaos regimes of the 1D DDNLS system (2.17).

A characteristic timescale for the system's chaotic dynamics is the Lyapunov time (3.24)

$$T_\Lambda = \frac{1}{\Lambda}, \quad (4.15)$$

which gives an estimation of the time it takes for a dynamical system to become chaotic. On the other hand, if we assume that the wave packet dynamics is mainly characterized by its second moment m_2 (3.5), then

$$T_M \sim \frac{1}{D}, \quad (4.16)$$

describes a timescale above which the subdiffusive spreading effectively starts. Note that

$$D \sim \frac{dm_2}{dt}, \quad (4.17)$$

as the behavior $m_2 \sim Dt$ is assumed by definition of the diffusion coefficient D (see also Sec. 2.5.1). Alternatively, if we assume that it is the participation number which mainly measures the wave packet subdiffusive spreading, we could define in a similar way the spreading timescale

$$T_P \sim \frac{1}{\dot{P}}, \quad (4.18)$$

where $\dot{P} = dP/dt$. In the case of the spreading regime mentioned here, we have $m_2 \sim t^{\alpha_m}$ and $P \sim t^{\alpha_m/2}$. We also saw that $\Lambda \sim t^{\alpha_\Lambda}$. Consequently,

$$\frac{T_M}{T_L} \sim t^{1+\alpha_\Lambda-\alpha_m}, \quad \frac{T_P}{T_L} \sim t^{1+\alpha_\Lambda-\alpha_m/2}, \quad (4.19)$$

which reduce to

$$\frac{T_M}{T_L} \sim t^{5/12}, \quad \frac{T_P}{T_L} \sim t^{7/12}, \quad (4.20)$$

for the weak chaos spreading regime in which $\alpha_m = 1/3$, $\alpha_\Lambda = -0.25$ was found, and to

$$\frac{T_M}{T_L} \sim t^{1/5}, \quad \frac{T_P}{T_L} \sim t^{9/20} \quad (4.21)$$

in the strong chaos case where we obtained $\alpha_m = 1/2$ and $\alpha_\Lambda = -0.3$. Consequently the Lyapunov time T_L (4.15) always remains smaller than the spreading timescales defined by T_M (4.16) and T_P (4.18), so that the wave packet chaoticization is always faster than its spreading to new lattice's sites.

The fact that the DV needed for the computation of the MLE is aligned to the most chaotic direction is helpful to visualize the motion of chaotic seeds. We identified chaotic seeds as regions in the lattice which are highly sensitive to initial perturbations. Because the region where the NMs overlap and exchange the energy in a deterministic chaotic manner is finite, we expected to see chaotic spots (seeds) which are localized in time. In addition, these chaotic seeds randomly meander within the wave packet interior due to the presence of a stochastic force $f(t)$ in Eq. (2.108) acting on the modes when the system is within a thermalized state. This process is often related to the homogenization of chaos and promote the wave packet thermalization of more lattice sites.

In order to test this hypothesis, we computed the DVD's ξ_l^D (3.25) second moment m_2^D (3.5), and participation number P^D (3.6) for both the weak and strong chaos regimes. Our numerical results suggest that the DVD remains localized within the wave packet with size of about a mode localization volume. This saturation is reached faster in the strong chaos case compared to the weak chaos where increase of the DVD extent, following $m_2^D \propto t^{0.14}$ and $P^D \propto t^{0.04}$ was still seen up to the largest simulation time. In addition, the center of the DVD exhibits random fluctuations with increasing amplitudes inside the wave packet width.

We computed the size of the region visited by the DVD center and saw that its extent monotonically increases with time, reaching values of $R \approx 10^3$ for the strong chaos case at the final time of integration ($\log_{10} t \approx 10^8$). This is a clear indication that the DVD is visiting modes (and sites) far outside from the initially excited one. A power law $R \propto t^{0.24}$, was noticed for the weak chaos, while for the strong chaos a faster growth $R \propto t^{\alpha_R}$ is reported with $\alpha_R > 0.24$ for several decades, which asymptotically tends to the same $\alpha_R \approx 0.24$ values observed in the weak chaos regime. This is related to the fact that strong chaos is a transient regime which asymptotically evolves to the weak chaos one.

All these results suggest that a non-zero chaotic strength coupled to random fluctuations of the chaotic seeds are the two ingredients for the subdiffusive spreading of the wave packet in the 1D DDNLS model. Thus, as long as they are present in the system no crossover of the extended wave packet to regular dynamics is expected to take place. This fact is general as it has been also observed for the 1D DKG model [Senyange et al. \[2018\]](#).

Chapter 5

Chaotic dynamics of wave packet spreading in the two-dimensional disordered nonlinear Schrödinger equation

5.1 Introduction

In this chapter, we will investigate the characteristics of wave packet spreading in the weak and strong chaos regimes conjectured in Secs. 2.3 and 2.5.2 for the 2D DDNLS model (2.20). The main obstacle facing this study is related to the long-time numerical integration of the 2D DDNLS model (2.20) which is a computationally hard task. This is seen for instance in the literature where up to date only a few works on the subject are available. More specifically, [Garcia-Mata and Shepelyansky, 2009] studied the wave packet spreading in the 2D DDNLS model (2.20) only for a single weak chaos case which requires smaller lattice sizes up to a final time of $t_f = 10^6$ time units, averaging over only 10 disorder realizations. Further [Sales et al., 2018] studied the diffusion of localized excitations in a similar model of the 2D DDNLS system, with non-diagonal nonlinear terms, integrating the phase space trajectories up to $t_f = 10^5$, and averaging over few disorder realizations for each case. On the other hand, [Laptyeva et al., 2012] performed an analysis of over 400 disorder realizations of the spreading in the weak and strong chaos regimes for the generalized 2D DKG system \mathcal{H}_{2K} (2.27) whose equations of motion are much easier to simulate numerically. Thus the numerical investigation of wave packet spreading in the 2D DDNLS lattice (2.20) we consider in this thesis remains largely unexplored. The novelty of this work is two fold as we not only compute the characteristics of the wave packet spreading, but also we investigate the system's chaotic dynamics in detail, to the best of our knowledge for the first time.

The chapter is structured as follows: In Sec. 5.2 we present additional numerical considerations for the integration of the variational equations of the 2D lattice. Section 5.3 is devoted to presenting the results of our computations of the MLE for several cases of localized excitations in the weak and strong chaos regimes. In Sec. 5.4 we investigate the local nature of chaos, analyzing the dynamical behavior of the DVD in every spreading regime. The discussion of our findings and the summary of our work are presented in Sec. 5.5. The outputs of this chapter are heavily based on the research paper [Many Manda et al., 2020].

5.2 Some aspects related to our numerical simulations

5.2.1 Choice of the initial deviation vector

We start our investigation by first analyzing the dynamical behavior of the tangent dynamics of the 2D DDNLS model (2.20) and more specifically its dependence on the type of the used initial DV when a central localized excitation is set as initial state of the lattice. To that end, we consider a typical initial condition consisting of exciting only the central site of a 201×201 lattice with a total norm (2.23) $S_{2D} = 0.375$. The total energy (2.20) is $\mathcal{H}_{2D} \approx 0.7$ for the particular realization of disorder we choose, with the other parameters set to $W = 10$ and $\beta = 10$. We integrate the equations of motion and the variational equations of the system up to a final time $t_f = 10^6$, using the *s11ABC6* SI (3.84). The integration time step $\tau = 0.24$ used, leads to relative energy (3.92) E_r and norm (3.93) S_r errors always

remaining below 10^{-3} . For the initial condition of the variational equations, we implement the following choices of DVs:

Case DV₁. We give random values to the $\delta q_{l,m}$ and $\delta p_{l,m}$ coordinates of a square with size equal to about the average localization volume of a NM (see Table 5.1 below) i.e. $L \times L = 5 \times 5$ at the center of the lattice. The related spatial distribution of the DVD $\xi_{l,m}^D$ (5.2) is shown in Fig. 5.1(b).

Case DV₂. Similar to the case of DV₁ but the size of the initially excited square is approximately 100 times larger than the average localization volume of a NM i.e. $L \times L = 50 \times 50$, leading to the spatial arrangement of the DVD $\xi_{l,m}^D$ (5.2) seen in Fig. 5.2(b).

Case DV₃. Similar to case DV₂ but the size of the initially excited square is 4 times larger, corresponding to a spatial distribution of the DVD $\xi_{l,m}^D$ (5.2) in Fig. 5.3(b).

Case DV₄. We randomly excite the $\delta q_{l,m}$ and $\delta p_{l,m}$ coordinates of only the edge layer of the 2D lattice, leading to the spatial arrangement of the DVD $\xi_{l,m}^D$ (5.2) in Fig. 5.4(b).

The results of our computations for each considered DV are shown as follows: for DV₁ in Fig. 5.1, DV₂ in Fig. 5.2, DV₃ in Fig. 5.3 and DV₄ in Fig. 5.4. In each of these figures, panels (a), (c) and (e) present snapshots of the temporal evolution of the spatial extent of the norm density distribution (3.1)

$$\xi_{l,m}(t) = \frac{s_{l,m}(t)}{\mathcal{S}_{2D}}, \quad s_{l,m}(t) = \frac{1}{2} (q_{l,m}^2(t) + p_{l,m}^2(t)), \quad (5.1)$$

while panels (b), (d) and (f) show the related DVD (3.25)

$$\xi_{l,m}^D(t) = \frac{\delta q_{l,m}^2(t) + \delta p_{l,m}^2(t)}{\sum_{l,m} \delta q_{l,m}^2(t) + \delta p_{l,m}^2(t)}, \quad (5.2)$$

at times $\log_{10} t = 0$ [panels (a) and (b)], $\log_{10} t \approx 2.45$ [panels (c) and (d)] and $\log_{10} t \approx 5.95$ [panels (e) and (f)]. It is worth noticing that the $s_{l,m}$ in Eq. (5.1) is the local norm at site (l, m) of the 2D DDNLS lattice (as in Chap. 4, we will often use s instead of $s_{l,m}$ when referring to its average value over the entire excited part of the lattice). Evidently, the time evolution of the $\xi_{l,m}$ (5.1) is the same in all simulations [panels (a), (c) and (e)], indicating a chaotic wave packet whose extent increases in time, as this state belongs to the thermal region of the energy-norm parameter space of Fig. 2.6. On the other hand, as the initial DVs are different in each computation, we expect the tangent dynamics to depict qualitatively different outputs at least in the initial parts of the evolution of the variational equations.

The results of the computation of the DVD $\xi_{l,m}^D$ (5.2) up to times around $\log_{10} t \approx 2.45$ in panels (d) of Figs. 5.1, 5.2, 5.3 and 5.4, respectively for the cases DV₁, DV₂, DV₃ and DV₄ confirm our predictions, as we see a completely different behavior of the DVs in each case. For the DV₁, a clear expansion of the DVD takes place with the distribution remaining well inside the wave packet extent [see panels (c) and (d) of Fig. 5.1], where the deterministic chaotic dynamics is concentrated in the 2D lattice. For the DV₂, the DVD $\xi_{l,m}^D$ spreads over the whole lattice with the unexcited background [from the point of view of $\xi_{l,m}$ in Fig. 5.2(c)] having smaller values compared to the chaotic part of the lattice [panel (d) of Fig. 5.2]. In the case of DV₃, a similar behavior to the one of DV₂ is observed. However, a much stronger contribution of the unexcited background is seen, as the values of the $\xi_{l,m}^D$ there are much larger when compared to the DV₂ case. The DV₄ choice depicts a completely different behavior to the three previous cases as only the unexcited part of the lattice possesses $\xi_{l,m}^D$ values during the transient phase of the dynamics. As we did for the 1D DDNLS model (2.17) in Sec. 4.2.1, we correlate the dynamics of the DVD to the behavior of the evolution of the ftMLEs (3.21) plotted in Fig. 5.5. Indeed, at short times, the DV₁ leads to the largest ftMLE [see (b)lue curve in Fig. 5.5], as its evolution is contained within the chaotic domain of the lattice from the earlier stages of the evolution. On the other hand, the contribution of the wide unexcited backgrounds whose dynamics are regular in the cases DV₂ and DV₃, lowers the value of their ftMLEs compared to the DV₁ case, with the DV₂ displaying a larger ftMLE than DV₃ [respectively the (g)reen and (r)ed curves in Fig. 5.5]. With the DV₄ evolving solely on the initially unexcited part of the lattice, we expect its ftMLE values to be very small, at least compared to the other ftMLEs at the first stages of the dynamics, something which is clearly seen on the evolution of the (c)yan curve in Fig. 5.5.

During the last two decades of the evolution of the ftMLEs in Fig. 5.5, all the DV cases present similar values for their ftMLEs, as a result of the fact that all DVs align to the same most chaotic direction related to the system's reference orbit, whose exponential rate of changes measures its MLE. Consequently, all the spatial distributions of the DVDs tend to be practically the same as shown in the panels (f) of Figs. 5.1, 5.2, 5.3 and 5.4 whose snapshots were taken at time $\log_{10} t \approx 5.95$. Note that the most chaotic direction possesses coordinates $\delta q_{l,m}$ and $\delta p_{l,m}$ only at the lattice's excited sites where the chaotic dynamics of the system takes place.

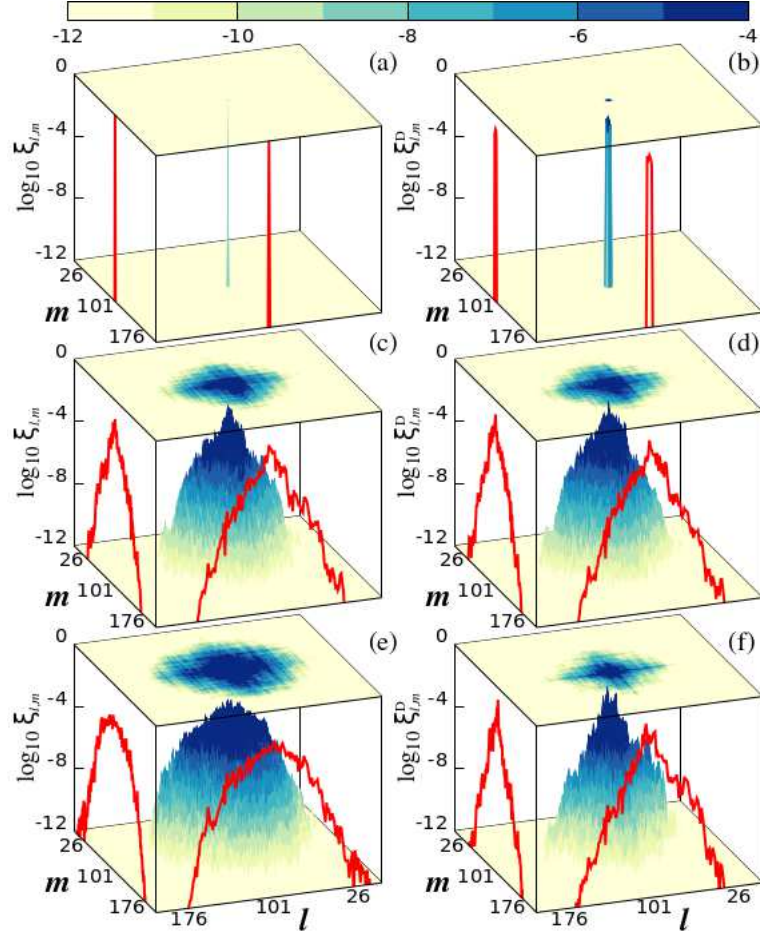


Figure 5.1: 3D spatial distributions and the associated 2D color maps (upper sides) snapshots of the norm density $\xi_{l,m}$ (5.1) [panels (a), (c) and (e)] and the DVD $\xi_{l,m}^D$ (5.2) [panels (b), (d) and (f)] profiles for a representative case of localized initial excitation in the 2D DDNLS lattice (2.20). We excite the central site of a 201×201 lattice with a norm (2.23) $\mathcal{S}_{2D} = 0.375$ at $W = 10$ and $\beta = 10$. The system's total energy is $\mathcal{H}_{2D} \approx 0.7$ (2.20). The initial condition for the variational equations is DV_1 (see text for details). Panels (a) and (b) correspond to the configurations of the $\xi_{l,m}$ and $\xi_{l,m}^D$ at time $\log_{10} t = 0$, while panels (c) and (d) at $\log_{10} t \approx 2.45$ and panels (e) and (f) at $\log_{10} t \approx 5.95$. The red curves on the sides are the distribution's projections along the l and m directions. The coloring of the distributions is done with respect to the $\log_{10} \xi_{l,m}$ and $\log_{10} \xi_{l,m}^D$ values according to the horizontal color scales presented at the top of the figure.

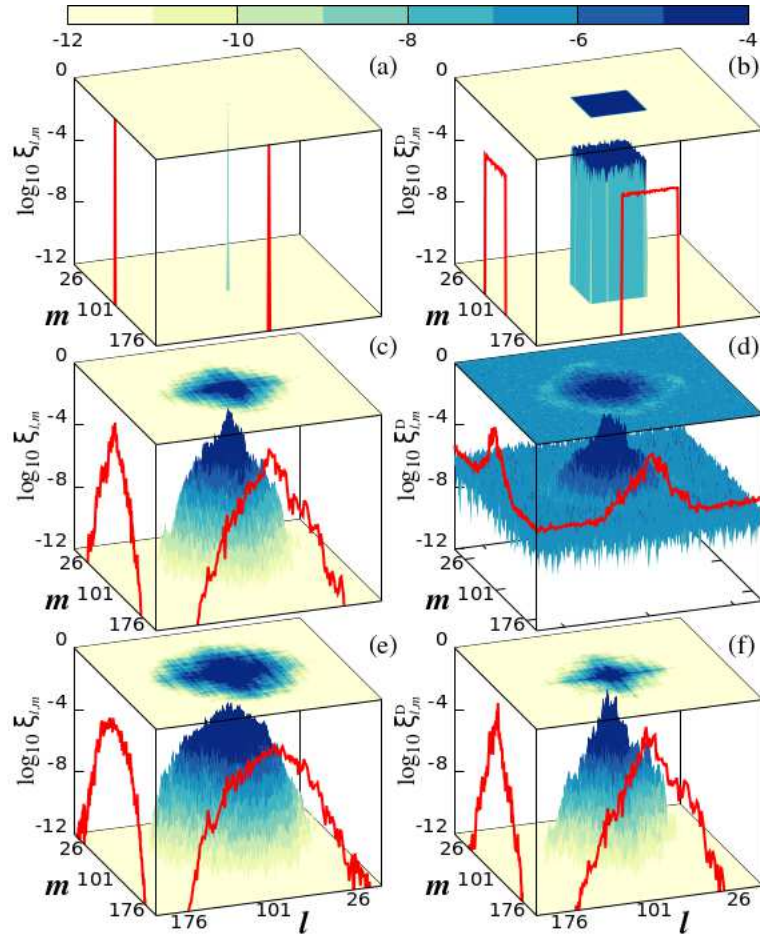


Figure 5.2: Similar to Fig. 5.1, but for the initial condition DV_2 (see text for details) for the variational equations of the Hamiltonian function of the 2D DDNLS model \mathcal{H}_{2D} (2.20).

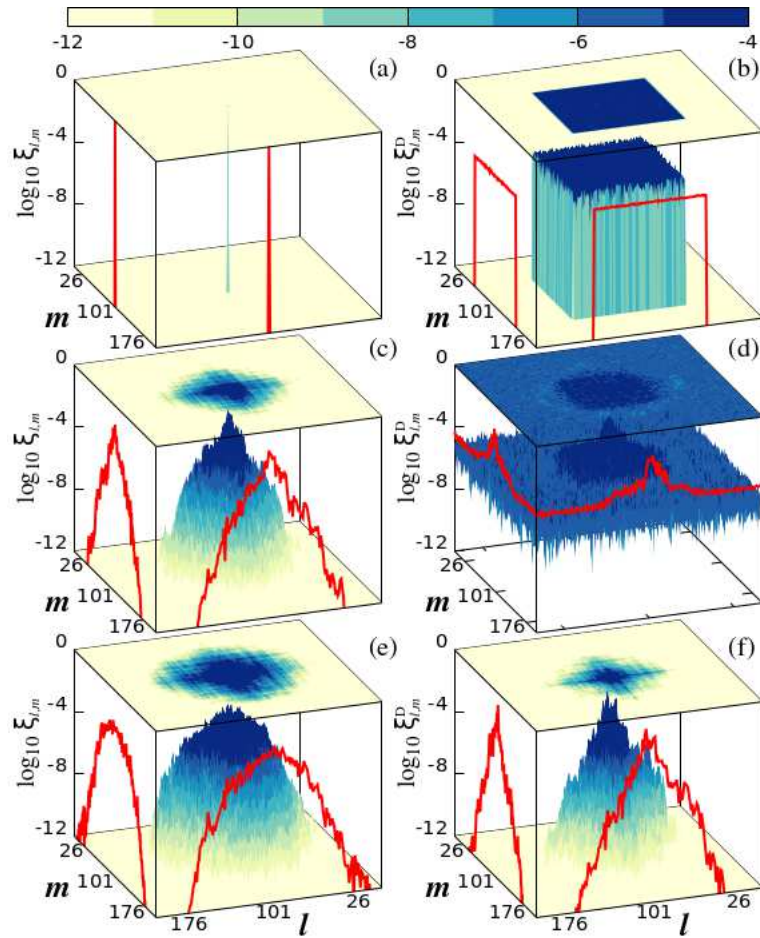


Figure 5.3: Similar to Fig. 5.1, but for the initial condition DV_3 (see text for details) for the variational equations of the Hamiltonian function of the 2D DDNLS model \mathcal{H}_{2D} (2.20).

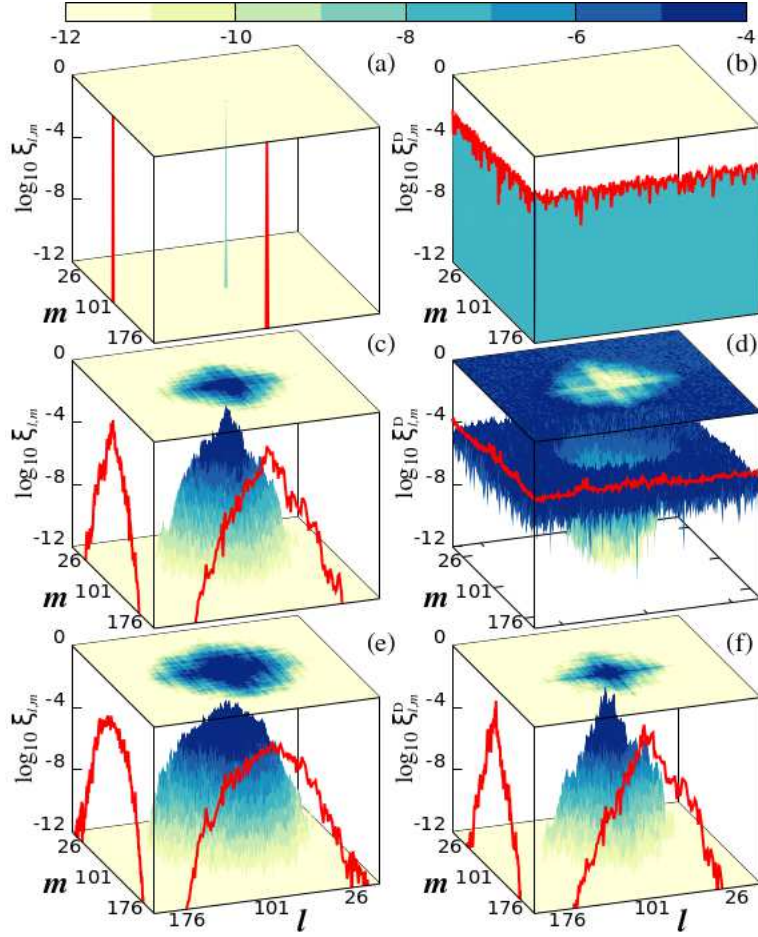


Figure 5.4: Similar to Fig. 5.1, but for the initial condition DV_4 (see text for details) for the variational equations of the Hamiltonian function of the 2D DDNLS model \mathcal{H}_{2D} (2.20). Note that as only the last sites of the lattice's edges initially receive the $\xi_{l,m}^D$ (5.2) values, it is visible only on the 3D heatmap of panel (b). The size of the DVD's excited region is too small compared to the lattice's dimension to be visible in the upper color map of panel (b).

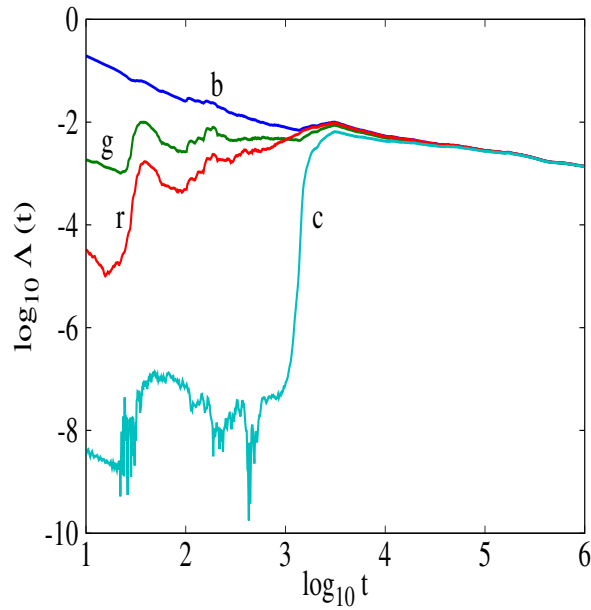


Figure 5.5: Time evolution of the ftMLE $\Lambda(t)$ (3.21) for the representative initial condition of the 2D DDNLS lattice (2.20) used in Figs. 5.1, 5.2, 5.3 and 5.4. The curves correspond to results obtained for the DV_1 [(b)lue], DV_2 [(g)reen], DV_3 [(r)ed] and DV_4 [(c)yan] (see text for details).

Based on these numerical experiments, we conclude that initial DVs with random values of the $\delta q_{l,m}$ and $\delta p_{l,m}$ coordinates on a square with area smaller or of the order of the NM average localization volume in the region of the lattice's initially excited sites are good choices. Otherwise the DV dynamics has a tendency to initially spread over the unexcited part of the lattice and consequently converging much more slowly to the most chaotic direction of the system's computed trajectory.

5.2.2 The dynamic lattice expansion

Let us now discuss how we implement the dynamic lattice technique of Sec. 4.2.2 in the 2D system, as a way of saving CPU time. This is in contrast to using a *fixed* large $N \times M$ lattice from the beginning of the dynamical evolution of orbits, so that the lattice edges are practically not reached by the wave packet at the end of the integration. In the dynamic lattice approach we start with a much smaller lattice around the initially excited sites and expand it whenever it is required by \mathcal{N} sites at the edges of all lattice's sides. As for the 1D DDNLS model (2.17) this method requires a criterion which checks if the wave packet's front has hit the boundaries. For the 2D DDNLS system (2.20), we use the criterion

$$\max_{l \in \mathcal{D}} s_{l,m} > \delta_{\mathcal{D}}, \quad (5.3)$$

where \mathcal{D} represents a ribbon at the outermost layer of the lattice and $\delta_{\mathcal{D}}$ is a threshold number. Notice that this condition is different to the one used in the 1D DDNLS system (4.1)

$$\frac{1}{\mathcal{D}} \sum_{l,m} s_{l,m} > \delta_{\mathcal{D}}. \quad (5.4)$$

Nevertheless, we numerically checked that results obtained from the two conditions (5.4) and (5.3) are similar. In our study we prefer using the condition (5.3) as it can be easily applied in the case of 2D lattice.

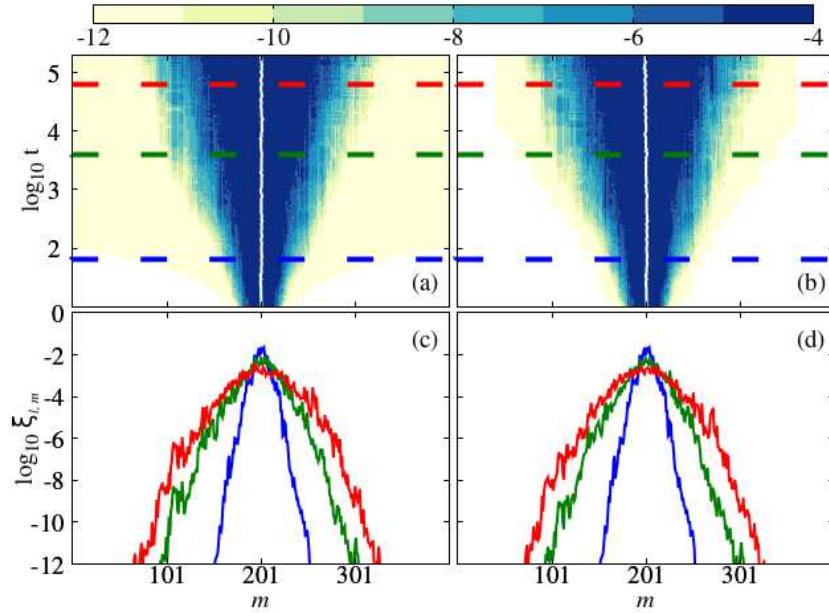


Figure 5.6: Spatiotemporal dependence of the projection of the norm density distribution $\xi_{l,m}$ (5.1) and its related DVD $\xi_{l,m}^D$ (5.2) for 7×7 central square excitation in a 401×401 2D DDNLS lattice (2.20). Each excited site is given a norm $s = 0.72$ such that the total norm $\mathcal{S}_{2D} = 35.28$ (2.23) with $W = 10$ and $\beta = 1$. For the particular disorder realization, the total energy (2.20) is $\mathcal{H}_{2D} \approx -4.714$. The color scales at the top of the figure are used for coloring the lattice sites according to their $\log_{10} \xi_{l,m}$ values. In both panels, the white curves represent the motion of the distribution projections' centers. Panels (c) and (d) contain snapshots of the spatial dependence of the distribution's projections respectively at times $\log_{10} t \approx 1.8$ [(b)lue curves], $\log_{10} t \approx 3.6$ [(g)reen curves] and $\log_{10} t \approx 4.8$ [(r)ed curves]. These times are also indicated using the same colors for the dashed horizontal lines in panels (a) and (b).

The results of a numerical comparison between the fixed and dynamic lattice simulations are shown in Fig. 5.6. The initial excitation considered there corresponds to all sites in a square of size $L \times L = 7 \times 7$ at the center of a 401×401 lattice (the center of the square coincides with the lattice center) having the

same norm per site $s_{l,m} = 0.72$. This means that the total norm of the system (2.23) is $\mathcal{S}_{2D} = 35.28$, while the value of the Hamiltonian (2.20) is $\mathcal{H}_{2D} \approx -4.174$ for the disorder realization we choose, corresponding to a thermal state in the energy-norm parameter space in Fig. 2.6 of the system. In addition, we set $W = 10$ and $\beta = 1$. We integrate the system using the *s11ABC6* SI (3.84) of order 6 with an integration time step $\tau = 0.135$ which kept the relative energy E_r (3.92) and norm S_r (3.93) errors below 10^{-4} up to the final time of integration $t_f \approx 10^5$. The initial size of the active dynamic lattice was set to 101×101

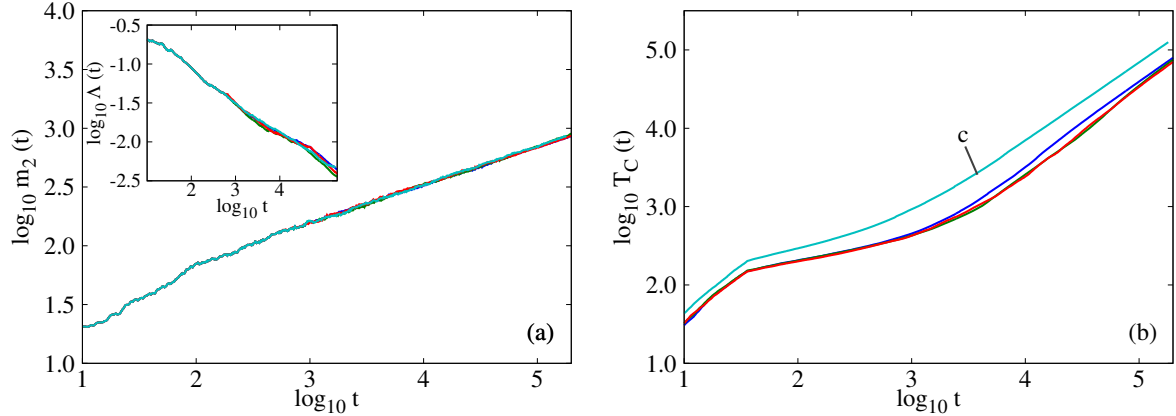


Figure 5.7: Time evolution of the second moment $m_2(t)$ (5.5) [panel (a)], the ftMLE $\Lambda(t)$ (3.21) [inset of panel (a)] and the CPU time T_C [panel (b)] for a particular setup of the initial excitation of the 2D DDNLS system (2.20) when the dynamic lattice approach is used in comparison to the fixed lattice computation. The curve's coloring corresponds to $\delta_{\mathcal{D}} = 10^{-12}$ [(b)lue curves], $\delta_{\mathcal{D}} = 10^{-10}$ [(g)reen curves], $\delta_{\mathcal{D}} = 10^{-8}$ [(r)ed curves] and the fixed lattice [(c)yan curves] computations.

which is much larger than the average localization volume of the NMs ($\bar{V} \approx 35$ for $W = 10$ as seen in Table 5.1 below). In addition, we use $\delta_{\mathcal{D}} = 10^{-12}$ and $\mathcal{N} = 10$.

The spatiotemporal evolution of the projection along the m axis of the system of the norm density distribution $\xi_{l,m}$ (5.1) in the case of the fixed lattice computation is presented in Fig. 5.6(a) along with snapshots in Fig. 5.6(c), at times indicated by the dashed lines in Fig. 5.6(a). A residual norm $s \lesssim 10^{-12}$ spreads over the entire lattice due to numerical fluctuations [see lighter areas in Fig. 5.6(a)]. The same results obtained using the dynamic lattice simulation after 11 expansions of the initial lattice is shown in Fig. 5.6(b) with its related snapshots taken at the same times [in Fig. 5.6(d)] as for the fixed lattice run. Note that the white areas in Fig. 5.6(b) correspond to unexcited regions i.e. these sites possess zero norm ($s_{l,m} = 0$). Clearly, the two simulations give practically the same wave packet evolution.

We repeat the same simulations, using different thresholds $\delta_{\mathcal{D}}$ [see Eq. (5.3)] for the dynamic lattice simulations. In Fig. 5.7 we show the result of such numerical computations where the values $\delta_{\mathcal{D}} = 10^{-12}$ [(b)lue curves], $\delta_{\mathcal{D}} = 10^{-10}$ [(g)reen curves], $\delta_{\mathcal{D}} = 10^{-8}$ [(r)ed curves] and the fixed lattice [(c)yan curves] computations are used. We plot the evolution of the second moment of the norm density distribution $\xi_{l,m}$ (5.1)

$$m_2 = \sum_{l,m} [(l - \bar{l})^2 + (m - \bar{m})^2] \xi_{l,m}, \quad \bar{l} = \sum_{l,m} l \xi_{l,m}, \quad \bar{m} = \sum_{l,m} m \xi_{l,m}, \quad (5.5)$$

in Fig. 5.7(a), and the evolution of the associated ftMLEs Λ (3.21) for all cases in the inset of Fig. 5.7(a). A good correspondence is visible between all the cases. Similarly to what we did for the 1D DDNLS model (2.17) in Sec. 4.2.1, our choice of the $\delta_{\mathcal{D}}$ depends on the final values of the norm per site attained in our widest wave packet. In the 2D DDNLS model (2.20), we are reaching wave packet width $m_{2,f} \propto 10^3$ sites. Since the constant total norm (2.23) $\mathcal{S}_{2D} \approx 10^0 - 10^2$ is shared among all the excited sites, the final average norm per site

$$s_f \propto \frac{\mathcal{S}_{2D}}{m_{2,f}} \sim 10^{-3} - 10^{-1}, \quad (5.6)$$

such that using

$$\delta_{\mathcal{D}} = 10^{-8}, \quad (5.7)$$

we capture the wave packet spreading with a rather good precision as shown in Fig. 5.7(a) up to the final time of integration $t_f \approx 2 \times 10^6$.

In Fig. 5.7(b) we plot the time evolution of the cumulative CPU time $T_C(t)$ necessary for the simulations. As in the 1D case [Figs. 4.4(d) and 4.5(b)], the fixed lattice simulation takes longer to complete than the dynamic lattice ones. The dynamic lattice approach with a threshold (5.3) $\delta_{\mathcal{D}} = 10^{-8}$ gives the smallest T_C value as expected. Overall, a gain (4.2) $g \approx 36\%$, 40% and 43% is seen for the

$\delta_{\mathcal{D}} = 10^{-12}$, $\delta_{\mathcal{D}} = 10^{-10}$ and $\delta_{\mathcal{D}} = 10^{-8}$ threshold values respectively. In the remaining part of this chapter, we will use $\delta_{\mathcal{D}} = 10^{-8}$ for our simulations.

5.3 The maximum Lyapunov exponent

In order to avoid repetition of similar information in the rest of this chapter, let us note that we perform simulations of lattice up to sizes 451×451 in order to avoid finite size effects, integrating the equations of motion and the variational equations up to final time $t_f \approx 2 \times 10^6$ by the *s11ABC6* SI (3.84). The choice of the integration time step, $\tau = 0.1 - 0.25$, leads to relative energy E_r (3.92) and norm S_r (3.93) errors always remaining below 10^{-3} and 10^{-2} respectively. We excite all sites in a square of side L at the center of the lattice with the same norm per site s (or the same rescaled norm $x = \beta s$), averaging our observables over 50 disorder realizations. Notice that similar to what was done in the 1D DDNLS system, when $\beta > 0$ in \mathcal{H}_{2D} (2.20), we set the disorder parameter $\epsilon_{l,m}$ of lattice's central site to zero. In that way, single site excitation of all disorder realizations with the same total norm \mathcal{S}_{2D} (2.23) has the same total energy value (2.20) $\mathcal{H}_{2D} = \beta \mathcal{S}_{2D}/2$, which always belongs to the thermal phase of the energy-norm space in Fig. 2.6. On the other hand, for multi-site wave packet excitations, all disorder realizations have the same value of the total norm \mathcal{S}_{2D} (2.23) and we ensure that the values of the total energy \mathcal{H}_{2D} (2.20) remain bounded within the thermal phase of the energy-norm space of the 2D DDNLS system. As an additional remark, let us note that we are using the energy-norm space of Fig. 2.6 of the 1D DDNLS model (2.17) for the 2D case (2.20), as they are very similar to each other. In fact, the only difference is that the extra dimension of the 2D system renormalizes the ground states of Fig. 2.6 in the thermodynamic limit, which is now located well below that of the 1D system. Nevertheless, as we are not interested to the dynamics of the system close to the ground states, it makes Fig. 2.6 sufficient for exploring the thermal states of the 2D DDNLS Hamiltonian model (2.20).

5.3.1 The weak chaos regime

Let us now investigate the chaotic dynamics of wave packet spreading in the weak chaos regime of the 2D DDNLS system (2.20). We consider the following cases:

- **Case W1_{2D}.** $W = 10$, $\beta = 0.15$, $L = 2$, $x = 0.15$.
- **Case W2_{2D}.** $W = 10$, $\beta = 0.92$, $L = 1$, $x = 0.92$.
- **Case W3_{2D}.** $W = 10$, $\beta = 4$, $L = 1$, $x = 1$.
- **Case W4_{2D}.** $W = 12$, $\beta = 1.75$, $L = 1$, $x = 1.75$.

Let us explain why these cases theoretically belong to the weak chaos regime of the 2D DDNLS model of Figs. 2.5 and 2.6. In the case of W1_{2D}, which is a multi-site initial excitation, we apply the first condition of Eq. (2.56),

$$x \frac{L^2}{\bar{V}} < d, \quad (5.8)$$

where $x = \beta s$ is the initial frequency shift, \bar{V} is the average localization volume, d is the average spacing between NMs in a NM volume and L^2 is the area of the initial excitation (note that for the 1D DDNLS model, we have L instead of L^2). The estimations of \bar{V} (2.61), and d (2.16) are listed in Table 5.1 for the values of the disorder strength W we use. It is worth mentioning that the \bar{V} is not obtained through the analysis of the NM themselves, but rather by evolving a single site excitation within the 2D DDLS model (i.e. \mathcal{H}_{2D} (2.20) with $\beta = 0$), up to a time when a halt in the evolution is observed. Then, the average participation number P (3.6) over several disorder realizations of the norm density distribution $\xi_{l,m}$ (5.1) is a rough measure of the NM localization volume. Thus, using the values $x = 0.15$, $L = 2$, $\bar{V} = 35$ and $d = 0.51$ we obtain the inequality $0.017 < 0.51$ from Eq. (5.8) which is true. The remaining initial conditions of cases W2_{2D}, W3_{2D} and W4_{2D} correspond to single site excitations. Consequently, we apply the first condition of Eq. (2.57)

$$x < \Delta, \quad (5.9)$$

such that the $x = 0.92$, $x = 1$ and $x = 1.75$ of cases W2_{2D}, W3_{2D} and W4_{2D} are respectively always smaller than the frequency bandwidths $\Delta = 18$, 18 and 20 of $W = 10$, 10 and 12 seen in Table 5.1.

In Fig. 5.8(a), we plot the time evolution of the second moment $m_2(t)$ (5.5) of the norm distribution $\xi_{l,m}$ (5.1). For all cases, a diffusive behavior of the wave packet is seen, which is well fitted by the monotonic power law $m_2 \propto t^{\alpha_m}$ with $0 < \alpha_m < 1$ in the last decades of the evolution. The time dependence of the power law exponents $\alpha_m(t)$ is shown in Fig. 5.8(b) for each studied case. A clear saturation of the $\alpha_m(t)$ values to $\alpha_m \approx 0.2$ is visible, in agreement with the predictions of [Flach, 2010;

2D NM properties	$W = 10$	$W = 10.5$	$W = 11$	$W = 12$	$W = 14$
\bar{V}	35	28	23	16	10
Δ	18	18.5	19	20	22
$d = \Delta/\bar{V}$	0.51	0.66	0.83	1.25	2.2

Table 5.1: Average NM localization volume \bar{V} , frequency bandwidth $\Delta = W + 8$ and average spacing between NM $d = \Delta/\bar{V}$ (2.16) in the case of a central multi-site excitation of width $L^2 \approx \bar{V}$ sites at the center of the 2D DDNLS lattice system (2.20). Note that the values of \bar{V} are obtained by averaging the participation number P (3.6) of the excited part at the end of the integration of the 2D DDLS model (i.e. $\beta = 0$ in \mathcal{H}_{2D} (2.20)) up to final times $t_f \approx 10^5 - 10^6$ over 10 disorder realizations.

[Laptyeva et al., 2012] (see also Sec. 2.5). This power exponent value is numerically retrieved from our data, averaging all the $\alpha_m(t)$ values in Fig. 5.8(b) after the 6th decade where a clear convergence is seen. This power law exponent was also numerically obtained by [Laptyeva et al., 2012] for the 2D DKG system (2.27). For all these weak chaos cases, we evaluate the wave packet's chaotic strength, through

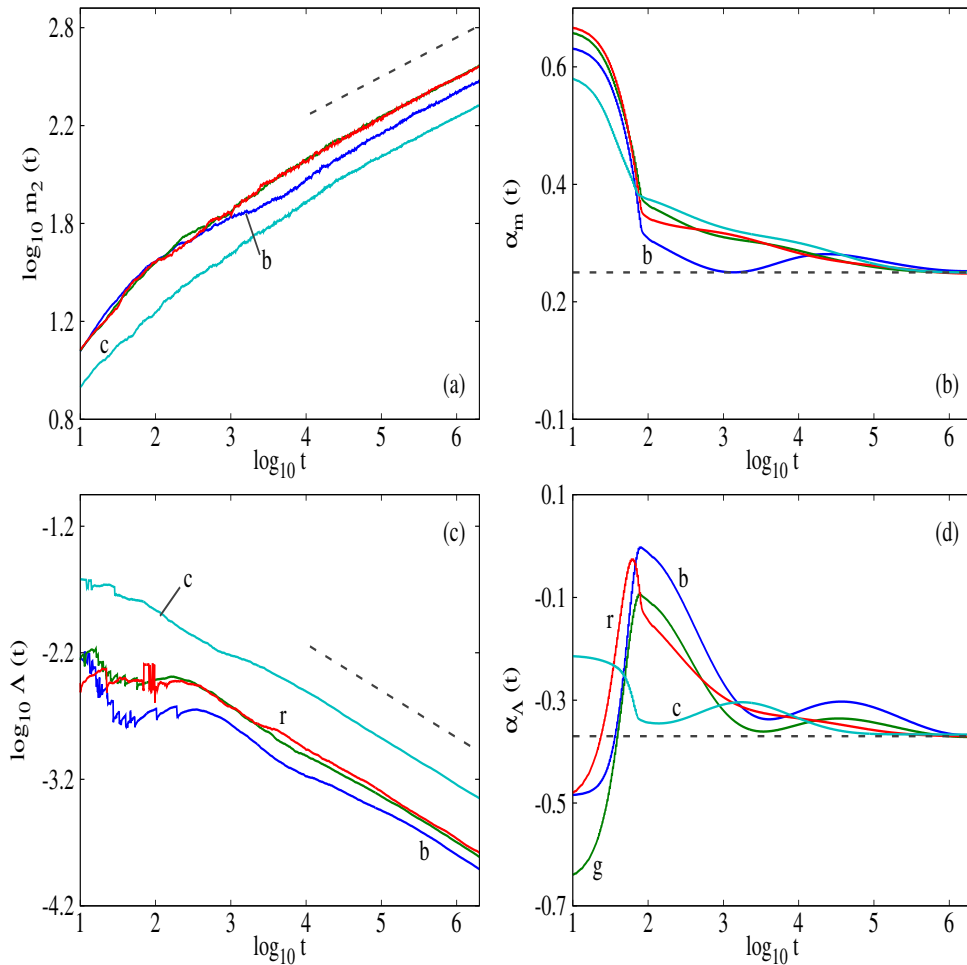


Figure 5.8: Results of the time evolution of the second moment $m_2(t)$ (5.5) [panel (a)] of the norm density distribution $\xi_{l,m}$ (5.1) and of the related ftMLEs $\Lambda(t)$ (3.21) [panel (c)] for the weak chaos cases W_{12D} [(b)lue curves], W_{22D} [(g)reen curves], W_{32D} [(r)ed curves] and W_{42D} [(c)yan curves] (see text for details). In panels (b) and (d) we see the associated power law exponents when the data are fitted with the relations $m_2(t) \propto t^{\alpha_m}$ and $\Lambda(t) \sim t^{\alpha_\Lambda}$ respectively. The black dashed lines guide the eye for slopes 0.2 [panel (a)] and -0.37 [panel (c)]. The horizontal dashed lines indicate the values 0.2 in panel (b) and -0.37 in panel (d). Each case has been averaged over 50 disorder realizations.

the computation of their ftMLEs $\Lambda(t)$ (3.21) depicted in Fig. 5.8 (c). A clear decay of the $\Lambda(t)$ values is visible for all the cases following a power law $\Lambda \propto t^{\alpha_\Lambda}$ ($\alpha_\Lambda < 0$) similarly to what was observed in the 1D case [Sec. 4.3.2]. The values of the time evolution of $\alpha_\Lambda(t)$ are presented in Fig. 5.8(d), showing a tendency to saturate around $\alpha_\Lambda \approx -0.37$. This result of the wave packet chaoticity is not particular to

the 2D DDNLS system (2.20), as it was also found for the 2D DKG model (2.27) [Many Manda et al., 2020].

5.3.2 The strong chaos regime

We also study the strong chaos regime of the 2D DDNLS system (2.20) of Figs. 2.5 and 2.6, by considering the following cases:

- **Case S_{12D}**. $W = 10.5$, $\beta = 0.145$, $L = 21$, $x = 0.145$.
- **Case S_{22D}**. $W = 11$, $\beta = 0.68$, $L = 10$, $x = 0.68$.
- **Case S_{32D}**. $W = 12$, $\beta = 0.35$, $L = 21$, $x = 0.35$.
- **Case S_{42D}**. $W = 14$, $\beta = 6$, $L = 15$, $x = 0.72$.

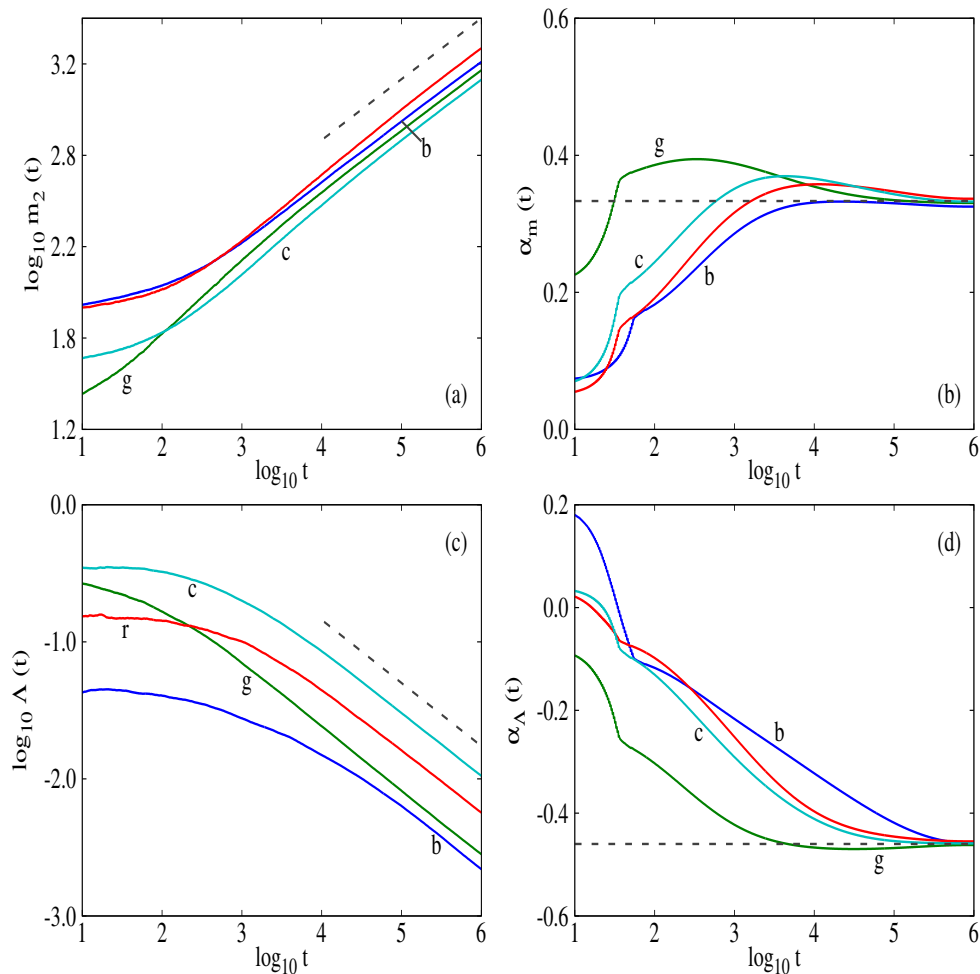


Figure 5.9: Similar to Fig. 5.8, but for the strong chaos cases S_{12D} [(b)lue curves], S_{22D} [(g)reen curves], S_{32D} [(r)ed curves] and S_{42D} [(c)yan curves] (see text for details). The dashed lines in panels (a) and (c) guide the eye for slopes 0.33 and -0.46 respectively. The horizontal dashed lines indicate the value 0.33 in panel (b) and -0.46 in panel (d). The presented results are averaged over 50 disorder realizations.

Note that here, we use extended localized initial excitations as the value of L^2 is much greater than our estimation of the NM average localization volume shown in Table 5.1. In Sec. 2.6, we discussed a particular condition (2.119) for setting up the initial wave packet within the strong chaos region of Figs. 2.5 and 2.6, which for the 2D DDNLS system becomes

$$L^2 \gtrsim \frac{W}{x}. \quad (5.10)$$

The advantage of this approach is that it does not depend on the characteristics of the NMs of the 2D DDLS system (i.e. $\beta = 0$ in \mathcal{H}_{2D} (2.20)), which have not yet been extensively studied. Consequently, using the parameter values of the cases S_{12D}, S_{22D}, S_{32D} and S_{42D} we compute L^2 to respectively be

441, 100, 441 and 225. These values are always much greater than $W/x \approx 72, 16, 34$ and 19 respectively so that condition (5.10) is satisfied.

Let us note that, both the conditions of strong chaos in Eq. (2.56)

$$x \frac{L^2}{\overline{V}} > d, \quad (5.11)$$

which depends on the NM characteristics (\overline{V} (2.61) and d (2.16)), and the one of Eq. (5.10) are equivalent. Indeed, using the following simple algebraic manipulations

$$x \frac{L^2}{\overline{V}} > d \Rightarrow x \frac{L^2}{\overline{V}} > \frac{\Delta}{\overline{V}} \Rightarrow xL^2 > \Delta \Rightarrow L^2 \gtrsim \frac{W}{x}, \quad (5.12)$$

[where we assumed $\Delta \sim W$ for the 2D system (2.20)] we can relate the two inequalities. In order to be completely certain about our argumentation, we have also checked using Eq. (5.11) that our cases qualitatively belong to the strong chaos region of the 2D DDNLS model (2.20). Indeed, using the parameter values for the cases $S1_{2D}$, $S2_{2D}$, $S3_{2D}$ and $S4_{2D}$ and the NM average localization volume \overline{V} in Table 5.1, we compute xL^2/\overline{V} to respectively get $0.145 \cdot 21^2/28 \approx 2.28$, $0.68 \cdot 10^2/23 \approx 2.96$, $0.35 \cdot 21^2/16 \approx 9.65$ and $0.72 \cdot 15^2/10 \approx 16.2$. These numbers are always much higher than the d values 0.66, 0.83, 1.25 and 2.2 for the disorder strengths $W = 10.5, 11, 12$ and 14.

The result of the computation of the second moment $m_2(t)$ (5.5) of the norm distribution $\xi_{l,m}$ (5.1) is shown in Fig. 5.9 (a) for all the strong chaos cases. Again, a spreading of wave packets appears for all the cases as the $m_2(t)$ values monotonically increase for all times. These increases are well fitted by a power law $m_2(t) \propto t^{\alpha_m}$, with $0 < \alpha_m < 1$. The time evolution of the power law exponents $\alpha_m(t)$ are shown in Fig. 5.9(d) for all these cases. Clearly, the values of $\alpha_m(t)$ reach $\alpha_m \approx 0.33$ at some point of their evolution, in agreement with the theory [Flach, 2010; Lapyteva et al., 2012] (see also Sec. 2.5). Results about of the time dependence of the ftMLEs $\Lambda(t)$ (3.21) for all the strong chaos cases are shown in Fig. 5.9(c). Again, a monotonic decay is evident for the ftMLEs, well fitted by $\Lambda(t) \propto t^{\alpha_\Lambda}$ with $\alpha_\Lambda < 0$. The values of the power law exponents converge toward $\alpha_\Lambda \approx -0.46$ [Fig. 5.9(d)]. Both estimations $\alpha_m = 0.33$ and $\alpha_\Lambda = -0.46$, are obtained from averaging results from all the cases studied in the interval of time where the saturation is seen. These behaviors of the wave packet's chaoticity in the strong chaos regime were also found for the 2D DKG model (2.27) in [Many Manda et al., 2020].

5.4 The deviation vector distribution

The computation of the spatiotemporal evolution of the DVD obtained during the computation of the ftMLEs was used in the case of 1D DDNLS model (2.17) to visualize the motion of chaotic seeds in the lattice's excited part. We perform a similar dynamical investigation for the DVD (5.2) in the 2D DDNLS model (2.20).

5.4.1 The weak chaos regime

Let us first study the behavior of the DVD $\xi_{l,m}^D$ (5.2) in the weak chaos regime. In Fig. 5.10 we show the time evolution of the norm density distribution $\xi_{l,m}$ (5.1) [panels (a), (c) and (e)] and the DVD $\xi_{l,m}^D$ (5.2) [panels (b), (d) and (f)] for a representative disorder realization of the $W1_{2D}$ case. The snapshots of the distributions are taken at times $\log_{10} t \approx 3.15$ [panels (a) and (b)], $\log_{10} t \approx 5.04$ [panels (c) and (d)] and $\log_{10} t \approx 6.09$ [panels (e) and (f)]. The results of Figs. 5.10(a), (c) and (e) clearly show that the norm distribution is spreading as its extent (represented for instance by the red curves of the side projections of $\xi_{l,m}$) grows rather smoothly and symmetrically about the wave packet center which remains practically fixed [see white region at the center of the 2D color map on the upper sides of Figs. 5.10(a), (c) and (e)]. On the other hand, the DVD $\xi_{l,m}^D$ (5.2) keeps a rather localized pointy shape (although its extent slightly increases in time), which remains well inside the wave packet width [see for example the red curves of the side projections in Figs. 5.10(b), (d) and (f)]. Its center is meandering inside the lattice's excited part with increasing amplitudes [see white areas at the upper sides of the 2D color maps in Figs. 4.11(b), (d) and (f)].

In order to quantify the observations made about the DVD's behavior in Fig. 5.10, we compute the second moment $m_2^D(t)$ (5.5) and participation number $P^D(t)$ (3.6) of $\xi_{l,m}^D$ (5.2). The obtained results are shown in Figs. 5.11(a) and (b) respectively. A steady increase of the $m_2^D(t)$ values [Fig. 5.11(a)] is observed for all the weak chaos cases, which is well fitted by $m_2^D(t) \propto t^{0.12}$, exhibiting a much slower growth than the $m_2(t) \propto t^{0.2}$ behavior of the wave packet expansion observed in Figs. 5.8(a) and (b). In addition, a clear saturation of the $P^D(t)$ values is visible at the later stage of the evolution, which tend to fluctuate around numbers of the order of the NM average localization volume. For instance, for cases

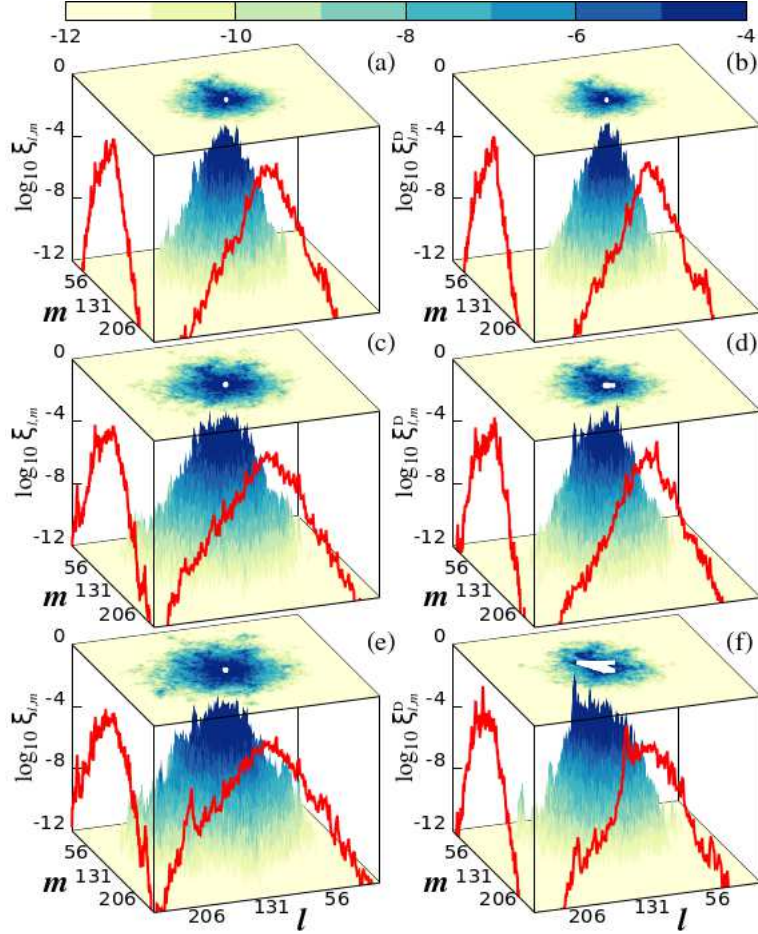


Figure 5.10: 3D spatial distribution and the associated 2D color map (upper sides) snapshots of the norm density $\xi_{l,m}$ (5.1) [panels (a), (c) and (e)] and the DVD $\xi_{l,m}^D$ (5.2) for a representative realization of the case $W1_{2D}$ (see text for details). Panels (a) and (b) correspond to the configurations of the $\xi_{l,m}$ and $\xi_{l,m}^D$ at time $\log_{10} t \approx 3.15$, panels (c) and (d) at $\log_{10} t \approx 5.04$ and panels (e) and (f) at $\log_{10} t \approx 6.09$. The red curves on the sides are the distributions' projections along the l and m directions. The white areas in the upper 2D color map represent the motion of the distribution's center. The coloring of the distributions is done with respect to the $\log_{10} \xi_{l,m}$ and $\log_{10} \xi_{l,m}^D$ values according to the horizontal color scales presented at the top of the figure.

$W1_{2D}$ [(b)lue curve], $W2_{2D}$ [(g)reen curve] and $W3_{2D}$ [(r)ed curve] in Fig. 5.8(b), the DVD's participation number attains values $P^D \approx 10^{1.5} \approx 31$ similar to the $\bar{V} \approx 35$ observed for $W = 10$ in Table 5.1. This behavior is due to the localized pointy shapes of the $\xi_{l,m}^D$ (5.2) seen in Figs. 5.10(b), (d) and (f) whose extents approximately span the average volume of a NM. Note that larger fluctuations of the $P^D(t)$ values in Figs. 5.8(b) compared to the 1D case in Fig. 4.12(b) can be attributed to the smaller number of disorder realizations used in the 2D case and to the fact that the geometrical characteristics of the NMs in 2D lattices is more complex compared to the 1D case, leading for instance to larger discrepancies in the measurement of the NM localization length.

We also investigate the motion of the DVD's center $\bar{\mathbf{r}}^D = (\bar{l}^D, \bar{m}^D)$, by computing the quantity

$$A(t) = R_x(t) \cdot R_y(t), \quad (5.13)$$

at each time $t > 0$ of the evolution. Here,

$$R_x(t) = \max_{[0,t]} \{\bar{l}^D(t)\} - \min_{[0,t]} \{\bar{l}^D(t)\}, \quad R_y(t) = \max_{[0,t]} \{\bar{m}^D(t)\} - \min_{[0,t]} \{\bar{m}^D(t)\}. \quad (5.14)$$

similar to the quantity R (4.10) used in the 1D case. The A quantity (5.13) tries to quantify the area visited by the DVD (whose extent possesses fuzzy borders), by measuring the surface of the smallest rectangle containing the white area in panels (b), (d) and (f) of Figs. 5.10 and 5.13.

The fate of the wave packet can be conjectured based on the behavior of the area A (5.13) in a similar way to the one followed in the 1D case for the length R (4.10). Indeed, if

$$A \lesssim \bar{V}, \quad A(t) \sim t^0, \quad (5.15)$$

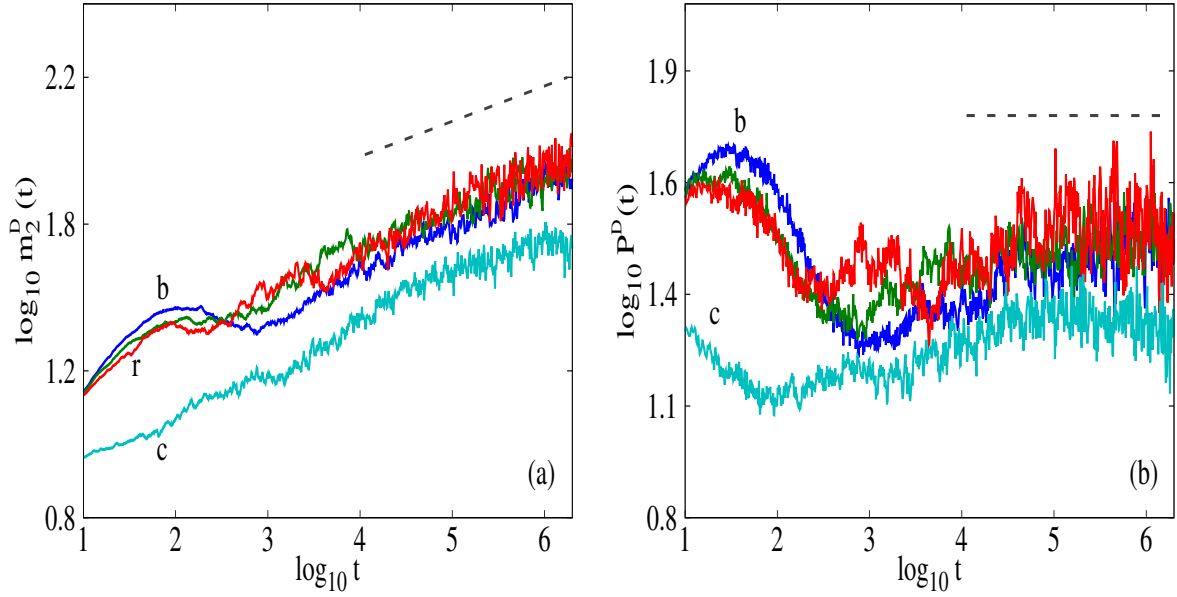


Figure 5.11: Time evolution of observables of the tangent dynamics in the weak chaos regime. (a) The second moment m_2^D (5.5) and (b) the participation number P^D (3.6) of the DVD $\xi_{l,m}^D$ (5.2). The dashed lines in panels (a) and (b) guide the eye for slopes 0.12 and 0.0 respectively. The curve's colors correspond to the ones used in Fig. 5.8.

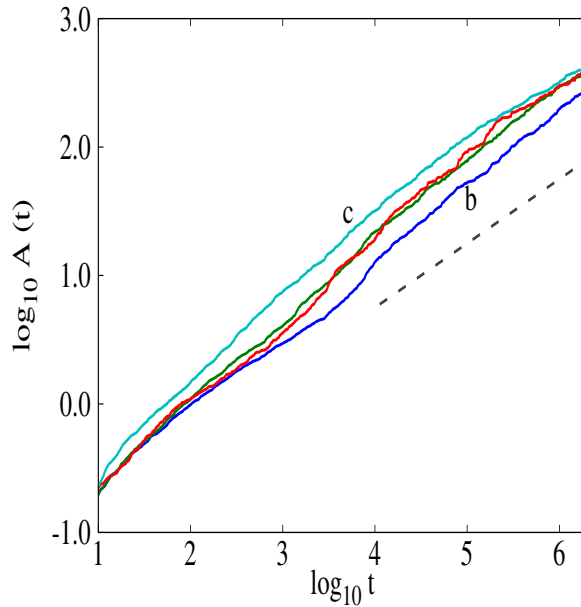


Figure 5.12: Time dependence of the area A (5.13) covered by the DVD's center $\mathbf{r}^D = (\bar{l}^D, \bar{m}^D)$ in cases belonging to the weak chaos regime of the 2D DDNLS system (2.20). The dashed line indicates slope 0.5. The curve's colors correspond to the ones used in Fig. 5.8.

the DVD does not visit sites outside the initially excited central ones. In this case, no spreading of the wave packet will be observed. On the other hand, when

$$A(t) > \bar{V}, \quad (5.16)$$

after a certain amount of time, two scenarios are possible. If the values of A saturate i.e $A(t) \sim t^0$ after some time, then the DVD's center has only reached sites in close proximity of the central ones. Thus, a subdiffusion of the wave packet will be visible, followed by a slowing down of the wave packet spreading which will eventually halt forever. This corresponds to the situation discussed in [Johansson et al., 2010; Aubry, 2011; Pikovsky and Fishman, 2011]. On the other hand, if the $A(t)$ values show a monotonic increase such that at large times $A(t) \gg V$, then the DVD center is visiting sites far away from the initially excited ones, leading to the case of wave packet which is spreading indefinitely as described

in [Pikovsky and Shepelyansky, 2008; Garcia-Mata and Shepelyansky, 2009; Flach, 2010; Lapyteva et al., 2012].

The time evolution of the $A(t)$ (5.14) values is depicted in Fig. 5.12 for all the weak chaos cases of Fig. 5.8. A clear monotonic increase of $A(t)$ is visible. The values of $A(t)$ are well fitted by a power law $A(t) \propto t^{\alpha_A}$ with $\alpha_A \approx 0.5$ [black dashed line in Fig. 5.12]. The slight slowing down observed for cases W3_{2D} and W4_{2D} [(r)ed and (c)yan curves in Fig. 5.12] at the end of the integration is likely due to the fact that the integration time is not enough to display a firm asymptotic behavior of the chaotic seeds. This is supported by the fact that for all cases, the second moment $m_2(t)$ (5.5) in Figs. 5.8(a) and (b) showed that the system has truly reached the weak chaos regime around the last decade of the evolution. Nevertheless, the fact that the $A(t)$ values monotonically increase up to $A(t) \propto 10^{2.5} \approx 300$ sites at the final stages of the simulations, which correspond to areas much larger than the estimates of the NM localization volume is a strong evidence that the chaotic seeds are visiting sites far away from the lattice's center.

5.4.2 The strong chaos regime

We also investigate the behavior of the DVD (5.2) in the strong chaos regime. In Fig. 5.13, we show

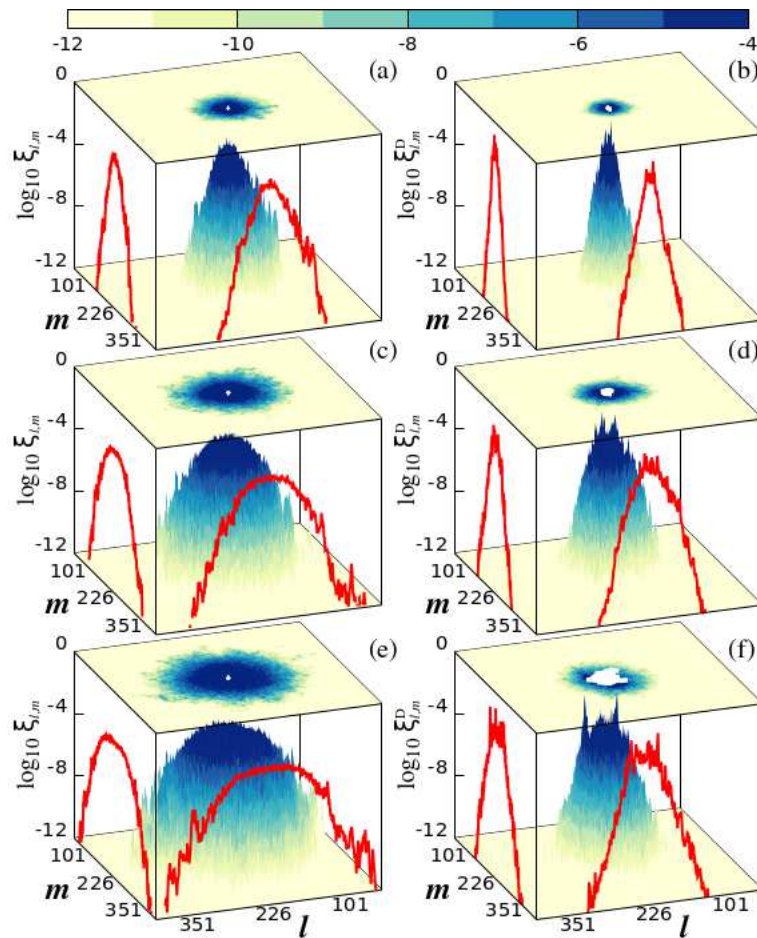


Figure 5.13: Similar to Fig. 5.10 but for a representative realization of the S1_{2D} strong chaos case. Panels (a) and (b) correspond to the configurations of the $\xi_{l,m}$ (5.1) and $\xi_{l,m}^D$ (5.2) at $\log_{10} t \approx 3$, panels (c) and (d) at $\log_{10} t \approx 4.8$ and panels (e) and (f) at $\log_{10} t \approx 5.90$.

the evolution of the norm density $\xi_{l,m}$ (5.1) and its related DVD $\xi_{l,m}^D$ (5.2) at three different times $\log_{10} t \approx 3.0$ [panels (a) and (b)], $\log_{10} t \approx 4.8$ [panels (c) and (d)] and $\log_{10} t \approx 5.9$ [panels (e) and (f)] for a representative disorder realization of the S1_{2D} case. Similarly to the weak chaos case [Figs. 5.10(a), (c) and (e)], in Figs. 5.13(a), (c) and (e) we see that the norm density $\xi_{l,m}$ (5.1) spreads more or less evenly around its center [white region in the color map of the upper sides of Figs. 5.13(a), (c) and (e)] which remains practically fixed. On the other hand the DVD $\xi_{l,m}^D$ (5.2) maintains a rather localized pointy shape. In addition, its center meanders inside the wave packet interior with increasing amplitude, as indicated by the always growing white regions at the center of the upper sides of Fig. 5.13 (b), (d) and (f). These oscillations are much larger compared to what was observed in the weak chaos case [see

Figs. 5.10(b), (d) and (f)].

In order to substantiate these observations, in Figs. 4.14(a) and (b) we respectively show the time evolution of the DVD's second moment $m_2^D(t)$ (5.5), and participation number $P^D(t)$ (3.6). A slow increase of the values of the $m_2^D(t)$, which are well fitted by the power law $m_2^D(t) \propto t^{0.17}$ is observed, much smaller than the wave packet's second moment evolution $m_2(t) \propto t^{0.33}$ in Figs. 5.9(a) and (b). The saturation of the P^D values is clearly seen in Fig. 5.14(b), where fluctuations in the interval $P^D \approx 10$ for $S_{4_{2D}}$ [(c)yan curve in Fig. 5.14(b)] up to $P^D \approx 10^{1.4} \approx 25$ in the case of $S_{1_{2D}}$ [(b)lue curve in Fig. 5.14(b)] are observed. In both cases the P^D values are of the order of the NM localization volume $\bar{V} \approx 10$ and 28, respectively at $W = 14$ and 10.5 [Table 5.1]. Consequently, the DVD $\xi_{l,m}^D$ (5.2) remains localized during the system's evolution, with its extent reaching approximately the NM's average localization volume. Similarly to the weak chaos case, we understand the larger fluctuations in the calculations of the $m_2^D(t)$ (5.5) and $P^D(t)$ (3.6) based on the rather small number of considered disorder realizations and the complex geometry of 2D NMs.

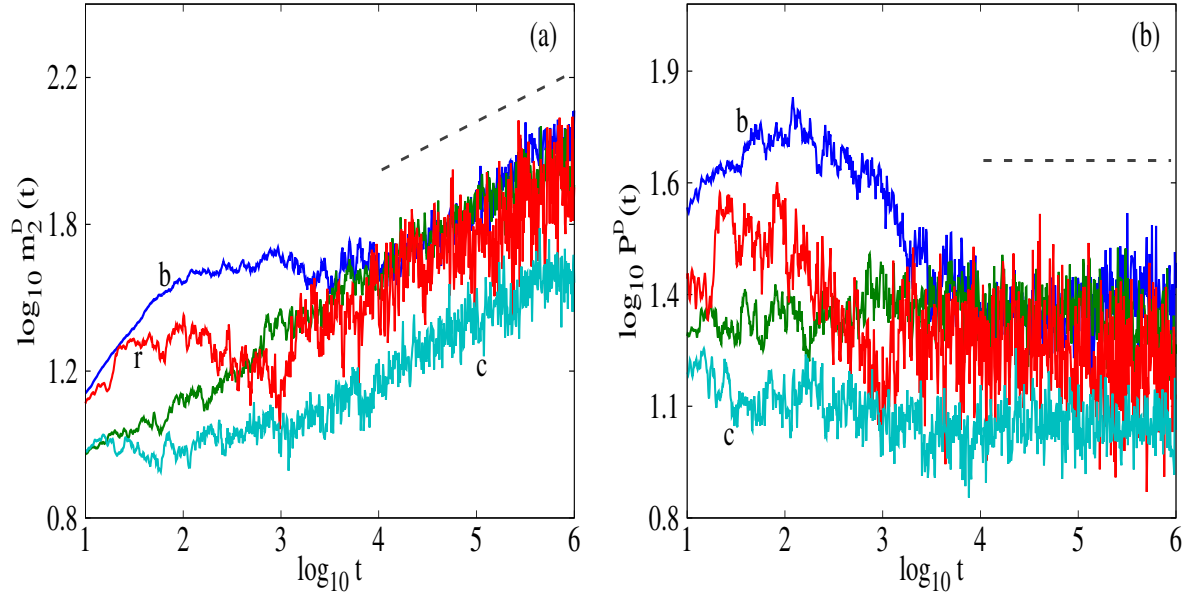


Figure 5.14: Similar to Fig. 5.11, but for the strong chaos regime of the 2D DDNLS system (2.20). The dashed lines in panels (a) and (b) guide the eye for slopes 0.17 and 0.0 respectively. The curve's colors correspond to the ones used in Fig. 5.9.

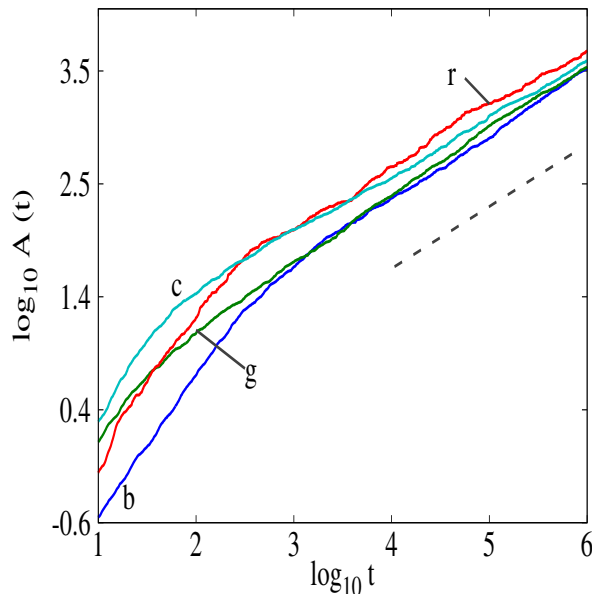


Figure 5.15: Similar to Fig. 5.12, but for the strong chaos regime of the 2D DDNLS system (2.20). The dashed line indicates slope 0.55. The curve's colors correspond to the ones used in Fig. 5.9.

The time dependence of the area $A(t)$ (5.14) visited by the DVD center is shown in Fig. 5.15 for all the strong chaos cases of Fig. 5.14. As in the case of weak chaos, a monotonic increase of the A values is observed for all cases. At the final integration time ($\log_{10} t = 10^6$), this quantity has reached values $A \approx 10^{3.5} \approx 3162$ for all cases, which are much larger than any NM average localization volume [see Table 5.1]. In addition, the values of $A(t)$ are well fitted by a power law $A \propto t^{\alpha_A}$ with $\alpha_A \approx 0.55$. Consequently, this provides a strong indication that the chaotic seeds are consistently visiting sites far from the central part of the lattice. It is worth mentioning that similar results were also obtained for the 2D DKG system (2.27) in [Many Manda et al., 2020].

5.5 Discussion and summary

Let us now summarize the main features of the chaotic dynamics of the wave packet spreading in the 2D DDNLS lattice (2.20). The chaos strength of the wave packet spreading was performed through the computation of the system's ftMLE $\Lambda(t)$ (3.21). More specifically, we found that the $\Lambda(t) \propto t^{-0.37}$ in the weak and $\Lambda(t) \propto t^{-0.46}$ for the strong chaos regimes. These behaviors are clearly different from what is observed in the case of regular motion ($\Lambda \propto t^{-1}$), confirming that the wave packet remains chaotic although its chaos strength decreases in time. As to the question of whether wave packet chaotization is fast enough to support the wave packet subdiffusion, we can compare the wave packet's spreading timescale $T_M = 1/D$, with $D = dm_2/dt$ to its Lyapunov time $T_L = 1/\Lambda$ (4.15). By doing that, we find that since $m_2 \sim t^{\alpha_m}$ and $\Lambda \sim t^{\alpha_\Lambda}$

$$\frac{T_M}{T_L} \sim t^{1-\alpha_\Lambda-\alpha_m}, \quad (5.17)$$

which leads to

$$\frac{T_M}{T_L} \sim t^{0.43}, \quad (5.18)$$

for the weak chaos regime where $\alpha_m = 1/5$ and $\alpha_\Lambda = -0.37$, and to

$$\frac{T_M}{T_L} \sim t^{0.21}, \quad (5.19)$$

for the strong chaos regime where $\alpha_m = 1/3$ and $\alpha_\Lambda = -0.46$. Thus, T_L is always smaller than T_M , such that the wave packet chaotization happens faster than its spreading to more sites.

By examining the ratios T_M/T_L obtained in all spreading dynamical regimes for both the 1D and 2D DDNLS models i.e.

$$\frac{T_M}{T_L} \sim t^{0.43} \quad (\text{weak chaos}), \quad \frac{T_M}{T_L} \sim t^{0.21} \quad (\text{strong chaos}) \quad (5.20)$$

obtained in Eq. (5.18) and (5.19) for the 2D DDNLS model (2.20) and

$$\frac{T_M}{T_L} \sim t^{0.42} \quad (\text{weak chaos}), \quad \frac{T_M}{T_L} \sim t^{0.20} \quad (\text{strong chaos}), \quad (5.21)$$

observed for the 1D DDNLS system (2.17) in Sec. 4.5, we see a remarkable closeness of exponents in Eqs. (5.20) and (5.21). This is a strong indication that nonlinear interactions of the same nature are responsible for the wave packet spreading in the cases of both spatial dimensions within the thermal region of the energy-norm parameter space. This is in agreement with the theoretical calculations performed in Sec. 2.5. Indeed, for both the 1D and 2D DDNLS systems, we ended up with the same reduced equation of the asymptotic dynamics

$$i\frac{\partial\phi_\nu}{\partial t} \sim E_\nu\phi_\nu + \beta\mathcal{P}(\beta\phi_{\nu_1}^2)\phi_{\nu_1}^3 f(t). \quad (5.22)$$

Here, the nonlinear term $\beta\mathcal{P}(\beta\phi_{\nu_1}^2)\phi_{\nu_1}^3 f(t)$ is responsible for the thermalization of more sites in both lattices. Note that in Eq. (5.22) ν and ν_1 represent respectively the non-thermalized and thermalized modes. Thus, only the geometry of the problem affects the spreading and the chaotic dynamics of the wave packet.

Notice that equating the T_M/T_L ratios of Eqs. (5.20) and (5.21) for each dynamical regime, we can write

$$\frac{\Lambda^1}{m_2^1} = \frac{\Lambda}{m_2}, \quad (5.23)$$

where the subscript '1' refers to the 1D lattice. Equation (5.23) allows the prediction of the characteristics of chaos of the wave packet dynamics. For example, using the relations describing the time evolution

of the wave packet second moment m_2 in Chap. 2 and the results obtained for the computation of the ftMLEs of the 1D DDNLS system in Chap. 4, we get from Eq. (5.23)

$$\Lambda \sim t^{\alpha_m - \alpha_m^1 + \alpha_\Lambda^1}. \quad (5.24)$$

Then, we obtain for the behavior of the ftMLE in the case of the 2D lattice

$$\Lambda \sim t^{-0.38}, \quad (5.25)$$

for the weak chaos regime where $\alpha_m^1 = 1/3$, $\alpha_m = 1/5$ and $\alpha_\Lambda = -0.25$, and

$$\Lambda \sim t^{-0.47}, \quad (5.26)$$

in the strong chaos case where $\alpha_m^1 = 1/2$, $\alpha_m = 1/3$ and $\alpha_\Lambda = -0.3$. Both laws (5.25) and (5.26) are extremely similar to the $\Lambda \sim t^{-0.37}$ and $\Lambda \sim t^{-0.46}$ found numerically in Sec. 5.3.

Similarly to what was seen in the 1D case, the evolution of the DVD revealed the mechanism of wave packet chaotization: Localized chaotic seeds randomly oscillate in the wave packet's interior, homogenizing chaos for the lattice's excited region and thermalizing neighboring initially unexcited sites. Indeed, our numerical computations showed a DVD's second moment $m_2^D(t)$ (5.5) which slowly increases in time following a $m_2(t) \propto t^{0.12} - t^{0.17}$ law. In addition, the DVD's participation number P^D saturated at values of the order of the NM average localization volume. Thus, the DVD always retains a rather localized and pointy shape, which randomly meanders inside the wave packet's interior in both the weak and strong chaos regimes.

The numerical computations of the area A (5.13) visited by the the DVD's center showed a monotonically increasing relation with time, reaching values $A \approx 300$ sites in the weak and $A \approx 3000$ sites in the strong chaos regimes for final integration time $t_f \approx 2 \times 10^6$. Fitting the variations of A with the power law t^{α_A} , we found $\alpha_A \approx 0.5$ (weak chaos) and $\alpha_A \approx 0.55$ (strong chaos). The fact that we observed larger values of A and larger increase rates in the strong chaos case compared to the weak chaos one is in agreement with the results of Chap. 2 [see e.g. Flach, 2010]. Indeed, as in the 1D DDNLS lattice, the faster spreading in the strong chaos case implies that chaotic seeds visit larger regions of the lattice as faster homogenization of chaos and thermalization of more lattice sites is required.

The fact that all these behaviors have been found in both the 1D and 2D lattices of the DDNLS and DKG models is a clear indication of the generality of our findings.

Chapter 6

Summary and outlook

This work presented results regarding the contribution of chaotic dynamics to wave packet spreading in disordered multidimensional Hamiltonian models. In particular, we focussed on the well known one (1D) and two dimensional (2D) disordered discrete nonlinear Schrödinger (DDNLS) models, which are generic in modelling physical systems such as the conductivity of metals, the propagation of light in optical media or the expansion of trapped Bose-Einstein condensates. The aim of this work was to give more insights into the long standing question of whether a wave packet spreading in a disordered medium will expand forever or halt after a certain amount of time, based on the computation of observables of the system's tangent dynamics such as the maximum Lyapunov exponent (MLE) and its related deviation vector distribution (DVD). This question is of utmost importance as it links up to several physical aspects like the ergodic, chaotic and statistical properties of multidimensional nonlinear systems which are still widely debated. In the next paragraphs, we recapitulate our work and give some of the possible open avenues along which this study could be taken forward.

As a preliminary step to reaching our goal, in Chap. 2 we presented the theory behind the wave packet spreading in the 1D and 2D DDNLS systems. Firstly, we outlined the so called Anderson localization (AL), whereby in a disordered linear model, localized excitations remain in that state forever, not diffusing through the lattice. Then, we discussed what happens to the AL when nonlinearity is introduced into the system. Upon examining the dynamical behavior of normal modes (NMs), we found that when AL prevails, the NMs possess a discrete frequency spectrum coupled to a spatially localized nature which gets more pronounced when the disorder becomes stronger in the system. On the other hand, when nonlinearity is switched on, the NMs overlap and interact, allowing the energy to move from mode to mode in a deterministic chaotic manner. Consequently, the AL does not survive, leading to an avenue for a subdiffusive spreading of the initially localized excitation. Depending on the strength of the overlapping part, which is expressed as a function of the norm \mathcal{S} , the total energy \mathcal{H} , the magnitude of the nonlinear coefficient β and the disorder strength W , we discussed how two different subdiffusive behaviors of the localized excitation can take place. In particular, the so-called weak chaos regime where the wave packet extent, measured through the second moment m_2 (3.5) [participation number P (3.6)], increases according to $m_2 \sim t^{\alpha_m}$ [$P \sim t^{\alpha_P}$] with $\alpha_m = 1/3$ [$\alpha_P = 1/6$] for the 1D DDNLS model and $\alpha_m = 1/5$ [$\alpha_P = 1/5$] in the case of the 2D system. In addition, the so-called strong chaos regime, with a faster wave packet expansion where the power law exponents for the m_2 [P] are $\alpha_m = 1/2$ [$\alpha_P = 1/4$] in the case of the 1D and $\alpha_m = 1/3$ [$\alpha_P = 1/3$] for the 2D DDNLS system can also appear.

In order to investigate the chaotic dynamics of the spreading regimes mentioned above, we mainly relied on numerical experiments. This is motivated by the difficulty involved with an analytical treatment of the stochasticity appearing both in the system's equations of motion and tangent dynamics. Due to the complexity of integrating the equations of motion of the DDNLS models compared to other multidimensional lattice models like the disordered Klein-Gordon (DKG) and Fermi-Pasta-Ulam-Tsingou (FPUT) chains of nonlinear oscillators, no particular effort in designing efficient numerical methods for integrating the variational equations of the former were undertaken to date. Thus, a large part of Chap. 3 is dedicated to designing efficient, accurate and fast numerical integration techniques for the long time integration of the system's equations of motion and the variational equations required in this study. We exploited symplectic integrators (SIs), which are numerical schemes specifically built for integrating the equations of motion of Hamiltonian models, along with the tangent map method [see e. g. Skokos and Gerlach, 2010] in order to evolve the variational equations. Note that SIs keep the computed energy of the system constant up to a certain level of accuracy which can be associated with the precision of the integrator. We presented methods based on the two part (only for the 1D DDNLS model) and three part split approaches of the Hamiltonian functions of the 1D and 2D DDNLS systems and compared their performances based on standard schemes like the *DOP853* [Hairer et al., 1993], a Runge-Kutta (RK)

integrator of order 8 based on the Dormand and Prince method and the *TIDES* algorithm based on Taylor/Lie series expansions of the system's field equations [Abad et al., 2012, 2014].

Then, we studied the performance of the designed SIs in Sec. 3.8 of Chap. 3 based on their ability to accurately reproduce the system's dynamical behavior. For instance, this was quantified by checking the constancy of the total energy \mathcal{H} and norm \mathcal{S} through the computation of the relative energy and norm errors, respectively denoted as E_r and S_r . We also calculated the characteristics of the wave packet spreading, i.e. the time evolution of the second moment m_2 and the participation number P , and evaluated the precision of the evolution of the variational equations based on the computed finite time maximum Lyapunov exponent (ftMLE) Λ for several initial conditions. We focussed on two energy accuracy levels: moderate accuracy with $E_r \lesssim 10^{-5}$, which is often considered to be a good precision in nonlinear lattice studies [see e.g. Lapyteva et al., 2010; Skokos et al., 2013], as well as high accuracy where the threshold values $E_r \lesssim 10^{-9}$ were used [see e.g. Sales et al., 2018]. All the tested numerical integrators produced similar results for both the evolution of system's phase space and tangent dynamics. Although the *DOP853* and the *TIDES* are the most accurate of all the integrators we tested, the fact that they do not preserve the values of the computed total energy and norm (E_r and S_r are not bounded from above) makes them a not ideal choice for the long time evolution of the system's dynamical equations. On the other hand, we found that SIs in general take less CPU time than the *DOP853* and *TIDES* in order to reproduce the same system dynamics with the three part split SIs performing better than the two part split SIs for large lattice sizes, i.e. when the number of degrees of freedom $N \gtrsim 70$. In particular the *s11ABC6* and *s9ABC6* SIs of order 6 along with the *s17ABC8* and *s19ABC8* SIs of order 8 proved to be the best integrators respectively for moderate ($E_r \lesssim 10^{-5}$) and high ($E_r \lesssim 10^{-9}$) accuracies. The results of these investigations were presented in a recent research paper [Danieli et al., 2019a].

In Chap. 4, we computed the time evolution of the finite time MLE (ftMLE) and the spatiotemporal evolution of its related DVD for the 1D DDNLS model in the weak and strong chaos spreading regimes. We considered a total of 8 cases, 4 cases in the weak chaos and 4 in the strong chaos regimes. For each case, we averaged the observables of the system's phase space and tangent dynamics over 100 different realizations i.e. different values of the lattice's disorder parameters ϵ_l , for norm and energy values located in the same thermal regime. In all cases, a decay of the ftMLE Λ following the power law $\Lambda \sim t^{\alpha_\Lambda}$ was seen. For the weak chaos case the power law exponent was fitted to $\alpha_\Lambda \approx -0.25$ while in the strong chaos regime, a smaller exponent value $\alpha_\Lambda \approx -0.3$ was found. As both exponents are different from $\alpha_\Lambda = -1$ observed for regular motion, we concluded that these wave packet dynamics remain always chaotic up to the largest times of our simulations ($t_f \approx 10^8$). We correlated the different values of α_Λ of the weak and strong chaos regimes to the wave packet spreading dynamics. Indeed, as the wave packet spreading is faster in the strong chaos, the constant total norm is shared to a larger number of thermalized lattice sites resulting in a faster decay of the norm per site s and consequently of the effective nonlinearity, which is approximately βs^2 . As a result, the system is driven to the integrable limit quicker in the strong chaos regime, and the $\alpha_\Lambda = -0.3$ value is closer to the regular case ($\alpha_\Lambda = -1$) compared to $\alpha_\Lambda = -0.25$ seen in the weak chaos case.

The motion of the DVD related to the computation of the MLE showed random fluctuations of chaotic spots (called chaotic seeds) which are known to homogenize chaos inside the excited part of the lattice and contribute to the wave packet thermalization. The computation of the second moment m_2^D and the participation number P^D of the DVD in the weak chaos regime showed that the DVD extent increases slowly in time as $m_2^D \sim t^{0.14}$ and $P^D \sim t^{0.04}$, with P^D showing a tendency to saturate to values of the order of the NM's localization volume. This process is faster in the strong chaos case where a clear constancy of the m_2^D and P^D was visible from time $t \gtrsim 10^5$. In addition, we computed the length R of the region visited by the DVD center and found that this quantity monotonically increases in time for all cases, to values $R \approx 10^2$ and $R \approx 10^3$ at the largest times of our simulations in the weak and strong chaos regimes respectively. These values of R are much larger than the NM localization volume and therefore constitute clear numerical evidence that modes other than the initially excited ones also contribute to the wave packet thermalization. The obtainment of larger R values in the strong chaos case is likely related to the fact that a faster spreading of the wave packet is seen in that regime, so that chaotic seeds have to travel to larger excited regions of the lattice. In addition, we found that the time dependence of R is well fitted by $R \sim t^{\alpha_R}$, where $\alpha \approx 0.24$ for the weak chaos case, while the strong chaos case, exhibits higher values of α_R which decrease in time toward $\alpha_R \approx 0.24$. This result can be explained by taking into account the fact that the strong chaos regime is a transient one, meaning that an asymptotic crossover of the chaotic dynamics of the system to the weak chaos behavior has to be seen after a finite amount of time. A large part of the results of Chap. 4 have been reported in [Senyange et al., 2018].

Chapter 5, focussed to the same questions as in Chap. 4 but this time for the 2D DDNLS model. Notice that, to the best of our knowledge, this is the first time that such a detailed investigation has been performed for this model mainly due to the fact that the integration of the equations of motion and variational equations of this system is a computationally very difficult task. In our study, we considered

4 initial conditions in the weak chaos and 4 in the strong chaos regions. For each case, we averaged the observables of the system's phase space and tangent dynamics over 50 disorder realizations. Our numerical computations confirmed the theoretical expected values of the wave packet spreading characteristics i.e. $m_2 \sim t^{\alpha_m}$ with $\alpha_m = 1/5$ in the weak and $\alpha_m = 1/3$ for the strong chaos regimes respectively. Furthermore, the computation of Λ showed a decaying chaos strength, whose time dependence was well fitted by $\Lambda \sim t^{\alpha_\Lambda}$ with $\alpha_\Lambda < 0$ being similar to the 1D system. Actually, the values $\alpha_\Lambda \approx -0.37$ and $\alpha_\Lambda \approx -0.46$ were found respectively for the weak and strong chaos cases. It is worth noticing again that these values are different from $\alpha_\Lambda = -1$ which is seen in the case of regular motion. Thus the wave packet always remains chaotic in the 2D DDNLS model as well. Furthermore we found a dimension independent scaling between the wave packet dynamics (measured through the m_2) and its degree of chaoticity (measured through the Λ) between the 1D and 2D models. It will be interesting to check if this relation also holds for three dimensional models as well.

Chaos is not the only ingredient needed for wave packet spreading, as the other necessary component is the random oscillations of chaotic seeds within the lattice's excited part. The evolution of the DVD obtained during the computation of the ftMLEs in the 2D DDNLS system also revealed the existence of localized chaotic spots which randomly wander inside the excited part of the lattice. Indeed, in the weak chaos case a timid spatial expansion of the DVD was observed over time as its second moment grew as $m_2^D \sim t^{0.12}$ and the participation number P^D showed a tendency to saturate to values similar to the 2D NM's localization volume at later stages of the evolution. The saturation of these observables was again much faster for the strong chaos cases as a relation of the form $P^D \sim t^0$ could be fitted to the data over a larger period of time compared to the weak chaos case. In addition, we computed the area A ($A \sim R^2$) visited by the DVD center and found a monotonic increase, leading to values much larger than the NM's localization volume. Specifically, the values $A \approx 10^2$ and $A \approx 10^4$ are found for the weak and strong chaos regimes at the final time of integration, suggesting that the DVD visited sites far from the lattice's center. Further, the temporal dependence of A was well fitted by $A \sim t^{\alpha_A}$, where the values $\alpha_A \approx 0.5$ and $\alpha_A \approx 0.55$ were obtained for the weak and strong chaos regimes respectively. Similarly to the 1D DDNLS model, the higher values of A and stronger variations of α_A observed in the strong chaos regime can be related to the faster spreading of the wave packet in that regime, meaning that the DVD has to cover larger areas of the excited part of the lattice than in the weak chaos case. Consequently, the mechanisms of chaos responsible of the wave packet spreading in the 1D and 2D DDNLS systems are similar. Most of findings of this chapter have been reported in a recent research paper [Many Manda et al., 2020].

It is worth noting that similar results to the ones presented in Chaps. 4 and 5 of this thesis have been obtained for the 1D and 2D DKG models in [Skokos et al., 2013; Senyange et al., 2018; Many Manda et al., 2020], emphasizing the generality of our findings.

Although our study contributed in comprehending several aspects of the dynamical behavior of localized initial excitations in disordered systems, several issues still need to be investigated. For instance the energy-norm density spaces of the 1D and 2D DDNLS systems discussed in Sec. 2.4 revealed a more complex partition between the wave packet spreading regions and the thermal and non-thermal phases, also underlined in a recent work [Kati et al., 2020]. Thus, the techniques used in this work to study the weak and strong chaos spreading regimes could be used in further investigating the connection between the wave packet spreading and the ergodic properties of these two models. Another important aspect is the theoretical determination of the observed power law exponents of the ftMLE seen in this work for both the 1D and 2D DDNLS systems. Achieving this goal could help, for instance in predicting the system's dynamical characteristics for nonlinear strengths and model's dimensionalities far from the reach of current computer simulations. In addition, we pinned the motion of the DVD as random and therefore the evolution of the DVD center could be approximated by the spatial evolution of a random walker evolving in a field of one or two spatial dimensions. This means that, the total length/area covered represents only a single possible measurement among many others of the characteristics of the DVD as a wide theory exists around random walks. Furthermore, as the DVD generated during the computation of the MLE shows the location of only the chaotic spot with the largest instantaneous chaoticity, another important challenge is related to the construction of a method to investigate most, if not all, of the chaotic spots, as they are central in understanding the NM interactions. Pursuing methods to extend all these ideas could potentially reveal more subtle changes in the wave packet spreading dynamical behavior, allowing a better in depth understanding of chaos properties in multidimensional systems.



List of abbreviations

The following abbreviations are used throughout the content of this thesis.

- 1D – One-Dimensional/One-Dimension.
- 2D – Two-Dimensional/Two-Dimension.
- AL – Anderson Localization.
- BCH – Baker-Campbell-Hausdorff.
- CPU – Central Processing Unit.
- DDLS – Disordered Discrete Linear Schrödinger.
- DDLSE – Disordered Discrete Linear Schrödinger Equation.
- DDNLS – Disordered Discrete NonLinear Schrödinger.
- DKG – Disordered Klein-Gordon.
- DOP – Dormand and Prince.
- DV – Deviation Vector.
- DVD – Deviation Vector Distribution.
- FPUT – Fermi-Pasta-Ulam-Tsingou.
- ftMLE – finite-time Maximum Lyapunov Exponent.
- KAM – Kolmogorov-Arnol'd-Moser.
- MLE – Maximum Lyapunov Exponent.
- NM – Normal Mode.
- ODE – Ordinary Differential Equation.
- RK – Runge-Kutta.
- SI – Symplectic Integration/Symplectic Integrator.



Appendix A

Frequency spectrum of the 1D DDLS model and the 1D DKG system of harmonic oscillators

A.1 The 1D DDLS model

Here we analytically determine the characteristics of the bandwidth of the frequency spectrum of the DDLS model. Its Hamiltonian takes the form [see Eq. (2.1)]

$$\mathcal{H}_L = \sum_l \epsilon_l |\psi_l|^2 - (\psi_l^* \psi_{l+1} + \psi_l \psi_{l+1}^*), \quad (\text{A.1})$$

where $\psi_l \in \mathbb{C}$ is the wave function and ϵ_l the disorder parameter at site l . The values of ϵ_l in (A.1) are chosen from a uniform probability distribution $\mathcal{P}_W = 1/W$ on the interval $[-W/2, W/2]$, with W denoting the system's disorder strength. As has already been mentioned many times in this thesis, plane waves describe the solution of Hamiltonian (A.1). Consequently we write the wave function at site l with norm s_l and phase θ_l (which modulates the value of the energy h_l), as

$$\psi_l = \sqrt{s_l} \exp(i\theta_l). \quad (\text{A.2})$$

In this thesis we have been working (without loss of generality) with homogeneous initial wave packets so that $s = s_l$, for all the initially excited sites. In this situation, the Hamiltonian (A.1) becomes

$$\mathcal{H}_L = \sum_l \epsilon_l s - 2s \cos(\theta_{l+1} - \theta_l). \quad (\text{A.3})$$

Since the cosine function is bounded, the value of \mathcal{H}_L can also be bounded as

$$\sum_l (\epsilon_l - 2) s \leq \sum_l \epsilon_l s - 2s \cos(\theta_{l+1} - \theta_l) \leq \sum_l (\epsilon_l + 2) s. \quad (\text{A.4})$$

In particular, the extreme case for the lower bound of (A.4) leads to a minimum value when all sites have $\epsilon_l^- = -W/2$. In the same way, the scenario corresponding to the maximum possible value of the upper bound in (A.4) is all sites having $\epsilon_l^+ = W/2$. Thus,

$$\sum_l \left(-\frac{W}{2} - 2 \right) s \leq \sum_l \epsilon_l s - 2s \cos(\theta_{l+1} - \theta_l) \leq \sum_l \left(\frac{W}{2} + 2 \right) s. \quad (\text{A.5})$$

Summing up each term of (A.5), we get

$$\mathcal{H}_L^- = E^- \mathcal{S}_{1D} \leq \mathcal{H}_L \leq E^+ \mathcal{S}_{1D} = \mathcal{H}_L^+, \quad (\text{A.6})$$

with

$$E^- = -2 - \frac{W}{2}, \quad E^+ = 2 + \frac{W}{2}, \quad (\text{A.7})$$

and $\mathcal{S}_{1D} = \sum_l s$ being the total norm of the system which is a conserved quantity. It is worth noticing that the Hamiltonian functions $\mathcal{H}_L^\pm = E^\pm \mathcal{S}_{1D}$ model independent harmonic oscillators, each one of which

has the same proper frequency E^\pm . The inequality in (A.6) involves solely macroscopic quantities and therefore is valid for all kinds of initial states of the system.

Applying the linear differentiation operator $\frac{\partial}{\partial(i\psi_r^*)}$ in (A.6), we obtain

$$\begin{aligned} \begin{pmatrix} E^- & 0 & \dots & 0 & 0 \\ 0 & E^- & \dots & 0 & 0 \\ \vdots & \vdots & \ddots & \vdots & \vdots \\ 0 & 0 & \dots & E^- & 0 \\ 0 & 0 & \dots & 0 & E^- \end{pmatrix} \begin{pmatrix} \psi_1 \\ \psi_2 \\ \vdots \\ \psi_{N-1} \\ \psi_N \end{pmatrix} &\leq \begin{pmatrix} \epsilon_1 & -1 & 0 & \dots & 0 & 0 \\ -1 & \epsilon_2 & -1 & \dots & 0 & 0 \\ \vdots & \vdots & \vdots & \ddots & \vdots & \vdots \\ 0 & 0 & 0 & \dots & \epsilon_{N-1} & 0 \\ 0 & 0 & 0 & \dots & -1 & \epsilon_N \end{pmatrix} \begin{pmatrix} \psi_1 \\ \psi_2 \\ \vdots \\ \psi_{N-1} \\ \psi_N \end{pmatrix} \\ &\leq \begin{pmatrix} E^+ & 0 & \dots & 0 & 0 \\ 0 & E^+ & \dots & 0 & 0 \\ \vdots & \vdots & \ddots & \vdots & \vdots \\ 0 & 0 & \dots & E^+ & 0 \\ 0 & 0 & \dots & 0 & E^+ \end{pmatrix} \begin{pmatrix} \psi_1 \\ \psi_2 \\ \vdots \\ \psi_{N-1} \\ \psi_N \end{pmatrix}, \end{aligned} \quad (\text{A.8})$$

where the ‘ \leq ’ compares the system’s field vectors element by element. Equation (A.8), can be reduced to a matrix form

$$\mathbf{D}^- \Psi \leq \tilde{\mathbf{A}} \Psi \leq \mathbf{D}^+ \Psi, \quad (\text{A.9})$$

with

$$\mathbf{D}^\pm = \begin{pmatrix} E^\pm & 0 & \dots & 0 & 0 \\ 0 & E^\pm & \dots & 0 & 0 \\ \vdots & \vdots & \ddots & \vdots & \vdots \\ 0 & 0 & \dots & E^\pm & 0 \\ 0 & 0 & \dots & 0 & E^\pm \end{pmatrix}, \quad \text{and} \quad \Psi = \begin{pmatrix} \psi_1 \\ \psi_2 \\ \vdots \\ \psi_{N-1} \\ \psi_N \end{pmatrix}. \quad (\text{A.10})$$

In addition in (A.9) $\tilde{\mathbf{A}}$ is a tridiagonal matrix with entries

$$\tilde{\mathbf{A}} = \begin{pmatrix} \epsilon_1 & -1 & 0 & \dots & 0 & 0 \\ -1 & \epsilon_2 & -1 & \dots & 0 & 0 \\ \vdots & \vdots & \vdots & \ddots & \vdots & \vdots \\ 0 & 0 & 0 & \dots & \epsilon_{N-1} & -1 \\ 0 & 0 & 0 & \dots & -1 & \epsilon_N \end{pmatrix}. \quad (\text{A.11})$$

The matrix $\tilde{\mathbf{A}}$ is diagonalizable [Gershgorin, 1931; Wolkowicz and Styan, 1980; Smith, 1985; Losonczi, 1992; Yueh, 2005; Da Fonseca and Kowalenko, 2019]. Its corresponding diagonal matrix \mathbf{D} has as diagonal elements the eigenvalues E_ν , $\nu = 1, 2, \dots, N$ of $\tilde{\mathbf{A}}$. Defining \mathbf{P} a matrix having as columns the normalized eigenvectors related to the eigenvalues of \mathbf{D} , we get

$$\mathbf{D}^- \Psi \leq \mathbf{P} \mathbf{D} \mathbf{P}^{-1} \Psi \leq \mathbf{D}^+ \Psi. \quad (\text{A.12})$$

Multiplying from the left side (A.12) by \mathbf{P}^{-1} leads to

$$\mathbf{D}^- \mathbf{P}^{-1} \Psi \leq \mathbf{D} \mathbf{P}^{-1} \Psi \leq \mathbf{D}^+ \mathbf{P}^{-1} \Psi, \quad (\text{A.13})$$

where we used $\mathbf{P}^{-1} \mathbf{P} = \mathbf{P} \mathbf{P}^{-1} = \mathbf{I}_N$ with \mathbf{I}_N being the $N \times N$ identity matrix. Setting the state vector $\mathbf{U} = \mathbf{P}^{-1} \Psi$, we therefore end up with a set of uncoupled oscillators

$$\mathbf{D}^- \mathbf{U} \leq \mathbf{D} \mathbf{U} \leq \mathbf{D}^+ \mathbf{U}, \quad (\text{A.14})$$

whose frequency spectra can be compared wave number by wave number in the matrices of (A.14). What comes out from this comparison is the inequality

$$E^- \leq E_\nu \leq E^+, \quad (\text{A.15})$$

with E_ν , $\nu = 1, 2, \dots, N$ representing the eigenvalues of matrix $\tilde{\mathbf{A}}$. Therefore, the width of the frequency spectrum is

$$\Delta = E^+ - E^- = W + 4, \quad (\text{A.16})$$

since

$$E_\nu \in \left[-2 - \frac{W}{2}, 2 + \frac{W}{2} \right]. \quad (\text{A.17})$$

A.2 The 1D DKG system of harmonic oscillators

We can express the linear characteristics of the DKG model in terms of the DDLS model. The Hamiltonian function of the linear DKG model of harmonic oscillators reads [see e.g. [Skokos et al., 2009](#)]

$$\mathcal{H}_{LK} = \sum_l \frac{p_l^2}{2} + \frac{\tilde{\epsilon}_l}{2} q_l^2 + \frac{1}{2W} (q_{l+1} - q_l)^2, \quad (\text{A.18})$$

and its related equations of motion can be written as

$$\ddot{q}_l = \tilde{\epsilon}_l q_l + \frac{1}{W} (2q_l - q_{l-1} - q_{l+1}), \quad (\text{A.19})$$

where q_l and p_l are respectively the generalized position and conjugate momentum and $\tilde{\epsilon}_l$ denotes disorder parameter at site l . The values of ϵ_l are chosen on the interval $[1/2, 3/2]$ following a random uniform distribution. Here W denotes the disorder strength because it controls the size of the normal mode's localization volume \bar{V} [[Skokos et al., 2009](#); [Senyange et al., 2020](#)].

The solutions of (A.19) are of the form

$$q_l = A_l \exp(i\omega t), \quad (\text{A.20})$$

with A_l being the amplitude at site l and ω the frequency of oscillation. By substituting (A.20) to (A.19) we obtain the following eigenvalue problem

$$(\omega^2 W - W - 2) A_l = W (\tilde{\epsilon}_l - 1) A_l - A_{l-1} - A_{l+1}. \quad (\text{A.21})$$

The normal modes of (A.21) $\Psi_\nu = (A_{\nu,1}, A_{\nu,2}, \dots, A_{\nu,N})$, match the ones of the DDLS system (2.17) given in (2.5) by setting

$$E = \omega^2 W - W - 2, \quad (\text{A.22})$$

$$\epsilon_l = W (\tilde{\epsilon}_l - 1). \quad (\text{A.23})$$

Consequently Eq. (A.22) allows us to determine the limits of the frequency spectrum for the DKG system of linear oscillators (A.18) based on the results obtained for the DDLS model in Sec. A.1. In particular, using (A.7) the lower squared frequency ω_-^2 of the bandwidth is

$$E^- = \omega_-^2 W - W - 2 \Rightarrow -2 - \frac{W}{2} = \omega_-^2 W - W - 2 \Rightarrow \omega_-^2 = \frac{1}{2}, \quad (\text{A.24})$$

and the upper bound ω_+^2 is given by

$$E^+ = \omega_+^2 W - W - 2 \Rightarrow 2 + \frac{W}{2} = \omega_+^2 W - W - 2 \Rightarrow \omega_+^2 = \frac{3}{2} + \frac{4}{W}. \quad (\text{A.25})$$

Thus the size of the squared frequency spectrum of the DKG system of linear oscillators is

$$\Delta_K = \frac{3}{2} + \frac{4}{W} - \frac{1}{2} \Rightarrow \Delta_K = 1 + \frac{4}{W}. \quad (\text{A.26})$$

A more general derivation of this relation can be found in [[Senyange et al., 2020](#)].

Appendix B

Equations of motion of the 1D DDNLS system in the NM space

We recall the equations of motion of the 1D DDNLS system (2.18) are

$$i\dot{\psi}_l = \epsilon_l \psi_l + \beta |\psi_l|^2 \psi_l - (\psi_{l-1} + \psi_{l+1}). \quad (\text{B.1})$$

Writing the solution of Eq. (B.1) in the NM space of the system as a weighted sum over its linear NMs $\Psi_\nu \propto \bar{\zeta}^{-1/2} \exp[-(l - \bar{l}_\nu)/\bar{\zeta}]$

$$\psi_l = \sum_\nu \phi_\nu \Psi_\nu = \sum_\nu \phi_\nu A_{\nu,l}, \quad (\text{B.2})$$

where $\Psi_\nu = (A_{\nu,1}, A_{\nu,2}, \dots, A_{\nu,N})$ is the NM and ϕ_ν the time dependent amplitude at mode ν with $\nu = 1, 2, \dots, N$ (N being the lattice size), and substituting this expression in Eq. (B.1), we obtain

$$i \sum_\nu A_{\nu,l} \dot{\phi}_\nu = \sum_\nu \epsilon_l A_{\nu,l} \phi_\nu - \sum_\nu \phi_\nu A_{\nu,l-1} - \sum_\nu \phi_\nu A_{\nu,l+1} + \beta \sum_{\nu_1 \nu_2 \nu_3} A_{\nu_1,l}^* A_{\nu_2,l} A_{\nu_3,l} \phi_{\nu_1}^* \phi_{\nu_2} \phi_{\nu_3}. \quad (\text{B.3})$$

Taking into account Eq. (2.5) i.e. $EA_l = \epsilon_l A_l - A_{l-1} - A_{l+1}$, we rewrite (B.3) as

$$i \sum_\nu A_{\nu,l} \dot{\phi}_\nu = \sum_\nu E_\nu A_{\nu,l} \phi_\nu + \beta \sum_{\nu_1 \nu_2 \nu_3} A_{\nu_1,l}^* A_{\nu_2,l} A_{\nu_3,l} \phi_{\nu_1}^* \phi_{\nu_2} \phi_{\nu_3}, \quad (\text{B.4})$$

where E_ν is the frequency of the normal mode ν . We then multiply Eq. (B.4) by $\Psi_{\nu'}^*$, and get

$$i \sum_\nu \sum_l A_{\nu',l}^* A_{\nu,l} \dot{\phi}_\nu = \sum_\nu \sum_l A_{\nu',l}^* E_\nu A_{\nu,l} \phi_\nu + \beta \sum_{\nu_1 \nu_2 \nu_3} \sum_l A_{\nu',l}^* A_{\nu_1,l}^* A_{\nu_2,l} A_{\nu_3,l} \phi_{\nu_1}^* \phi_{\nu_2} \phi_{\nu_3}. \quad (\text{B.5})$$

At this point it is useful to emphasize few things:

(a) The orthogonality of the NMs leads to

$$\Psi_{\nu'}^* \Psi_\nu = \sum_l A_{\nu',l}^* A_{\nu,l} = \delta_{\nu',\nu}. \quad (\text{B.6})$$

(b) In the considered set up, initial conditions are chosen so that the total norm of any initial wave packet is set to unity. This leads to the condition

$$\sum_l |\psi_l|^2 = \sum_l \sum_{\nu'} \sum_\nu \phi_{\nu'}^* \phi_\nu \Psi_{\nu'}^* \Psi_\nu = \sum_\nu \sum_l A_{\nu,l}^* A_{\nu,l} \phi_\nu^* \phi_\nu = \sum_\nu |\phi_\nu|^2 = 1. \quad (\text{B.7})$$

Substituting Eq. (B.6) into Eq. (B.5) leads to

$$i\dot{\phi}_{\nu'} = E_{\nu'} \phi_{\nu'} + \beta \sum_{\nu_1 \nu_2 \nu_3} I_{\nu',\nu_1,\nu_2,\nu_3} \phi_{\nu_1}^* \phi_{\nu_2} \phi_{\nu_3}, \quad (\text{B.8})$$

where

$$I_{\nu',\nu_1,\nu_2,\nu_3} = \sum_l A_{\nu',l}^* A_{\nu_1,l}^* A_{\nu_2,l} A_{\nu_3,l}, \quad (\text{B.9})$$

is the so-called overlap-integral. Note that similar calculation can be performed for the DKG system [Laptyeva, 2013].



Appendix C

Statistical physics analytical computations

C.1 Derivation of Eq. (2.81)

We give here the detailed calculation of the integral

$$\tilde{y}_\beta(\tilde{\nu}, \mu_l) = \int_0^\infty dx e^{-\tilde{\nu}\mu_l x} e^{-\tilde{\nu}\frac{\beta}{2}x^2}, \quad (\text{C.1})$$

appearing in Eq. (2.80). In (C.1), $\tilde{\nu} = 1/T$ with T being the temperature of the system, β is the nonlinear coefficient of the 1D DDNLS model (2.17) and $\mu_l = \mu + \epsilon_l$ represents a kind of local chemical potential at site l of the lattice with ϵ_l being the disorder parameter of \mathcal{H}_{1D} (2.17). From the Taylor expansion of the exponential function $e^x = \sum_{n=0}^\infty x^n/n!$ we get

$$e^{-\tilde{\beta}\frac{x^2}{2}} = 1 - \frac{\tilde{\beta}x^2}{2} + \frac{\tilde{\beta}^2x^4}{8} + \dots, \quad (\text{C.2})$$

with $\tilde{\beta} = \beta\tilde{\nu}$. Substituting (C.2) into (C.1) leads to

$$\tilde{y}_\beta(\tilde{\nu}, \mu_l) = \int_0^\infty dx e^{-\tilde{\nu}\mu_l x} \left[1 - \frac{\tilde{\beta}x^2}{2} + \frac{\tilde{\beta}^2x^4}{8} + \dots \right]. \quad (\text{C.3})$$

Consequently, we can write

$$\tilde{y}_\beta(\tilde{\nu}, \mu_l) \approx \int_0^\infty dx e^{-\tilde{\nu}\mu_l x} - \int_0^\infty dx \frac{\tilde{\beta}x^2}{2} e^{-\tilde{\nu}\mu_l x} + \dots \quad (\text{C.4})$$

The first integral in (C.4) can be computed straightforwardly. For the following terms, we use the fact that [Abramowitz and Stegun, 1964; Johansson and Rasmussen, 2004]

$$\frac{\Gamma(n+1)}{a^{n+1}} = \int_0^\infty dx x^n e^{-ax}, \quad (\text{C.5})$$

where $a \in \mathbb{R}$ is a constant and Γ is the usual Γ function defined such that $\Gamma(n+1) = n\Gamma(n)$ if $n \in \mathbb{N}$. Therefore

$$\tilde{y}_\beta(\tilde{\nu}, \mu_l) = \frac{1}{\tilde{\nu}\mu_l} - \frac{\tilde{\beta}}{2} \frac{\Gamma(3)}{(\tilde{\nu}\mu_l)^3} + \frac{\tilde{\beta}^2}{8} \frac{\Gamma(5)}{(\tilde{\nu}\mu_l)^5} + \dots \quad (\text{C.6})$$

In the limit of $\tilde{\nu} \rightarrow 0$, because β is finite $\tilde{\beta}\nu \rightarrow 0$ we can neglect higher order terms in $\tilde{\beta}$ and obtain

$$\tilde{y}_\beta(\tilde{\nu}, \mu_l) \approx \frac{1}{\tilde{\nu}\mu_l} \left(1 - \frac{\beta\tilde{\nu}}{(\tilde{\nu}\mu_l)^2} \right). \quad (\text{C.7})$$

C.2 Derivation of Eq. (2.84)

The total energy \mathcal{H}_{1D} and the total norm \mathcal{S}_{1D} of the 1D DDNLS system (2.17) can be calculated from the grand partition function \mathcal{Z} (2.82) [Landau and Lifshitz, 1980; Tong, 2012]. Here we evaluate both the average norm $s = \mathcal{S}_{1D}/N$ and energy $h = \mathcal{H}_{1D}/N$ per site in terms of the system's parameters at

equilibrium. We recall the partition function $\ln \mathcal{Z}$ (2.82) containing all the information on the macroscopic states of the system was presented to be

$$\ln \mathcal{Z} \approx N \ln 2\pi - \sum_{l=1}^N \left[\ln(\tilde{\nu}\mu_l) + \frac{\tilde{\nu}\beta}{(\tilde{\nu}\mu_l)^2} \right], \quad (\text{C.8})$$

where $\tilde{\nu} = 1/T$, with T being the system temperature, β the nonlinear coefficient in the expression of \mathcal{H}_{1D} (2.17) and $\mu_l = \mu + \epsilon_l$, where μ is a chemical potential and ϵ_l the disorder parameter in (2.17). The total norm \mathcal{S}_{1D} is given by

$$\begin{aligned} \mathcal{S}_{1D} &= -\frac{1}{\tilde{\nu}} \frac{\partial}{\partial \mu_l} \ln \mathcal{Z}, \\ &= -\frac{1}{\tilde{\nu}} \left\{ -\sum_l \left[\frac{\tilde{\nu}}{\tilde{\nu}\mu_l} - \frac{2\tilde{\nu}^2\beta}{(\tilde{\nu}\mu_l)^3} \right] \right\}, \\ &= \sum_l \frac{1}{\tilde{\nu}\mu_l} - \sum_l \frac{2\beta}{(\tilde{\nu}\mu_l)^2\mu_l}. \end{aligned} \quad (\text{C.9})$$

We note that in the infinite temperature limit $\tilde{\nu} \rightarrow 0$, while the product $\tilde{\nu}\mu$ remains constant by definition [Landau and Lifshitz, 1980; Rasmussen et al., 2000; Johansson and Rasmussen, 2004; Tong, 2012; Flach, 2016]. Therefore the chemical potential $\mu \sim 1/\tilde{\nu}$. In addition since ϵ_l is finite, and $\tilde{\nu}$ is large, we also assume that $\mu_l \sim 1/\tilde{\nu}$. Consequently the second term in (C.9) becomes

$$\sum_l \frac{2\beta}{(\tilde{\nu}\mu_l)^2\mu_l} \sim \tilde{\nu} \sum_l \frac{2\beta}{(\tilde{\nu}\mu_l)^2} \rightarrow 0, \quad (\text{C.10})$$

for $\tilde{\nu} \rightarrow 0$. Thus, (C.10) can be used to provide the approximation

$$\mathcal{S}_{1D} \approx \sum_l \frac{1}{\tilde{\nu}\mu_l} = \sum_l \frac{1}{\tilde{\nu}(\mu + \epsilon_l)} = \sum_l \frac{1}{\tilde{\nu}\mu + \tilde{\nu}\epsilon_l} \sim \frac{N}{\tilde{\nu}\mu}, \quad (\text{C.11})$$

as $\tilde{\nu}\epsilon_l \rightarrow 0$ when $\tilde{\nu} \rightarrow 0$. From (C.11), we conclude that the expression of the average norm per site is

$$s = \frac{\mathcal{S}_{1D}}{N} \approx \frac{1}{\tilde{\nu}\mu}. \quad (\text{C.12})$$

Let us now estimate the average energy per site. The total energy \mathcal{H}_{1D} is given by

$$\mathcal{H}_{1D} = \left(\frac{\mu}{\tilde{\nu}} \frac{\partial}{\partial \mu_l} - \frac{\partial}{\partial \tilde{\nu}} \right) \ln \mathcal{Z}. \quad (\text{C.13})$$

Then (C.13), using the expression of \mathcal{Z} from (C.8) gives

$$\begin{aligned} \mathcal{H}_{1D} &= \frac{\mu}{\tilde{\nu}} \left(-\sum_l \left[\frac{\tilde{\nu}}{\tilde{\nu}\mu_l} - \frac{2\tilde{\nu}^2\beta}{(\tilde{\nu}\mu_l)^3} \right] \right) + \sum_l \left[\frac{\mu_l}{\tilde{\nu}\mu_l} - \frac{\beta}{(\tilde{\nu}\mu_l)^2} \right], \\ &= -\sum_l \frac{\mu}{\tilde{\nu}\mu_l} + \sum_l \frac{2\beta\mu}{(\tilde{\nu}\mu_l)^2\mu_l} + \sum_l \frac{\mu_l}{\tilde{\nu}\mu_l} - \sum_l \frac{\beta}{(\tilde{\nu}\mu_l)^2}, \\ &= \sum_l \frac{\epsilon_l}{\tilde{\nu}\mu_l} - \sum_l \frac{\beta\mu_l}{(\tilde{\nu}\mu_l)^2\mu_l} + \sum_l \frac{2\beta\mu}{(\tilde{\nu}\mu_l)^2\mu_l}, \\ &= \sum_l \frac{\epsilon_l}{\tilde{\nu}\mu_l} + \sum_l \frac{\beta}{(\tilde{\nu}\mu_l)^2} - \sum_l \frac{\beta\epsilon_l}{(\tilde{\nu}\mu_l)^2\mu_l}. \end{aligned} \quad (\text{C.14})$$

The last term in the final expression of \mathcal{H}_{1D} in (C.14) is similar to the one in the final expression of \mathcal{S}_{1D} in (C.9), which converges to zero in the limit of $\tilde{\nu} \rightarrow 0$. Thus

$$\mathcal{H}_{1D} \approx \sum_l \frac{\epsilon_l}{\tilde{\nu}\mu_l} + \sum_l \frac{\beta}{(\tilde{\nu}\mu_l)^2}. \quad (\text{C.15})$$

Let us look a bit closer each term of \mathcal{H}_{1D} (C.15). The first one can be written as

$$\sum_l \frac{\epsilon_l}{\tilde{\nu}\mu_l} = \sum_l \frac{\epsilon_l}{\tilde{\nu}(\mu + \epsilon_l)} = \frac{1}{\tilde{\nu}\mu} \sum_l \left(\frac{\epsilon_l}{1 + \frac{\epsilon_l}{\mu}} \right). \quad (\text{C.16})$$

Then, applying the Taylor expansion

$$\frac{\epsilon_l}{1 + \frac{\epsilon_l}{\mu}} = \epsilon_l \left(1 - \frac{\epsilon_l}{\mu} + \frac{\epsilon_l^2}{\mu^2} + \dots \right), \quad (\text{C.17})$$

and assuming that $\epsilon_l/\mu \ll 1$ as $\mu \sim 1/\tilde{\nu} \gg 1$, for $\tilde{\nu} \rightarrow 0$ in (C.16), we obtain

$$\sum_l \frac{\epsilon_l}{\tilde{\nu}(\mu + \epsilon_l)} \approx \frac{1}{\tilde{\nu}\mu} \left(\sum_l \epsilon_l - \frac{1}{\mu} \sum_l \epsilon_l^2 \right), \quad (\text{C.18})$$

where we considered only the first two leading terms in (C.17) [see also [\[Flach, 2016\]](#)]. In addition, in order for the value of σ_ϵ (see (2.63)) to be finite i.e. $\sup \sigma_\epsilon < \infty$, we must have

$$\sum_l \epsilon_l^2 \sim N \quad \Rightarrow \quad \sum_l \epsilon_l \sim \sqrt{N}. \quad (\text{C.19})$$

With these two approximations of (C.19), (C.18) gives

$$\sum_l \frac{\epsilon_l}{\tilde{\nu}(\mu + \epsilon_l)} \sim \frac{\sqrt{N}}{\tilde{\nu}\mu} - \frac{N\tilde{\nu}}{(\tilde{\nu}\mu)^2}. \quad (\text{C.20})$$

The second term in the right hand side of (C.20) can be neglected when $\tilde{\nu} \rightarrow 0$. In addition the variation of $\sqrt{N}/(\tilde{\nu}\mu)$ is too slow to contribute to the final energy-norm relation at infinite temperature [[Flach, 2016](#)]. Finally, only the second term in the right hand side of (C.15) remains, leading to

$$h = \frac{\mathcal{H}_{1D}}{N} \approx \frac{\beta}{(\tilde{\nu}\mu)^2} \quad \Rightarrow \quad h \approx \beta \left(\frac{1}{\tilde{\nu}\mu} \right)^2 \quad \Rightarrow \quad h \approx \beta s^2. \quad (\text{C.21})$$

Appendix D

Symplectic integration of the equations of motion and variational equations of the 1D and 2D DDNLS models

We present here the expression of the various operators needed for the implementation of SIs for the integration of the equations of motion and the variational equations for the 1D and 2D DDNLS systems. We note that the Hamiltonian of the 1D DDNLS model (2.17)

$$\mathcal{H}_{1D} = \sum_{l=1}^N \epsilon_l |\psi_l|^2 + \frac{\beta}{2} |\psi_l|^4 - (\psi_{l+1} \psi_l^* + \psi_{l+1}^* \psi_l), \quad (\text{D.1})$$

becomes

$$\mathcal{H}_{1D} = \sum_l \left\{ \frac{\epsilon_l}{2} (q_l^2 + p_l^2) + \frac{\beta}{8} (q_l^2 + p_l^2)^4 - p_{l+1} p_l - q_{l+1} q_l \right\}, \quad (\text{D.2})$$

with q_l and p_l being real variables, through the implementation of the transformation (3.90)

$$\psi_l = \frac{1}{\sqrt{2}} (q_l + ip_l). \quad (\text{D.3})$$

In a similar manner, the 2D DDNLS Hamiltonian function (2.20)

$$\mathcal{H}_{2D} = \sum_{l=1, m=1}^{N, M} \epsilon_{l,m} |\psi_{l,m}|^2 + \frac{\beta}{2} |\psi_{l,m}|^4 - (\psi_{l+1,m} \psi_{l,m}^* + \psi_{l,m+1} \psi_{l,m}^* + \psi_{l+1,m}^* \psi_{l,m} + \psi_{l,m+1}^* \psi_{l,m}), \quad (\text{D.4})$$

becomes

$$\mathcal{H}_{2D} = \sum_{l,m} \left\{ \frac{\epsilon_{l,m}}{2} (q_{l,m}^2 + p_{l,m}^2) + \frac{\beta}{8} (q_{l,m}^2 + p_{l,m}^2)^2 - q_{l,m+1} q_{l,m} - q_{l+1,m} q_{l,m} - p_{l,m+1} p_{l,m} - p_{l+1,m} p_{l,m} \right\}, \quad (\text{D.5})$$

after the implementation of the transformation

$$\psi_{l,m} = \frac{1}{\sqrt{2}} (q_{l,m} + ip_{l,m}). \quad (\text{D.6})$$

We note that for both Hamiltonians (D.2) and (D.5) we use fixed boundary conditions.

D.1 Two-part split symplectic integration of the 1D DDNLS model

As was mentioned in Sec. 3.8.1, the Hamiltonian function of the 1D DDNLS system can be split into two integrable parts as

$$\mathcal{H}_{1D} = A + B, \quad (\text{D.7})$$

with

$$A = \sum_l \frac{\epsilon_l}{2}(q_l^2 + p_l^2) + \frac{\beta}{8}(q_l^2 + p_l^2)^2, \quad B = \sum_l -p_{l+1}p_l - q_{l+1}q_l, \quad (\text{D.8})$$

whose solutions can be obtained in closed forms.

D.1.1 Analytic expression for the operator $e^{\tau \mathbf{L}_{AV}}$

Let us first consider the A part of the decomposition (D.8)

$$A = \sum_l \frac{\epsilon_l}{2}(q_l^2 + p_l^2) + \frac{\beta}{8}(q_l^2 + p_l^2)^2. \quad (\text{D.9})$$

Its equations of motion are

$$\frac{dz}{dt} = \mathbf{L}_A z: \begin{cases} \dot{q}_l &= p_l \left(\epsilon_l + \beta \frac{q_l^2 + p_l^2}{2} \right) \\ \dot{p}_l &= -q_l \left(\epsilon_l + \beta \frac{q_l^2 + p_l^2}{2} \right) \end{cases}, \quad (\text{D.10})$$

which conserve the value of A (D.9).

Let us express (D.9) and (D.10) in action-angles variables J, Θ through the canonical transformation [Herbert, 1980; Goldstein et al., 2002; Tong, 2004]

$$\Omega_A : (q_l, p_l) \mapsto (J_l, \Theta_l) : \begin{cases} J_l = \frac{1}{2}(q_l^2 + p_l^2) \\ \Theta_l = \arctan \frac{q_l}{p_l} \end{cases}. \quad (\text{D.11})$$

It is easily seen that the inverse of transformation Ω_A (D.11) is given by

$$\Omega_A^{-1} : (J_l, \Theta_l) \mapsto (q_l, p_l) : \begin{cases} q_l = \sqrt{2J_l} \sin \Theta_l \\ p_l = \sqrt{2J_l} \cos \Theta_l \end{cases}. \quad (\text{D.12})$$

In (D.11) and (D.12), the variable Θ_l plays the role of a generalized position and J_l of the generalized momentum. The application of (D.12) on Hamiltonian A (D.9) brings it to the form

$$A = \sum_l \epsilon_l J_l + \frac{\beta}{2} J_l^2. \quad (\text{D.13})$$

The corresponding equations of motion generated through the Hamilton equations of motion

$$\dot{\Theta}_l = \frac{\partial A}{\partial J_l}, \quad \dot{J}_l = -\frac{\partial A}{\partial \Theta_l}, \quad (\text{D.14})$$

are

$$\begin{cases} \dot{\Theta}_l &= \epsilon_l + \beta J_l \\ \dot{J}_l &= 0 \end{cases}. \quad (\text{D.15})$$

From the second equation of (D.15), we see that the actions $J_l, l = 1, 2, \dots, N$ are integrals of motion and their values are conserved along the system's evolution. Given an initial condition $(\Theta_l(0), J_l(0))$, the solution of (D.15) is given by

$$\begin{cases} \Theta_l(t) &= (\epsilon_l + \beta J_l(0))t + \Theta_l(0) \\ J_l(t) &= J_l(0) \end{cases}. \quad (\text{D.16})$$

Using the transformation Ω_A^{-1} (D.12), we rewrite the solution (D.16) in terms of the q_l and p_l variables as

$$\begin{cases} q_l(t) &= \sqrt{2J_l(0)} \sin [(\epsilon_l + \beta J_l(0))t + \Theta_l(0)] \\ p_l(t) &= \sqrt{2J_l(0)} \cos [(\epsilon_l + \beta J_l(0))t + \Theta_l(0)] \end{cases}, \quad (\text{D.17})$$

with

$$J_l(0) = \frac{1}{2} (q_l(0)^2 + p_l(0)^2), \quad \Theta_l(0) = \arctan \frac{q_l(0)}{p_l(0)}. \quad (\text{D.18})$$

Let us now discuss some particular cases related to (D.17).

Case A: $p_l(0) \neq 0$. No problems arise in this case and the substitution of (D.18) onto Eq. (D.17) leads to

$$\begin{cases} q_l(t) &= \sqrt{q_l(0)^2 + p_l(0)^2} [\sin [(\epsilon_l + \beta J_l(0))t] \cos \Theta_l(0) + \cos [(\epsilon_l + \beta J_l(0))t] \sin \Theta_l(0)] \\ p_l(t) &= \sqrt{q_l(0)^2 + p_l(0)^2} [\cos [(\epsilon_l + \beta J_l(0))t] \cos \Theta_l(0) - \sin [(\epsilon_l + \beta J_l(0))t] \sin \Theta_l(0)] \end{cases}, \quad (\text{D.19})$$

which can further be rewritten as

$$\begin{cases} q_l(t) &= \sqrt{q_l(0)^2 + p_l(0)^2} \left[\sin [(\epsilon_l + \beta J_l(0))t] \frac{1}{\sqrt{1 + \frac{q_l(0)^2}{p_l(0)^2}}} + \cos [(\epsilon_l + \beta J_l(0))t] \frac{\frac{q_l(0)}{p_l(0)}}{\sqrt{1 + \frac{q_l(0)^2}{p_l(0)^2}}} \right] \\ p_l(t) &= \sqrt{q_l(0)^2 + p_l(0)^2} \left[\cos [(\epsilon_l + \beta J_l(0))t] \frac{1}{\sqrt{1 + \frac{q_l(0)^2}{p_l(0)^2}}} - \sin [(\epsilon_l + \beta J_l(0))t] \frac{\frac{q_l(0)}{p_l(0)}}{\sqrt{1 + \frac{q_l(0)^2}{p_l(0)^2}}} \right]. \end{cases} \quad (\text{D.20})$$

We note that in deriving Eq. (D.20), we used the following trigonometric identities $\sin(a + b) = \sin a \cos b + \cos a \sin b$, $\cos(a + b) = \cos a \cos b - \sin a \sin b$, $\sin a = \tan a / \sqrt{1 + \tan^2 a}$ and $\cos a = 1 / \sqrt{1 + \tan^2 a}$. In this case the solution of the Hamilton equations of motion of A (D.9) is given by [Skokos et al., 2014; Gerlach et al., 2016; Danieli et al., 2019a]

$$\begin{cases} q_l(t) &= q_l(0) \cos \alpha_l t + p_l(0) \sin \alpha_l t \\ p_l(t) &= p_l(0) \cos \alpha_l t - q_l(0) \sin \alpha_l t \end{cases}, \quad (\text{D.21})$$

with

$$\alpha_l = \epsilon_l + \beta J_l(0) = \epsilon_l + \beta \frac{q_l(0)^2 + p_l(0)^2}{2},$$

being constant coefficients.

Case B: $p_l(0) = 0$. In this case, we have to consider two different options: $q_l(0) \neq 0$ and $q_l(0) = 0$.

Case B1: $q_l(0) = 0$. The equations of motion (D.10) become

$$\begin{cases} \dot{q}_l = 0 \\ \dot{p}_l = 0 \end{cases}, \quad (\text{D.22})$$

and can be trivially solved to get $q_l(t) = 0$ and $p_l(t) = 0$.

Case B2: $q_l(0) \neq 0$. In this case, we can have two possible values for $\Theta_l(0)$, namely

$$\begin{cases} \Theta_l(0) = \frac{\pi}{2} & \text{if } q_l(0) > 0 \\ \Theta_l(0) = -\frac{\pi}{2} & \text{if } q_l(0) < 0 \end{cases}. \quad (\text{D.23})$$

For the first case in (D.23), the solution (D.17) is written as

$$\begin{cases} q_l(t) &= \sqrt{2J_l(0)} \sin \left[(\epsilon_l + \beta J_l(0))t + \frac{\pi}{2} \right] \\ p_l(t) &= \sqrt{2J_l(0)} \cos \left[(\epsilon_l + \beta J_l(0))t + \frac{\pi}{2} \right] \end{cases}, \quad (\text{D.24})$$

or simply as

$$\begin{cases} q_l(t) &= q_l(0) \cos [(\epsilon_l + \beta J_l(0))t] \\ p_l(t) &= -q_l(0) \sin [(\epsilon_l + \beta J_l(0))t] \end{cases}. \quad (\text{D.25})$$

We note that going from (D.24) to (D.25), we used the trigonometric identities $\sin(a + \pi/2) = \cos a$ and $\cos(a + \pi/2) = -\sin a$, as well as the facts that $J_l(0) = \frac{1}{2}q_l(0)^2$ and $|q_l(0)| = q_l(0)$ ($q_l(0) > 0$). Following a similar process as in (D.24) and (D.25) in the second case of (D.23), and using the identities $\sin(a - \pi/2) = -\cos a$ and $\cos(a - \pi/2) = \sin a$, along with $|q_l(0)| = -q_l(0)$ on (D.24), we finally obtain the solution

$$\begin{cases} q_l(t) &= q_l(0) \cos [(\epsilon_l + \beta J_l(0))t] \\ p_l(t) &= -q_l(0) \sin [(\epsilon_l + \beta J_l(0))t] \end{cases}. \quad (\text{D.26})$$

The solutions (D.25) and (D.26) are identical. Consequently, no distinction between the cases B1 and B2 needs to be implemented in our computer program.

Let us now discuss the solution of the variational equations of the Hamiltonian A (D.9) which have the form

$$\frac{d\delta\mathbf{z}}{dt} = L_{A_V} \delta\mathbf{z} : \begin{cases} \delta\dot{q}_l = \beta q_l p_l \delta q_l + \left[\epsilon_l + \beta \frac{q_l^2 + p_l^2}{2} + \beta p_l^2 \right] \delta p_l \\ \delta\dot{p}_l = -\beta q_l p_l \delta p_l - \left[\epsilon_l + \beta \frac{q_l^2 + p_l^2}{2} + \beta q_l^2 \right] \delta q_l \end{cases}. \quad (\text{D.27})$$

In the action-angle variables, (D.27) obtains a much simpler form

$$\begin{cases} \delta\dot{\Theta}_l = \beta \delta J_l \\ \delta\dot{J}_l = 0 \end{cases}, \quad (\text{D.28})$$

whose analytic solution can be easily found. In particular, the solution of (D.28) for initial conditions $(\delta\Theta_l(0), \delta J_l(0))$, is

$$\begin{cases} \delta\Theta_l(t) = \beta \delta J_l(0)t + \delta\Theta_l(0) \\ \delta J_l(t) = \delta J_l(0) \end{cases}. \quad (\text{D.29})$$

The transformation relating (D.27) to (D.28), can be obtained via total differentiation of (D.11) and (D.12) and has the form

$$\delta\Omega_A : (\delta q_l, \delta p_l) \mapsto (\delta\Theta_l, \delta J_l) : \begin{cases} \delta\Theta_l(t) = \frac{p_l(t)}{2J_l(t)} \delta q_l(t) - \frac{q_l(t)}{2J_l(t)} \delta p_l(t) \\ \delta J_l(t) = q_l(t) \delta q_l(t) + p_l(t) \delta p_l(t) \end{cases}, \quad (\text{D.30})$$

while its inverse transformation is given by

$$\delta\Omega_A^{-1} : (\delta\Theta_l, \delta J_l) \mapsto (\delta q_l, \delta p_l) : \begin{cases} \delta q_l(t) = \left[\frac{1}{\sqrt{2J_l(t)}} \sin \Theta_l(t) \right] \delta J_l(t) + \left[\sqrt{2J_l(t)} \cos \Theta_l(t) \right] \delta\Theta_l(t) \\ \delta p_l(t) = \left[\frac{1}{\sqrt{2J_l(t)}} \cos \Theta_l(t) \right] \delta J_l(t) - \left[\sqrt{2J_l(t)} \sin \Theta_l(t) \right] \delta\Theta_l(t) \end{cases}. \quad (\text{D.31})$$

The equivalence of solution (D.29) (in action-angle variables) and (D.30) (in position and momentum variables) can be easily seen by differentiating (D.30). Let us see that in more detail for the $\delta\Theta_l$ variable. Applying the time derivative to the first equation of (D.30)

$$\begin{aligned} \frac{d\delta\Theta_l(t)}{dt} &= \frac{1}{2J_l(t)} \left[\dot{p}_l(t) \delta q_l(t) + p_l(t) \delta\dot{q}_l(t) - \dot{q}_l(t) \delta p_l(t) - q_l(t) \delta\dot{p}_l(t) \right], \\ &= \frac{1}{2J_l(t)} \left\{ \left[-q_l \left(\epsilon_l + \beta \frac{q_l^2 + p_l^2}{2} \right) \right] \delta q_l(t) + p_l(t) \left[\beta q_l p_l \delta q_l + \left(\epsilon_l + \beta \frac{q_l^2 + p_l^2}{2} + \beta p_l^2 \right) \delta p_l \right] \right. \\ &\quad \left. - \left[p_l \left(\epsilon_l + \beta \frac{q_l^2 + p_l^2}{2} \right) \right] \delta p_l(t) - q_l(t) \left[- \left(\epsilon_l + \beta \frac{q_l^2 + p_l^2}{2} + \beta q_l^2 \right) \delta q_l - \beta q_l p_l \delta p_l \right] \right\}, \\ &= \frac{1}{2J_l(t)} [2J_l \beta (q_l \delta q_l + p_l \delta p_l)], \\ &= \beta \delta J_l(t), \end{aligned} \quad (\text{D.32})$$

which is just the first equation of (D.28). A similar result for $\delta J_l(t)$ (D.30) can also be obtained.

In practice in order to obtain the solution of the system's variational equations we do the following: given an initial condition $(q_l(0), p_l(0), \delta q_l(0), \delta p_l(0))$, we compute the quantities

$$J_l(0) = \frac{1}{2}(q_l(0)^2 + p_l(0)^2), \quad \alpha_l = \epsilon_l + \beta J_l(0), \quad l = 1, 2, \dots, N,$$

and

$$\delta J_l(0) = q_l(0) \delta q_l(0) + p_l(0) \delta p_l(0), \quad \delta\Theta_l(0) = \frac{p_l(0)}{2J_l(0)} \delta q_l(0) - \frac{q_l(0)}{2J_l(0)} \delta p_l(0), \quad l = 1, 2, \dots, N.$$

Thus the solution (D.31) of the variational equations takes the form

$$\begin{cases} \delta q_l(t) = \frac{q_l(0) \cos \alpha_l t + p_l(0) \sin \alpha_l t}{2J_l(0)} \delta J_l(0) + (p_l(0) \cos \alpha_l t - q_l(0) \sin \alpha_l t) (\beta \delta J_l(0)t + \delta\Theta_l(0)) \\ \delta p_l(t) = \frac{p_l(0) \cos \alpha_l t - q_l(0) \sin \alpha_l t}{2J_l(0)} \delta J_l(0) - (q_l(0) \cos \alpha_l t + p_l(0) \sin \alpha_l t) (\beta \delta J_l(0)t + \delta\Theta_l(0)) \end{cases}, \quad (\text{D.33})$$

using the equalities

$$\sin \Theta_l(t) = \frac{q_l(t)}{\sqrt{2J_l(t)}} = \frac{q_l(0) \cos \alpha_l t + p_l(0) \sin \alpha_l t}{\sqrt{2J_l(0)}},$$

and

$$\sqrt{2J_l(t)} \cos \Theta(t) = p_l(t) = p_l(0) \cos \alpha_l t - q_l(0) \sin \alpha_l t.$$

along with (D.29).

In summary, the expression of the operator $e^{\tau L_{AV}}$ propagating $(q_l, p_l, \delta q_l, \delta p_l)$ at time t to $(q'_l, p'_l, \delta q'_l, \delta p'_l)$ at time $t + \tau$ is given by

$$e^{\tau L_{AV}} : \begin{cases} q'_l &= q_l \cos(\tau \alpha_l) + p_l \sin(\tau \alpha_l) \\ p'_l &= p_l \cos(\tau \alpha_l) - q_l \sin(\tau \alpha_l) \\ \delta q'_l &= \frac{q_l \cos(\tau \alpha_l) + p_l \sin(\tau \alpha_l)}{2J_l} \delta J_l + (p_l \cos(\tau \alpha_l) - q_l \sin(\tau \alpha_l)) (\beta \delta J_l \tau + \delta \Theta_l), \\ \delta p'_l &= \frac{p_l \cos(\tau \alpha_l) - q_l \sin(\tau \alpha_l)}{2J_l} \delta J_l - (q_l \cos(\tau \alpha_l) + p_l \sin(\tau \alpha_l)) (\beta \delta J_l \tau + \delta \Theta_l) \end{cases}, \quad (\text{D.34})$$

with

$$J_l = \frac{1}{2}(q_l^2 + p_l^2), \quad \alpha_l = \epsilon_l + \beta J_l, \\ \delta J_l = q_l \delta q_l + p_l \delta p_l, \quad \delta \Theta_l = \frac{p_l}{2J_l} \delta q_l - \frac{q_l}{2J_l} \delta p_l.$$

Let us now discuss in detail a particular problematic case appearing in (D.33) and (D.34), namely the situation where $J_l = (q_l^2 + p_l^2)/2 = 0$. In that case, $q_l = p_l = 0$. Then, from (D.27), we see that the variational equations take the form

$$\begin{cases} \dot{\delta q}_l = \epsilon_l \delta p_l \\ \dot{\delta p}_l = -\epsilon_l \delta q_l \end{cases}. \quad (\text{D.35})$$

The solution of this set of ODEs is given by

$$\begin{cases} \delta q_l(t) = \delta q_l(0) \cos(\epsilon_l t) + \delta p_l(0) \sin(\epsilon_l t) \\ \delta p_l(t) = \delta p_l(0) \cos(\epsilon_l t) - \delta q_l(0) \sin(\epsilon_l t) \end{cases}, \quad (\text{D.36})$$

assuming we started from $(\delta q_l(0), \delta p_l(0))$ at $t = 0$. Consequently, the general form of the operator $e^{\tau L_{AV}}$ is given by (D.34) except for the particular case $J_l = 0$ where we have

$$e^{L_{AV}\tau} := \begin{cases} q'_l = q_l = 0 \\ p'_l = p_l = 0 \\ \delta q'_l = \delta q_l \cos(\epsilon_l \tau) + \delta p_l \sin(\epsilon_l \tau) \\ \delta p'_l = \delta p_l \cos(\epsilon_l \tau) - \delta q_l \sin(\epsilon_l \tau) \end{cases}. \quad (\text{D.37})$$

D.1.2 Analytic expression for the operator $e^{\tau L_{BV}}$

Based on the analysis presented in the appendix of [Gerlach et al., 2016], let us now determine the solution of both the equations of motion and the variational equations of the B Hamiltonian part (D.8)

$$B = - \sum_l p_l p_{l+1} + q_l q_{l+1}, \quad (\text{D.38})$$

of the 1D DDNLS system (D.1). More specifically, we will determine the operator $e^{\tau L_{BV}}$ propagating an initial condition \mathbf{Z} at time t to \mathbf{Z}' at time $t + \tau$ according to

$$e^{\tau L_{BV}} : \mathbf{Z}' = \mathbf{\Gamma}(\tau) \cdot \mathbf{Z}, \quad (\text{D.39})$$

with $\mathbf{Z} = (\mathbf{z} \ \delta \mathbf{z})^T$ such that $\mathbf{z} = (\mathbf{q} \ \mathbf{p})^T = (q_1 \ q_2 \ \dots \ q_N \ p_1 \ p_2 \ \dots \ p_N)^T$, $\delta \mathbf{z} = \mathbf{w} = (\delta \mathbf{q} \ \delta \mathbf{p})^T = (\delta q_1 \ \delta q_2 \ \dots \ \delta q_N \ \delta p_1 \ \delta p_2 \ \dots \ \delta p_N)^T$ and $\mathbf{\Gamma}$ being a $4N \times 4N$ matrix. Since SIs are used for fixed integration time steps, matrix $\mathbf{\Gamma}(\tau)$ in (D.39) is constant (for fixed τ value). In addition, Hamiltonian B (D.38) is a quadratic function in its variables q_l and p_l which in turn means that the equations of motion, and the variational equations are linear in \mathbf{z} , and $\delta \mathbf{z}$ and independent of each other (see (D.42) and (D.59) below). Consequently, matrix $\mathbf{\Gamma}(\tau)$ takes the form

$$\mathbf{\Gamma}(\tau) = \begin{bmatrix} \mathbf{C}(\tau) & \mathbf{0}_{2N} \\ \mathbf{0}_{2N} & \mathbf{C}'(\tau) \end{bmatrix}, \quad (\text{D.40})$$

with $\mathbf{C}(\tau)$ and $\mathbf{C}'(\tau)$ being appropriate $2N \times 2N$ matrices respectively evolving the equations of motion and the variational equations according to

$$\begin{bmatrix} \mathbf{q}' \\ \mathbf{p}' \end{bmatrix} = \mathbf{C}(\tau) \cdot \begin{bmatrix} \mathbf{q} \\ \mathbf{p} \end{bmatrix}, \quad \begin{bmatrix} \delta \mathbf{q}' \\ \delta \mathbf{p}' \end{bmatrix} = \mathbf{C}'(\tau) \cdot \begin{bmatrix} \delta \mathbf{q} \\ \delta \mathbf{p} \end{bmatrix}. \quad (\text{D.41})$$

More specifically, the equations of motion of Hamiltonian B (D.38) take the form

$$\frac{dz}{dt} = \mathbf{L}_B z: \begin{cases} \dot{q}_1 = -p_2 \\ \dot{q}_l = -p_{l-1} - p_{l+1} & 2 \leq l \leq N-1 \\ \dot{q}_N = -p_{N-1} \\ \dot{p}_1 = q_2 \\ \dot{p}_l = q_{l-1} + q_{l+1} & 2 \leq l \leq N-1 \\ \dot{p}_N = q_{N-1} \end{cases}. \quad (\text{D.42})$$

Equation (D.42) can be written as

$$\frac{dz}{dt} = \mathbf{L}_B z = \begin{pmatrix} \mathbf{0} & \mathbf{A} \\ -\mathbf{A} & \mathbf{0} \end{pmatrix} \cdot z, \quad (\text{D.43})$$

with \mathbf{A} being a tridiagonal $N \times N$ matrix whose main diagonal elements are equal to zero ($\mathbf{A}_{l,l} = 0, l = 1, 2, \dots, N$), while all the elements of the first upper and lower diagonals are equal to -1 ($\mathbf{A}_{l,l+1} = \mathbf{A}_{l-1,l} = -1$) i.e.

$$\mathbf{A} = \begin{pmatrix} 0 & -1 & 0 & \dots & 0 & 0 \\ -1 & 0 & -1 & \dots & 0 & 0 \\ \vdots & \vdots & \ddots & \ddots & \vdots & \vdots \\ 0 & 0 & 0 & \dots & 0 & -1 \\ 0 & 0 & 0 & \dots & -1 & 0 \end{pmatrix}. \quad (\text{D.44})$$

The solution of (D.43) for an integration time step τ can be expressed in terms of a Lie series expansion (3.39) as

$$\mathbf{z}(t + \tau) = e^{\tau \mathbf{L}_B} \mathbf{z}(t) = \sum_{k=0}^{\infty} \frac{\tau^k}{k!} \mathbf{L}_B^k \mathbf{z}(t) = \mathbf{C}(\tau) \mathbf{z}(t), \quad (\text{D.45})$$

with

$$\mathbf{C}(\tau) = \sum_{k=0}^{\infty} \frac{\tau^k}{k!} \mathbf{L}_B^k. \quad (\text{D.46})$$

As we mentioned in Sec. 3.6.2, the next step to determine the expression of $\mathbf{C}(\tau)$ is to find the form of the operator \mathbf{L}_B^k in (D.46). Luckily, this task can be performed due to the rather simple form of operator \mathbf{L}_B (D.43). Let us initially note that

$$\mathbf{L}_B^{2k} = (-1)^k \begin{pmatrix} \mathbf{A}^{2k} & \mathbf{0} \\ \mathbf{0} & \mathbf{A}^{2k} \end{pmatrix}, \quad \mathbf{L}_B^{2k+1} = (-1)^k \begin{pmatrix} \mathbf{0} & \mathbf{A}^{2k+1} \\ -\mathbf{A}^{2k+1} & \mathbf{0} \end{pmatrix}. \quad (\text{D.47})$$

Then, using (D.46) and (D.47), we get

$$\mathbf{C}(\tau) = \begin{pmatrix} \sum_{k=0}^{\infty} \frac{(-1)^k}{(2k)!} \mathbf{A}^{2k} \tau^{2k} & \mathbf{0} \\ \mathbf{0} & \sum_{k=0}^{\infty} \frac{(-1)^k}{(2k)!} \mathbf{A}^{2k} \tau^{2k} \end{pmatrix} \quad (\text{D.48})$$

$$+ \begin{pmatrix} \mathbf{0} & \sum_{k=0}^{\infty} \frac{(-1)^k}{(2k+1)!} \mathbf{A}^{2k+1} \tau^{2k+1} \\ -\sum_{k=0}^{\infty} \frac{(-1)^k}{(2k+1)!} \mathbf{A}^{2k+1} \tau^{2k+1} & \mathbf{0} \end{pmatrix}, \quad (\text{D.49})$$

which is equivalent to

$$\mathbf{C}(\tau) = \begin{pmatrix} \cos(\mathbf{A}\tau) & \sin(\mathbf{A}\tau) \\ -\sin(\mathbf{A}\tau) & \cos(\mathbf{A}\tau) \end{pmatrix}. \quad (\text{D.50})$$

The evaluation of the elements of matrices $\cos(\mathbf{A}\tau)$ and $\sin(\mathbf{A}\tau)$ can be obtained through the determination of the eigenvalues and eigenvectors of matrix \mathbf{A} (D.44) itself [Smith, 1985]. In particular, the eigenvalues λ_k of \mathbf{A} are symmetric with respect to zero and are given by

$$\lambda_k = -2 \cos\left(\frac{k\pi}{N+1}\right), \quad k = 1, 2, \dots, N, \quad (\text{D.51})$$

while the normalized eigenvectors are orthogonal (since \mathbf{A} is a symmetric matrix) and have the form

$$\mathbf{v}_k = \frac{1}{V_k} \left(\sin\left(\frac{k\pi}{N+1}\right), \sin\left(\frac{2k\pi}{N+1}\right), \dots, \sin\left(\frac{jk\pi}{N+1}\right), \dots, \sin\left(\frac{Nk\pi}{N+1}\right) \right). \quad (\text{D.52})$$

The Euclidean norms V_k of these eigenvectors are

$$V_k^2 = \|\mathbf{v}_k\|^2 = \sum_{j=1}^N \sin^2\left(\frac{jk\pi}{N+1}\right) = \sum_{j=1}^N \left[\frac{1}{2} - \frac{1}{2} \sum_{j=1}^N \cos\left(\frac{2jk\pi}{N+1}\right) \right], \quad (\text{D.53})$$

$$= \frac{2N+1}{4} - \frac{\sin\left(\frac{2N+1}{N+1}k\pi\right)}{4 \sin\left(\frac{k\pi}{N+1}\right)}, \quad (\text{D.54})$$

$$= \frac{N+1}{2}. \quad (\text{D.55})$$

We note that going from (D.53) to (D.55), we appropriately used the identities,

$$\sum_{j=0}^N \cos(jx) = \frac{1}{2} \left[1 + \frac{\sin\left[\left(N + \frac{1}{2}\right)x\right]}{\sin\left(\frac{x}{2}\right)} \right], \quad (\text{D.56})$$

which can be found for example at [Jeffrey and Zwillinger, 2007] and

$$\sin\left(\frac{2N+1}{N+1}k\pi\right) = -\sin\left(\frac{k\pi}{N+1}\right). \quad (\text{D.57})$$

The matrix \mathbf{P} having as columns the eigenvectors (D.52) i.e. $\mathbf{P} = (\mathbf{v}_1^T \ \mathbf{v}_2^T \ \dots \ \mathbf{v}_N^T)$ can be used to diagonalize \mathbf{A} (D.44) so that

$$\mathbf{A} = \mathbf{P} \cdot \mathbf{D} \cdot \mathbf{P}^{-1} = \mathbf{P} \cdot \mathbf{D} \cdot \mathbf{P}. \quad (\text{D.58})$$

We note that in (D.58) \mathbf{P} is a unitary $N \times N$ matrix, i.e. $\mathbf{P} = \mathbf{P}^{-1} = \mathbf{P}^T$, and \mathbf{D} a diagonal $N \times N$ matrix having as non-zero elements the eigenvalues (D.51) i.e. $\mathbf{D} = \text{diag}(\lambda_1, \lambda_2, \dots, \lambda_N)$. Thus we can write the matrices $\cos(\mathbf{A}\tau)$ and $\sin(\mathbf{A}\tau)$ defining $\mathbf{C}(\tau)$ in (D.50) as

$$\cos(\mathbf{A}\tau) = \mathbf{P} \cdot \mathbf{D}_c \cdot \mathbf{P}, \quad \sin(\mathbf{A}\tau) = \mathbf{P} \cdot \mathbf{D}_s \cdot \mathbf{P},$$

with $\mathbf{D}_c = \text{diag}(\cos(\lambda_1\tau), \cos(\lambda_2\tau), \dots, \cos(\lambda_N\tau))$, and $\mathbf{D}_s = \text{diag}(\sin(\lambda_1\tau), \sin(\lambda_2\tau), \dots, \sin(\lambda_N\tau))$.

A similar treatment can be performed for the variational equations of the Hamiltonian B (D.38)

$$\frac{d\mathbf{w}}{dt} = \mathbf{L}_{B_V} \cdot \mathbf{w} : \begin{cases} \dot{\delta}q_1 = -\delta p_2 \\ \dot{\delta}q_l = -\delta p_{l-1} - \delta p_{l+1} & 2 \leq l \leq N-1 \\ \dot{\delta}q_N = -\delta p_{N-1} \\ \dot{\delta}p_1 = \delta q_2 \\ \dot{p}_l = \delta q_{l-1} + \delta q_{l+1} & 2 \leq l \leq N-1 \\ \dot{p}_N = \delta q_{N-1} \end{cases}, \quad (\text{D.59})$$

which can be rewritten as

$$\frac{d\mathbf{w}}{dt} = \mathbf{L}_{B_V} \mathbf{w} = \begin{pmatrix} \mathbf{0} & \mathbf{A} \\ -\mathbf{A} & \mathbf{0} \end{pmatrix} \cdot \mathbf{w}, \quad (\text{D.60})$$

is the system of ODEs (D.43). Thus,

$$\mathbf{C}'(\tau) = \mathbf{C}(\tau), \quad (\text{D.61})$$

in (D.40) and (D.41).

D.2 Three-part split symplectic integration of the 1D and 2D DDNLS models

Following [Skokos et al., 2014; Gerlach et al., 2016] and mainly [Danieli et al., 2019a], we present here the analytic expressions of the operators involved in the symplectic integration of the 1D and 2D DDNLS systems when they are split in three integrable parts.

D.2.1 The 1D DDNLS system

The Hamiltonian function \mathcal{H}_{1D} (D.2) of the 1D DDNLS system can be split into three integrable parts as

$$\mathcal{H}_{1D} = \mathcal{A} + \mathcal{B} + \mathcal{C}, \quad (\text{D.62})$$

with

$$\mathcal{A} = \sum_l \frac{\epsilon_l}{2} (q_l^2 + p_l^2) + \frac{\beta}{8} (q_l^2 + p_l^2)^2, \quad \mathcal{B} = \sum_l -p_{l+1}p_l, \quad \mathcal{C} = \sum_l -q_{l+1}q_l. \quad (\text{D.63})$$

Obviously, the \mathcal{A} part in (D.63) coincides with the A part in (D.8) so that the corresponding operator $e^{\tau \mathcal{L}_{\mathcal{A}_V}}$ is given by (D.34) and (D.37). The Hamiltonian functions \mathcal{B} and \mathcal{C} on the other hand possess N cyclic coordinates as \mathcal{B} depends only on momenta p_l and \mathcal{C} on the positions q_l . Therefore it is easy to find the analytic expression of the operators $e^{\tau \mathcal{L}_{\mathcal{B}_V}}$ and $e^{\tau \mathcal{L}_{\mathcal{C}_V}}$ for the integration of their equations of motion and the variational equations.

More specifically, for the \mathcal{B} , we have the following system of equations of motion and variational equations

$$\frac{d\mathbf{Z}}{dt} = \mathbf{L}_{\mathcal{B}_V} \mathbf{Z} : \begin{cases} \dot{q}_1 = -p_2 \\ \dot{q}_l = -p_{l-1} - p_{l+1} & l = 2, 3, \dots, N-1 \\ \dot{q}_N = -p_{N-1} \\ \dot{p}_l = 0 & l = 1, 2, \dots, N \\ \dot{\delta}q_1 = -\delta p_2 \\ \dot{\delta}q_l = -\delta p_{l-1} - \delta p_{l+1} & l = 2, 3, \dots, N-1 \\ \dot{\delta}q_N = -\delta p_{N-1} \\ \dot{\delta}p_l = 0 & l = 1, 2, \dots, N \end{cases}, \quad (\text{D.64})$$

which can be easily solved, leading to

$$e^{\tau \mathcal{L}_{\mathcal{B}_V}} : \begin{cases} q'_1 = q_1 - \tau p_2 \\ q'_l = q_l - \tau(p_{l-1} + p_{l+1}) & l = 2, 3, \dots, N-1 \\ q'_N = q_N - \tau p_{N-1} \\ p'_l = p_l & l = 1, 2, \dots, N \\ \delta q'_1 = \delta q_1 - \tau \delta p_2 \\ \delta q'_l = \delta q_l - \tau(\delta p_{l-1} + \delta p_{l+1}) & l = 2, 3, \dots, N-1 \\ \delta q'_N = \delta q_N - \tau \delta p_{N-1} \\ \delta p'_l = \delta p_l & l = 1, 2, \dots, N \end{cases}. \quad (\text{D.65})$$

Similarly, the system of equations of motion and variational equations for the \mathcal{C} Hamiltonian (D.63) is

$$\frac{d\mathbf{Z}}{dt} = \mathbf{L}_{\mathcal{C}_V} \mathbf{Z} : \begin{cases} \dot{p}_1 = \delta q_2 \\ \dot{p}_l = \delta q_{l-1} + \delta q_{l+1} & l = 2, 3, \dots, N-1 \\ \dot{p}_N = \delta q_{N-1} \\ \dot{q}_l = 0 & l = 1, 2, \dots, N \\ \dot{\delta}p_1 = \delta q_2 \\ \dot{\delta}p_l = \delta q_{l-1} + \delta q_{l+1} & l = 2, 3, \dots, N-1 \\ \dot{\delta}p_N = \delta q_{N-1} \\ \dot{\delta}q_l = 0 & l = 1, 2, \dots, N \end{cases}, \quad (\text{D.66})$$

and its solution is given by

$$e^{\tau \mathcal{L}_{\mathcal{C}_V}} : \begin{cases} q'_l = q_l & l = 1, 2, \dots, N \\ p'_1 = p_1 + \tau q_2 \\ p'_l = p_l + \tau(q_{l-1} + q_{l+1}) & l = 2, 3, \dots, N-1 \\ p'_N = p_N + \tau q_{N-1} \\ \delta q'_l = \delta q_l & l = 1, 2, \dots, N \\ \delta p'_1 = \delta p_1 + \tau \delta q_2 \\ \delta p'_l = \delta p_l + \tau(\delta q_{l-1} + \delta q_{l+1}) & l = 2, 3, \dots, N-1 \\ \delta p'_N = \delta p_N + \tau \delta q_{N-1} \end{cases}. \quad (\text{D.67})$$

D.2.2 The 2D DDNLS system

We can treat the 2D DDNLS Hamiltonian \mathcal{H}_{2D} (D.5) in a similar manner to the one implemented for the 1D DDNLS system in Sec. D.2.1. In particular, the Hamiltonian can be split

$$\mathcal{H}_{2D} = A + B + C, \quad (\text{D.68})$$

with

$$A = \sum_{l,m} \frac{\epsilon_{l,m}}{2} (q_{l,m}^2 + p_{l,m}^2) + \frac{\beta}{8} (q_{l,m}^2 + p_{l,m}^2)^2, \quad (\text{D.69})$$

$$B = \sum_{l,m} -p_{l,m+1}p_{l,m} - p_{l+1,m}p_{l,m}, \quad C = \sum_{l,m} -q_{l,m+1}q_{l,m} - q_{l+1,m}q_{l,m}. \quad (\text{D.70})$$

For the Hamiltonian A (D.69), following similar steps to the ones performed in Sec. D.1.1, we obtain the following set of equations of motion and variational equations

$$\frac{d\mathbf{Z}}{dt} = \mathbf{L}_{A_V} \mathbf{Z} : \begin{cases} \dot{q}_{l,m} = p_{l,m} \dot{\Theta}_{l,m} \\ \dot{p}_{l,m} = -q_{l,m} \dot{\Theta}_{l,m} \\ \delta \dot{q}_{l,m} = [\dot{\Theta}_{l,m} + \beta p_{l,m}^2] \delta p_{l,m} + \beta q_{l,m} p_{l,m} \delta q_{l,m} \\ \delta \dot{p}_{l,m} = -[\dot{\Theta}_{l,m} + \beta q_{l,m}^2] \delta q_{l,m} - \beta q_{l,m} p_{l,m} \delta p_{l,m} \end{cases}, \quad (\text{D.71})$$

where $\dot{\Theta}_{l,m} = \epsilon_{l,m} + \beta(q_{l,m}^2 + p_{l,m}^2)/2$ are constants of motion. Setting

$$J_{l,m} = \frac{1}{2}(q_{l,m}^2 + p_{l,m}^2), \quad \alpha_{l,m} = \epsilon_{l,m} + \beta J_{l,m},$$

and

$$\delta J_{l,m} = q_{l,m} \delta q_{l,m} + p_{l,m} \delta p_{l,m}, \quad \delta \Theta_{l,m} = \frac{p_{l,m}}{2J_{l,m}} \delta q_{l,m} - \frac{q_{l,m}}{2J_{l,m}} \delta p_{l,m},$$

the solution of system (D.71) for $J_{l,m} \neq 0$ is obtained through the application of the operator

$$e^{\tau \mathbf{L}_{A_V}} : \begin{cases} q'_{l,m} = q_{l,m} \cos(\tau \alpha_{l,m}) + p_{l,m} \sin(\tau \alpha_{l,m}) \\ p'_{l,m} = p_{l,m} \cos(\tau \alpha_{l,m}) - q_{l,m} \sin(\tau \alpha_{l,m}) \\ \delta q'_{l,m} = \frac{q_{l,m} \cos(\tau \alpha_{l,m}) + p_{l,m} \sin(\tau \alpha_{l,m})}{2J_{l,m}} \delta J_{l,m} + (p_{l,m} \cos(\tau \alpha_{l,m}) - q_{l,m} \sin(\tau \alpha_{l,m})) (\beta \delta J_{l,m} \tau + \delta \Theta_{l,m}) \\ \delta p'_{l,m} = \frac{p_{l,m} \cos(\tau \alpha_{l,m}) - q_{l,m} \sin(\tau \alpha_{l,m})}{2J_{l,m}} \delta J_{l,m} - (q_{l,m} \cos(\tau \alpha_{l,m}) + p_{l,m} \sin(\tau \alpha_{l,m})) (\beta \delta J_{l,m} \tau + \delta \Theta_{l,m}) \end{cases}, \quad (\text{D.72})$$

or when $J_{l,m} = 0$ through the operator

$$e^{\mathbf{L}_{A_V} \tau} : \begin{cases} q'_{l,m} = q_{l,m} = 0 \\ p'_{l,m} = p_{l,m} = 0 \\ \delta q'_{l,m} = \delta q_{l,m} \cos(\epsilon_{l,m} \tau) + \delta p_{l,m} \sin(\epsilon_{l,m} \tau) \\ \delta p'_{l,m} = \delta p_{l,m} \cos(\epsilon_{l,m} \tau) - \delta q_{l,m} \sin(\epsilon_{l,m} \tau) \end{cases}. \quad (\text{D.73})$$

For the Hamiltonian functions B and C (D.70) the set of equations of motion and variational

equations are respectively

$$\frac{d\mathbf{Z}}{dt} = \mathbf{L}_{B_V} \mathbf{Z} : \left\{ \begin{array}{ll} \dot{q}_{1,1} & = -p_{1,2} + p_{2,1} \\ \dot{q}_{N,1} & = -p_{N-1,1} + p_{N,2} \\ \dot{q}_{1,M} & = -p_{1,M-1} + p_{2,M} \\ \dot{q}_{N,M} & = -p_{N-1,M} + p_{N,M-1} \\ \dot{q}_{l,1} & = -p_{l-1,1} + p_{l,2} + p_{l+1,1} & 2 \leq l \leq N-1 \\ \dot{q}_{l,M} & = -p_{l-1,M} + p_{l,M-1} + p_{l+1,M} & 2 \leq l \leq N-1 \\ \dot{q}_{1,m} & = -p_{1,m-1} + p_{1,m+1} + p_{2,m} & 2 \leq m \leq M-1 \\ \dot{q}_{N,m} & = -p_{N-1,m} + p_{N,m-1} + p_{N,m+1} & 2 \leq m \leq M-1 \\ \dot{q}_{l,m} & = -p_{l-1,m} + p_{l,m-1} + p_{l,m+1} + p_{l+1,m} & 2 \leq l \leq N-1, 2 \leq m \leq M-1 \\ \dot{p}_{l,m} & = 0 & 1 \leq l \leq N, 1 \leq m \leq M \\ \delta \dot{q}_{1,1} & = -\delta p_{1,2} + \delta p_{2,1} \\ \delta \dot{q}_{N,1} & = -\delta p_{N-1,1} + \delta p_{N,2} \\ \delta \dot{q}_{1,M} & = -\delta p_{1,M-1} + \delta p_{2,M} \\ \delta \dot{q}_{N,M} & = -\delta p_{N-1,M} + \delta p_{N,M-1} \\ \delta \dot{q}_{l,1} & = -\delta p_{l-1,1} + \delta p_{l,2} + \delta p_{l+1,1} & 2 \leq l \leq N-1 \\ \delta \dot{q}_{l,M} & = -\delta p_{l-1,M} + \delta p_{l,M-1} + \delta p_{l+1,M} & 2 \leq l \leq N-1 \\ \delta \dot{q}_{1,m} & = -\delta p_{1,m-1} + \delta p_{1,m+1} + \delta p_{2,m} & 2 \leq m \leq M-1 \\ \delta \dot{q}_{N,m} & = -\delta p_{N-1,m} + \delta p_{N,m-1} + \delta p_{N,m+1} & 2 \leq m \leq M-1 \\ \delta \dot{q}_{l,m} & = -\delta p_{l-1,m} + \delta p_{l,m-1} + \delta p_{l,m+1} + \delta p_{l+1,m} & 2 \leq l \leq N-1, 2 \leq m \leq M-1 \\ \delta \dot{p}_{l,m} & = 0 & 1 \leq l \leq N, 1 \leq m \leq M \end{array} \right. , \quad (\text{D.74})$$

and

$$\frac{d\mathbf{Z}}{dt} = \mathbf{L}_{C_V} \mathbf{Z} : \left\{ \begin{array}{ll} \dot{q}_{l,m} & = 0 & 1 \leq l \leq N, 1 \leq m \leq M \\ \dot{p}_{1,1} & = q_{1,2} + q_{2,1} \\ \dot{p}_{N,1} & = q_{N-1,1} + q_{N,2} \\ \dot{p}_{1,M} & = q_{1,M-1} + q_{2,M} \\ \dot{p}_{N,M} & = q_{N-1,M} + q_{N,M-1} \\ \dot{p}_{l,1} & = q_{l-1,1} + q_{l,2} + q_{l+1,1} & 2 \leq l \leq N-1 \\ \dot{p}_{l,M} & = q_{l-1,M} + q_{l,M-1} + q_{l+1,M} & 2 \leq l \leq N-1 \\ \dot{p}_{1,m} & = q_{1,m-1} + q_{1,m+1} + q_{2,m} & 2 \leq m \leq M-1 \\ \dot{p}_{N,m} & = q_{N-1,m} + q_{N,m-1} + q_{N,m+1} & 2 \leq m \leq M-1 \\ \dot{p}_{l,m} & = q_{l-1,m} + q_{l,m-1} + q_{l,m+1} + q_{l+1,m} & 2 \leq l \leq N-1, 2 \leq m \leq M-1 \\ \delta \dot{q}_{l,m} & = 0 & 1 \leq l \leq N, 1 \leq m \leq M \\ \delta \dot{p}_{1,1} & = \delta q_{1,2} + \delta q_{2,1} \\ \delta \dot{p}_{N,1} & = \delta q_{N-1,1} + \delta q_{N,2} \\ \delta \dot{p}_{1,M} & = \delta q_{1,M-1} + \delta q_{2,M} \\ \delta \dot{p}_{N,M} & = \delta q_{N-1,M} + \delta q_{N,M-1} \\ \delta \dot{p}_{l,1} & = \delta q_{l-1,1} + \delta q_{l,2} + \delta q_{l+1,1} & 2 \leq l \leq N-1 \\ \delta \dot{p}_{l,M} & = \delta q_{l-1,M} + \delta q_{l,M-1} + \delta q_{l+1,M} & 2 \leq l \leq N-1 \\ \delta \dot{p}_{1,m} & = \delta q_{1,m-1} + \delta q_{1,m+1} + \delta q_{2,m} & 2 \leq m \leq M-1 \\ \delta \dot{p}_{N,m} & = \delta q_{N-1,m} + \delta q_{N,m-1} + \delta q_{N,m+1} & 2 \leq m \leq M-1 \\ \delta \dot{p}_{l,m} & = \delta q_{l-1,m} + \delta q_{l,m-1} + \delta q_{l,m+1} + \delta q_{l+1,m} & 2 \leq l \leq N-1, 2 \leq m \leq M-1 \end{array} \right. . \quad (\text{D.75})$$

Consequently, the operators $e^{\tau L_{Bv}}$ and $e^{\tau L_{Cv}}$ are given by

$$e^{\tau L_{Bv}} : \left\{ \begin{array}{ll} q'_{1,1} & = q_{1,1} - \tau (p_{1,2} + p_{2,1}) \\ q'_{N,1} & = q_{N,1} - \tau (p_{N-1,1} + p_{N,2}) \\ q'_{1,M} & = q_{1,M} - \tau (p_{1,M-1} + p_{2,M}) \\ q'_{N,M} & = q_{N,M} - \tau (p_{N-1,M} + p_{N,M-1}) \\ q'_{l,1} & = q_{l,1} - \tau (p_{l-1,1} + p_{l,2} + p_{l+1,1}) & 2 \leq l \leq N-1 \\ q'_{l,M} & = q_{l,M} - \tau (p_{l-1,M} + p_{l,M-1} + p_{l+1,M}) & 2 \leq l \leq N-1 \\ q'_{1,m} & = q_{1,m} - \tau (p_{1,m-1} + p_{1,m+1} + p_{2,m}) & 2 \leq m \leq M-1 \\ q'_{N,m} & = q_{N,m} - \tau (p_{N-1,m} + p_{N,m-1} + p_{N,m+1}) & 2 \leq m \leq M-1 \\ q'_{l,m} & = q_{l,m} - \tau (p_{l-1,m} + p_{l,m-1} + p_{l,m+1} + p_{l+1,m}) & 2 \leq l \leq N-1, 2 \leq m \leq M-1 \\ p'_{l,m} & = p_{l,m} & 1 \leq l \leq N, 1 \leq m \leq M \\ \delta q'_{1,1} & = \delta q_{1,1} - \tau (\delta p_{1,2} + \delta p_{2,1}) \\ \delta q'_{N,1} & = \delta q_{N,1} - \tau (\delta p_{N-1,1} + \delta p_{N,2}) \\ \delta q'_{1,M} & = \delta q_{1,M} - \tau (\delta p_{1,M-1} + \delta p_{2,M}) \\ \delta q'_{N,M} & = \delta q_{N,M} - \tau (\delta p_{N-1,M} + \delta p_{N,M-1}) \\ \delta q'_{l,1} & = \delta q_{l,1} - \tau (\delta p_{l-1,1} + \delta p_{l,2} + \delta p_{l+1,1}) & 2 \leq l \leq N-1 \\ \delta q'_{l,M} & = \delta q_{l,M} - \tau (\delta p_{l-1,M} + \delta p_{l,M-1} + \delta p_{l+1,M}) & 2 \leq l \leq N-1 \\ \delta q'_{1,m} & = \delta q_{1,m} - \tau (\delta p_{1,m-1} + \delta p_{1,m+1} + \delta p_{2,m}) & 2 \leq m \leq M-1 \\ \delta q'_{N,m} & = \delta q_{N,m} - \tau (\delta p_{N-1,m} + \delta p_{N,m-1} + \delta p_{N,m+1}) & 2 \leq m \leq M-1 \\ \delta q'_{l,m} & = \delta q_{l,m} - \tau (\delta p_{l-1,m} + \delta p_{l,m-1} + \delta p_{l,m+1} + \delta p_{l+1,m}) & 2 \leq l \leq N-1, 2 \leq m \leq M-1 \\ \delta p'_{l,m} & = \delta p_{l,m} & 1 \leq l \leq N, 1 \leq m \leq M \end{array} \right. , \quad (D.76)$$

and

$$e^{\tau L_{Cv}} : \left\{ \begin{array}{ll} q_{l,m} & = q_{l,m} & 1 \leq l \leq N, 1 \leq m \leq M \\ p'_{1,1} & = p_{1,1} + \tau (q_{1,2} + q_{2,1}) \\ p'_{N,1} & = p_{N,1} + \tau (q_{N-1,1} + q_{N,2}) \\ p'_{1,M} & = p_{1,M} + \tau (q_{1,M-1} + q_{2,M}) \\ p'_{N,M} & = p_{N,M} + \tau (q_{N-1,M} + q_{N,M-1}) \\ p'_{l,1} & = p_{l,1} + \tau (q_{l-1,1} + q_{l,2} + q_{l+1,1}) & 2 \leq l \leq N-1 \\ p'_{l,M} & = p_{l,M} + \tau (q_{l-1,M} + q_{l,M-1} + q_{l+1,M}) & 2 \leq l \leq N-1 \\ p'_{1,m} & = p_{1,m} + \tau (q_{1,m-1} + q_{1,m+1} + q_{2,m}) & 2 \leq m \leq M-1 \\ p'_{N,m} & = p_{N,m} + \tau (q_{N-1,m} + q_{N,m-1} + q_{N,m+1}) & 2 \leq m \leq M-1 \\ p'_{l,m} & = p_{l,m} + \tau (q_{l-1,m} + q_{l,m-1} + q_{l,m+1} + q_{l+1,m}) & 2 \leq l \leq N-1, 2 \leq m \leq M-1 \\ \delta q'_{l,m} & = \delta q_{l,m} & 1 \leq l \leq N, 1 \leq m \leq M \\ \delta p'_{1,1} & = \delta p_{1,1} + \tau (\delta q_{1,2} + \delta q_{2,1}) \\ \delta p'_{N,1} & = \delta p_{N,1} + \tau (\delta q_{N-1,1} + \delta q_{N,2}) \\ \delta p'_{1,M} & = \delta p_{1,M} + \tau (\delta q_{1,M-1} + \delta q_{2,M}) \\ \delta p'_{N,M} & = \delta p_{N,M} + \tau (\delta q_{N-1,M} + \delta q_{N,M-1}) \\ \delta p'_{l,1} & = \delta p_{l,1} + \tau (\delta q_{l-1,1} + \delta q_{l,2} + \delta q_{l+1,1}) & 2 \leq l \leq N-1 \\ \delta p'_{l,M} & = \delta p_{l,M} + \tau (\delta q_{l-1,M} + \delta q_{l,M-1} + \delta q_{l+1,M}) & 2 \leq l \leq N-1 \\ \delta p'_{1,m} & = \delta p_{1,m} + \tau (\delta q_{1,m-1} + \delta q_{1,m+1} + \delta q_{2,m}) & 2 \leq m \leq M-1 \\ \delta p'_{N,m} & = \delta p_{N,m} + \tau (\delta q_{N-1,m} + \delta q_{N,m-1} + \delta q_{N,m+1}) & 2 \leq m \leq M-1 \\ \delta p'_{l,m} & = \delta p_{l,m} + \tau (\delta q_{l-1,m} + \delta q_{l,m-1} + \delta q_{l,m+1} + \delta q_{l+1,m}) & 2 \leq l \leq N-1, 2 \leq m \leq M-1 \end{array} \right. . \quad (D.77)$$

Bibliography

- A. Abad, R. Barrio, F. Blesa, and M. Rodríguez. Algorithm 924: Tides, a Taylor series integrator for differential equations. *ACM Transactions on Mathematical Software (TOMS)*, 39(1):5, 2012.
- A. Abad, R. Barrio, F. Blesa, and M. Rodríguez. Tides: Taylor series integrator for differential equations, 2014. URL <https://sourceforge.net/projects/tidesodes/>.
- M. Abramowitz and I. A. Stegun. Handbook of mathematical functions (applied mathematics series 55). *Washington: National Bureau of Standards*, 1964.
- V. Achilleos, G. Theocharis, and C. Skokos. Energy transport in one-dimensional disordered granular solids. *Physical Review E*, 93(2):022903, 2016.
- V. Achilleos, G. Theocharis, and C. Skokos. Chaos and Anderson-like localization in polydisperse granular chains. *Physical Review E*, 97(4):042220, 2018.
- P. W. Anderson. Absence of diffusion in certain random lattices. *Physical Review*, 109(5):1492, 1958.
- C. G. Antonopoulos, T. Bountis, C. Skokos, and L. Drossos. Complex statistics and diffusion in nonlinear disordered particle chains. *Chaos: An Interdisciplinary Journal of Nonlinear Science*, 24(2):024405, 2014.
- C. G. Antonopoulos, T. Bountis, and L. Drossos. Coupled symplectic maps as models for subdiffusive processes in disordered Hamiltonian lattices. *Applied Numerical Mathematics*, 104:110–119, 2016.
- C. G. Antonopoulos, C. Skokos, T. Bountis, and S. Flach. Analyzing chaos in higher order disordered quartic-sextic Klein-Gordon lattices using q-statistics. *Chaos, Solitons & Fractals*, 104:129–134, 2017.
- S. Aubry. Kam tori and absence of diffusion of a wave-packet in the 1d random dnls model. *International Journal of Bifurcation and Chaos*, 21(08):2125–2145, 2011.
- J. Barré and T. Dauxois. Lyapunov exponents as a dynamical indicator of a phase transition. *EPL (Europhysics Letters)*, 55(2):164, 2001.
- R. Barrio. Performance of the Taylor series method for odes/daes. *Applied Mathematics and Computation*, 163(2):525–545, 2005.
- R. Barrio and A. Shilnikov. Parameter-sweeping techniques for temporal dynamics of neuronal systems: case study of Hindmarsh-Rose model. *The Journal of Mathematical Neuroscience*, 1(1):6, 2011.
- R. Barrio, A. Dena, and W. Tucker. A database of rigorous and high-precision periodic orbits of the Lorenz model. *Computer Physics Communications*, 194:76–83, 2015.
- D. Basko. Weak chaos in the disordered nonlinear Schrödinger chain: destruction of Anderson localization by Arnold diffusion. *Annals of Physics*, 326(7):1577–1655, 2011.
- D. Basko. Local nature and scaling of chaos in weakly nonlinear disordered chains. *Physical Review E*, 86(3):036202, 2012.
- D. Basko. Kinetic theory of nonlinear diffusion in a weakly disordered nonlinear Schrödinger chain in the regime of homogeneous chaos. *Physical Review E*, 89(2):022921, 2014.
- J. Bellissard and D. Shepelyanski. Boris Chirikov, a pioneer in classical and quantum chaos. In *Annales de l’IHP Physique théorique*, volume 68, pages 379–380, 1998.
- G. Benettin, L. Galgani, A. Giorgilli, and J.-M. Strelcyn. Lyapunov characteristic exponents for smooth dynamical systems and for Hamiltonian systems; a method for computing all of them. part 2: Numerical application. *Meccanica*, 15(1):21, 1980.

- G. Benettin, S. Pasquali, and A. Ponno. The Fermi–Pasta–Ulam problem and its underlying integrable dynamics: an approach through Lyapunov exponents. *Journal of Statistical Physics*, 171(4):521–542, 2018.
- G. Berman and F. Izrailev. The Fermi–Pasta–Ulam problem: fifty years of progress. *Chaos: An Interdisciplinary Journal of Nonlinear Science*, 15(1):015104, 2005.
- J. Billy, V. Josse, Z. Zuo, A. Bernard, B. Hambrecht, P. Lugan, D. Clément, L. Sanchez-Palencia, P. Bouyer, and A. Aspect. Direct observation of Anderson localization of matter waves in a controlled disorder. *Nature*, 453(7197):891–894, 2008.
- S. Blanes and F. Casas. *A concise introduction to geometric numerical integration*. Chapman and Hall/CRC, 2016.
- S. Blanes, F. Casas, A. Farres, J. Laskar, J. Makazaga, and A. Murua. New families of symplectic splitting methods for numerical integration in dynamical astronomy. *Applied Numerical Mathematics*, 68:58–72, 2013.
- J. Bodyfelt, T. Lapyteva, C. Skokos, D. Krimer, and S. Flach. Nonlinear waves in disordered chains: Probing the limits of chaos and spreading. *Physical Review E*, 84(1):016205, 2011a.
- J. D. Bodyfelt, T. Lapyteva, G. Gligoric, D. Krimer, C. Skokos, and S. Flach. Wave interactions in localizing media – A coin with many faces. *International Journal of Bifurcation and Chaos*, 21(08):2107–2124, 2011b.
- A. Bountis, K. Kaloudis, T. Oikonomou, B. M. Manda, and C. Skokos. Stability properties of 1-dimensional hamiltonian lattices with nonanalytic potentials. *International Journal of Bifurcation and Chaos*, 30(15):2030047, 2020.
- D. K. Campbell, S. Flach, and Y. S. Kivshar. Localizing energy through nonlinearity and discreteness. *Physics Today*, 57(1):43–49, 2004.
- D. K. Campbell, P. Rosenau, and G. M. Zaslavsky. Introduction: the Fermi–Pasta–Ulam problem – the first fifty years. *Chaos: An Interdisciplinary Journal of Nonlinear Science*, 15(1):015101, 2005.
- F. Casas and A. Escorihuela-Tomàs. Composition methods for dynamical systems separable into three parts. *Mathematics*, 8(4):533, 2020.
- A. Chabanov, M. Stoytchev, and A. Genack. Statistical signatures of photon localization. *Nature*, 404(6780):850–853, 2000.
- J. E. Chambers. A hybrid symplectic integrator that permits close encounters between massive bodies. *Monthly Notices of the Royal Astronomical Society*, 304(4):793–799, 1999.
- J. E. Chambers. N-body integrators for planets in binary star systems. In *Planets in Binary Star Systems*, pages 239–263. Springer, 2010.
- B. V. Chirikov. Research concerning the theory of non-linear resonance and stochasticity. Technical report, CM-P00100691, 1971.
- B. V. Chirikov. A universal instability of many-dimensional oscillator systems. *Physics Reports*, 52(5):263–379, 1979.
- D. N. Christodoulides, F. Lederer, and Y. Silberberg. Discretizing light behaviour in linear and nonlinear waveguide lattices. *Nature*, 424(6950):817–823, 2003.
- W. S. Cleveland and S. J. Devlin. Locally weighted regression: an approach to regression analysis by local fitting. *Journal of the American Statistical Association*, 83(403):596–610, 1988.
- C. M. Da Fonseca and V. Kowalenko. Eigenpairs of a family of tridiagonal matrices: three decades later. *Acta Mathematica Hungarica*, pages 1–14, 2019.
- A. Dang Koko, C. Tabi, H. Ekobena Fouda, A. Mohamadou, and T. Kofané. Nonlinear charge transport in the helicoidal dna molecule. *Chaos: An Interdisciplinary Journal of Nonlinear Science*, 22(4):043110, 2012.
- C. Danieli, D. Campbell, and S. Flach. Intermittent many-body dynamics at equilibrium. *Physical Review E*, 95(6):060202, 2017.

- C. Danieli, B. Many Manda, T. Mithun, and C. Skokos. Computational efficiency of numerical integration methods for the tangent dynamics of many-body Hamiltonian systems in one and two spatial dimensions. *Mathematics in Engineering*, 1:447–488, 2019a.
- C. Danieli, T. Mithun, Y. Kati, D. K. Campbell, and S. Flach. Dynamical glass in weakly nonintegrable Klein-Gordon chains. *Physical Review E*, 100(3):032217, 2019b.
- T. Dauxois, M. Peyrard, and A. R. Bishop. Entropy-driven dna denaturation. *Physical Review E*, 47(1):R44, 1993.
- T. Dauxois, S. Ruffo, and A. Torcini. Modulational estimate for the maximal Lyapunov exponent in Fermi–Pasta–Ulam chains. *Physical Review E*, 56(6):R6229, 1997.
- S. Eggl and R. Dvorak. An introduction to common numerical integration codes used in dynamical astronomy. In *Dynamics of small solar system bodies and exoplanets*, pages 431–480. Springer, 2010.
- L. Ermann and D. L. Shepelyansky. Destruction of Anderson localization by nonlinearity in kicked rotator at different effective dimensions. *Journal of Physics A: Mathematical and Theoretical*, 47(33):335101, 2014.
- A. Farrés, J. Laskar, S. Blanes, F. Casas, J. Makazaga, and A. Murua. High precision symplectic integrators for the solar system. *Celestial Mechanics and Dynamical Astronomy*, 116(2):141–174, 2013.
- S. Flach. Spreading of waves in nonlinear disordered media. *Chemical Physics*, 375(2-3):548–556, 2010.
- S. Flach. Nonlinear lattice waves in random potentials. In *Nonlinear Optical and Atomic Systems*, pages 1–48. Springer, 2015.
- S. Flach. Spreading, nonergodicity, and selftrapping: a puzzle of interacting disordered lattice waves. In *Nonlinear Dynamics: Materials, Theory and Experiments*, pages 45–57. Springer, 2016.
- S. Flach and A. V. Gorbach. Discrete breathers—advances in theory and applications. *Physics Reports*, 467(1-3):1–116, 2008.
- S. Flach and A. Ponno. The Fermi–Pasta–Ulam problem: Periodic orbits, normal forms and resonance overlap criteria. *Physica D: Nonlinear Phenomena*, 237(7):908–917, 2008.
- S. Flach and C. R. Willis. Discrete breathers. *Physics Reports*, 295(5):181–264, 1998.
- S. Flach, M. Ivanchenko, O. Kanakov, and K. Mishagin. Periodic orbits, localization in normal mode space, and the Fermi–Pasta–Ulam problem. *American Journal of Physics*, 76(4):453–459, 2008.
- S. Flach, D. Krimer, and C. Skokos. Universal spreading of wave packets in disordered nonlinear systems. *Physical Review Letters*, 102(2):024101, 2009.
- B. Fornberg. Generation of finite difference formulas on arbitrarily spaced grids. *Mathematics of Computation*, 51(184):699–706, 1988.
- B. Fornberg. Classroom note: Calculation of weights in finite difference formulas. *SIAM Review*, 40(3):685–691, 1998.
- C. Froeschlé. Numerical study of a four-dimensional mapping. *Astronomy and Astrophysics*, 16:172, 1972.
- I. Garcia-Mata and D. L. Shepelyansky. Delocalization induced by nonlinearity in systems with disorder. *Physical Review E*, 79(2):026205, 2009.
- A. Genack and A. Chabanov. Signatures of photon localization. *Journal of Physics A: Mathematical and General*, 38(49):10465, 2005.
- E. Gerlach and C. Skokos. Dynamical systems, differential equations and applications. *Discr. Cont. Dyn. Sys.-Supp. AIMS*, pages 475–84, 2011.
- E. Gerlach, S. Eggl, and C. Skokos. Efficient integration of the variational equations of multidimensional Hamiltonian systems: Application to the Fermi–Pasta–Ulam lattice. *International Journal of Bifurcation and Chaos*, 22(09):1250216, 2012.
- E. Gerlach, J. Meichsner, and C. Skokos. On the symplectic integration of the discrete nonlinear Schrödinger equation with disorder. *The European Physical Journal Special Topics*, 225(6-7):1103–1114, 2016.

- S. A. Gershgorin. Über die abgrenzung der eigenwerte einer matrix. *Izv. Akad. Nauk. USSR Otd. Fiz.-Mat. Nauk (in German)*, (6):749–754, 1931.
- H. Goldstein, C. Poole, and J. Safko. *Classical mechanics*, 2002.
- K. Goździewski, S. Breiter, and W. Borczyk. The long-term stability of extrasolar system HD 37124. Numerical study of resonance effects. *Monthly Notices of the Royal Astronomical Society*, 383(3): 989–999, 2008.
- S. A. Gredeskul and Y. S. Kivshar. Propagation and scattering of nonlinear waves in disordered systems. *Physics Reports*, 216(1):1–61, 1992.
- W. Gröbner. *Die Lie-reihen und ihre Anwendungen*, volume 3. Deutscher Verlag der Wissenschaften, 1967.
- E. Hairer. Fortran and matlab codes, 2009. URL <http://www.unige.ch/~hairer/software.html>.
- E. Hairer, S. Norsett, and G. Wanner. *Solving Ordinary Differential Equations I: Nonstiff Problems, volume Second Revised Edition*. Springer-Verlag, 1993.
- E. Hairer, C. Lubich, and G. Wanner. *Geometric numerical integration: structure-preserving algorithms for ordinary differential equations*, volume 31. Springer Science & Business Media, 2006.
- A. Hanslmeier and R. Dvorak. Numerical integration with lie series. *Astronomy and Astrophysics*, 132: 203, 1984.
- Y. He, Y. Sun, J. Liu, and H. Qin. Volume-preserving algorithms for charged particle dynamics. *Journal of Computational Physics*, 281:135–147, 2015.
- Y. He, Y. Sun, J. Liu, and H. Qin. Higher order volume-preserving schemes for charged particle dynamics. *Journal of Computational Physics*, 305:172–184, 2016.
- M. Hénon and C. Heiles. The applicability of the third integral of motion: some numerical experiments. *The Astronomical Journal*, 69:73, 1964.
- G. Herbert. *Classical Mechanics*. Addison-Wesley Publishing Company, 2nd edition, 1980.
- A. Hilboll. andreas-h/pyloess, 2007. URL <https://github.com/andreas-h/pyloess/blob/master/src/lowess.f>.
- M. Hillebrand, G. Kalosakas, A. Schwellnus, and C. Skokos. Heterogeneity and chaos in the Peyrard-Bishop-Dauxois dna model. *Physical Review E*, 99(2):022213, 2019.
- M. Hillebrand, B. Many Manda, G. Kalosakas, E. Gerlach, and C. Skokos. Chaotic dynamics of graphene and graphene nanoribbons. *Chaos: An Interdisciplinary Journal of Nonlinear Science*, 30(6):063150, 2020.
- H. Hu, A. Strybulevych, J. Page, S. E. Skipetrov, and B. A. van Tiggelen. Localization of ultrasound in a three-dimensional elastic network. *Nature Physics*, 4(12):945–948, 2008.
- A. Iomin. Subdiffusion in the nonlinear Schrödinger equation with disorder. *Physical Review E*, 81(1): 017601, 2010.
- A. Iomin. Subdiffusion in classical and quantum nonlinear Schrödinger equations with disorder. *Computers & Mathematics with Applications*, 73(6):914–930, 2017.
- A. Iserles and G. Quispel. Why geometric numerical integration? In *Discrete Mechanics, Geometric Integration and Lie-Butcher Series*, pages 1–28. Springer, 2018.
- M. Ivanchenko, T. Laptyeva, and S. Flach. Anderson localization or nonlinear waves: A matter of probability. *Physical Review Letters*, 107(24):240602, 2011.
- M. Ivanchenko, T. Laptyeva, and S. Flach. Quantum chaotic subdiffusion in random potentials. *Physical Review B*, 89(6):060301, 2014.
- F. M. Izrailev. Simple models of quantum chaos: spectrum and eigenfunctions. *Physics Reports*, 196 (5-6):299–392, 1990.
- A. Jeffrey and D. Zwillinger. *Table of integrals, series, and products*. Elsevier, 2007.

- M. Johansson. Discrete nonlinear Schrödinger approximation of a mixed Klein–Gordon/Fermi–Pasta–Ulam chain: Modulational instability and a statistical condition for creation of thermodynamic breathers. *Physica D: Nonlinear Phenomena*, 216(1):62–70, 2006.
- M. Johansson and K. Ø. Rasmussen. Statistical mechanics of general discrete nonlinear Schrödinger models: Localization transition and its relevance for Klein-Gordon lattices. *Physical Review E*, 70(6):066610, 2004.
- M. Johansson, G. Kopidakis, and S. Aubry. Kam tori in 1d random discrete nonlinear Schrödinger model? *Europhysics Letters*, 91(5):50001, 2010.
- W. Kahan and R.-C. Li. Composition constants for raising the orders of unconventional schemes for ordinary differential equations. *Mathematics of computation*, 66(219):1089–1099, 1997.
- Y. Kati, X. Yu, and S. Flach. Density resolved wave packet spreading in disordered Gross-Pitaevskii lattices. *SciPost Phys. Core*, 3:6, 2020.
- Y. S. Kivshar and G. P. Agrawal. *Optical solitons: from fibers to photonic crystals*. Academic press, 2003.
- Y. S. Kivshar and M. Peyrard. Modulational instabilities in discrete lattices. *Physical Review A*, 46(6):3198, 1992.
- Y. Kominis, K. Hizanidis, D. Constantinescu, and O. Dumbrajs. Explicit near-symplectic mappings of Hamiltonian systems with Lie-generating functions. *Journal of Physics A: Mathematical and Theoretical*, 41(11):115202, 2008.
- S. Kondov, W. McGehee, J. Zirbel, and B. DeMarco. Three-dimensional Anderson localization of ultracold matter. *Science*, 334(6052):66–68, 2011.
- G. Kopidakis, S. Komineas, S. Flach, and S. Aubry. Absence of wave packet diffusion in disordered nonlinear systems. *Physical Review Letters*, 100(8):084103, 2008.
- P. Koseleff. Exhaustive search of symplectic integrators using computer algebra. *Integration algorithms and classical mechanics (Toronto, ON, 1993)*, *Fields Inst. Commun*, 10:103–119, 1996.
- B. Kramer and A. MacKinnon. Localization: theory and experiment. *Reports on Progress in Physics*, 56(12):1469, 1993.
- D. Krimer and S. Flach. Statistics of wave interactions in nonlinear disordered systems. *Physical Review E*, 82(4):046221, 2010.
- D. O. Krimer, R. Khomeriki, and S. Flach. Delocalization and spreading in a nonlinear stark ladder. *Physical Review E*, 80(3):036201, 2009.
- Y. Lahini, A. Avidan, F. Pozzi, M. Sorel, R. Morandotti, D. N. Christodoulides, and Y. Silberberg. Anderson localization and nonlinearity in one-dimensional disordered photonic lattices. *Physical Review Letters*, 100(1):013906, 2008.
- Y. Lahini, R. Pugatch, F. Pozzi, M. Sorel, R. Morandotti, N. Davidson, and Y. Silberberg. Observation of a localization transition in quasiperiodic photonic lattices. *Physical Review Letters*, 103(1):013901, 2009.
- L. D. Landau and E. M. Lifshitz. *Statistical Physics*, volume 5 of Course of Theoretical Physics. Elsevier Butterworth-Heinemann, third edition, 1980.
- T. Laptjeva, J. Bodyfelt, D. Krimer, C. Skokos, and S. Flach. The crossover from strong to weak chaos for nonlinear waves in disordered systems. *EPL (Europhysics Letters)*, 91(3):30001, 2010.
- T. Laptjeva, J. Bodyfelt, and S. Flach. Subdiffusion of nonlinear waves in two-dimensional disordered lattices. *Europhysics Letters*, 98(6):60002, 2012.
- T. Laptjeva, J. Bodyfelt, and S. Flach. Do nonlinear waves in random media follow nonlinear diffusion equations? *Physica D: Nonlinear Phenomena*, 256:1–6, 2013.
- T. Laptjeva, M. Ivanchenko, and S. Flach. Nonlinear lattice waves in heterogeneous media. *Journal of Physics A: Mathematical and Theoretical*, 47(49):493001, 2014.

- T. V. Lapyteva. *Nonlinear waves in random lattices: localization and spreading*. PhD thesis, Max-Planck-Institut für Physik komplexer Systeme Dresden angefertigt, 2013.
- J. Laskar and P. Robutel. High order symplectic integrators for perturbed Hamiltonian systems. *Celestial Mechanics and Dynamical Astronomy*, 80(1):39–62, 2001.
- J. Laskar and T. Vaillant. Dedicated symplectic integrators for rotation motions. *Celestial Mechanics and Dynamical Astronomy*, 131(3):15, 2019.
- A. J. Lichtenberg and M. A. Lieberman. *Regular and chaotic dynamics*, volume 38. Springer Science & Business Media, 2013.
- L. Losonczy. Eigenvalues and eigenvectors of some tridiagonal matrices. *Acta Mathematica Hungarica*, 60(3-4):309–322, 1992.
- E. Lucioni, B. Deissler, L. Tanzi, G. Roati, M. Zaccanti, M. Modugno, M. Larcher, F. Dalfovo, M. Inguscio, and G. Modugno. Observation of subdiffusion in a disordered interacting system. *Physical Review Letters*, 106(23):230403, 2011.
- E. Lucioni, L. Tanzi, C. D’Errico, M. Moratti, M. Inguscio, and G. Modugno. Modeling the transport of interacting matter waves in a disordered system by a nonlinear diffusion equation. *Physical Review E*, 87(4):042922, 2013.
- R. MacKay and S. Aubry. Proof of existence of breathers for time-reversible or Hamiltonian networks of weakly coupled oscillators. *Nonlinearity*, 7(6):1623, 1994.
- A. Mallick, T. Mithun, and S. Flach. Quench dynamics in disordered two-dimensional Gross-Pitaevskii lattices. *Phys. Rev. A*, 102:033301, 2020.
- B. Many Manda, B. Senyange, and C. Skokos. Chaotic wave-packet spreading in two-dimensional disordered nonlinear lattices. *Physical Review E*, 101(3):032206, 2020.
- A. J. Martínez, P. G. Kevrekidis, and M. A. Porter. Superdiffusive transport and energy localization in disordered granular crystals. *Physical Review E*, 93(2):022902, 2016.
- R. I. McLachlan. Composition methods in the presence of small parameters. *BIT Numerical Mathematics*, 35(2):258–268, 1995.
- E. Michaely and S. Fishman. Effective noise theory for the nonlinear Schrödinger equation with disorder. *Physical Review E*, 85(4):046218, 2012.
- A. Milovanov and A. Iomin. Localization-delocalization transition on a separatrix system of nonlinear Schrödinger equation with disorder. *EPL (Europhysics Letters)*, 100(1):10006, 2012.
- L. Miranda Filho, M. Amato, Y. Elskens, and T. Rocha Filho. Contribution of individual degrees of freedom to Lyapunov vectors in many-body systems. *Communications in Nonlinear Science and Numerical Simulation*, 74:236–247, 2019.
- T. Mithun, Y. Kati, C. Danieli, and S. Flach. Weakly nonergodic dynamics in the Gross-Pitaevskii lattice. *Physical Review Letters*, 120(18):184101, 2018.
- T. Mithun, C. Danieli, Y. Kati, and S. Flach. Dynamical glass and ergodization times in classical Josephson junction chains. *Physical Review Letters*, 122(5):054102, 2019.
- M. Molina. Transport of localized and extended excitations in a nonlinear Anderson model. *Physical Review B*, 58(19):12547, 1998.
- M. Molina, N. Lazarides, and G. Tsironis. Optical surface modes in the presence of nonlinearity and disorder. *Physical Review E*, 85(1):017601, 2012.
- O. Morsch and M. Oberthaler. Dynamics of Bose-Einstein condensates in optical lattices. *Reviews of Modern Physics*, 78(1):179, 2006.
- M. Mulansky. Scaling of chaos in strongly nonlinear lattices. *Chaos: An Interdisciplinary Journal of Nonlinear Science*, 24(2):024401, 2014.
- M. Mulansky and A. Pikovsky. Spreading in disordered lattices with different nonlinearities. *EPL (Europhysics Letters)*, 90(1):10015, 2010.

- M. Mulansky and A. Pikovsky. Scaling properties of energy spreading in nonlinear Hamiltonian two-dimensional lattices. *Physical Review E*, 86(5):056214, 2012.
- M. Mulansky and A. Pikovsky. Energy spreading in strongly nonlinear disordered lattices. *New Journal of Physics*, 15(5):053015, 2013.
- M. Mulansky, K. Ahnert, A. Pikovsky, and D. L. Shepelyansky. Dynamical thermalization of disordered nonlinear lattices. *Physical Review E*, 80(5):056212, 2009.
- M. Mulansky, K. Ahnert, and A. Pikovsky. Scaling of energy spreading in strongly nonlinear disordered lattices. *Physical Review E*, 83(2):026205, 2011.
- F. Neri. Lie algebras and canonical integration. *Department of Physics, University of Maryland*, preprint, 1988.
- A. Ngapasare, G. Theocharis, O. Richoux, C. Skokos, and V. Achilleos. Chaos and Anderson localization in disordered classical chains: Hertzian versus Fermi–Pasta–Ulam–Tsingou models. *Physical Review E*, 99(3):032211, 2019.
- V. Oganesyan, A. Pal, and D. A. Huse. Energy transport in disordered classical spin chains. *Physical Review B*, 80(11):115104, 2009.
- A. A. Ovchinnikov, N. S. Erikhman, and K. A. Pronin. *Vibrational-rotational excitations in nonlinear molecular systems*. Springer Science & Business Media, 2012.
- M. Peyrard. Nonlinear dynamics and statistical physics of dna. *Nonlinearity*, 17(2):R1, 2004.
- A. Pikovsky. Scaling of energy spreading in a disordered ding-dong lattice. *Journal of Statistical Mechanics: Theory and Experiment*, 2020(5):053301, 2020.
- A. Pikovsky and S. Fishman. Scaling properties of weak chaos in nonlinear disordered lattices. *Physical Review E*, 83(2):025201, 2011.
- A. Pikovsky and A. Politi. *Lyapunov exponents: a tool to explore complex dynamics*. Cambridge University Press, 2016.
- A. Pikovsky and D. Shepelyansky. Destruction of Anderson localization by a weak nonlinearity. *Physical Review Letters*, 100(9):094101, 2008.
- T. Prosen and M. Robnik. Energy transport and detailed verification of Fourier heat law in a chain of colliding harmonic oscillators. *Journal of Physics A: Mathematical and General*, 25(12):3449, 1992.
- T. Quinn, R. P. Perrine, D. C. Richardson, and R. Barnes. A symplectic integrator for Hill’s equations. *The Astronomical Journal*, 139(2):803, 2010.
- K. Rasmussen, T. Cretegny, P. Kevrekidis, and N. Grønbech-Jensen. Statistical mechanics of a discrete nonlinear system. *Physical Review Letters*, 84(17):3740, 2000.
- D. Rivas and M. I. Molina. Seltrapping in flat band lattices with nonlinear disorder. *Scientific Reports*, 10(1):1–9, 2020.
- G. Roati, C. D’Errico, L. Fallani, M. Fattori, C. Fort, M. Zaccanti, G. Modugno, M. Modugno, and M. Inguscio. Anderson localization of a non-interacting Bose–Einstein condensate. *Nature*, 453(7197):895–898, 2008.
- S. Roy and A. Pikovsky. Spreading of energy in the ding-dong model. *Chaos: An Interdisciplinary Journal of Nonlinear Science*, 22(2):026118, 2012.
- E. Runge and R. Zimmermann. Manifestations of Anderson localization in semiconductor optics. In *Anderson localization and Its Ramifications*, pages 145–156. Springer, 2003.
- R. D. Ruth. A canonical integration technique. *IEEE Trans. Nucl. Sci.*, 30(CERN-LEP-TH-83-14):2669–2671, 1983.
- M. Sales, W. Dias, A. R. Neto, M. Lyra, and F. de Moura. Sub-diffusive spreading and anomalous localization in a 2d Anderson model with off-diagonal nonlinearity. *Solid State Communications*, 270:6–11, 2018.

- Y. Sato and R. Klages. Anomalous diffusion in random dynamical systems. *Physical Review Letters*, 122(17):174101, 2019.
- A. V. Savin, Y. S. Kivshar, and B. Hu. Suppression of thermal conductivity in graphene nanoribbons with rough edges. *Physical Review B*, 82(19):195422, 2010.
- B. J. Schroers. *Ordinary differential equations: a practical guide*. Cambridge University Press, 2011.
- T. Schwartz, G. Bartal, S. Fishman, and M. Segev. Transport and Anderson localization in disordered two-dimensional photonic lattices. *Nature*, 446(7131):52–55, 2007.
- B. Senyange. *Chaotic behavior of one-dimensional disordered nonlinear lattices*. PhD thesis, University of Cape Town, 2021.
- B. Senyange and C. Skokos. Computational efficiency of symplectic integration schemes: application to multidimensional disordered Klein–Gordon lattices. *The European Physical Journal Special Topics*, 227(5-6):625–643, 2018.
- B. Senyange, B. M. Manda, and C. Skokos. Characteristics of chaos evolution in one-dimensional disordered nonlinear lattices. *Physical Review E*, 98(5):052229, 2018.
- B. Senyange, J.-J. du Plessis, B. Many Manda, and C. Skokos. Properties of normal modes in a modified disordered Klein-Gordon lattice: From disorder to order. *Nonlinear Phenomena in Complex System: An Interdisciplinary Journal*, 23:165–171, 2020.
- B. Shapiro. Expansion of a Bose-Einstein condensate in the presence of disorder. *Physical Review Letters*, 99(6):060602, 2007.
- H. H. Sheinflux, Y. Lumer, G. Ankonina, A. Z. Genack, G. Bartal, and M. Segev. Observation of Anderson localization in disordered nanophotonic structures. *Science*, 356(6341):953–956, 2017.
- D. Shepelyansky. Delocalization of quantum chaos by weak nonlinearity. *Physical Review Letters*, 70(12):1787, 1993.
- D. Shepelyansky. Quantum localization, chaos and nonlinear interactions. *Physica D: Nonlinear Phenomena*, 86(1-2):45–52, 1995.
- C. Skokos. Alignment indices: a new, simple method for determining the ordered or chaotic nature of orbits. *Journal of Physics A: Mathematical and General*, 34(47):10029, 2001.
- C. Skokos. The Lyapunov characteristic exponents and their computation. In *Dynamics of Small Solar System Bodies and Exoplanets*, pages 63–135. Springer, 2010.
- C. Skokos and S. Flach. Spreading of wave packets in disordered systems with tunable nonlinearity. *Physical Review E*, 82(1):016208, 2010.
- C. Skokos and E. Gerlach. Numerical integration of variational equations. *Physical Review E*, 82(3):036704, 2010.
- C. Skokos and T. Manos. The smaller (SALI) and the generalized (GALI) alignment indices: Efficient methods of chaos detection. In *Chaos Detection and Predictability*, pages 129–181. Springer, 2016.
- C. Skokos, D. Krimer, S. Komineas, and S. Flach. Delocalization of wave packets in disordered nonlinear chains. *Physical Review E*, 79(5):056211, 2009.
- C. Skokos, I. Gkolias, and S. Flach. Nonequilibrium chaos of disordered nonlinear waves. *Physical Review Letters*, 111(6):064101, 2013.
- C. Skokos, E. Gerlach, J. Bodyfelt, G. Papamikos, and S. Ettl. High order three part split symplectic integrators: Efficient techniques for the long time simulation of the disordered discrete nonlinear Schrödinger equation. *Physics Letters A*, 378(26-27):1809–1815, 2014.
- G. D. Smith. *Numerical solution of partial differential equations: finite difference methods*. Oxford University Press, 1985.
- M. Sofroniou and G. Spaletta. Derivation of symmetric composition constants for symmetric integrators. *Optimization Methods and Software*, 20(4-5):597–613, 2005.

- M. Störzer, P. Gross, C. M. Aegerter, and G. Maret. Observation of the critical regime near Anderson localization of light. *Physical Review Letters*, 96(6):063904, 2006.
- Z.-Y. Sun and X. Yu. Anomalous diffusion of discrete solitons driven by evolving disorder. *Physical Review E*, 101(6):062211, 2020.
- M. Suzuki. Fractal decomposition of exponential operators with applications to many-body theories and Monte Carlo simulations. *Physics Letters A*, 146(6):319–323, 1990.
- M. Suzuki. General theory of fractal path integrals with applications to many-body theories and statistical physics. *Journal of Mathematical Physics*, 32(2):400–407, 1991.
- O. Tieleman, C. Skokos, and A. Lazarides. Chaoticity without thermalisation in disordered lattices. *EPL (Europhysics Letters)*, 105(2):20001, 2014.
- D. Tong. Classical dynamics. *University of Cambridge, Cambridge*, 2004.
- D. Tong. Statistical physics. *University of Cambridge, Cambridge*, 2012.
- G. Tsironis and S. Aubry. Slow relaxation phenomena induced by breathers in nonlinear lattices. *Physical Review Letters*, 77(26):5225, 1996.
- I. Vakulchyk, M. V. Fistul, and S. Flach. Wave packet spreading with disordered nonlinear discrete-time quantum walks. *Physical Review Letters*, 122(4):040501, 2019.
- H. Veksler, Y. Krivolapov, and S. Fishman. Spreading for the generalized nonlinear Schrödinger equation with disorder. *Physical Review E*, 80(3):037201, 2009.
- B. Vermersch and J. C. Garreau. Interacting ultracold Bosons in disordered lattices: Sensitivity of the dynamics to the initial state. *Physical Review E*, 85(4):046213, 2012.
- B. Vermersch and J. C. Garreau. Spectral description of the dynamics of ultracold interacting Bosons in disordered lattices. *New Journal of Physics*, 15(4):045030, 2013.
- R. B. White. *The theory of toroidally confined plasmas*. World Scientific Publishing Company, 2013.
- D. S. Wiersma, P. Bartolini, A. Lagendijk, and R. Righini. Localization of light in a disordered medium. *Nature*, 390(6661):671–673, 1997.
- D. Wilczak, S. Serrano, and R. Barrio. Coexistence and dynamical connections between hyperchaos and chaos in the 4d Rossler system: a computer-assisted proof. *SIAM Journal on Applied Dynamical Systems*, 15(1):356–390, 2016.
- A. Wingen, K. Spatschek, and S. Abdullaev. Stochastic transport of magnetic field lines in the symmetric tokamak. *Contributions to Plasma Physics*, 45(7):500–513, 2005.
- H. Wolkowicz and G. P. Styan. Bounds for eigenvalues using traces. *Linear algebra and its applications*, 29:471–506, 1980.
- T. F. Xavier. Derivatives on unequally spaced grids, 2019. URL http://cococubed.asu.edu/code_pages/fdcoef.shtml.
- H. Yoshida. Construction of higher order symplectic integrators. *Physics Letters A*, 150(5-7):262–268, 1990.
- H. Yoshida. Recent progress in the theory and application of symplectic integrators. In *Qualitative and Quantitative Behaviour of Planetary Systems*, pages 27–43. Springer, 1993.
- W.-C. Yueh. Eigenvalues of several tridiagonal matrices. *Applied Mathematics e-notes*, 5(66-74):210–230, 2005.
- I. I. Yusipov, T. V. Lapyeva, A. Y. Pirova, I. B. Meyerov, S. Flach, and M. V. Ivanchenko. Quantum subdiffusion with two-and three-body interactions. *The European Physical Journal B*, 90(4):66, 2017.